



TEXAS TECH UNIVERSITY

Multidisciplinary Research in Transportation

Develop Mechanistic-Empirical Design for CRCP

Soojun Ha, Jungheum Yeon, Byounghooi Choi,
Yoonsu Jung, Dan G. Zollinger, Andrew Wimsatt,
Moon C. Won

Texas Department of Transportation

Report #: 0-5832-1
www.techmrt.ttu.edu/reports.php

May 2012

NOTICE

The United States Government and the State of Texas do not endorse products or manufacturers. Trade or manufacturers' names appear herein solely because they are considered essential to the object of this report

1. Report No. FHWA/TX-11-0-5832-1	2. Government Accession No.:	3. Recipient's Catalog No.:	
4. Title and Subtitle: Develop Mechanistic-Empirical Design for CRCP		5. Report Date: February 2011	
7. Author(s): Soojun Ha, Jungheum Yeon, Byounghooi Choi, Younsu Jung, Dan G. Zollinger, Andrew Wimsatt, Moon C. Won,		8. Performing Organization Report No. 0-5832-1	
9. Performing Organization Name and Address: Texas Tech University College of Engineering Box 41023 Lubbock, Texas 79409-1023		10. Work Unit No.(TRAIS):	
		11. Contract or Grant No.: Project 0-5832	
12. Sponsoring Agency Name And Address Texas Department Of Transportation Research and Technology Implementation Office P.O. Box 5080 Austin, TX 78763-5080		13. Type of Report and Period Cover: Technical Report 09/2007-08/2010	
		14. Sponsoring Agency Code:	
15. Supplementary Notes: Project performed in cooperation with Texas Department of Transportation and the Federal Highway Administration			
16. Abstract: Currently, TxDOT uses the AASHTO 93 design guide for the slab thickness design of continuously reinforced concrete pavement (CRCP). The AASHTO 93 design guide was developed based on the AASHTO road test, where JCP (jointed plain concrete pavement) was the major pavement evaluated and CRCP was not included. From a purely technical standpoint, the AASHTO 93 design guide is not appropriate for the design of CRCP. With ever-increasing traffic on major highways in Texas where CRCP is widely used, there is a need for a more mechanistic-empirical (ME) based pavement design procedure for CRCP. An ME-based pavement design method will allow TxDOT to optimize pavement structures to best utilize the limited financial resources available. To develop an ME based CRCP design procedure, the mechanism of punchouts was identified by field evaluations of CRCP, which included coring, deflection testing using falling weight deflectometer (FWD), and other non-destructive testing. Once the punchout mechanism was identified, mechanistic modeling was performed using a 3-dimensional finite element program. Another important element in the ME based pavement design procedures is the accuracy of a transfer function. A transfer function was developed using the data from TxDOT PMIS. A CRCP design program based on ME principles was developed, called TxCRCP-ME, with a User's Guide for the program. In the program, the effect of non-uniformity of subbase support, or the effect of erosion, was not directly addressed. From a theoretical standpoint, the effect is included in a transfer function. Sensitivity analysis was conducted to evaluate the effects of input variables and the reasonableness of the results. Since the reasonableness of TxCRCP-ME depends on the accuracy of transfer function, further efforts are recommended to refine the transfer function by collecting more accurate information on traffic, construction information and distress data. Once an accurate transfer function is developed, further sensitivity analysis will be needed to evaluate the reasonableness of the TxCRCP-ME. For the spalling issue, extensive field evaluations were conducted for the performance of spalling. A spalling model was developed and calibrated with field evaluation data.			
17. Key Words: CRCP, punchout, spalling, mechanistic-empirical pavement design, transfer function		18. Distribution Statement No Restrictions. This document is available to the public through the National Technical Information Service, Springfield, VA 22161, www.ntis.gov	
19. Security Classif. (of this report) Unclassified	20. Security Classif. (of this page) Unclassified	21. No. Of Pages 246	22. Price

DEVELOP MECHANISTIC-EMPIRICAL DESIGN FOR CRCP

By

Soojun Ha

Jungheum Yeon

Byounghooi Choi

Yoonsu Jung

Dan G Zollinger

Andrew Wimsatt

Moon C. Won

Texas Tech University

Project Report 0-5832-1

Project Number 0-5832

Performed in Cooperation with the
Texas Department of Transportation
and the
Federal Highway Administration
Center for Multidisciplinary Research in Transportation
Department of Civil and Environmental Engineering
Texas Tech University
Box 41023
Lubbock, TX 79409-1023

Acknowledgments

The authors express their appreciation to the project director, Ms. Hua Chen and the PMC members - Ms. Darlene Goehl, Mr. Joe Leidy, Ms. Elizabeth Lukefahr, Mr. James Mack, Mr. Mark McDaniel, Mr. Abbas Mehdibeigi, Mr. Magdy Mikhail, Mr. Elias Rmeili, and Mr. Richard Rogers - for their support and contribution throughout the project. The support provided by Dr. German Claros of RTI for this project is also appreciated.

Products

This report contains no products.

AUTHOR'S DISCLAIMER

The contents of this report reflect the views of the authors who are responsible for the facts and the accuracy of the data presented herein. The contents do not necessarily reflect the official view of policies of the Texas Department of Transportation or the Federal Highway Administration. This report does not constitute a standard, specification, or regulation.

A limited set of CRCP field performance data was used to develop the TxCRCP-ME. To refine TxCRCP- ME punchout mode, more accurate field performances are collected by Research project 0-6274 Project Level Performance Database for Rigid Pavements in Texas, Phase II. The Spalling model has not been validated by field performances.

PATENT DISCLAIMER

There was no invention or discovery conceived or first actually reduced to practice in the course of or under this contract, including any art, method, process, machine, manufacture, design or composition of matter, or any new useful improvement thereof, or any variety of plant which is or may be patentable under the patent laws of the United States of America or any foreign country.

ENGINEERING DISCLAIMER

Not intended for construction, bidding, or permit purposes.

TRADE NAMES AND MANUFACTURERS' NAMES

The United States Government and the State of Texas do not endorse products or manufacturers. Trade or manufacturers' names appear herein solely because they are considered essential to the object of this report.

Table of Contents

Acknowledgements iv

Disclaimers.....v

Table of Contents vii

List of Figures..... xi

List of Tables xvii

Chapter 1 Introduction..... 1

Chapter 2 CRCP Distresses and Their Mechanisms5

2.1 Punchouts in CRCP.....4

2.2 Types of Punchout in Texas.....6

2.2.1 Distresses in transverse construction joint6

2.2.2 Distresses due to horizontal cracking9

2.2.3 Distresses due to construction quality.....15

2.2.4 Distresses due to deficient support of base/subgrade material15

2.2.5 Distresses due to poor load transfer at longitudinal joints16

2.3 Punchout development mechanism.....18

**Chapter 3 Mechanistic Modeling of Punchouts and Development of Mechanistic-Empirical
CRCP Design Procedures.....23**

3.1 Introduction.....23

3.2 Preliminary Analysis.....23

3.2.1 Behavior of CRCP without transverse cracks.....24

3.2.2 Behavior of CRCP with transverse cracks.....	30
3.3 Development of Mechanistic Modeling.....	36
3.3.1 Finite element modeling	37
3.3.2 Material properties	40
3.3.3 Variables for sensitivity analysis	41
3.4 Numerical Results.....	46
3.4.1 Response to traffic loading	46
3.4.2 Response to environmental loading	57
3.4.3 Response to combined loading	62
3.4.4 Effect of aggregate interlock.....	97
Chapter 4 CRCP Mechanistic Empirical Design Program.....	103
4.1 Formulation of TxCRCP-ME	104
4.1.1 Assembly of input values.....	105
4.1.2 Concrete stress evaluations.....	105
4.1.3 Fatigue life of concrete slab and damage estimation	107
4.1.4 Prediction of punchouts	108
4.1.5 Presentation of analysis results	108
4.1.6 Summary	109
4.2 Development of transfer function	109
4.3 Sensitivity analysis.....	114
4.3.1 Effect of design ESALs	115
4.3.2 Effect of longitudinal steel amount.....	116
4.3.3 Effect of slab thickness	117
4.3.4 Effect of concrete setting temperature	117
4.3.5 Effect of concrete coefficient of thermal expansion (CTE).....	119
4.3.6 Effect of concrete strength and modulus of elasticity.....	120

4.3.7 Summary	121
Chapter 5 Spalling Performance	123
5.1 Field Performance	124
5.2 Nature of Spalling	125
5.3 Field Performance Sites	127
5.3.1 US 290-Hempstead	128
5.3.2 US 290-Cypress	135
5.3.3 SH 99	141
5.3.4 SH 225	143
5.3.5 SH 288	148
5.3.6 FM 1960	154
5.4 Summary Observations from Field Survey	155
Chapter 6 Modeling Spalling Performance	159
6.1 Delamination Modeling	159
6.2 Sensitivity of Moisture on Delamination Stress	162
6.3 Concrete Strength Related to Delamination	165
6.4 Delamination Prediction	168
6.5 Spall Stress Performance Modeling	172
6.6 Spalling Stress	174
6.7 Approach to Spalling Calibration	175
6.8 Assessment of Traffic Data	175
6.9 Calibration Loads to Failure	177
6.10 Spalling – Damage Model Calibration	180
6.11 Application of Field Performance Calibration to Design	183

6.12 Adjustment of Design Parameter for Chipping and Shallow Spalling	184
6.13 Application of Factorial Design Analysis to Calibration.....	187
6.14 Validation of α and β Parameters for Prediction of Spalling.....	188
6.15 Spalling Validation	189
6.16 Conclusions.....	190
Chapter 7 Conclusions and Recommendations	193
7.1 Conclusions.....	193
7.2 Recommendations.....	196
References	197
Appendix A.....	202
Appendix B.....	209
Appendix C.....	210
Appendix D.....	214
Appendix E.....	220

List of Figures

Figure 2.1 (a) Punchout in LTPP Document	6
Figure 2.1 (b) Punchout in NCHRP document	6
Figure 2.2 (a) Distress at transverse construction joint	7
Figure 2.2 (b) Distress at transverse construction joint	7
Figure 2.3 (a) Slab displacement measurement at transverse construction joint.....	8
Figure 2.3 (b) Slab displacement for 2 days after concrete placement.....	8
Figure 2.4 (a) Horizontal cracking observed in IH35 in 1999	10
Figure 2.4 (b) Distress resulting from early age horizontal cracking	10
Figure 2.5 (a) Horizontal cracking on IH35 observed in 2010.....	11
Figure 2.5 (b) Distress due to horizontal cracking.....	11
Figure 2.6 (a) 6-in. CRCP on US281 in Wichita Falls	12
Figure 2.6 (b) Horizontal and longitudinal cracks on US281 in Wichita Falls	12
Figure 2.7 (a) Horizontal shear stress as affected by modulus ratio	13
Figure 2.7 (b) Horizontal shear stress as affected by slab thickness	13
Figure 2.8 (a) Close-up view of distress in 6-in CRCP in Dallas	14
Figure 2.8 (b) Condition of 6-in CRCP in Houston.....	14
Figure 2.9 (a) CRCP distress due to construction quality issues	15
Figure 2.9 (b) CRCP distress due to construction quality issues	15
Figure 2.10 (a) Distress due to consolidation of subgrade/subbase.....	16
Figure 2.10 (b) Distress due to consolidation of subgrade/subbase.....	16
Figure 2.11 (a) Distress due to poor load transfer at longitudinal joint.....	17
Figure 2.11 (b) Distress due to poor load transfer at longitudinal joint.....	17
Figure 2.12 (a) Slab edge deflection with different shoulder type	18

Figure 2.12 (b) Slab edge deflection for various slab thicknesses and k values.....	18
Figure 2.13 (a) Distress observed on August 23, 2005.....	19
Figure 2.13 (b) Distress observed on November 16, 2007.....	19
Figure 2.13 (c) Distress observed on August 12, 2008.....	19
Figure 2.13 (d) Coring locations and cores taken on November 13, 2008.....	19
Figure 2.14 (a) Longitudinal cracking in the wheel path.....	20
Figure 2.14 (b) Core showing horizontal cracking and longitudinal crack on steel.....	20
Figure 2.15 (a) Longitudinal crack due to poor slab support.....	20
Figure 2.15 (b) Close-up view of longitudinal crack, showing steel.....	20
Figure 3.1 Geometric configuration of a concrete slab.....	24
Figure 3.2 Finite element mesh model.....	25
Figure 3.3 Numerical results for the slab under edge loading.....	26
Figure 3.4 Numerical results for the slab under center loading.....	28
Figure 3.5 Maximum principal stress according to the loading position.....	29
Figure 3.6 Maximum surface deflection according to the loading position.....	29
Figure 3.7 Geometric configuration of a concrete slab and analysis cases.....	31
Figure 3.8 Finite element mesh model.....	32
Figure 3.9 Surface deflection along line AA'.....	33
Figure 3.10 Surface deflection near the wheel loading.....	34
Figure 3.11 Modeling of reinforcing steel and its interface with surrounding concrete.....	36
Figure 3.12 Geometric configuration of a concrete slab.....	37
Figure 3.13 Finite element mesh model.....	39
Figure 3.14 Bond-slip behavior between concrete and longitudinal steel.....	41
Figure 3.15 Friction-slip behavior between concrete and subgrade.....	43
Figure 3.16 Distribution of drying shrinkage strain.....	43

Figure 3.17 Thermal loading.....	44
Figure 3.18 Deformed shape and surface deflection	47
Figure 3.19 Principal stresses at the top and bottom of the slab.....	48
Figure 3.20 Principal stresses at the loaded transverse crack surface.....	49
Figure 3.21 Influence of design parameters on maximum principal stresses at top and bottom of slab	53
Figure 3.22 Influence of design parameters on maximum principal stresses at the loaded transverse crack surface	56
Figure 3.23 Principal stresses at the loaded transverse crack surface.....	59
Figure 3.24 Influence of material properties and environmental conditions on maximum principal stresses at the loaded transverse crack surface	61
Figure 3.25 Principal stresses in the vicinity of the longitudinal steel	63
Figure 3.26 Influence of slab thickness	67
Figure 3.27 Influence of longitudinal steel ratio.....	70
Figure 3.28 Influence of the modulus of subgrade reaction	73
Figure 3.29 Influence of change in concrete temperature.....	76
Figure 3.30 Influence of ultimate drying shrinkage strain.....	79
Figure 3.31 Influence of the coefficient of thermal expansion of concrete	82
Figure 3.32 Influence of frictional stress-slip stiffness.....	85
Figure 3.33 Range of crack stiffness values	99
Figure 3.34 Principal stresses in the vicinity of the longitudinal steel	100
Figure 3.35 Maximum principal stresses according to crack stiffness	101
Figure 4.1 Overall algorithm of mechanistic-empirical CRCP design program	103
Figure 4.2 Input screen with typical input values	105
Figure 4.3 Output screen showing analysis results.....	108

Figure 4.4 Graphical presentation of punchout prediction results	109
Figure 4.5 Accumulated damage and punchout per mile and transfer function	111
Figure 4.6 Revised transfer function without data from US290 section in Houston	112
Figure 4.7 Comparison of punchouts per mile with two different transfer functions.....	113
Figure 4.8 Effect of design traffic on punchouts per mile	116
Figure 4.9 Effect of longitudinal steel amount on punchouts per mile.....	117
Figure 4.10 Effect of slab thickness on punchouts per mile	118
Figure 4.11 Effect of concrete setting temperature on punchouts per mile	119
Figure 4.12 Effect of concrete coefficient of thermal expansion on punchouts per mile	120
Figure 4.13 Effect of concrete strength on punchouts per mile	121
Figure 5.1 Spalling and delamination	123
Figure 5.2 Formation of Horizontal Delamination	124
Figure 5.3 Low and medium severity chipping, respectively, in US 290, Cypress.....	125
Figure 5.4 Low and medium severity shallow spalling, respectively, in US 290, Hempstead	126
Figure 5.5 Medium severity spalling, SH 225 and low severity spalling, SH 288, respectively	126
Figure 5.6 Map of the investigated district in Houston	128
Figure 5.7 Layout of Numbered test sections in US 290-Hempstead.....	129
Figure 5.8 Average crack spacing over each section	132
Figure 5.9 Methods of construction (skewed steel, transverse cuts, and control)	133
Figure 5.10 Shallow spalling of section used with transverse cuts.....	133
Figure 5.11 Curing methods with respect to shallow spalling distress.....	134
Figure 5.12 Curing methods with respect to spalling	134
Figure 5.13 US-290 Hempstead Section 31 (day paving, polycuring).....	135

Figure 5.14 US-290 Hempstead Section 21 (day paving and blended aggregate)	135
Figure 5.15 Layout of test sections in US 290-Cypress	136
Figure 5.16 Layout of test section methods of curing US 290-Cypress	137
Figure 5.17 Aggregate contents (%limestone content).....	139
Figure 5.18 Method of curing in US 290-Cypress.....	139
Figure 5.19 US 290-Cypress, water base, mix 1 (100% limestone).....	140
Figure 5.20 US 290-Cypress, mix 1 (100% limestone).....	140
Figure 5.21 US 290-Cypress, mix 4 (gravel).....	141
Figure 5.22 Distance vs. the incidence of spalling	141
Figure 5.23 Percentage of spalling distress on SH 99	142
Figure 5.24 Photos of SH99 spalling distress	142
Figure 5.25 SH 99 PMIS data vs field observation with respect to spalling (%)	143
Figure 5.26 Layout of test section of SH 225	144
Figure 5.27 Percentage of chipping on SH 225 with respect to curing methods.....	145
Figure 5.28 Method of curing to shallow spalling.....	145
Figure 5.29 Effect of method of crack control on shallow spalling.....	146
Figure 5.30 Effect of method of curing on spalling.....	146
Figure 5.31 Effect of method of crack control in SH 225 test sections	147
Figure 5.32 Medium severity spalling, SH 225	148
Figure 5.33 SH 225 PMIS data vs. field observation with respect to spalling	148
Figure 3.34 Percentage of chipping in SH 288 with respect to curing methods.....	151
Figure 5.35 Method of curing	152
Figure 5.36 Method of batching.....	152
Figure 5.37 Type of SCM.....	153
Figure 5.38 Crack initiation day vs % of chipping in SH 288.....	154

Figure 5.39 Crack initiation day vs % of spalling in SH 288	154
Figure 5.40 High severity spalling, FM 1960	155
Figure 5.41 Spalling (%) vs distance	155
Figure 6.1 Coordination of corner curling and warping deformation model.....	160
Figure 6.2 Sensitivity study for delamination stress.....	164
Figure 6.3 Curing quality relationship	165
Figure 6.4 Evaporation rate nomograph for ACI.....	166
Figure 6.5 Laboratory shear strength at 6 and 9 hours	167
Figure 6.6 Shear strength vs equivalent age (hours).....	168
Figure 6.7 Determination of probability of delamination.....	170
Figure 6.8 Concrete Pavement spall mechanism and model	174
Figure 6.9 Calibration concept for spalling performance	175
Figure 6.10 λ and γ determined from trends of spalling and traffic	180
Figure 6.11 α and β determined from trends displayed	183
Figure 6.12 Calibrated curve in SH 225 vs US 290-Hempstead with respect to service year.....	189
Figure 6.13 Calibrated curve in SH 225 vs US 290-Hempstead with respect to damage	190

List of Tables

Table 3.1 Comparison of numerical results with Westergaard's solutions	30
Table 3.2 LTE according to longitudinal steel spacing and loading position.....	35
Table 3.3 Variation of longitudinal steel spacing	42
Table 3.4 Influencing factors and their variations	44
Table 3.5 Analysis cases	45
Table 3.6 Maximum principal stresses due to combined loading.....	86
Table 3.7 Summary of laboratory and field studies on aggregate interlock	98
Table 4.1 Pavement and punchout information used for transfer function development.....	111
Table 4.2 Detailed classification of punchouts	114
Table 4.3 Default input values selected for sensitivity analysis	115
Table 5.1 Project categories of spalling distress	127
Table 5.2 Sample section inventory at US 290-Hempstead	129
Table 5.3 Weather information during paving operations	129
Table 5.4 Summarizations of construction methods used in US 290-Hempstead.....	130
Table 5.5 Concrete mix properties, US 290-Hempstead Sections 21 and 22	131
Table 5.6 Results of spalling surveyed in US 290-Hempstead.....	131
Table 5.7 Sample section inventory at US 290-Cypress.....	136
Table 5.8 Weather information during construction period.....	136
Table 5.9 Four mix design combinations used in US 290-Cypress test section.....	138
Table 5.10 Sample section inventory at SH 99.....	142
Table 5.11 Sample section inventory at SH 225.....	144
Table 5.12 Weather information during construction period.....	144
Table 5.13 Sample section inventory at SH 288.....	149

Table 5.14 Weather information during construction period.....	149
Table 5.15 Specific information used in SH 288.....	150
Table 5.16 Sample section inventory at FM 1960	155
Table 5.17 Summaries of findings in all surveyed sites	157
Table 6.1 Corner curling and warping curvature coefficients	161
Table 6.2 Key parameters of corner curling and warping coefficient equations	162
Table 6.3 Typical values of parameters of delamination model.....	163
Table 6.4 Probability of delamination and the number of cracks that could delaminate in each site	172
Table 6.5 Database used to determine load to failure parameters	180
Table 6.6 Database used to determine damage parameters	182
Table 6.7 Determination of loads to failure parameters among all test sections	184
Table 6.8 Factorial design and shape factor of shallow spalling % at SH 288.....	185
Table 6.9 First factorial design of main effects and levels with respect to shallow spalling.	186
Table 6.10 Second factorial design of main effects and levels.....	186
Table 6.11 List of a equation with respect to chipping and shallow spalling distress.....	186
Table 6.12 Comparison estimated $\Delta\alpha$ with measured $\Delta\alpha$ used with 1 st factorial design ...	188
Table 6.13 Comparison estimated $\Delta\alpha$ with measured $\Delta\alpha$ used with 2 nd factorial design ..	189

CHAPTER 1 INTRODUCTION

Continuously reinforced concrete pavement (CRCP) is Portland cement concrete (PCC) pavement with continuous longitudinal steel reinforcement. No intermediate transverse expansion or contraction joints are provided. With temperature and moisture variations, the concrete is allowed to crack in a random pattern and the cracks are held tightly closed by the longitudinal steel reinforcement. These cracks do not cause performance issues as long as they are kept tight. Based on the experience of the early uses of CRCP, an adequate amount of steel needed for good performance was determined. The use of this amount of longitudinal steel virtually eliminated distresses observed at early uses of CRCP. Adequate slab thickness is another important design requirement for satisfactory performance of CRCP.

CRCP design consists of two elements: slab thickness design and steel reinforcement design. The first national CRCP design procedures for slab thickness were developed with information from the AASHO Road Test and included in the 1972 AASHTO Interim Guide for Design of Pavement Structures (AASHTO, 1981). CRCP was not included in the AASHO Road Test. A primary distress in jointed concrete pavement (JCP) at the AASHO Road Test was cracking along the wheel path, which is quite different from the distresses observed in modern CRCP. In addition, the concept of present serviceability index (PSI) was used as an input for initial and terminal condition of the pavement under design. In JCP, slope variance, cracking, and patching were the primary variables affecting PSI. In CRCP, cracking is normal behavior and does not contribute to degradation of serviceability. In short, the behavior of JCP and CRCP and their effect on pavement performance are quite different from each other. The use of the AASHO Road data for the development of CRCP design procedures is not rational. In some sense, state DOTs reverse-engineered the AASHTO design equations for CRCP design by selecting reasonable values for selected input variables. In 1986 and 1993, extensive revisions were made to the 1972 Interim Guide and newer versions of the design guides were published. However, very little effort was made to improve the CRCP design portion, except that steel design equations were incorporated.

Currently, the Texas Department of Transportation (TxDOT) uses the AASHTO 93 Guide (referred to as the 93 Guide in this report) for the design of CRCP. The 93 Guide has served TxDOT well for the design of CRCP; however, with the increase of truck traffic and the design period extended to 30 years, the required slab thicknesses on some of the major routes in Texas from the 93 Guide were unreasonably large. In 2003, TxDOT added a 15 in. maximum slab thickness limit. The 1972 AASHTO Interim Guide recommends the use of 0.6 % for the longitudinal reinforcement design. The 93 Guide provides nomographs for reinforcement design. The nomographs were developed based on computer program CRCP-3, developed at the University of Texas at Austin. The nomographs normally underestimate the required steel amount. In March 2004, NCHRP 1-37 reports and mechanistic-empirical pavement design guide software (MEPDG) were released (ARA, 2004). In 2005, recognizing the need for extensive data for a potential implementation of MEPDG, TxDOT initiated a rigid pavement database project (Won et al., 2009). At the same time, TxDOT initiated another research study to evaluate the MEPDG for potential implementation at TxDOT. The study recommended, for various

reasons, not to implement the MEPDG as a replacement for the design methods used at that time (Freeman, 2006). In 2007, TxDOT initiated a research study, 0-5832, to develop its own mechanistic-empirical CRCP design procedures (Won, 2010).

The performance of CRCP in the early days in Texas varied. Some performed well, and some didn't. Based on the experience with CRCP, TxDOT in the 1980s improved CRCP construction practices. New practices included the use of stabilized base and tied concrete shoulders. The benefits of these two changes have been so overwhelming that the TxDOT Project Monitoring Committee (PMC) decided to keep those two features for future CRCP construction and instructed the research team to develop design procedures for CRCP with non-erodible stabilized base and tied concrete shoulders. Initially, the use of a two-dimensional finite element method (FEM) program was considered for the mechanistic analysis of CRCP due to environmental (temperature and moisture variations) and wheel loading. Later on, the importance and significance of the interaction between longitudinal steel and surrounding concrete became evident, and two-dimensional FEM programs cannot be used for interaction analysis. Three-dimensional analysis was conducted for in-depth analysis of mechanistic behavior of CRCP, including the interactions between longitudinal steel and concrete.

The TxDOT PMC also instructed the research team that the CRCP design program be developed in MS Excel. The MS Excel format will allow TxDOT pavement design engineers to keep track of the design process and to understand the process better.

The primary objective of this research study was to develop a CRCP design procedure based on mechanistic-empirical (ME) design principles. To achieve this objective efficiently, both field evaluations of CRCP sections in Texas and theoretical structural analysis were conducted.

Scope of the Research

This research project was a joint project among Texas Tech University (TTU), the University of Texas at Austin (UT) and Texas A&M University (TAMU). The major task for TTU and UT was to develop mechanistic-empirical CRCP design procedures, and for TAMU was to evaluate spalling problems in Texas.

Chapter 2 discusses field evaluations conducted to identify punchout mechanisms.

Chapter 3 presents detailed discussions on mechanistic analysis of CRCP using a three-dimensional finite element method.

Chapter 4 describes ME CRCP program developed in this study. Sensitivity analysis results are also discussed.

Chapter 5 presents spalling performance in CRCP in Texas. Extensive field evaluations were conducted and the findings are discussed.

Chapter 6 discusses the spalling modeling and sensitivity of several variables. It also includes spall stress performance modeling and its calibration.

Chapter 7 presents conclusions and recommendations.

Chapters 2, 3 and 4 were prepared by the research team at TTU and UT. Chapters 5 and 6 were developed by the research team at TAMU.

CHAPTER 2 CRCP DISTRESSES AND THEIR MECHANISMS

Currently, there are two distress types in CRCP recognized by the pavement community: spalling and punchout. Spalling is a functional distress that doesn't appear to be due to structural capacity of the CRCP. Punchout is a structural distress that structural pavement design is supposed to address. Discussions on spalling, including its mechanisms and mechanistic modeling, are presented in Chapters 5 and 6. In these chapters, a general description of punchouts is presented first, and the findings from the efforts to identify punchout mechanisms through field evaluations are discussed. The objective of the field evaluation of punchouts was to accurately identify punchout mechanisms and develop rational punchout prediction algorithms that will be used to develop mechanistic-empirical CRCP design procedures.

2.1 Punchouts in CRCP

LTPP (Long-Term Pavement Performance) Distress Manual provides a description of the punchout as follows (John et al., 2003):

The area enclosed by two closely spaced (usually < 2 ft) transverse cracks, a short longitudinal crack and the edge of the pavement or a longitudinal joint. Also includes "Y" cracks that exhibit spalling, breakup or faulting.

NCHRP 1-37(A) provides the following description for punchouts (ARA, 2004):

Punchouts develop between two closely spaced transverse cracks as a result of crack load transfer efficiency (LTE) loss and a longitudinal fatigue crack that defines the punchout segment along the pavement edge.

TxDOT's Pavement Management Information System (PMIS) Rater's Manual provides a definition of punchouts as (TxDOT, 2009):

A full depth block of pavement formed when one longitudinal crack crosses two transverse cracks. Although usually rectangular in shape, some punchouts may appear in other shapes.

These descriptions provide a common characteristic of punchouts – a block of concrete bordered by two transverse cracks, a longitudinal crack and a pavement edge. Since transverse cracks are expected to develop in CRCP and thus are considered normal, the only element in a punchout that is not a normal feature in CRCP is a longitudinal crack. If a longitudinal crack is prevented all together in CRCP, a punchout will not occur.

Figure 2.1-(a) shows a punchout from LTPP Distress Manual, and Figure 2.1-(b) is a punchout illustrated in NCHRP 1-37(A) Report. In both examples, it is shown that the spacing between transverse cracks is relatively small, and multiple longitudinal cracks exist. There is a difference between the two. The punchout in Figure 2.1-(a) is at the longitudinal joint, whereas the one in Figure 2.1-(b) is at the edge of the pavement with asphalt shoulder. The difference might suggest that the distress mechanisms for these two punchouts are different. In Texas, punchout information has been collected under the

TxDOT rigid pavement database project (0-6274) and there appear to be a number of different types of distresses that are currently classified as “punchouts.” Some are caused by structural deficiency, some develop due to materials- and construction-quality related issues, and some are design-detail related. To develop a rational mechanistic-empirical CRCP design procedure, it is necessary to identify the exact mechanisms of distresses that were caused by structural deficiency of the pavement, i.e., the distresses that would have been delayed if the slab thickness was larger. In the punchout analysis for structural pavement design development, punchouts developed by causes other than structural deficiency should not be included.

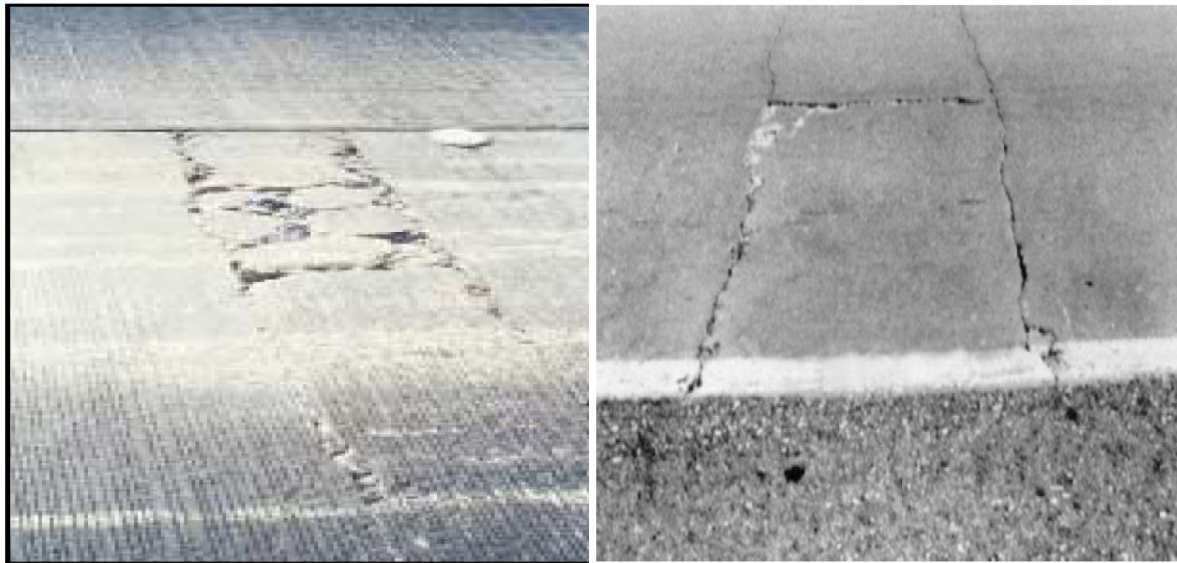


Figure 2.1-(a) Punchout in LTPP document Figure 2.1-(b) Punchout in NCHRP document

2.2 Types of Punchouts in Texas

Since there are currently only two types of distresses recognized in CRCP – spalling and punchouts – all the distresses that are not obvious spalling are classified as punchouts. On the other hand, there are distresses that are neither spalling nor punchouts caused by structural deficiency of CRCP that are still classified as punchouts in the state DOT’s PMIS system and national LTPP program. This section lists distress types that are currently classified as punchouts in Texas.

2.2.1 Distresses in transverse construction joints

Figures 2.2-(a) and 2.2-(b) show distresses observed in transverse construction joints. These distresses actually meet the LTPP definition of punchouts, except that one side of the distress is not a transverse crack. Since this distress is not spalling, it is recorded as a punchout in the TxDOT PMIS. This type of distress occurs in relatively new CRCP where other structural distresses don’t exist, which indicates that this distress is not structural capacity related. There could be multiple causes for this type of distress. The concrete supplied in this area is either the first batch of the day or the last batch of the day, and the quality of the concrete might be a little different from that of the concrete

supplied during the day. Also, the slip-form paver cannot start from the beginning of the header joint and the concrete in this area is usually consolidated and finished by manual work, which requires concrete with a larger slump. Figure 2.2-(b) shows that the width of this distress is about 20 in. The length of the additional longitudinal steel at a transverse construction joint is 21 in, and it appears that the transverse crack is at the end of the additional longitudinal steel. The concrete slab displacement in the longitudinal direction was measured at the transverse construction joint as shown in Figure 2.3-(a). This 12-in CRCP on 4-in asphalt layer is on US287 in the Wichita Falls District. The concrete was placed on August 26, 2005, which was a Friday.



Figure 2.2-(a) Distress at transverse construction joint



Figure 2.2-(b) Distress at transverse construction joint

The construction crew had to leave in the middle of the day, and the concrete placement was completed in the late morning. When the concrete was set, the headers were removed and four LVDTs (linear variable differential transducers) were placed in the longitudinal direction as shown in Figure 2.3-(a). LVDT #4 was placed against invar as a reference.



Figure 2.3-(a) Slab displacement measurement at transverse construction joint

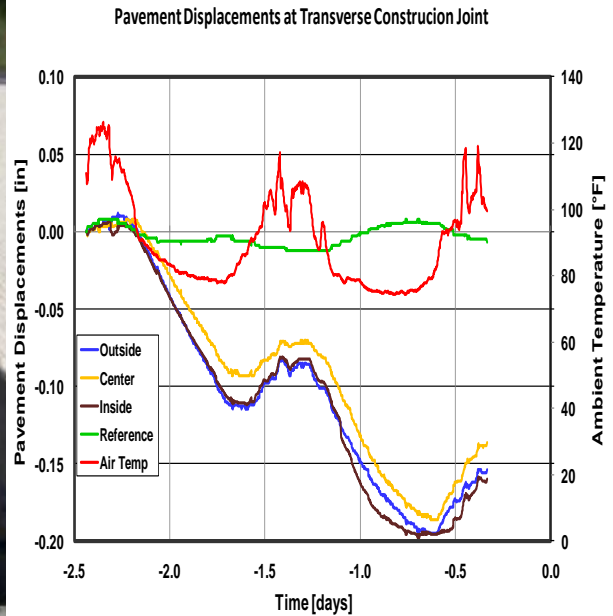


Figure 2.3-(b) Slab displacements for two days after concrete placement

The other three LVDTs were installed directly against concrete at the mid-depth of the slab. The data gathering started at 1:28 pm on August 26, 2005 every two minutes until 3:58 pm on August 28, 2005 (Sunday). The construction crew had to do preparation work for Monday concrete placement and the LVDTs were removed. Figure 2.3-(b) illustrates the concrete displacements along with ambient temperature. Large variations in ambient temperature are noted. Also, there are variations in displacements of LVDT against invar, even though they are not large. The variations are due to volume changes in the invar and the LVDT. If the invar was placed perfectly vertical, the variations could have been smaller or almost negligible. The other three lines illustrate the concrete displacements in three locations – inside, center, and outside. Large contractions of concrete were noted. In the x-axis, a whole number indicates midnight. Minus 2.0 indicates midnight on Friday. Minus 1.5 and -1.0 indicate noon Friday and midnight on Saturday, respectively. By Sunday morning, there was about 0.2 in. of concrete contraction. By the time concrete was placed on the other side of the joint Monday morning, the concrete placed Friday must have already achieved quite a large stiffness. Tuesday morning, when the ambient and concrete temperature became low, concrete at both sides of the joint could have contracted, pulling against each other. At this time, there could be a large imbalance in pulling force as the pulling force is proportional to the modulus of elasticity of concrete on both sides. As a result, the concrete placed on Monday would be pulled towards the other side of the joint. During this process, the additional longitudinal steel at the joint in the Monday placed section could pull the concrete towards the joint, potentially causing a transverse crack at the end of the additional steel and resulting in a higher probability of delaminations at the depth of the steel. Another mechanism of this distress could be the tie bars near the transverse construction joint. Due to the need for various construction phases to accommodate traffic flow during construction and the limitations of the slip-

form paving machine in the maximum width of paving, new concrete lanes are tied to previously placed concrete using tie bars. Newly placed concrete at the transverse construction joint will undergo more displacements due to drying shrinkage of concrete compared with previously placed concrete. This might cause high stresses in the newly placed concrete, which could cause transverse cracking and potentially cause delaminations at the depth of tie bars, because previously placed concrete in the adjacent lane has a much higher stiffness and the displacements in concrete will be very little. This might explain why the distress in Figure 2.2-(b) is on one side of the lane only. To summarize, this type of distress is not related to structural capacity of the CRCP and cannot be effectively prevented by increasing slab thickness. This distress type shouldn't be included in the development of a transfer function and in the calibration of a CRCP mechanistic model.

2.2.2 Distresses due to horizontal cracking

Another prevalent distress type in CRCP is distress due to horizontal cracking at the depth of the steel. Based on the work conducted in TxDOT research project 0-5549 "Horizontal Cracking in Concrete Pavement" and field observations of distresses due to horizontal cracking, it appears that there are two different mechanisms that cause horizontal cracking in CRCP (Choi, 2010). One is horizontal cracking that takes place at very early age CRCP, and the other takes place at a later age CRCP.

Figure 2.4-(a) shows horizontal cracking observed on IH35 in the Waco District. This CRCP – 14 in. slab on 4 in. asphalt stabilized base – was placed in 1999. Horizontal cracking was observed in 1999 before the pavement was open to traffic. There were two different reinforcement strategies in the construction project. In one reinforcement strategies, one-mat of longitudinal steel with #7 bar was placed at the mid-depth of the steel. In the other reinforcement strategies, two-mats of longitudinal steel with #6 bar were placed. In 1999, a number of horizontal cracks were observed in the reinforcement strategies where one-mat of #7 bar was used. No horizontal cracking was observed where two-mat steel was used. Figure 2.4-(b) illustrates CRCP distresses observed in 2009 in the same section of highway. It took about 10 years for early age horizontal cracks to develop distresses under heavy truck traffic on IH35.



Figure 2.4-(a) Horizontal cracking observed on IH35 in 1999



Figure 2.4-(b) Distress resulting from early age horizontal cracking

The distress shown in Figure 2.4-(b) meets the LTPP punchout definition – closely spaced transverse cracks and connecting longitudinal cracking. However, this distress is not due to the structural deficiency of the CRCP. The slab is 14-in thick, and the deflection testing in a Level I test section in this area for the TxDOT rigid pavement database (0-6274) shows an average of 1 mil, which is quite low. It is believed that this distress was caused by horizontal cracks that developed at early ages. In Figure 2.4-(a), the transverse crack on the right side looks like a normal transverse crack in CRCP. On the other hand, the crack on the left side is extremely tight, which is a common feature of this type of distress. It appears that the normal transverse crack occurred at early ages, while the tight crack occurred at a later age. Figure 2.5-(a) shows the horizontal cracking observed in 2010 on the side of the outside shoulder. The horizontal crack occurred at the mid-depth of the slab in the outside shoulder; however, horizontal cracking did not develop into distress yet. It is quite possible that the absence of wheel loading applications kept the horizontal crack from developing into distress. Figure 2.5-(b) shows an early stage of CRCP distress due to horizontal cracking. Sounding testing confirmed the existence of delaminations. This section of CRCP on US59 in the Atlanta District with 12-in CRCP on 4-in ACP was built in 2001. This section experienced horizontal cracking while the pavement was still under construction. Considering the age of the pavement, the slab thickness with a good base, the use of a tied concrete shoulder, along with not very heavy truck traffic (15 million ESALs for 30 years from 2008), this distress appears to be due to the horizontal cracking.



Figure 2.5-(a) Horizontal cracking on IH35 observed in 2010 Figure 2.5-(b) Distress due to horizontal cracking

There are numerous examples of this distress type in Texas. One of the common characteristics of the pavement with this distress type is the coarse aggregate type used. It's quite rare to observe this type of distress in CRCP with concrete containing soft limestone as coarse aggregate. On the other hand, CRCP with concrete containing siliceous river gravel has a higher probability of this distress type. A high coefficient of thermal expansion (CTE) and modulus of elasticity, along with unfavorable environmental conditions during and right after concrete placement, appear to be responsible for horizontal cracking in CRCP.

There are CRCP sections built in the early 1960s with deficient slab thickness by today's standards, even though the design at that time with the projected design traffic was adequate. Horizontal cracking is observed in some of these sections. Figure 2.6-(a) shows 6-in CRCP on US281 in the Wichita Falls District. Figure 2.6-(b) illustrates horizontal cracking at the depth of longitudinal steel and notes longitudinal cracks along the longitudinal steel. The coarse aggregate type in this concrete is crushed limestone. In Texas, concrete containing limestone generally has a low CTE and modulus of elasticity. Accordingly, horizontal cracks are not expected at early ages in CRCP with concrete containing limestone coarse aggregate. Instead, it is postulated that deficient slab thickness with insufficient slab support for truck traffic loading caused the horizontal cracking and resulting distresses.



Figure 2.6-(a) 6-in CRCP on US281 in Wichita Falls



Figure 2.6-(b) Horizontal and longitudinal cracks on US281 in Wichita Falls

Figure 2.7-(a) illustrates the effect of the stiffness ratio (E_1/E_2) of the surface layer to the layer below on shear stresses in the pavement layers due to wheel loading obtained from layered theory (Yoder et al., 1975). It shows that the larger the stiffness ratio, the greater the shear stress at the mid-depth of the surface layer. It is noted that this result is somewhat different from Westergaard's solution, which states that concrete normal stress at the bottom of the slab due to wheel loading applications is not as much affected by the stiffness under the concrete slab (Westergaard, 1926). When a concrete slab is placed directly over the subgrade, which is the case in the pavement shown in Figure 2.6-(b), this ratio becomes quite large. For example, in the pavement shown in Figure 2.6-(b), this ratio could be more than 400 (5,000,000 psi/10,000 psi). The shear stress at the mid-slab could be quite large. Figure 2.7-(b) illustrates the effect of surface layer thickness on the shear stress in the surface layer for E_1/E_2 ratio of 20. This illustration of radius of load area shows that the smaller the surface layer thickness, the larger the shear stress.

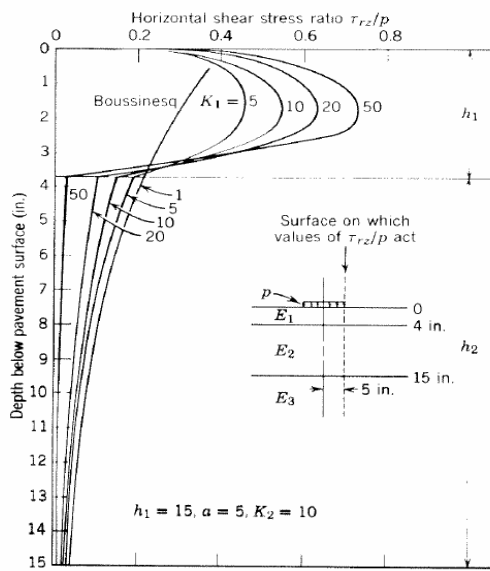


Figure 2.7-(a) Horizontal shear stress as affected by modulus ratio

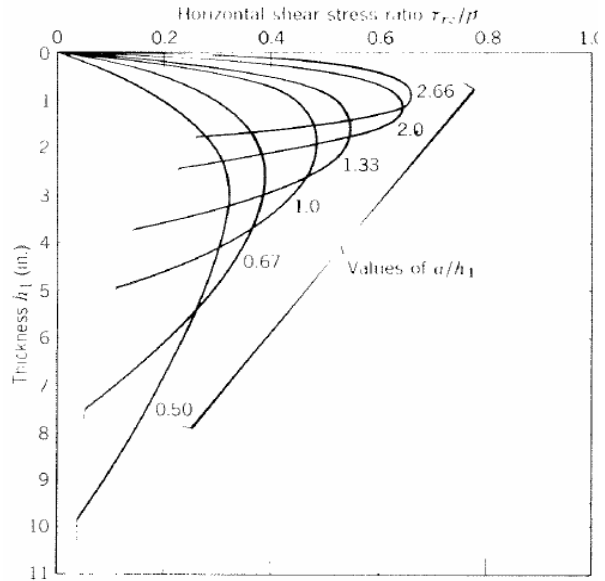


Figure 2.7-(b) Horizontal shear stress as affected by slab thickness

For CRCP with a smaller slab thickness and placed directly on top of the subgrade, such as CRCP sections built in the early 1960s in Texas, shear stresses at the mid-depth of the slab could be quite large due to wheel loading applications, leading to horizontal cracking at the mid-slab and punchouts.

There are two CRCP sections with 6-in slab thickness built in early 1960 that show the effect of base stiffness. One section is in the Dallas District on Loop 12 South, which was completed in 1963. In this project, the concrete was placed directly on top of 3% lime-treated subgrade. The second section is in the Houston District on the Loop 610 frontage road, which was completed in 1961. Cement stabilized base was placed under the concrete. The stiffness ratio of the concrete layer to the layer below in the Dallas section should be much higher than that in the Houston section. Figure 2.8-(a) shows the Dallas section and Figure 2.8-(b) shows the section in Houston. Deflection testing was conducted on both sections, and the average deflection in the Dallas section was 16.3 mils while that for the Houston section was 7.3 mils. This large difference in slab deflections in CRCP with the same slab thickness indicates the difference in base support condition, and explains a marked difference in performance.



Figure 2.8-(a) Close-up view of distress in 6-in CRCP in Dallas



Figure 2.8-(b) Condition of 6-in CRCP in Houston

There are many distresses in the Dallas section while the frequency of distress in the Houston section is much smaller. Sounding testing showed delaminations in the Dallas section. The marked difference in the performance after more than 45 years of service could be explained by the difference in the stiffness ratio of concrete layer to the layer below.

It is recognized that there are two different mechanisms in horizontal cracking at the mid-depth in CRCP. One is the horizontal cracking taking place at the early ages due to high values of CTE and modulus of concrete along with unfavorable environmental conditions during the concrete placement. Horizontal cracking induced by this mechanism could develop into distresses resembling punchouts. Increasing structural capacity of the CRCP system with a thicker concrete slab does not provide a solution to this problem. This problem should be addressed with material selection, construction quality control or variations in reinforcement design. It could be that CRCP may not be the most appropriate pavement type when coarse aggregate has quite a high CTE. For those coarse aggregate types, jointed plain concrete pavement (JCP) might be a more appropriate pavement type, with provisions that will ensure no spalling at transverse contraction joints.

The other mechanism for horizontal cracking at the mid-depth of CRCP takes place at later ages by wheel loading applications due to structural deficiency of the CRCP system, especially when the stiffness ratio of concrete layer to the layer below is quite high and the slab thickness is small. CRCP structural design should address this distress type to ensure that CRCP provides good performance for the design life by minimizing this distress type. As discussed above, this can be achieved by the use of a base course with sufficient stiffness and/or by increasing slab thickness.

2.2.3 Distresses due to construction quality

According to the current TxDOT Pavement Management Information System Rater's Manual, a surface defect that is greater than 12-in long or wide is rated as a punchout (TxDOT, 2009). Figures 2.9-(a) and 2.9-(b) illustrate surface defects that were greater than 12-in and therefore rated as punchout in the TxDOT PMIS condition survey. These distresses could be classified as spalling. The coarse aggregate in the section shown in Figure 2.9-(a) is limestone and it's quite rare to have this type of distress in concrete with limestone coarse aggregate. In Figure 2.9-(b), the far left and far right surface defects are not related to transverse cracks. They are in the middle portion between two transverse cracks. Normally, spalling occurs at transverse cracks. It is believed that this distress occurred due to construction quality issues during concrete placement.



Figure 2.9-(a) CRCP distress due to construction quality issue



Figure 2.9-(b) CRCP distress due to construction quality issue

2.2.4 Distresses due to deficient support of base/subgrade material

There are areas where efficient compaction of base material is quite difficult or areas where compaction is not done uniformly, such as around manholes and at the slab edge. Typical distresses in these areas are shown in Figure 2.10-(a) in the manhole area and in Figure 2.10-(b) at the slab edge. The distress in Figure 2.10-(a) was recorded as a punchout in a TxDOT PMIS condition survey. Since this is not spalling, the rater didn't have a choice but to record this distress as a punchout. It also meets the LTPP definition of a punchout. A half-moon shaped crack was also observed, which indicates that there was a deficiency in slab support. The best way to prevent this distress would be proper compaction of the base material. Increasing slab thickness in this area could be an option. The distress shown in Figure 2.10-(b) is due to the deficiency of the slab support at the

pavement edge. Evidence of depression at the joint between the outside lane and asphalt shoulder is noted; however, there was no evidence of pumping. This type of distress was prevalent in CRCP in Texas until TxDOT started using tied concrete shoulders. The use of tied concrete shoulders, along with stabilized base, practically eliminated this type of distress altogether. There may be distresses observed with tied concrete shoulders; they are normally due to poor load transfer from deficient tie bar installation or tie bar size. Simply increasing slab thickness would not be the best method, from a technical and cost standpoint, to address this distress type. Further discussion is provided in the next section.



Figure 2.10-(a) Distress due to consolidation of subgrade/subbase



Figure 2.10-(b) Distress due to consolidation of subgrade/subbase

2.2.5 Distresses due to poor load transfer at longitudinal joints

There are distresses observed in inside lanes as shown in Figures 2.11-(a) and 2.11-(b). These distresses are usually caused by poor load transfer at longitudinal joints as evidenced by faulting at longitudinal joints. The need for adequate load transfer at longitudinal joints has not gained as much attention as it deserves. The term, load transfer efficiency (LTE), has been used almost exclusively for transverse contraction joints in JCP. Poor load transfer at transverse contraction joints in JCP contributes to faulting, which causes degradation in pavement smoothness. Field evaluations of LTE at transverse cracks conducted under TxDOT 0-6274 show that LTE is maintained quite high, above 90 % regardless of slab thickness, age of pavement, time of testing (winter vs. summer) and crack spacing as long as the adequate amount of longitudinal steel is used. It is quite rare to observe punchout distresses due to poor load transfer at transverse cracks. On the other hand, a number of punchout distresses were observed due to poor load transfer at longitudinal joints. When tie bars at longitudinal construction joints or transverse steel at longitudinal warping joints are not adequate, deflections of the slab under wheel loading will increase substantially. It is because deficient tie bars or transverse steel puts the pavement in a so-called “edge” condition, not “interior”

condition. According to Westergaard's closed form solutions for deflections, deflections at edge condition are about three times as large as deflections in the interior condition. The large deflections, if the support condition happens to be deficient, could cause distresses in CRCP.



Figure 2.11-(a) Distress due to poor load transfer at longitudinal joint



Figure 2.11-(b) Distress due to poor load transfer at longitudinal joint

An 8-in CRCP section on IH35W in the Dallas District was built in 1966 and punchout distresses were observed. In this section, some portions had tied concrete shoulders and the rest had asphalt shoulders. Almost all the distresses, in the form of edge punchouts, occurred in CRCP with asphalt shoulders. Deflection testing was conducted at the pavement edge in both CRCP with tied concrete shoulders and CRCP with asphalt shoulders. Figure 2.12-(a) illustrates the deflections. Deflections of a little larger than 12 mils were observed at the pavement edge with asphalt shoulders, while the deflection at the pavement edge with tied concrete shoulders was about 4.5 mils. A substantial difference in edge deflections between tied concrete shoulders and asphalt shoulders was observed. Figure 2.12-(b) shows the edge deflections at 9,000 lb loading for various slab thicknesses and modulus of subgrade reaction values from Westergaard closed form solution. Comparison of the deflections in Figures 2.12-(a) and 2.12-(b) implies the modulus of subgrade reaction value on IH35W might be close to 300 psi/in. Deflections of an 8-in slab at the interior condition with 300 psi/in modulus of subgrade reaction are 4.4 mils per Westergaard equation, which was quite close to the measured value at pavement edge with a tied concrete shoulder as shown in Figure 2.12-(a). This indicates that a tied concrete shoulder rendered the condition of the slab at pavement edge to "interior" from "edge." To achieve the same slab deflection at the interior condition for the slab with asphalt shoulders, Figure 2.12-(b) shows that the thickness should be greater than 15-in. Westergaard's equation for interior condition shows that a 17-in thick slab will have 4.4 mils of deflection at pavement edge. In other words, to achieve slab deflections equivalent to those of a tied concrete shoulder for CRCP with asphalt

shoulders, slab thickness has to be more than doubled. This will be quite an expensive alternative. This also indicates that slab thickness is not the most significant variable in ensuring good CRCP performance. There are other design variables that can be and need to be considered to optimize CRCP designs.

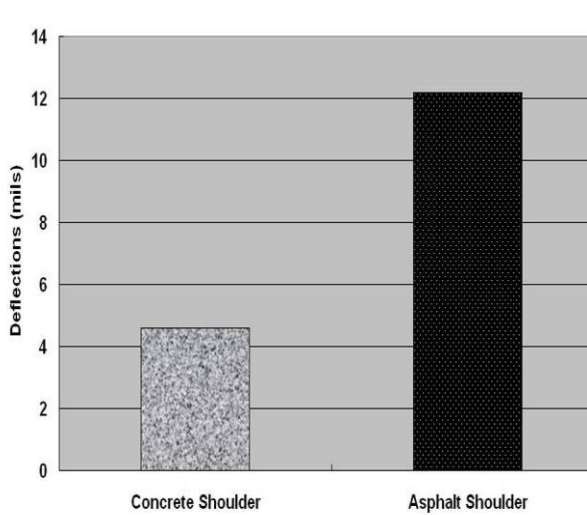


Figure 2.12-(a) Slab edge deflection with different shoulder type

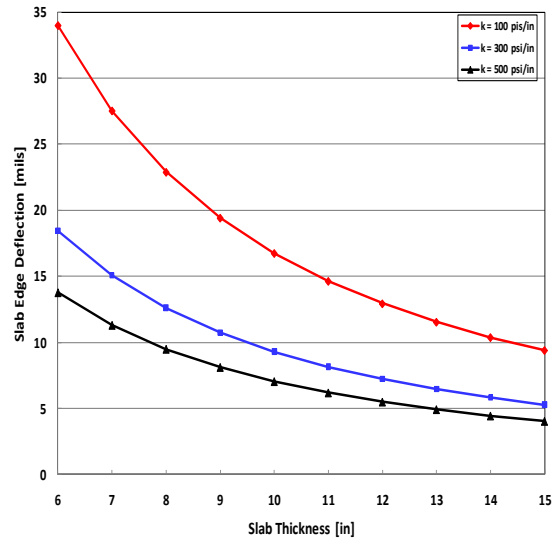


Figure 2.12-(b) Slab edge deflection for various slab thicknesses and k values

2.3 Punchout development mechanism

As discussed in the previous section, there are a number of different causes of distresses in CRCP that are currently classified as “punchout.” Many of them are not related to structural deficiency of CRCP, and proper measures should be taken to minimize those distresses, but not by simply increasing slab thicknesses. To develop mechanistic-empirical CRCP design procedures, it is important to properly identify the mechanisms of punchouts that are caused by the deficiency of slab thickness. One of the difficulties for the research in this area is that it takes a long while for a punchout due to structural deficiency to fully develop. By the time a punchout is observed, it’s quite difficult to understand the full process of the distress. It would be ideal if a distress is observed at its early age and its entire course to the full punchout is followed.

A 7.1-mile CRCP section of US287 in the Wichita Falls District from one mile west of Iowa City Park to 7.7 miles east of Electra was completed in 1970. The pavement structure consisted of 8-in CRCP, plus 4-in asphalt stabilized base, plus 6-in treated subgrade, with asphalt shoulders both inside and outside of the driving lane. In 2005, a distress at an early stage was observed in the westbound outside lane, at the reference marker between 328 and 329. Figure 2.13-(a) shows the condition of the distress observed on August 23, 2005. It shows that longitudinal cracks developed between transverse cracks. Figure 2.13-(b) is the condition of the distress on November 16, 2007. Pieces of concrete came out from the distressed area, and faulting was observed at transverse cracks. Asphalt patch materials were placed to provide an even surface.

Longitudinal cracks started to form at the two transverse cracks. Figure 2.13-(c) shows the condition of the distress on August 12, 2008. Longitudinal cracks emanating from two transverse cracks are visible. It took three years for the distress to progress from the condition shown in Figure 2.13-(a) to Figure 2.13-(c). A decision was made to take cores at three areas – where longitudinal cracks in three different levels (tight, relatively tight and wide) meet transverse cracks. Cores were taken on November 13, 2008 and Figure 2.13-(d) shows the condition of the cores taken from the three areas.



Figure 2.13-(a) Distress observed on August 23, 2005



Figure 2.13-(b) Distress observed on November 16, 2007



Figure 2.13-(c) Distress observed on August 12, 2008



Figure 2.13-(d) Coring locations and cores taken on November 13, 2008

On December 10, 2009, deflection testing using a falling weight deflectometer (FWD) was conducted to evaluate LTE at transverse cracks. LTE was quite high in all transverse cracks evaluated including the cracks with punchouts, with the average of 93 %, even though the air temperature during the testing was about 35° F. This testing shows that, even though a punchout was in progress, LTE at transverse cracks was quite high. In other words, it appears that this punchout was not caused by low LTE.

The findings from the examination of cores can be summarized as follows:

- 1) All the longitudinal cracks were along the longitudinal steel.
- 2) A core taken from the more visible longitudinal crack had delamination at the depth of the longitudinal steel.
- 3) Initial stage of horizontal cracking at the depth of longitudinal steel was observed in a core taken from the intermediate level of longitudinal cracking.
- 4) Only a longitudinal crack was observed in a core taken from the longitudinal crack with the least crack width.

The observations above indicate strong interactions between longitudinal steel and surrounding concrete due to wheel loading applications. High wheel loading stresses from the interactions between longitudinal steel and surrounding concrete at the depth of the steel could induce longitudinal cracking. This mechanism was observed in a number of locations in Texas, and two examples are presented.



Figure 2.14-(a) Longitudinal cracking in the wheel path



Figure 2.14-(b) Core showing horizontal cracking and longitudinal crack on steel

Figure 2.14-(a) shows a longitudinal crack along the outside wheel path. A core was taken at this location and Figure 2.14-(b) shows that the longitudinal crack is along the longitudinal steel, which indicates strong interactions between longitudinal steel and

concrete due to wheel loading applications. A horizontal crack at the depth of longitudinal steel is also observed.



Figure 2.15-(a) Longitudinal crack due to poor slab support



Figure 2.15-(b) Close-up view of longitudinal crack, showing steel

Figure 2.15-(a) shows a longitudinal crack traversing several transverse cracks. It appears that the slab support was not adequate and a longitudinal crack developed near the middle of the lane. Figure 2.15-(b) illustrates that the longitudinal crack was again along the longitudinal steel. It illustrates the strong interactions between longitudinal steel and surrounding concrete.

Mechanistic analysis of CRCP should include these interactions in estimating concrete stresses to predict cracking and punchouts. Without the interactions included, the accuracy of the analysis results may be severely compromised. Based on the field evaluations to identify the punchout mechanism, it appears that punchout development follows the following mechanism:

- 1) Wheel loading applications near transverse cracks induce stresses in concrete near longitudinal steel. The magnitude of the concrete stress will depend on the slab thickness and base support condition.
- 2) Continued wheel loading applications will cause damage in the concrete at the depth of longitudinal steel. If the cumulative damage exceeds the critical damage value, concrete cracks will result. The critical damage value, over which a crack will develop in the concrete, will depend on the quality of concrete materials and the effectiveness of concrete consolidation around the steel.
- 3) Once cracks develop, CRCP loses structural integrity and the concrete will start disintegrating, with the rate of concrete disintegration dependent on wheel loading magnitude and frequency, slab thickness, base support, LTE at transverse and longitudinal cracks, among other factors.

Field evaluations show that this process of punchout development could proceed even when LTE at transverse cracks is maintained at quite a high level. Transverse cracks in the inside half of the lane were kept quite tight, even though a punchout was progressing in the outside half of the lane. Also, the FWD testing conducted at transverse cracks in the inside half of the lane where a punchout was in progress as shown in Figure 2.13 showed quite a high LTE. It is clear that low LTE is not a necessary condition for a punchout to proceed. Once a punchout takes place, transverse cracks within the punchout area look wide. The large crack width in the punchout area is not necessarily the cause of punchout; rather, it is a consequence of punchout.

Mechanistic analysis of CRCP for punchout evaluation should consider the interactions between longitudinal steel and surrounding concrete. Accordingly, the process should be based on three-dimensional analysis. In this study, three-dimensional analysis was employed for the analysis of CRCP, and is described in the next chapter.

CHAPTER 3 MECHANISTIC MODELING OF PUNCHOUTS AND DEVELOPMENT OF MECHANISTIC-EMPIRICAL CRCP DESIGN PROCEDURES

3.1. Introduction

This chapter describes the development of mechanistic-empirical (ME) CRCP design procedures. First, the development of a mechanistic model of punchouts in CRCP and its application to evaluate the effects of some design parameters on the occurrence of punchouts are presented. It is essential to understand the exact mechanism for punchout development in order to develop an accurate punchout prediction model. Detailed descriptions on punchout mechanisms were provided in the previous chapter. Rather extensive field observations indicate that the interactions between longitudinal steel and concrete due to environmental and traffic loading applications are the primary mechanism for punchouts in CRCP in Texas. In this chapter, descriptions on the mechanistic modeling and analysis conducted for punchout development are provided first, followed by explanations on how the findings from the mechanistic modeling and analysis were incorporated in the ME CRCP design procedures, called TxCRCP-ME.

To validate a probable mechanism of this type of punchout, a three-dimensional mechanistic model was developed and the effects of some design parameters on concrete stresses were investigated by performing a series of analyses with emphasis on evaluating longitudinal steel-concrete interactions. The analysis was performed with the aid of the commercial finite element analysis program DIANA (DISplacement method ANALyzer) ver. 8.1.2 (DIANA, 2003). DIANA is a general purpose finite element code, based on the displacement method. It was developed by engineers from a civil engineering perspective in 1972. It has been under development at TNO located in Delft, the Netherlands. DIANA ver. 9.4.2 was recently launched. Civil, mechanical, biomechanical, and other engineering problems can be solved with the DIANA program. Its most appealing capabilities are in the fields of concrete and soil. Standard DIANA application work includes concrete cracking, excavation, tunneling, composites, plasticity, creep, cooling of concrete, groundwater flow, fluid-structure interactions, temperature-dependent material behavior, heat conduction, stability analysis, buckling, phased analysis, substructuring, etc.

3.2 Preliminary Analysis

To examine the accuracy and applicability of finite element analysis using DIANA, two preliminary analyses were performed: (1) CRCP without transverse cracks was analyzed through three-dimensional analysis using solid elements, and the numerical results were compared with Westergaard's solutions; and (2) CRCP with transverse cracks was analyzed through three-dimensional analysis using flat shell elements, and the deflections and LTEs were estimated.

3.2.1 Behavior of CRCP without transverse cracks

Based on the assumption of an infinite or semi-infinite slab over a dense liquid foundation (Winkler foundation), Westergaard obtained closed-form formulas for stresses and deflections of a slab with a single-wheel loading applied near the corner, in the interior of a slab at a considerable distance from any edge, and near the edge far from any corner. However, because of somewhat unrealistic assumptions, these formulas have limitations in their ability to analyze a finite-size slab where the loading is applied randomly and transferred across joints. Fortunately, with the introduction of the finite element method and with the ever-increasing speed and storage of personal computers, a slab in various conditions can be analyzed with a realistic modeling.

To evaluate the stresses and deflections in CRCP without transverse cracks, a 24 ft-wide and 40 ft-long slab with a thickness of 10 in. was analyzed as shown in Figure 3.1. A preliminary analysis showed that a length extending 20 ft on each side of the loaded area with no boundary restraints is adequate to consider the structural characteristics of CRCP. A 9-kip single-wheel loading was uniformly distributed over a circle with a radius of 6 in., and the distance from the slab edge to the center of the loading varied from 0.5 to 1.5, 2.5, 3.5, 4.5, 5.5, 6.5, 8.5, 10.5, and 12.0 ft. Material properties were assumed to be linear elastic and to have the properties as follows: (1) the elastic modulus and Poisson's ratio of concrete are 5×10^6 psi and 0.15, respectively; and (2) the moduli of subgrade reaction are 300 and 150 psi/in. for vertical and horizontal directions, respectively.

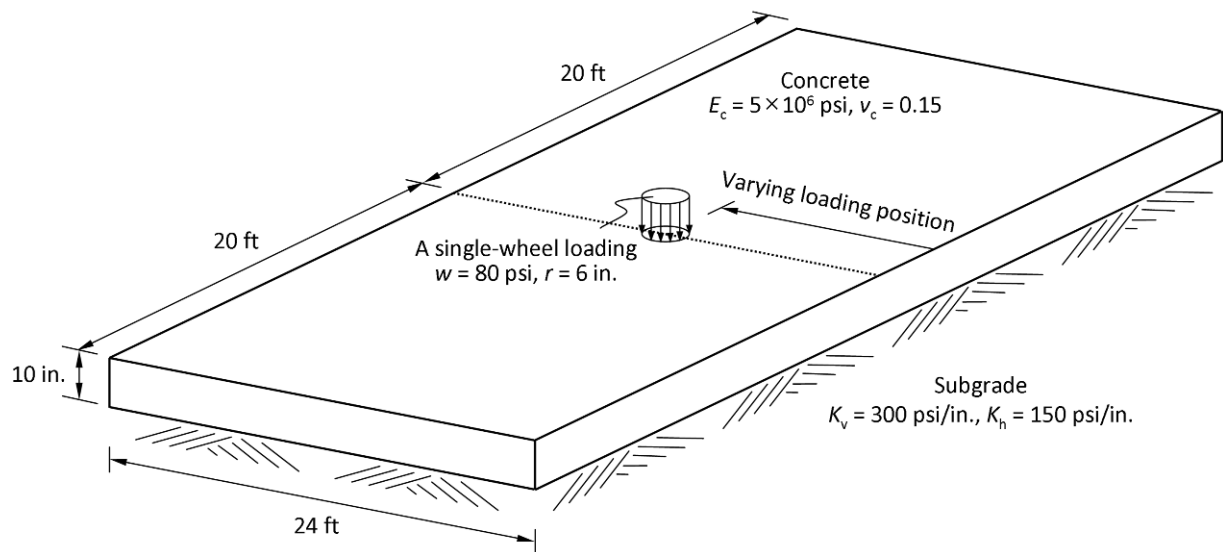


Figure 3.1: Geometric configuration of a concrete slab

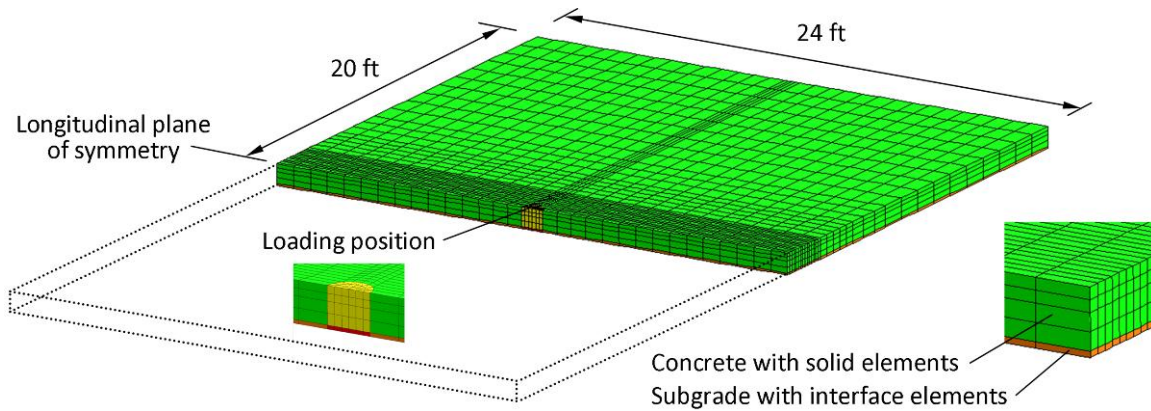


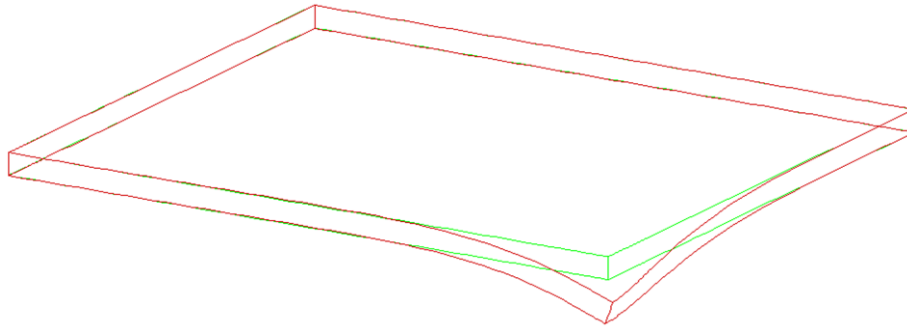
Figure 3.2: Finite element mesh model

Figure 3.2 describes the finite element mesh model of the slab where the loading is applied at a distance of 12 ft from the slab edge. The slab was modeled in three dimensions and only half of the slab was modeled to take advantage of the symmetry in the longitudinal direction. Twenty-node isoparametric solid brick elements and fifteen-node isoparametric solid wedge elements were used in the mesh representation of concrete. Subgrade was modeled in a smeared sense by means of linear elastic bedding with 8+8-node plane quadrilateral interface elements and 6+6-node plane triangular interface elements. A preliminary analysis was performed to determine the mesh fineness, and a time-efficient mesh size was chosen considering the accuracy of numerical results.

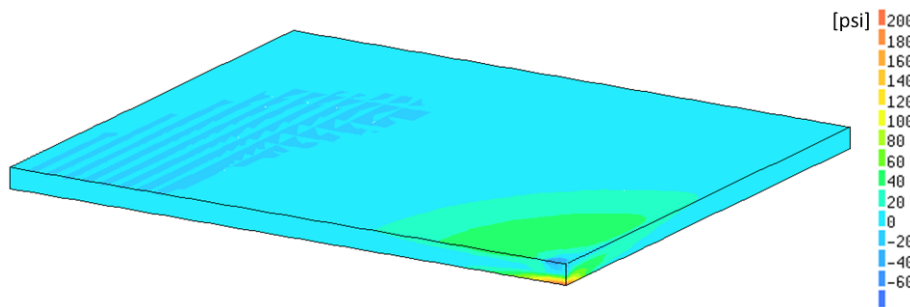
Figure 3.3 shows the numerical results for the slab under edge loading (0.5-ft loading). The deflection increases as it gets closer to the slab edge and has the maximum value of 9.80×10^{-3} in. The maximum principal stress develops at the bottom of the slab at a distance of 0.17 ft from the slab edge and has the value of 216 psi. Figure 3.4 shows the numerical results for the slab under center loading (12-ft loading). The deflection decreases as it gets farther from the loading and has the maximum value of 3.33×10^{-3} in. The maximum principal stress occurs at the bottom of the slab directly below the loading and has the value of 117 psi.

Figure 3.5 shows the location and magnitude of maximum principal stresses for various loading positions. Red and blue arrows represent the wheel loading and corresponding maximum principal stress, respectively. For example, the 1.5-ft loading results in the maximum principal stress of 143 psi at the bottom of the slab at a distance of 1.33 ft from the slab edge. The maximum principal stress occurs at the bottom of the slab in the longitudinal direction regardless of loading position, and its magnitude decreases as the loading is applied farther away from the slab edge. Figure 3.6 represents the location and magnitude of maximum deflections for various loading positions. The maximum deflection occurs at the slab edge if the loading is applied within 3 ft of the slab edge and its magnitude decreases as the loading is applied farther away from the slab edge. Table 3.1 shows good agreement between Westergaard's solutions and numerical results

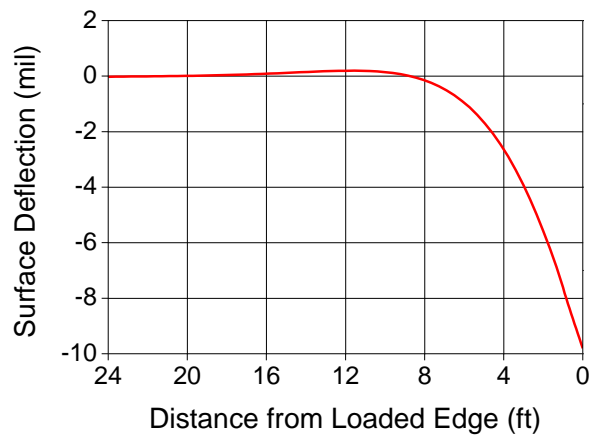
although the maximum deflection is slightly higher and the maximum principal stress is slightly lower than Westergaard's solutions.



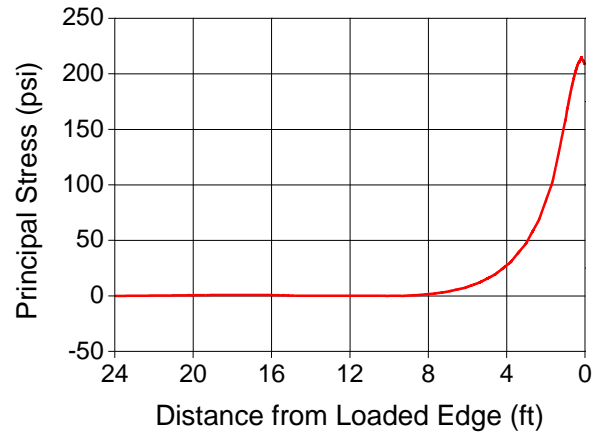
(a) Deformed shape



(b) Distribution of principal stresses

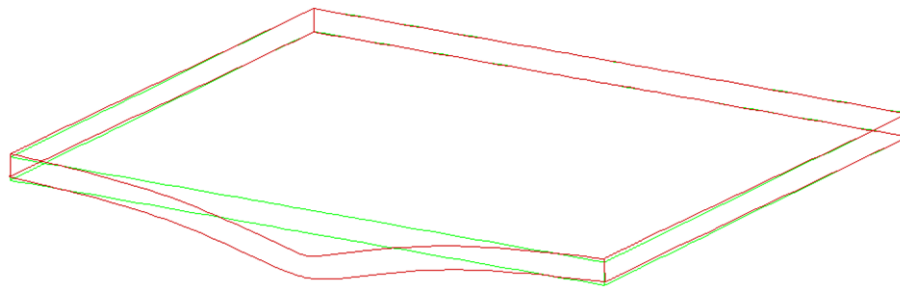


(c) Surface deflection along top centerline

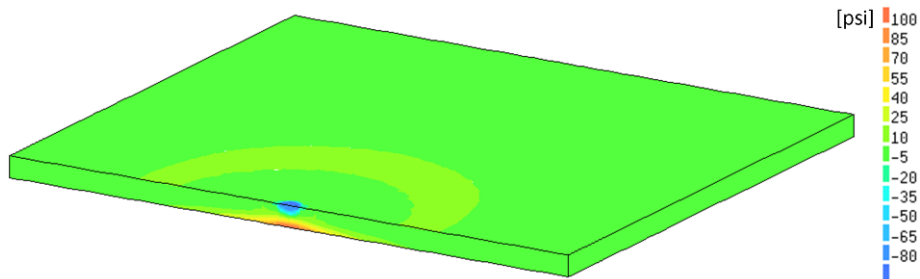


(d) Principal stress along bottom centerline

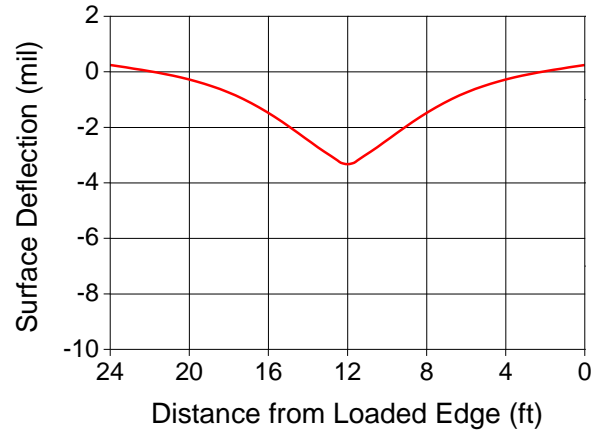
Figure 3.3: Numerical results for the slab under edge loading



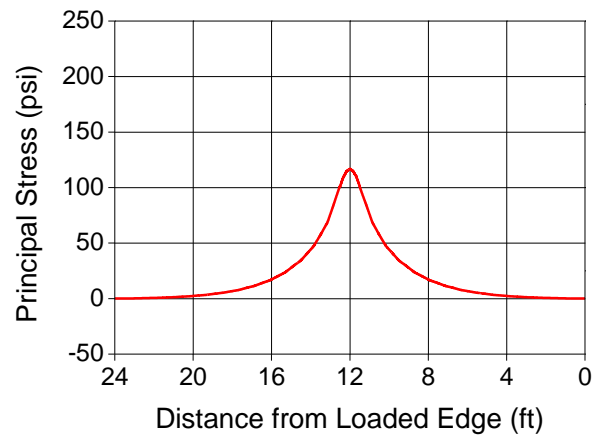
(a) Deformed shape



(b) Distribution of principal stresses



(c) Surface deflection along top centerline



(d) Principal stress along bottom centerline

Figure 3.4: Numerical results for the slab under center loading

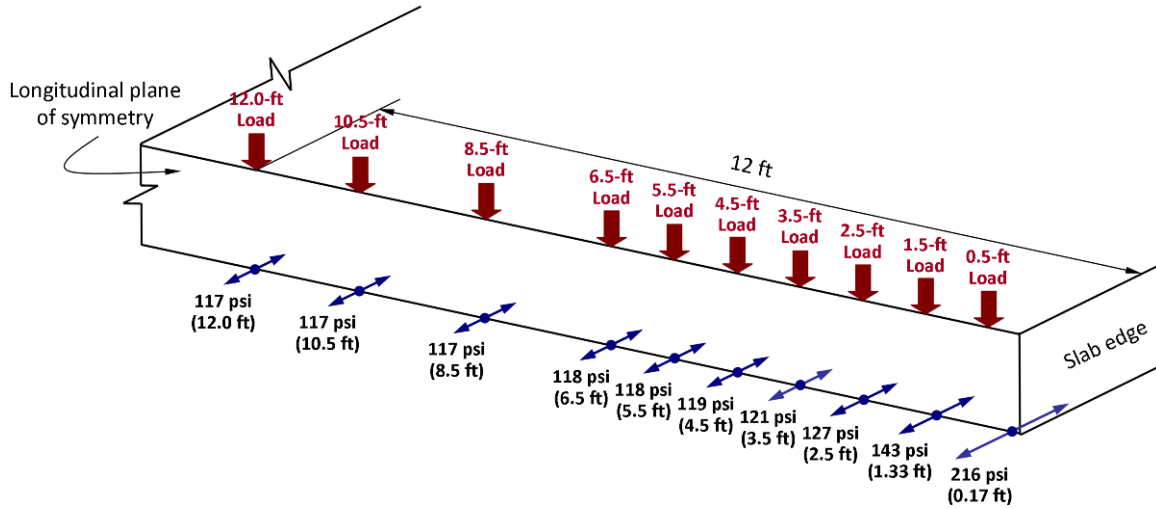


Figure 3.5: Maximum principal stress according to the loading position

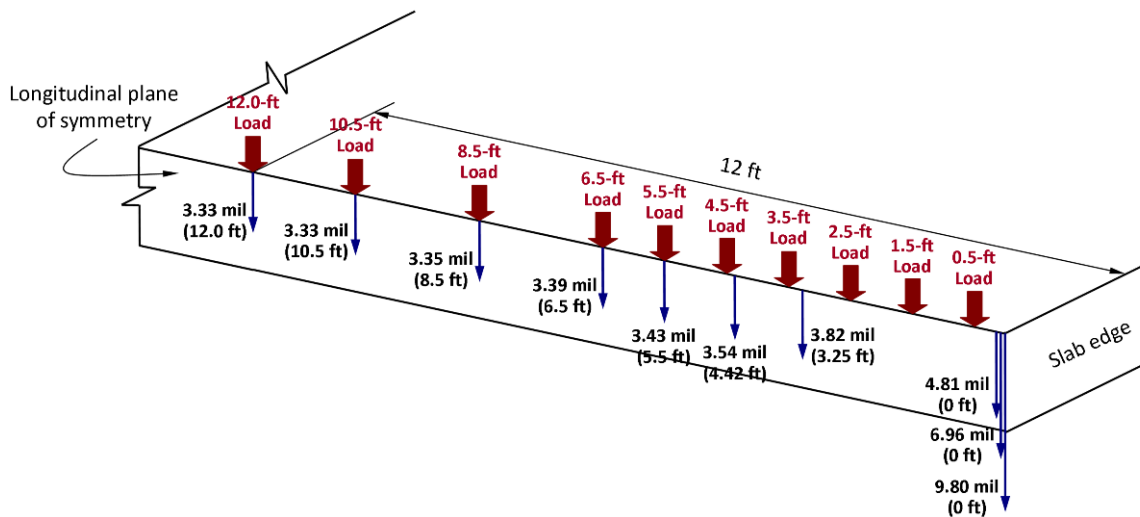


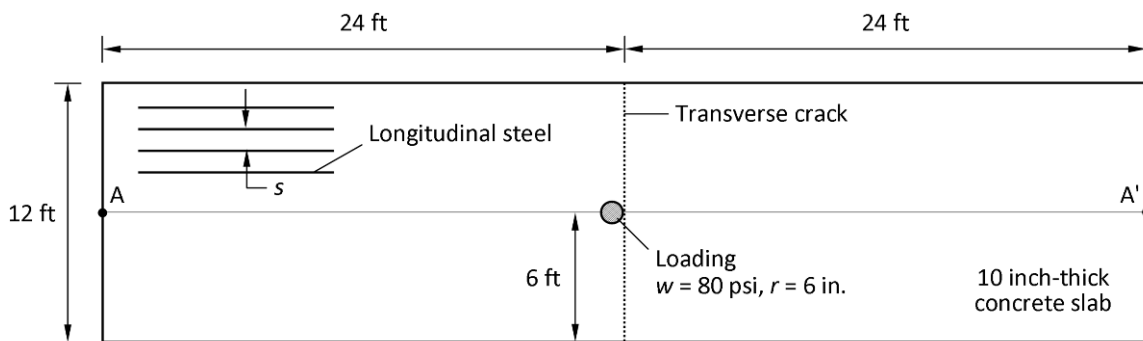
Figure 3.6: Maximum surface deflection according to the loading position

Table 3.1: Comparison of numerical results with Westergaard's solutions

Loading Condition	Maximum Principal Stress (psi)		Maximum Surface Deflection (mil)	
	Numerical Result	Westergaard's Solution	Numerical Result	Westergaard's Solution
Edge Loading	216	226	9.80	9.30
Center Loading	117	119	3.33	3.10

3.2.2 Behavior of CRCP with transverse cracks

To evaluate the deflections and LTEs in CRCP with transverse cracks, a 12 ft-wide and 48 ft-long slab with a thickness of 10 in. was analyzed as shown in Figure 3.7. The slab has one transverse crack which is located in the middle of the slab. A 9-kip single-wheel loading was uniformly distributed over a circle with a radius of 6 in. The loading is tangent to the transverse crack and located at a distance of 6 ft from the slab edge. The four sides of the slab were restrained in the direction perpendicular to each side. Material properties were assumed to be linear elastic as follows: (1) the elastic modulus and Poisson's ratio are 5×10^6 psi and 0.15 for concrete and 2.9×10^7 psi and 0.30 for steel, respectively; and (2) the moduli of subgrade reaction are 300 and 150 psi/in. for vertical and horizontal directions, respectively. It was assumed that longitudinal rebar with a diameter of 0.75 in. were placed at mid-depth.



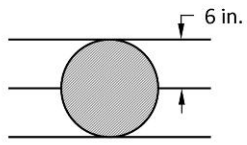
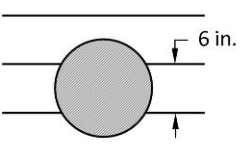
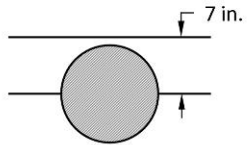
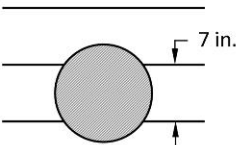
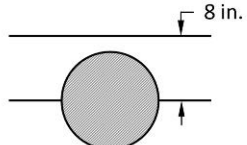
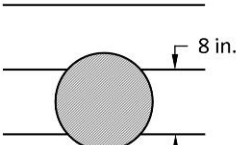
	Loading position L1	Loading position L2
$s = 6 \text{ in.}$		
$s = 7 \text{ in.}$		
$s = 8 \text{ in.}$		

Figure 3.7: Geometric configuration of a concrete slab and analysis cases

The evaluations were conducted for different longitudinal steel spacing and loading positions as shown in Figure 3.7. Three levels of longitudinal steel spacing were selected: 6, 7, and 8 in. Two types of loading position were taken into consideration: the loading whose center is directly above longitudinal steel (L1) and the loading whose center is directly above the middle of two adjacent longitudinal rebars (L2).

Figure 3.8 describes the finite element mesh model of the slab with a longitudinal steel spacing of 6 in under the loading condition of L1. The slab was modeled in three dimensions. Eight-node quadrilateral isoparametric flat shell elements and six-node triangular isoparametric flat shell elements were used in the mesh representation of concrete. Subgrade was modeled in a smeared sense by means of linear elastic bedding with 8+8-node plane quadrilateral interface elements and 6+6-node plane triangular interface elements. Three-dimensional beam elements were used to model longitudinal rebar. It was assumed that aggregate interlock does not exist, which means that the loading is transferred only through longitudinal rebar across the transverse crack. Perfect bond between longitudinal steel and surrounding concrete was assumed.

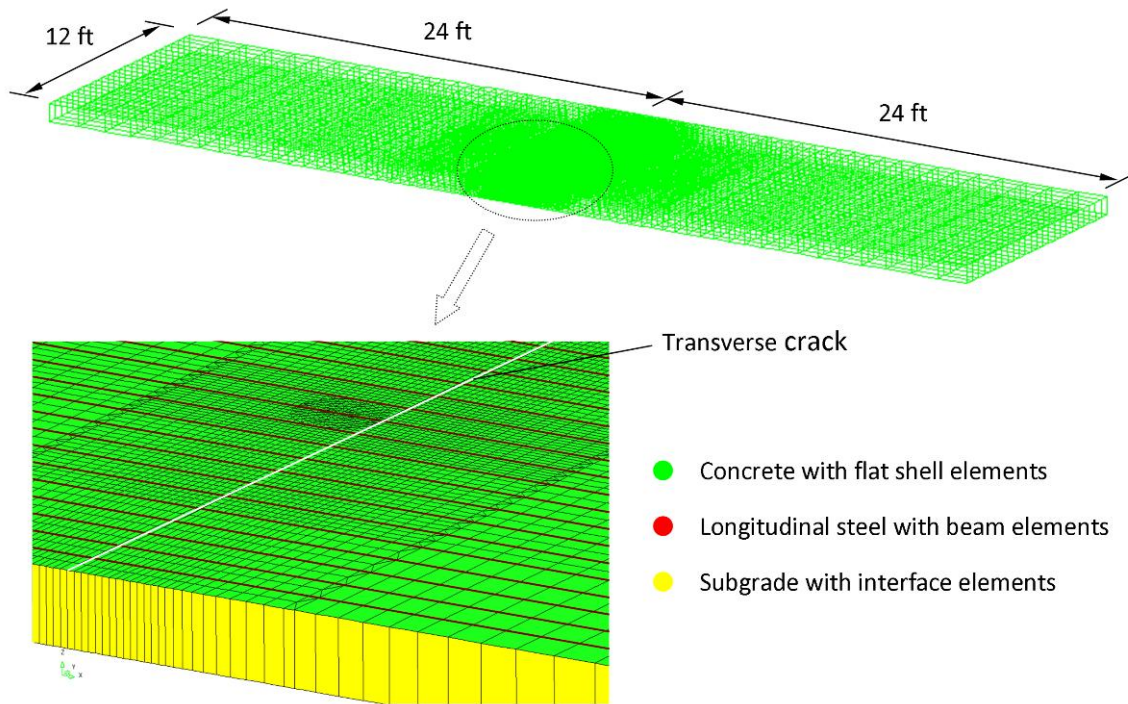
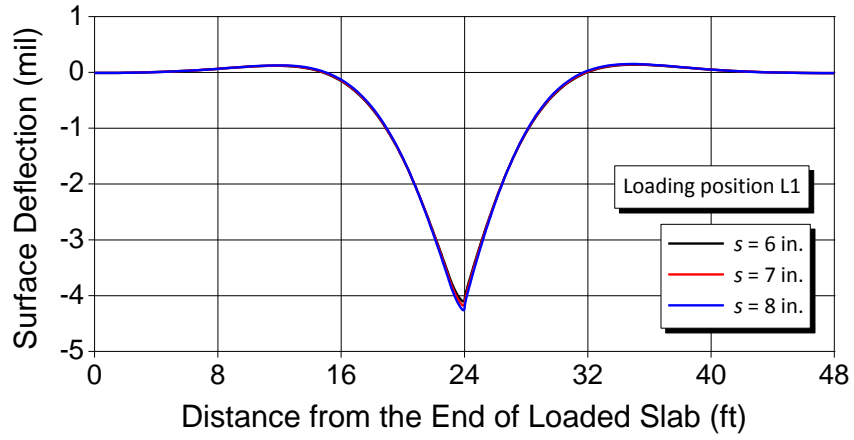


Figure 3.8: Finite element mesh model

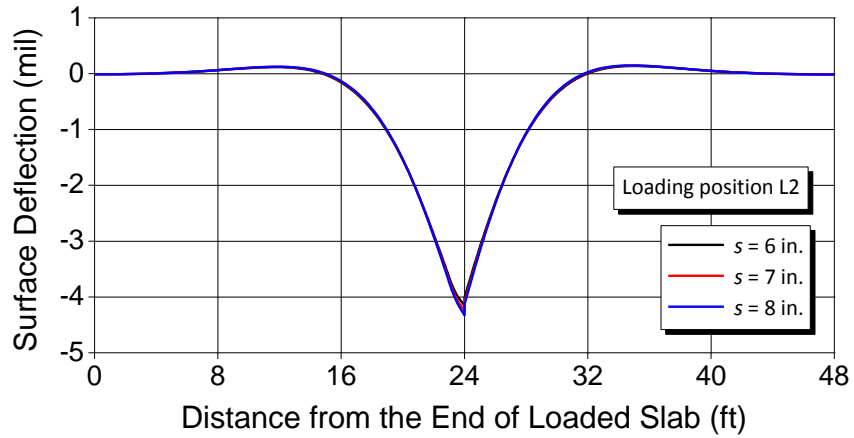
Figure 3.9 shows the deflection along line AA'. Figure 3.10 shows closely the deflection near the loading. The maximum deflection occurs near the transverse crack under the loading condition of L1, while it occurs at the transverse crack under the loading condition of L2. The maximum deflection decreases as longitudinal rebars are more closely spaced. The loading condition of L2 results in a larger maximum deflection. The deflection curve is continuous under the loading condition of L1, while it has a discontinuity at the transverse crack under the loading condition of L2. The jump in deflection at the transverse crack increases as the longitudinal steel spacing is larger. However, the overall deflection is not heavily influenced by the longitudinal steel spacing and loading position when longitudinal rebars are spaced 6 to 8 in. apart, as shown in Figure 3.9. However, in a range of large steel spacing – transverse rebars are spaced up to 36 in apart – the effects of steel spacing and loading position could be significant.

LTEs are summarized in Table 3.2. LTE was defined as the ratio of the deflection at a distance of 1 ft from the center of loading in the direction of the end of the unloaded slab to the deflection at the same distance from the center of loading in the opposite direction (see Figure 3.10). LTE is almost uninfluenced by the longitudinal steel spacing and loading position when the longitudinal steel spacing is in the range of 6 to 8 in. The calculated LTE is maintained at a quite high value, which agrees well with the field observations (Won, 2009). On the other hand, maximum deflections are influenced by the spacing of longitudinal steel; the larger the spacing, the greater the deflection. This

finding, along with field data, questions the utility of the LTE in evaluating CRCP structural condition.

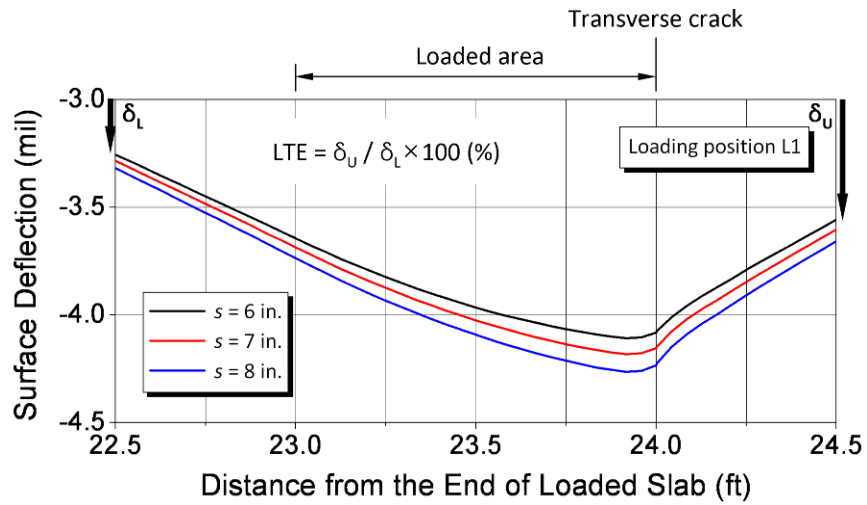


(a) Loading position L1

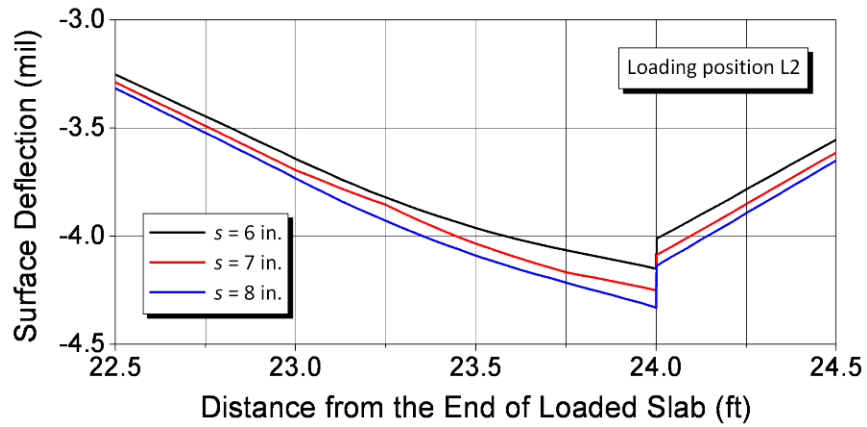


(b) Loading position L2

Figure 3.9: Surface deflection along line AA'



(a) Loading position L1

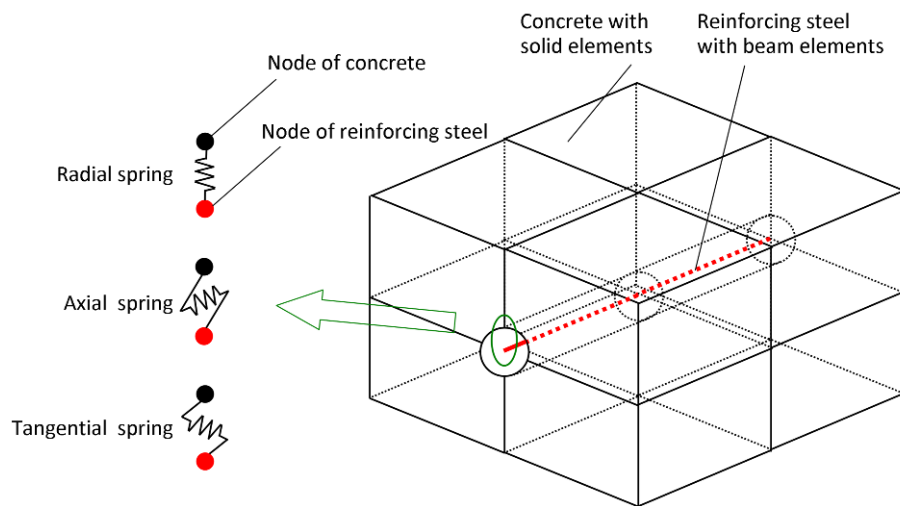


(b) Loading position L2

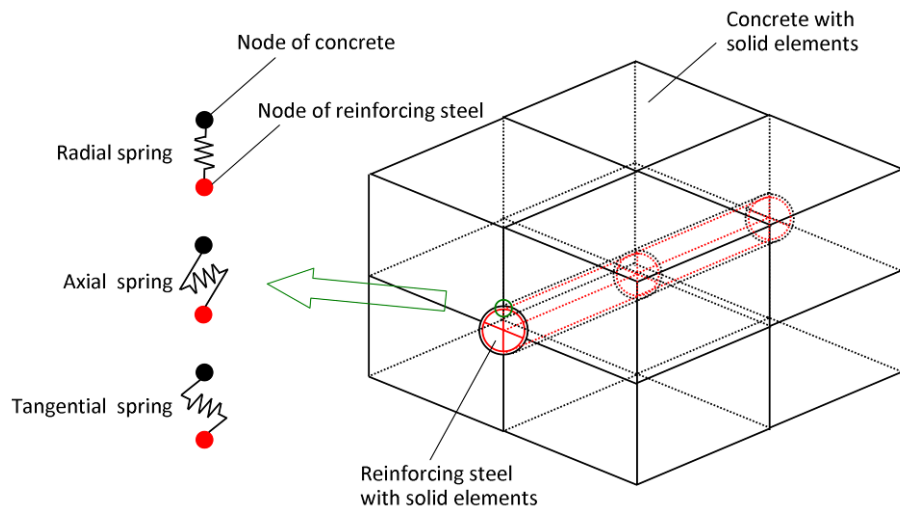
Figure 3.10: Surface deflection near the wheel loading

Table 3.2: LTE according to longitudinal steel spacing and loading position

Longitudinal Steel Spacing (in.)	Loading Position L1			Loading Position L2		
	δ_L (mil)	δ_U (mil)	LTE (%)	δ_L (mil)	δ_U (mil)	LTE (%)
6	-3.255	-3.557	109	-3.252	-3.552	109
7	-3.283	-3.602	110	-3.288	-3.611	110
8	-3.318	-3.656	110	-3.314	-3.648	110



(a) Simplified modeling of reinforcing steel using beam elements



(b) Detailed modeling of reinforcing steel using solid elements

Figure 3.11: Modeling of reinforcing steel and its interface with surrounding concrete

3.3 Development of Mechanistic Modeling

Several three-dimensional finite element analyses have been performed to simulate the behavior of concrete pavements. However, in most three-dimensional numerical approaches, spring or beam elements have been used to model reinforcing steel as

described in Figure 3.11(a) and summarized in reference (Shoukry et al., 2007). Although these simplified three-dimensional models are definitely enhanced in comparison with two-dimensional models, it can only be justified when predicting the overall behavior of cracked CRCP and/or doweled JCP. This is because modeling of reinforcing steel with beam elements cannot consider Poisson effect, and more important, it may cause stress localization problems in the concrete around the reinforcing steel. If the modeling objective includes the examination of concrete stresses developed around the reinforcing steel, detailed three-dimensional modeling of reinforcing steel using solid elements is essential, although it takes more effort and computation time due to the requirement of using very refined meshes. Accordingly, a concrete slab shown in Figure 3.12 was analyzed using a three-dimensional finite element model which utilizes only solid elements for modeling reinforcing steel as well as for the concrete, as illustrated in Figure 3.11(b).

3.3.1 Finite element modeling

Figure 3.12 shows the geometric configuration of the concrete slab. The slab is 29 ft long and 12 ft wide. It has transverse cracks spaced 4.5 ft apart with the exception of a spacing of 2 ft in the middle of the slab (Segment #5). The two longitudinal ends of the slab were restrained in the longitudinal direction considering the structural characteristics of CRCP.

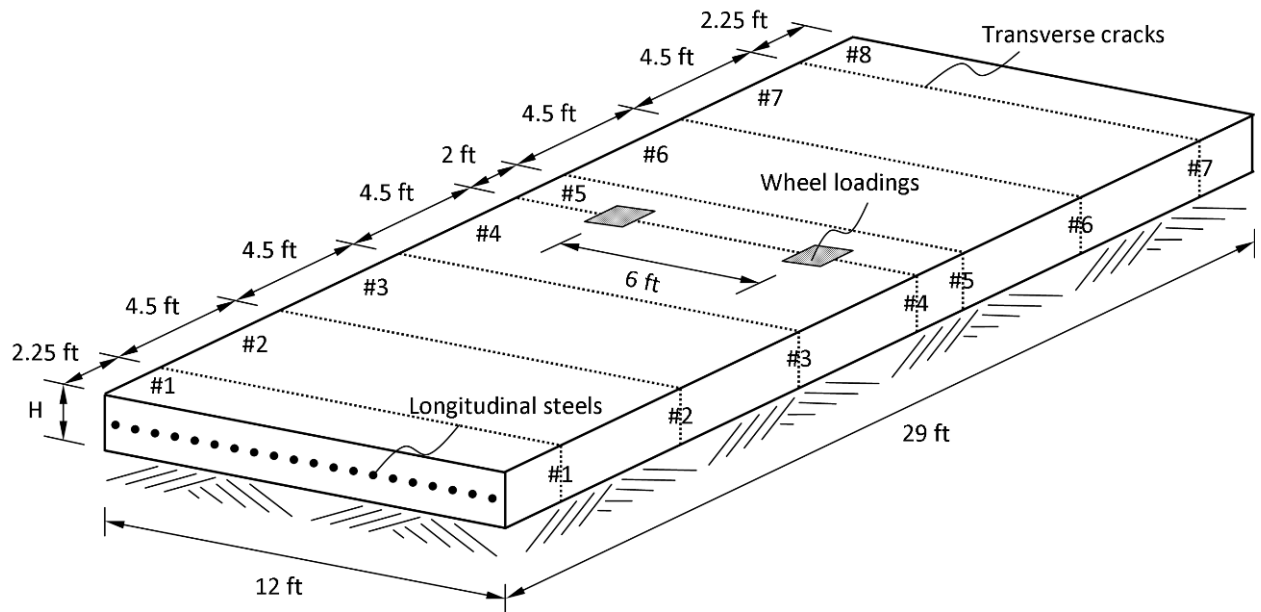
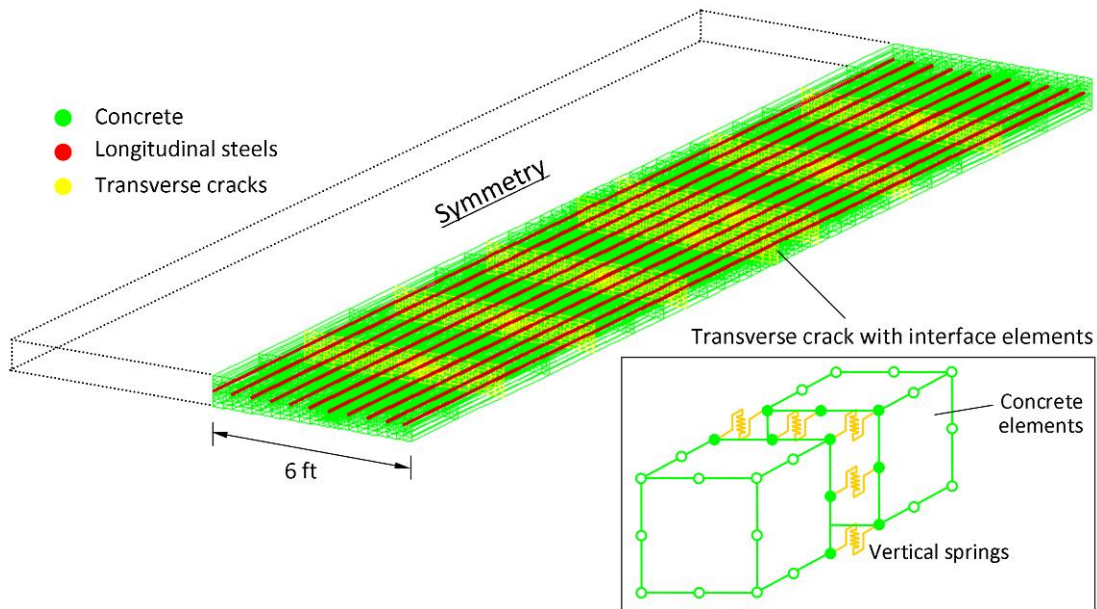


Figure 3.12: Geometric configuration of a concrete slab

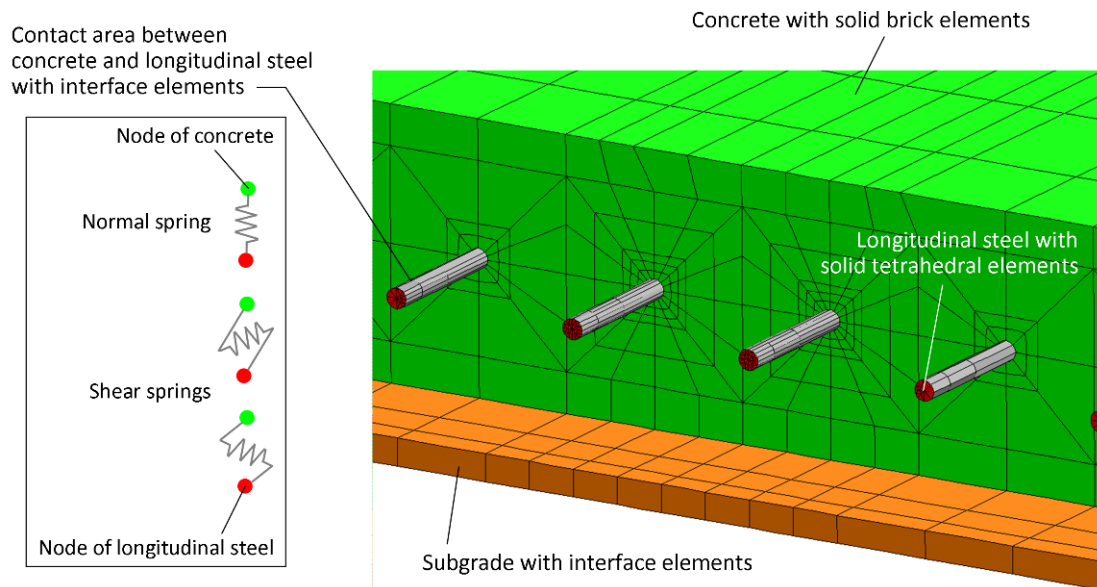
Figure 3.13 shows the finite element mesh model. A half model of the concrete slab was used to take advantage of symmetry along the transverse axis. Twenty-node

isoparametric solid brick elements were used in the mesh representation of concrete. To accurately predict the distribution of strain and stress fields in the concrete around longitudinal steel, fifteen-node isoparametric solid wedge elements were used in the mesh representation of longitudinal steel. For consistency, equal-sized elements were allocated to the concrete around longitudinal steel regardless of design parameters such as slab thicknesses, longitudinal steel ratios, etc.

The interactions between longitudinal steel and surrounding concrete were considered by modeling their contact area using 8+8-node plane quadrilateral interface elements. The interface element, which is equivalent to a series of spring elements, was placed between the faces of concrete and longitudinal steel elements. Although the faces of concrete and longitudinal steel elements have the same coordinate values – the interface element has zero-thickness – they are definitely separate faces connected by the interface element. The interface element defines a relation between tractions and relative displacements across the interface. These have normal and shear components. The relation between shear traction and shear relative displacement describes bond-slip behavior between longitudinal steel and surrounding concrete. The relation between normal traction and normal relative displacement describes debonding behavior.



(a) A half model of the concrete slab



(b) Zoomed-in shaded view

Figure 3.13: Finite element mesh model

Aggregate interlock is a natural mechanism effective in providing load transfer across discontinuities, such as joints and cracks in plain or reinforced concrete pavement systems. It is known that aggregate interlock highly depends on crack opening and the shearing and frictional properties of aggregate particles along crack surfaces. It is also dependent on a number of factors such as the type and size of aggregates, the strength of concrete and subgrade, and the magnitude and repetitions of loading. For realistic modeling of the local response across cracks in concrete, several advanced models were developed as summarized in references (Jefferson, 2002; Brink, 2003). However, these models are limited in their use because of difficulties in the determination of a number of variables. It is seen from literature, in the finite element representation of concrete pavements, discontinuities at cracks have traditionally been modeled by a set of vertical linear spring elements adjoining two adjacent slabs (Korovesis, 1990; Khazanovich and Gotlif, 2003; Brink, 2003; Dere et al., 2006; Jensen and Hansen, 2006; Maitra et al., 2010). Accordingly, the interlock action of aggregate was modeled by placing 8+8-node plane quadrilateral interface elements between transverse crack faces. The relation between shear traction and shear relative displacement describes the capability of concrete to transmit shear stresses across transverse cracks.

Subgrade was modeled with 8+8-node plane quadrilateral interface elements. The relation between normal traction and normal relative displacement describes the vertical stiffness of subgrade. The relation between shear traction and shear relative displacement characterizes friction-slip behavior between concrete and subgrade.

3.3.2 Material properties

The elastic modulus and Poisson's ratio of concrete were assumed to be 5×10^6 psi and 0.15, respectively. The elastic modulus, Poisson's ratio, and the coefficient of thermal expansion of steel were assumed to be 2.9×10^7 psi, 0.30, and 6.4×10^{-6} /°F, respectively. Longitudinal steel with a diameter of 0.75 in was placed at mid-depth.

The bond-slip behavior was characterized using plane interface elements with the relation between shear traction and shear relative displacement, as shown in Figure 3.14 (Kim et al., 2000). A large stiffness was assigned to the relationship between normal traction and normal relative displacement to keep the debonding between longitudinal steel and surrounding concrete to a minimum.

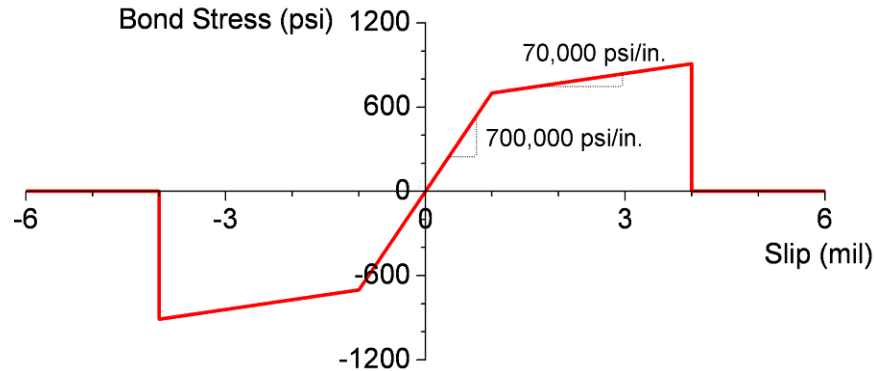


Figure 3.14: Bond-slip behavior between concrete and longitudinal steel

A conservative assumption was made that aggregate interlock does not exist due to repeated traffic and environmental loading, and therefore the load is transferred only through longitudinal steel across transverse cracks. Accordingly, a small stiffness was assigned to the relationship between shear traction and shear relative displacement.

As for traffic loading, two 9-kip wheel loadings were applied in the wheel path as shown in Figure 3.12. They are six ft apart and located over the transverse crack in the middle of the slab (Crack #4). Each wheel loading is uniformly distributed over a square which is equal in area to a circle with a radius of 6 in.

3.3.3 Variables for sensitivity analysis

The effects of design parameters, material properties, and environmental conditions on the behavior of concrete slabs were analyzed through parametric studies. The evaluations were conducted for different slab thicknesses (H), longitudinal steel ratios (ρ_s), the moduli of subgrade reaction (K_v), friction between concrete and subgrade (K_h), coefficients of thermal expansion of concrete (α_c), drying shrinkage strains (ϵ_{sh}), and changes in concrete temperature (ΔT_c). These influencing factors varied as follows:

- (1) Five levels of slab thickness were selected: 6, 8, 10, 12, and 14 in.
- (2) Three levels of longitudinal steel ratio were used: 0.5, 0.6, and 0.7%. The longitudinal steel ratio was varied by changing the longitudinal steel spacing and keeping the diameter of longitudinal steel constant. Table 3.3 shows the longitudinal steel spacing assigned to each combination of slab thickness and longitudinal steel ratio. TxDOT uses a longitudinal steel ratio of 0.6% for CRCP (TxDOT, 2003).
- (3) Three levels of modulus of subgrade reaction were selected in compression: 100, 300, and 500 psi/in. It was assumed that subgrade has zero stiffness in tension.
- (4) The friction-slip behavior between concrete and subgrade was characterized using

plane interface elements with the relation between shear traction and shear relative displacement, as shown in Figure 3.15 (Kim et al., 1997). Three levels of frictional stress-slip stiffness were considered: 100, 300, and 500 psi/in. The yield slip was assumed to be 0.02 in.

- (5) Three levels of coefficient of thermal expansion of concrete were used: 4.0×10^{-6} , 5.5×10^{-6} , and 7.0×10^{-6} /°F.
- (6) As for drying shrinkage, eighth-order nonlinear polynomials were used to define the distribution of drying shrinkage strain along the depth axis. As shown in Figure 3.16, three levels of ultimate drying shrinkage strain at the top of the slab were considered: 300, 500, and 600 μ .
- (7) As for thermal loading, third-order nonlinear negative and positive thermal gradients at ± 1.5 °F per inch of slab thickness were assumed (Choi and Won, 2009). As shown in Figure 3.17, six levels of change in concrete temperature were used: -110, -80, -50, -20, 10, and 40 °F. The change in concrete temperature is defined as the difference between the setting temperature and the concrete temperature at the top of the slab at night. Negative changes in concrete temperature mean that the concrete temperature drops below the setting temperature.

Table 3.3: Variation of longitudinal steel spacing

Longitudinal Steel Ratio (%)	Longitudinal Steel Spacing (in.)				
	Slab Thickness (in.)				
	6	8	10	12	14
0.5	15	11½	9	7½	6¼
0.6	12½	9	7	6	5
0.7	10½	7½	6	5	4¼

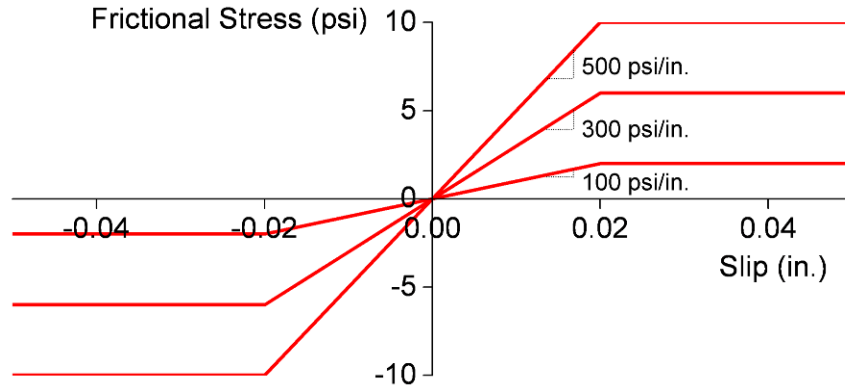


Figure 3.15: Friction-slip behavior between concrete and subgrade

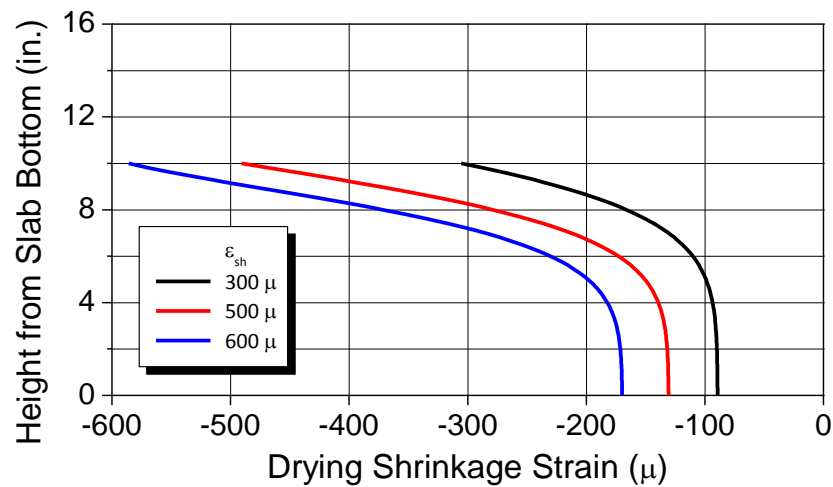


Figure 3.16: Distribution of drying shrinkage strain

The influencing factors and their variations are summarized in Table 3.4. Table 3.5 shows analysis cases generated from changes in each influence factor. It was assumed that the four influencing factors – K_h , α_c , ϵ_{sh} , and ΔT_c – have little influence on concrete stresses caused by traffic loading. These influencing factors were kept constant for the evaluation of traffic load-induced concrete stresses as follows: $K_h = 300$ psi/in. and no values were specified for the other influencing factors (Cases 1 ~ 45). It was assumed that the three influencing factors – H , ρ_s , and K_v – have no significant influence on concrete stresses induced by environmental loading. These influencing factors were kept constant for the evaluation of environmental load-induced concrete stresses as follows: $H = 10$ in., $\rho_s = 0.6\%$, and $K_v = 300$ psi/in. (Cases 46 ~ 207).

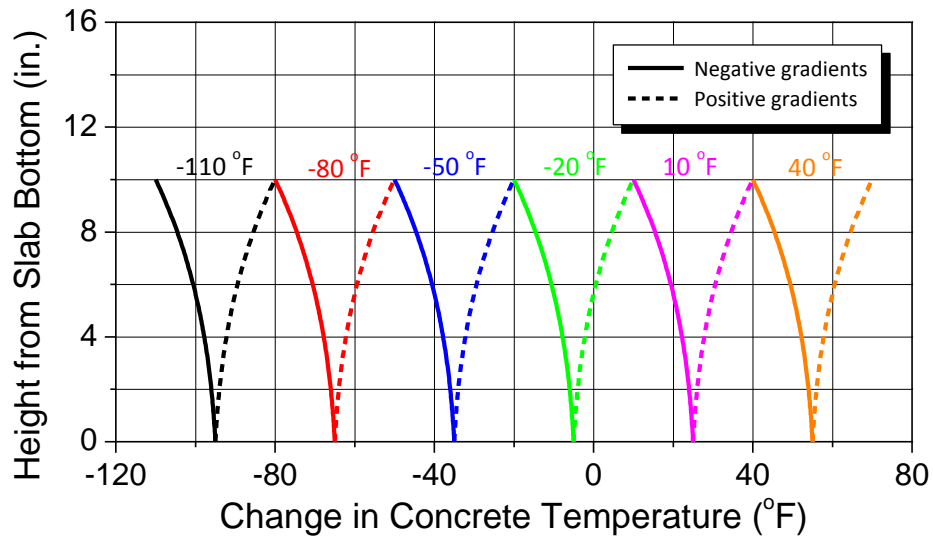


Figure 3.17: Thermal loading

Table 3.4: Influencing factors and their variations

Parameters	Values				
Slab Thickness (in.)	6	8	10	12	14
Longitudinal Steel Ratio (%)	0.5	0.6	0.7		
Modulus of Subgrade Reaction (psi/in.)	100	300	500		
Frictional Stress-Slip Stiffness (psi/in.)	100	300	500		
Coefficient of Thermal Expansion of Concrete ($\times 10^{-6}$ /°F)	4.0	5.5	7.0		
Ultimate Drying Shrinkage Strain (μ)	300	500	600		
Change in Concrete Temperature (°F)	-110	-80	-50	-20	10 40

Table 3.5: Analysis cases

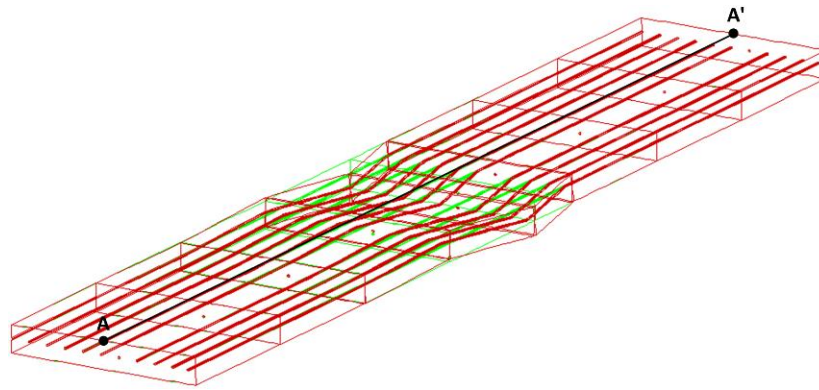
Slab Thickness H (in.)	Change in Concrete Temperature ΔT_c (°F)	Ultimate Drying Shrinkage Strain ϵ_{sh} (μ)	Coefficient of Thermal Expansion of Concrete α_c ($\times 10^{-6}$ /°F)	Frictional Stress-Slip Stiffness K_h (psi/in.)	Case Number								
					Longitudinal Steel Ratio ρ_s (%)								
					0.5			0.6			0.7		
					Modulus of Subgrade Reaction K_v (psi/in.)			Modulus of Subgrade Reaction K_v (psi/in.)			Modulus of Subgrade Reaction K_v (psi/in.)		
					100	300	500	100	300	500	100	300	500
6	-	-	-	300	1	2	3	4	5	6	7	8	9
8					10	11	12	13	14	15	16	17	18
10					19	20	21	22	23	24	25	26	27
12					28	29	30	31	32	33	34	35	36
14					37	38	39	40	41	42	43	44	45
Slab Thickness H (in.)	Longitudinal Steel Ratio ρ_s (%)	Modulus of Subgrade Reaction K_v (psi/in.)	Change in Concrete Temperature ΔT_c (°F)	Ultimate Drying Shrinkage Strain ϵ_{sh} (μ)	Case Number								
					Coefficient of Thermal Expansion of Concrete α_c ($\times 10^{-6}$ /°F)								
					4.0			5.5			7.0		
					Frictional Stress-Slip Stiffness K_h (psi/in.)			Frictional Stress-Slip Stiffness K_h (psi/in.)			Frictional Stress-Slip Stiffness K_h (psi/in.)		
					100	300	500	100	300	500	100	300	500
10	0.6	300	-110	300	46	47	48	49	50	51	52	53	54
				500	55	56	57	58	59	60	61	62	63
				600	64	65	66	67	68	69	70	71	72
			-80	300	73	74	75	76	77	78	79	80	81
				500	82	83	84	85	86	87	88	89	90
				600	91	92	93	94	95	96	97	98	99
			-50	300	100	101	102	103	104	105	106	107	108

				500	109	110	111	112	113	114	115	116	117
				600	118	119	120	121	122	123	124	125	126
			-20	300	127	128	129	130	131	132	133	134	135
				500	136	137	138	139	140	141	142	143	144
				600	145	146	147	148	149	150	151	152	153
			10	300	154	155	156	157	158	159	160	161	162
				500	163	164	165	166	167	168	169	170	171
				600	172	173	174	175	176	177	178	179	180
			20	300	181	182	183	184	185	186	187	188	189
				500	190	191	192	193	194	195	196	197	198
				600	199	200	201	202	203	204	205	206	207

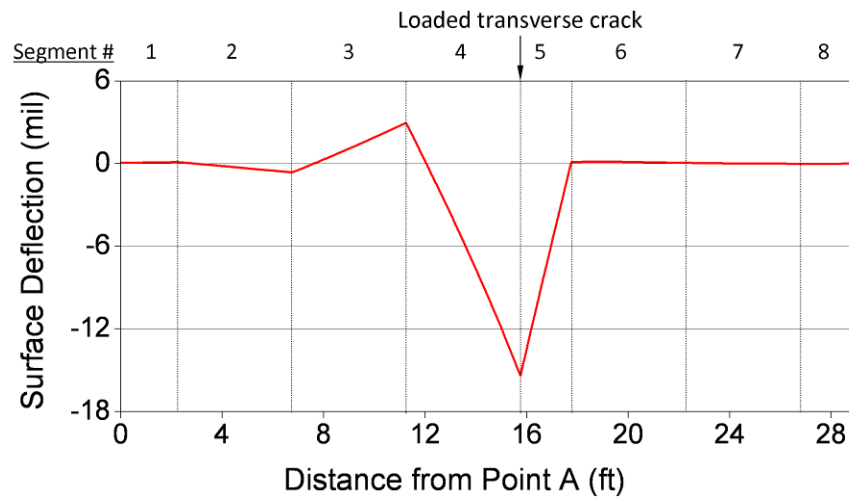
3.4 Numerical Results

3.4.1 Response to traffic loading

A 10-inch thick concrete slab with a longitudinal steel ratio of 0.6% was analyzed assuming the modulus of subgrade reaction to be 300 psi/in. (Case 23). Figure 3.18 shows the deformed shape – magnified 350 times – and deflection along line AA'. The maximum deflection occurs at the loaded transverse crack. The segments enclosed by the loaded transverse crack (Segments #4 and #5) undergo large deflection. Figure 3.19 shows the distribution of principal stresses at the top and bottom of the slab. At the top of the slab, the maximum stress of 75 psi develops in the longitudinal direction and occurs in the wheel path in Segment #4. At the bottom of the slab, slightly larger peak stress of 84 psi occurs in the transverse direction below the wheel loading.

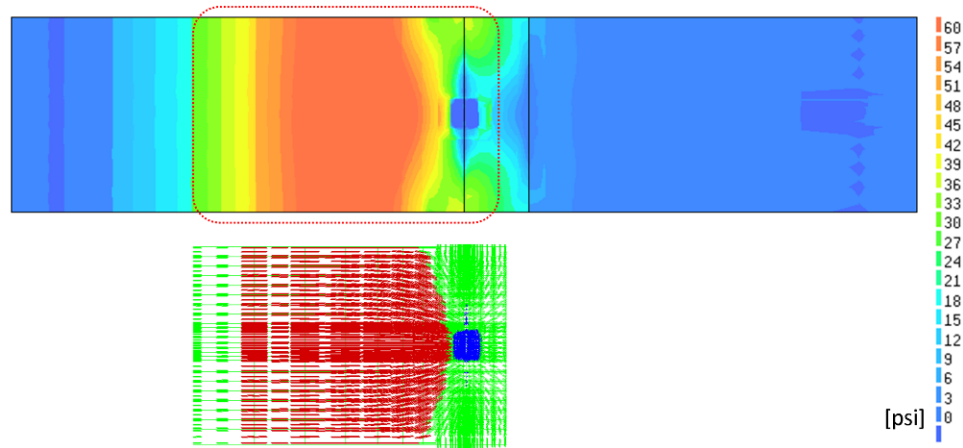


(a) Deformed shape

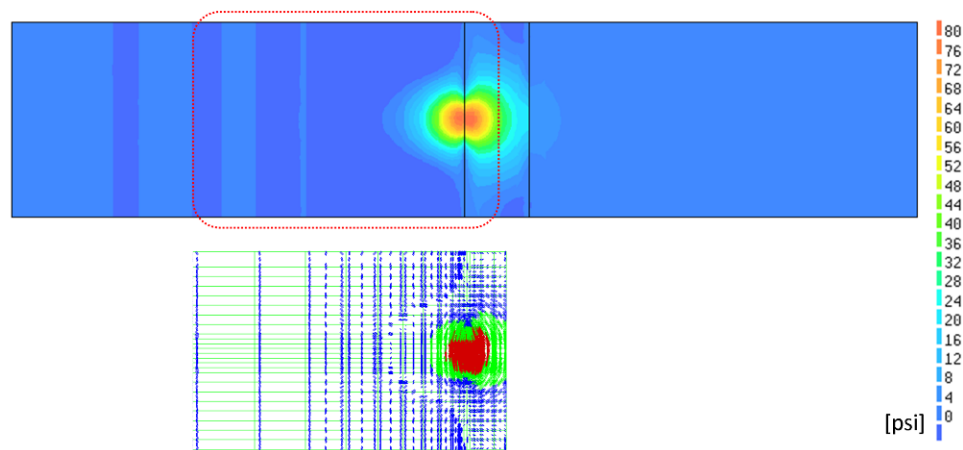


(b) Surface deflection along line AA'

Figure 3.18: Deformed shape and surface deflection



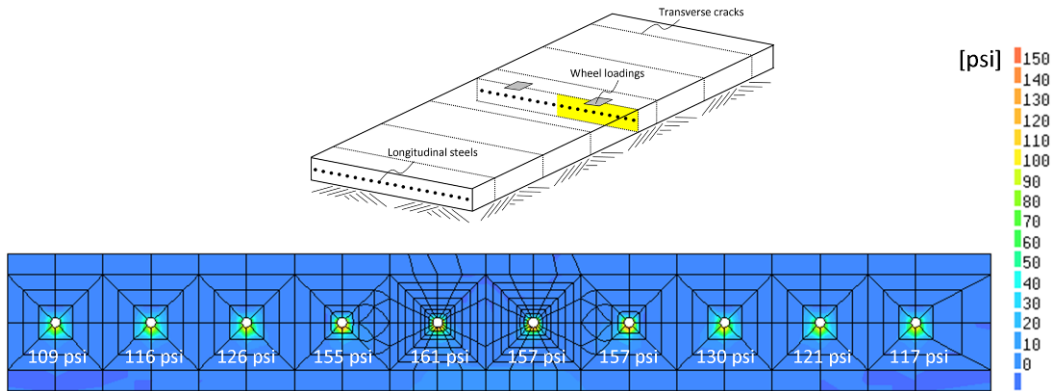
(a) At the top of the slab



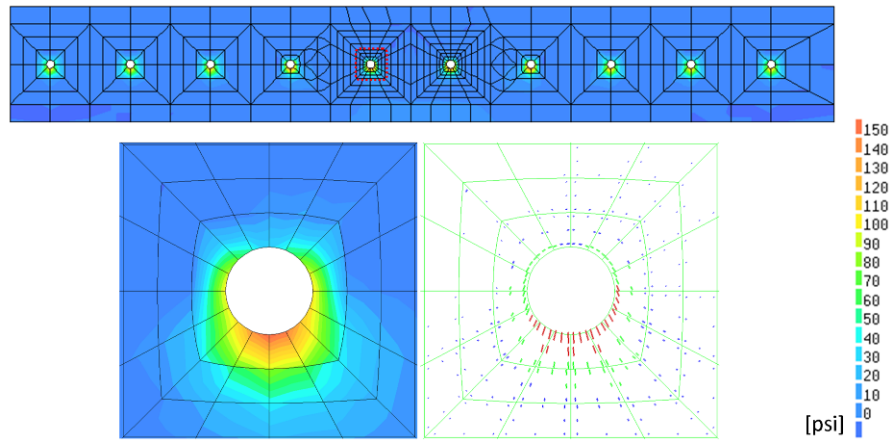
(b) At the bottom of the slab

Figure 3.19: Principal stresses at the top and bottom of the slab

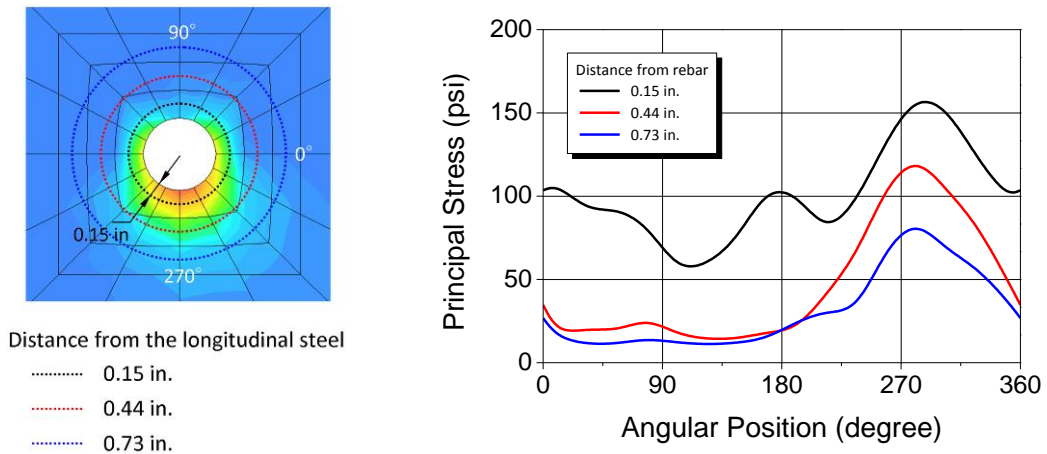
The distribution of principal stresses at the loaded transverse crack surface – the yellow plane – is shown in Figure 3.20(a). More precisely speaking, the values in this figure were calculated at points 0.54 in. inside Segment #5. Large tensile stresses develop in the concrete surrounding each longitudinal steel, unlike uncracked CRCP whose tensile stresses occur at the bottom of the slab. Their magnitudes decrease with an increase in distance from the position of wheel loading. The maximum stress approaches 161 psi.



(a) Overall distribution



(b) Distribution around the longitudinal steel below the wheel loading



(c) Stress levels in the vicinity of the longitudinal steel

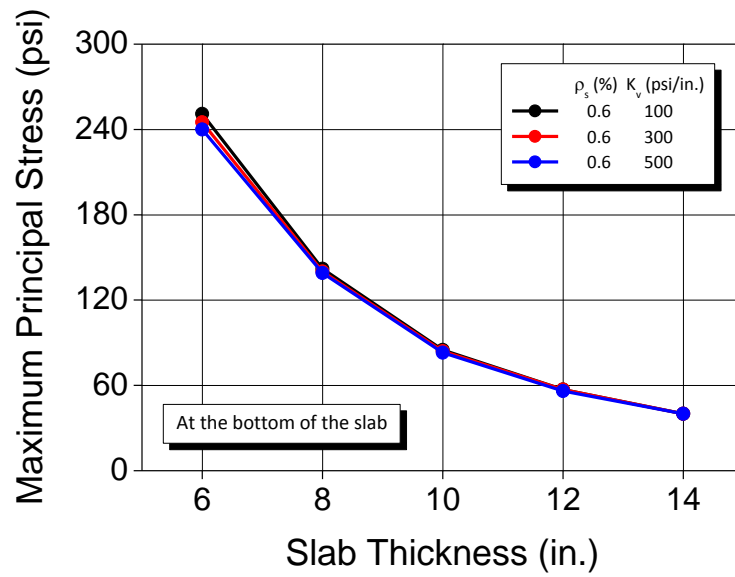
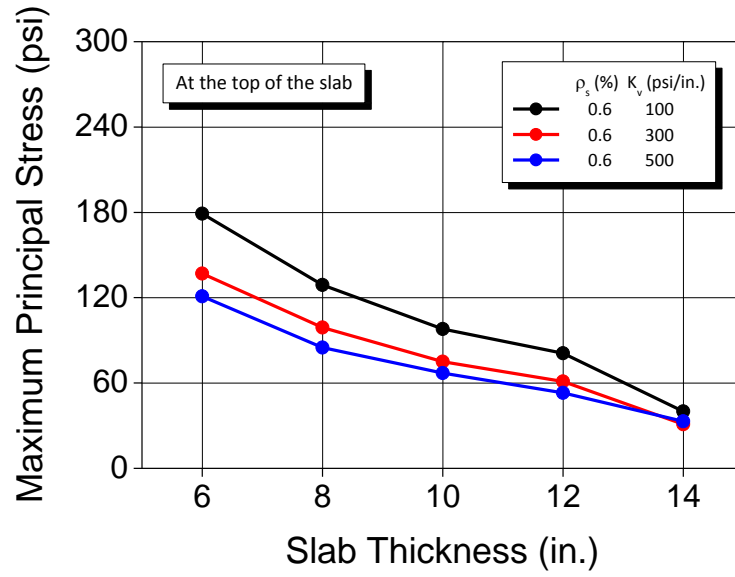
Figure 3.20: Principal stresses at the loaded transverse crack surface

Figure 3.20(b) shows closely the distribution of principal stresses in the concrete around the longitudinal steel which is located below the wheel loading. A large tensile stress zone – the red fringe – is observed below the longitudinal steel. Since the principal stresses in this zone are in the radial direction, horizontal cracking is likely to occur below the longitudinal steel. It seems that the large stresses are induced by an upward reaction of the longitudinal steel; when the segment enclosed by the two 2-ft apart transverse cracks (Segment #5) moves downward, the reaction is generated because the longitudinal steel is connected to the adjacent segment (Segment #4) through the transverse crack. Moreover, it is interesting that the principal stresses above the longitudinal steel are in the tangential direction – even though their levels are not so high – which implies that longitudinal cracking may take place along the longitudinal steel.

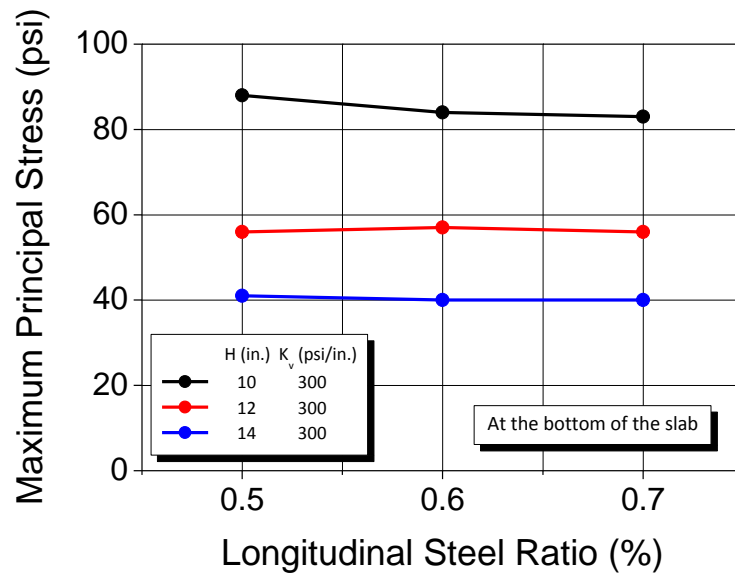
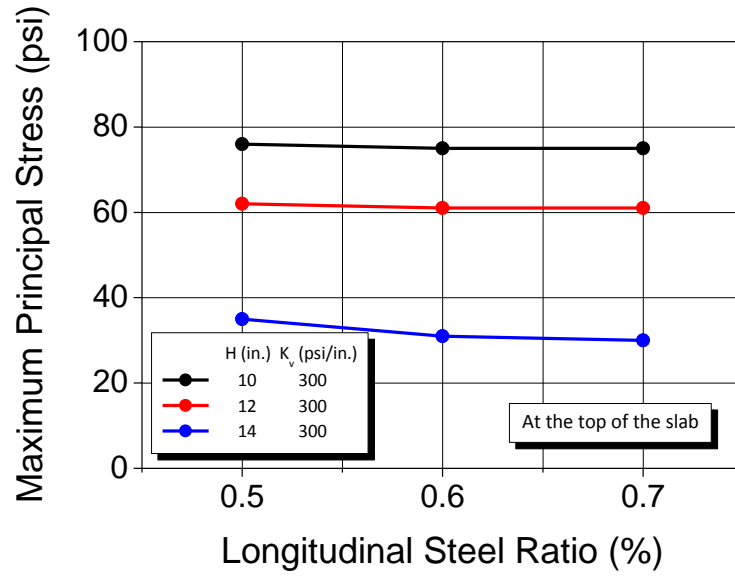
Figure 3.20(c) represents the principal stress plotted versus the angular position around the longitudinal steel; for example, angular positions of 90° and 270° indicate the top and bottom of the longitudinal steel, respectively. Principal stresses at three different distances from the circumference of the longitudinal steel are plotted: 0.15, 0.44, and 0.73 in. The maximum stress develops below the longitudinal steel and the minimum stress develops above the longitudinal steel, regardless of the distance from the circumference of the longitudinal steel. This indicates that, under repeated traffic loading, the potential for horizontal cracking is greater than that for longitudinal cracking (see principal stress vectors in Figure 3.20(b)). On the other hand, the stress decreases sharply away from the longitudinal steel in the radial direction. Other results also showed that the stress decreases rapidly away from the loaded transverse crack in the longitudinal direction. It can be inferred from these results that the region in the vicinity of longitudinal steel at transverse crack surface is most susceptible to cracking.

Based on the numerical results, a probable mechanism for punchouts caused by structural deficiency can be derived as follows: (1) the wheel loading causes large tensile stresses – even though their magnitudes are well below the tensile strength of concrete – in the concrete surrounding the longitudinal steel; (2) the cracking potential increases with time due to the fatigue of concrete from repeated wheel loading applications; (3) localized small horizontal cracks begin to form below longitudinal steels in the wheel path; (4) horizontal cracks propagate with the increasing number of loading cycles; (5) beginning later than horizontal cracks, localized small longitudinal cracks initiate above the longitudinal steel in the wheel path; and (6) longitudinal cracks propagate due to further repeated traffic loading, which eventually leads to punchouts.

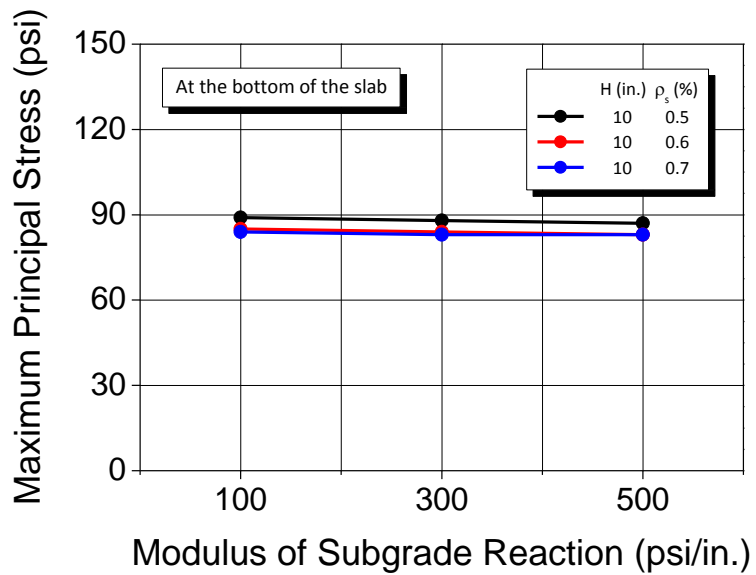
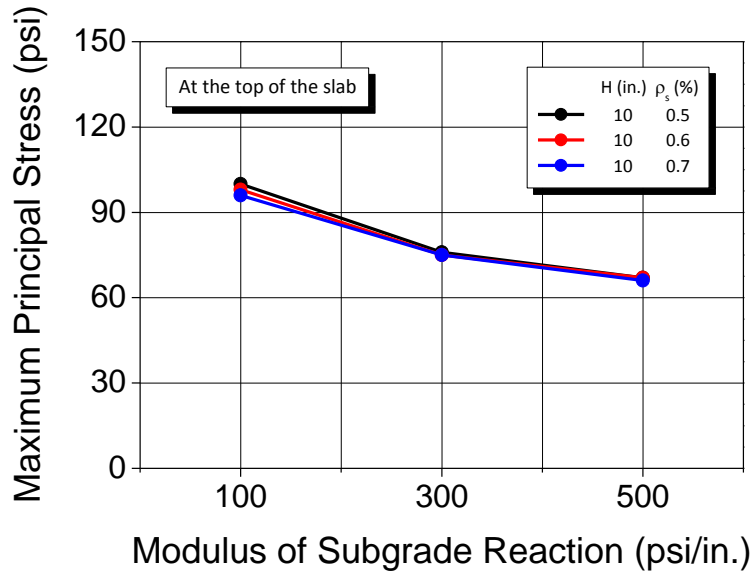
Figure 3.21 shows the influence of the design parameters – slab thicknesses, longitudinal steel ratios, and the moduli of subgrade reaction – on the maximum principal stresses at the top and bottom of the slab. The maximum principal stress at the top of the slab decreases with increases in the slab thickness and the modulus of subgrade reaction. The maximum principal stress at the bottom of the slab decreases with an increase in the slab thickness while it is almost uninfluenced by the modulus of subgrade reaction. Longitudinal steel ratios have little effect on the maximum principal stress at the top and bottom of the slab.



(a) Influence of slab thickness

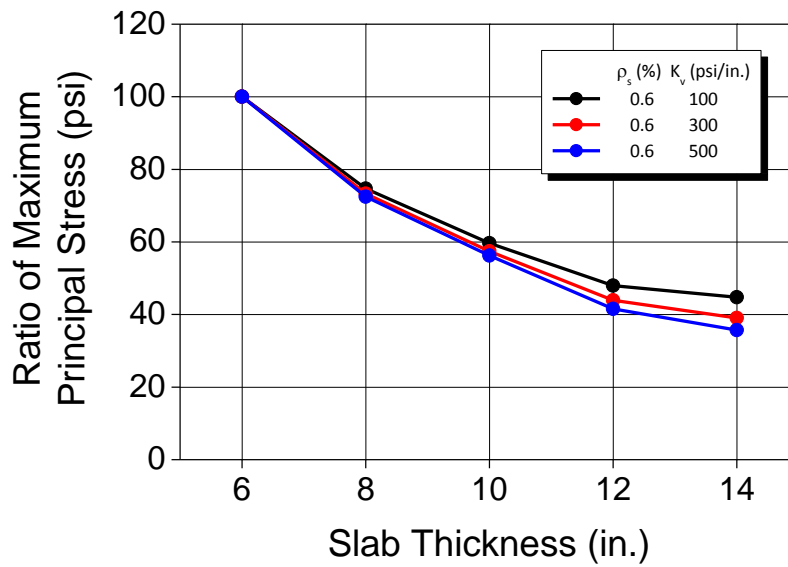
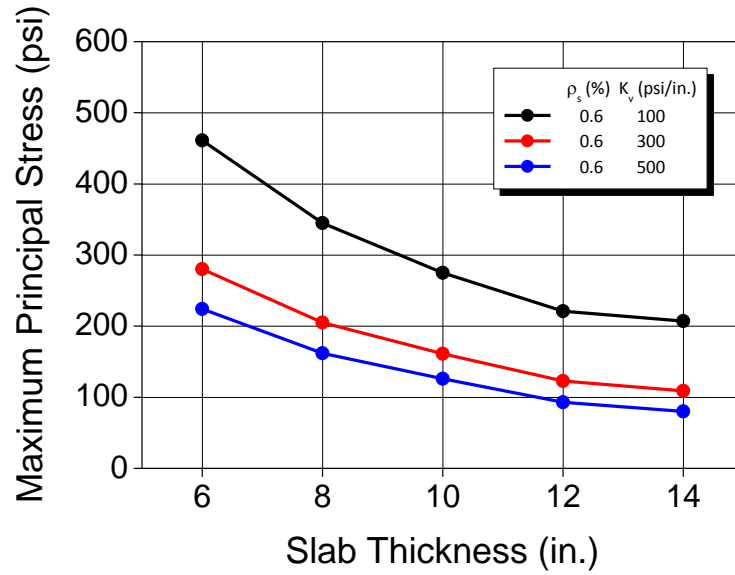


(b) Influence of longitudinal steel ratio

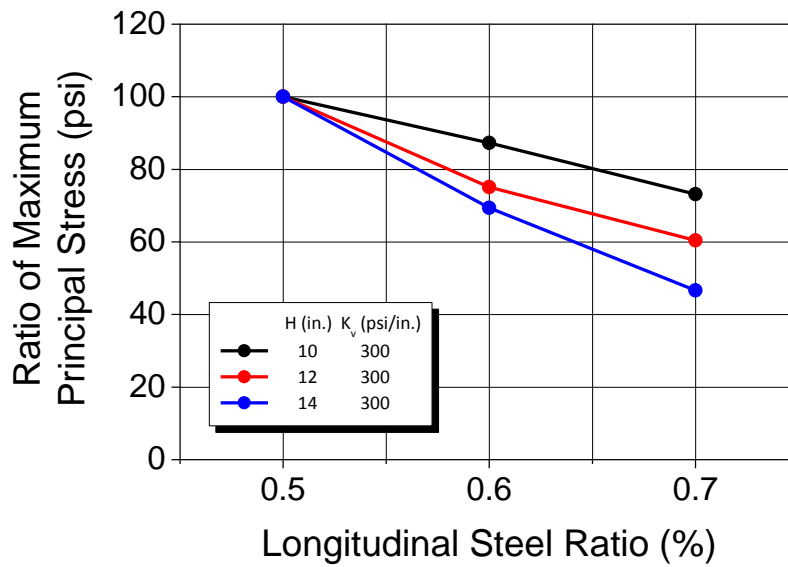
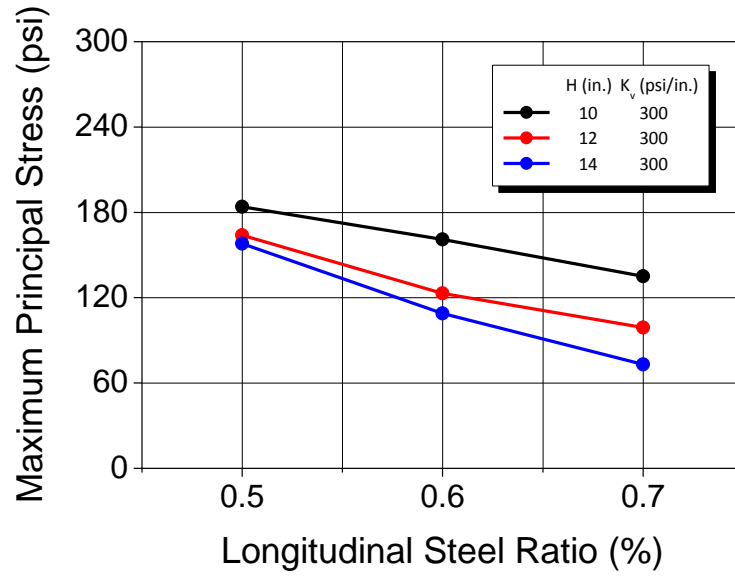


(c) Influence of the modulus of subgrade reaction

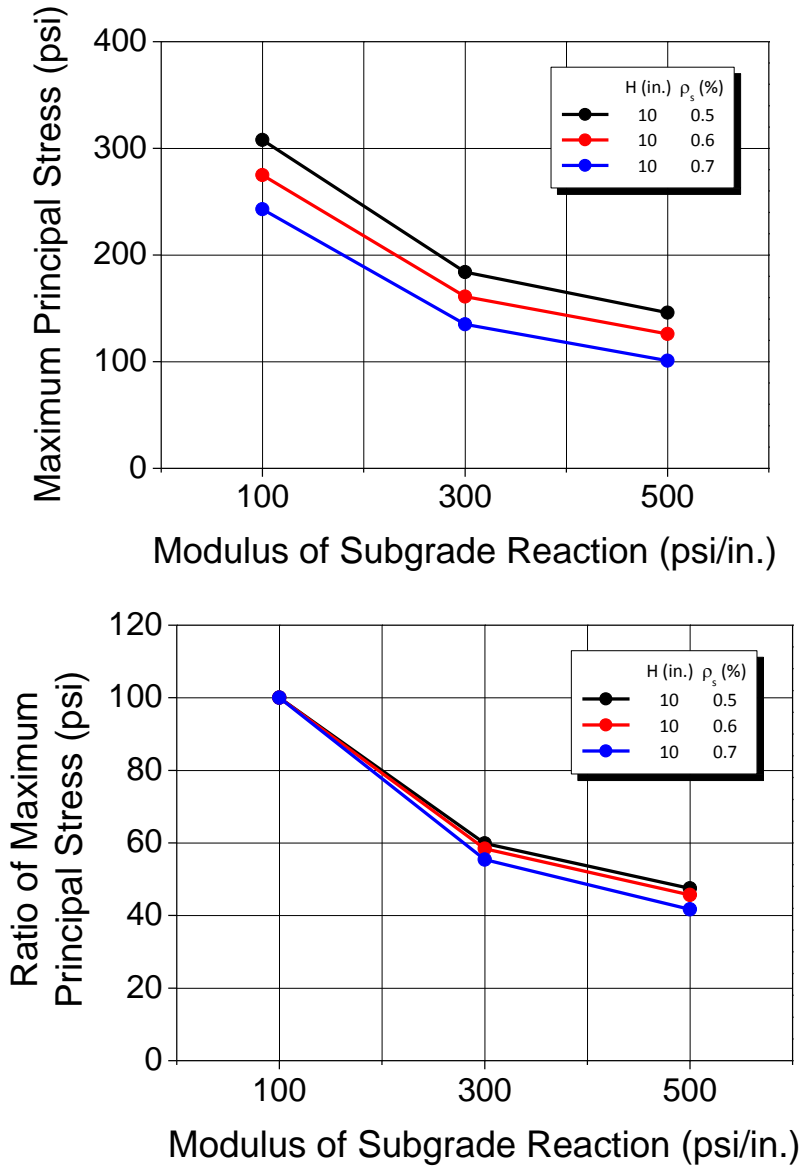
Figure 3.21: Influence of design parameters on maximum principal stresses at the top and bottom of the slab



(a) Influence of slab thickness



(b) Influence of longitudinal steel ratio



(c) Influence of the modulus of subgrade reaction

Figure 3.22: Influence of design parameters on maximum principal stresses at the loaded transverse crack surface

Figure 3.22 shows the influence of the design parameters on the maximum principal stress in the vicinity of longitudinal steel at the loaded transverse crack surface. In all cases that were made by a combination of the design parameters, the peak concrete stress develops in the vicinity of longitudinal steel at the loaded transverse crack surface. The maximum principal stress is larger in thinner concrete slabs with lower longitudinal steel ratios, and it increases as the modulus of subgrade reaction decreases. The normalized graph in Figure 3.22(c) indicates that the quantitative effect (as a percentage) of the

modulus of subgrade reaction is not significantly influenced by the other design parameters; an increase in the modulus of subgrade reaction from 100 to 500 psi/in. results in 55% reduction in the maximum principal stress regardless of longitudinal steel ratio. A similar tendency is observed in the slab thickness. However, the influence of longitudinal steel ratio is more significant in thicker concrete slabs.

3.4.2 Response to environmental loading

A 10-inch thick concrete slab subjected to environmental loading was analyzed by assuming the design parameters, material properties, and environmental conditions as follows (Case 113): $\rho_s = 0.6\%$, $K_v = 300$ psi/in., $\Delta T_c = -50$ °F, $\varepsilon_{sh} = 500$ μ , $\alpha_c = 5.5 \times 10^{-6}$ /°F, and $K_h = 300$ psi/in. Creep is defined as the increase in strain under sustained stresses. Since the concrete slab is subjected to long-term loading, concrete creep should be taken into consideration. However, since the analysis performed in this study is not a transient analysis, it is not available to perform a rigorous creep analysis. Accordingly, an approximate method – the Age-adjusted Effective Modulus Method (AEMM) (Bazant, 1972) – was used to predict the effect of concrete creep. The AEMM is a simple adjustment to the Effective Modulus Method (EMM) to account for aging effects and stress variations. The age-adjusted effective modulus is defined as follows:

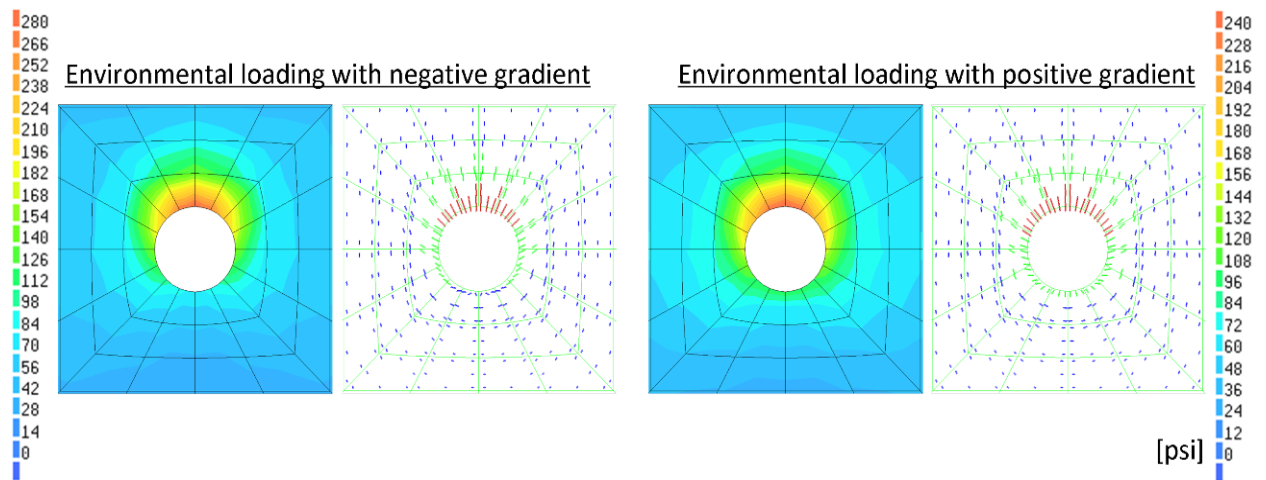
$$E''(t, t_0) = \frac{E(t_0)}{1 + \chi(t, t_0)\phi(t, t_0)} \quad (3.1)$$

where t is the time from casting of concrete, t_0 is the time when loading is applied, $E(t_0)$ is the elastic modulus of concrete at t_0 , $\phi(t, t_0)$ is the creep coefficient at t for loading at t_0 , and $\chi(t, t_0)$ is the aging coefficient at t for loading at t_0 . The ratio of modulus – $E''(t, t_0) / E(t_0)$ – was calculated by employing a step-by-step procedure with computer code in FORTRAN (Ghali et al., 2002). The values required in the calculation were determined based on the equations of CEB-FIP Model Code 1990 (CEB, 1993). The ratio of modulus falls within a range of 0.4 to 0.45 when $t = 30$ years and $t_0 = 3 \sim 7$ days. Accordingly, obtained concrete stresses were multiplied by a factor of 0.4 in consideration of the effect of concrete creep.

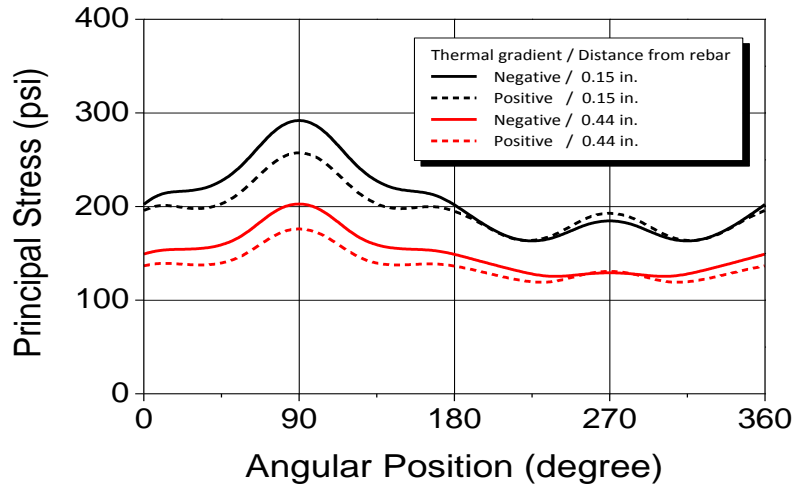
Figure 3.23 shows the distribution of principal stresses in the concrete around the longitudinal steel which was modeled in Figure 3.20(b). As shown in this figure, environmental loading causes tensile stresses in the vicinity of the longitudinal steel, as in the concrete slab under the wheel loading. However, unlike the concrete slab under the wheel loading, the principal stress reaches its maximum above the longitudinal steel. The principal stresses above the longitudinal steel are in the radial direction because a downward reaction is exerted by the longitudinal steel when the concrete slab curls up; when each segment of the slab curls up, the longitudinal steel bends downward at

transverse cracks and applies downward reaction to the concrete because the longitudinal steel is continuously placed through transverse cracks.

Figure 3.23(b) shows that principal stresses induced by environmental loading with the negative thermal gradient are larger than those induced by environmental loading with the positive thermal gradient. This is because the positive thermal gradient makes the concrete slab curl down while drying shrinkage and the negative thermal gradient make the concrete slab curl up; drying shrinkage causes a downward reaction of the longitudinal steel while the positive thermal gradient causes an upward reaction of the longitudinal steel. The principal stress decays rapidly with an increase in distance from the longitudinal steel in the radial direction, as in the concrete slab under the wheel loading.

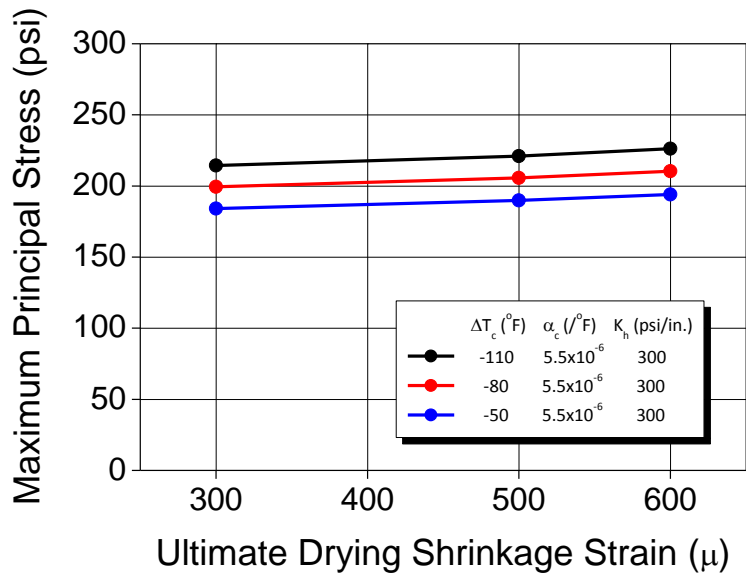
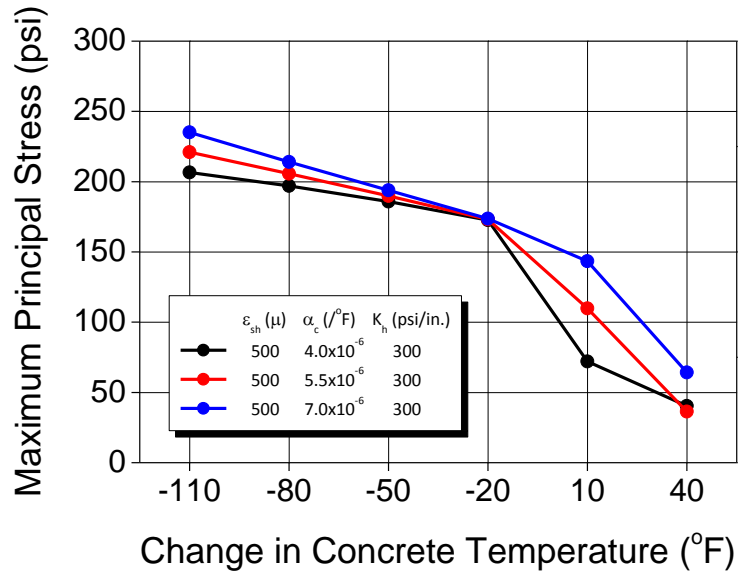


(a) Distribution around the longitudinal steel



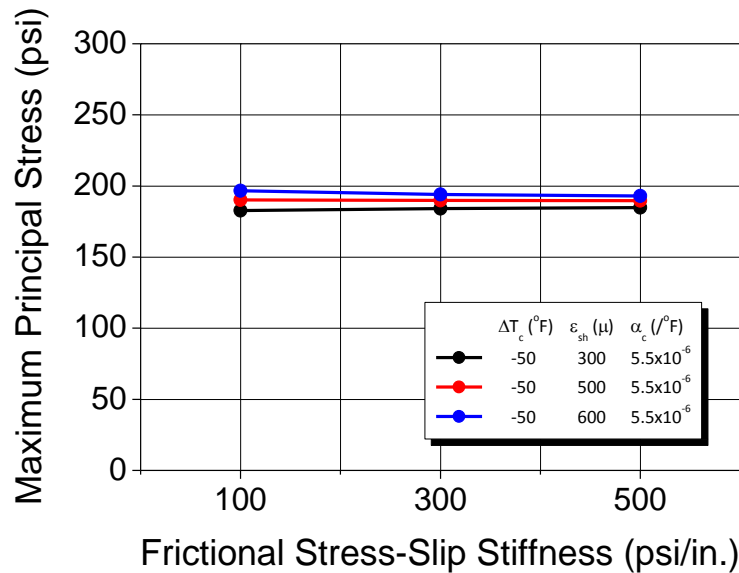
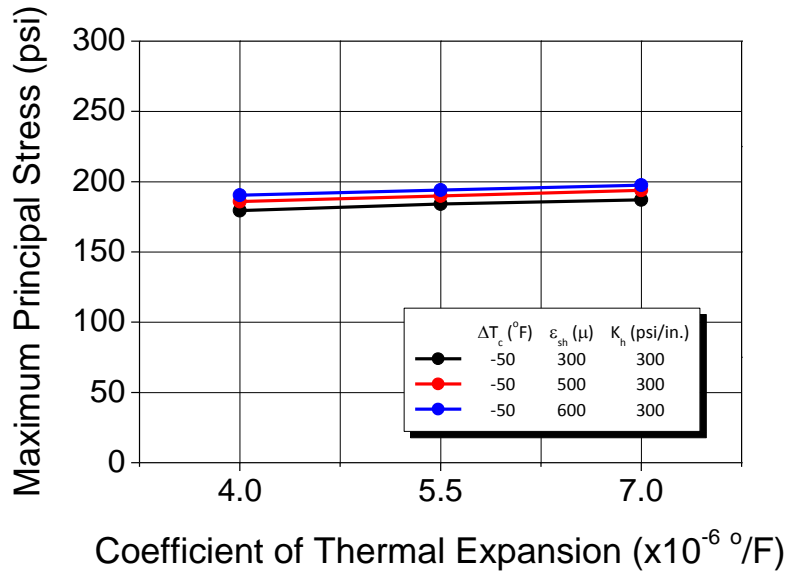
(b) Stress levels in the vicinity of the longitudinal steel

Figure 3.23: Principal stresses at the loaded transverse crack surface



(a) Effect of change in concrete temperature

(b) Effect of ultimate drying shrinkage strain



(c) Effect of the coefficient of thermal expansion

(d) Effect of frictional stress-slip stiffness

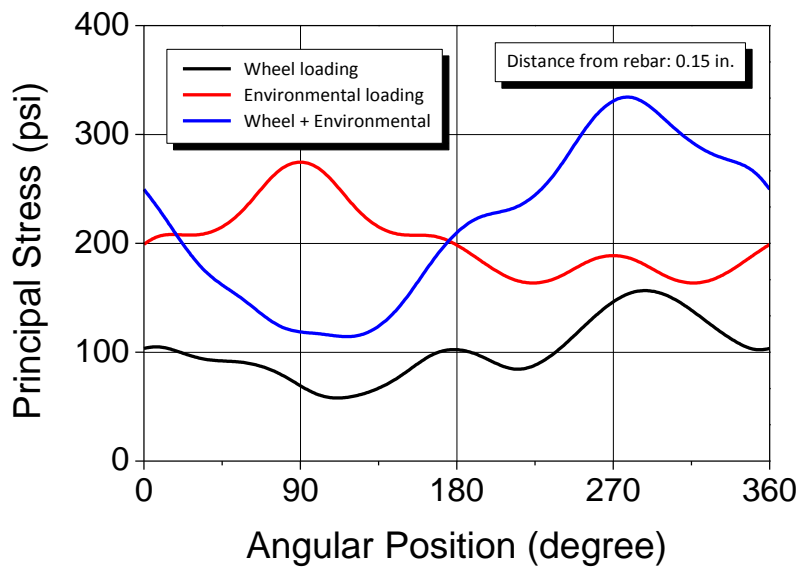
Figure 3.24: Influence of material properties and environmental conditions on maximum principal stresses at the loaded transverse crack surface

Figure 3.24 shows the effects of material properties and environmental conditions on the maximum principal stress developed in the concrete below the longitudinal steel. The value described in this figure represents the average of the maximum principal stress induced by environmental loading with the positive thermal gradient and that induced by environmental loading with the negative thermal gradient. As shown in this figure, the change in concrete temperature has the most significant effect on the maximum principal stress. Larger concrete stress develops as the concrete slab undergoes a larger temperature

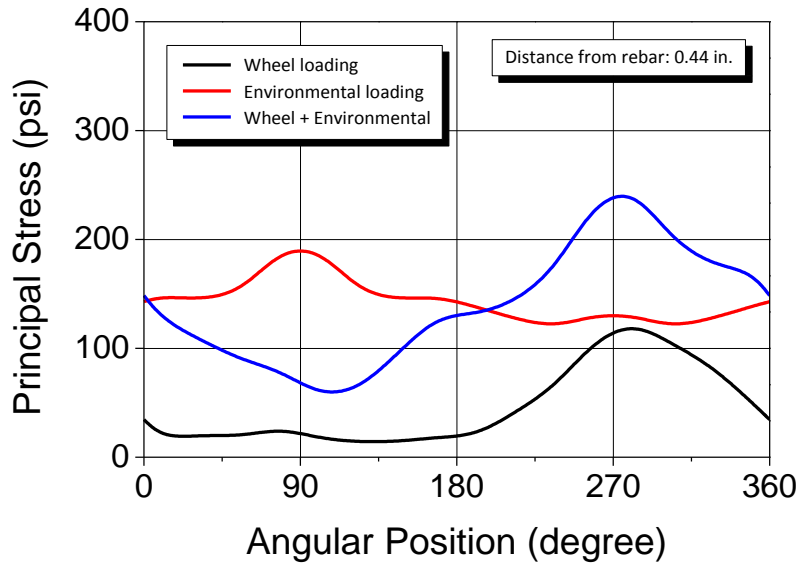
drop from the setting temperature. The maximum principal stress slightly increases with increases in the ultimate drying shrinkage strain and the coefficient of thermal expansion of concrete. On the other hand, the friction-slip characteristic between concrete and subgrade has little effect on the maximum principal stress.

3.4.3 Response to combined loading

Figure 3.25 shows the distribution of principal stresses caused by a combined traffic and environmental loading in the concrete around the longitudinal steel which was modeled in Figure 3.20(b). The design parameters, material properties, and environmental conditions were assumed as follows: $H = 10$ in., $\rho_s = 0.6\%$, $K_v = 300$ psi/in., $\Delta T_c = -50$ °F, $\epsilon_{sh} = 500$ μ , $\alpha_c = 5.5 \times 10^{-6}$ /°F, and $K_h = 300$ psi/in. Six components of concrete stress – σ_x , σ_y , σ_z , τ_{xy} , τ_{yz} , and τ_{zx} – due to the wheel loading and those due to environmental loading were summed up respectively, and the principal stress was calculated based on the sum of stress components. The principal stress due to environmental loading in this figure represents the average of that caused by environmental loading with the positive thermal gradient and that caused by environmental loading with the negative thermal gradient.



(a) At 0.15 in. from the circumference of the longitudinal steel



(b) At 0.44 in. from the circumference of the longitudinal steel

Figure 3.25: Principal stresses in the vicinity of the longitudinal steel

As shown in Figure 3.25, the combined loading produces tensile stresses in the concrete around the longitudinal steel, as in the concrete slab under the wheel loading only and in the concrete slab subjected to environmental loading only. However, the pattern of principal stresses caused by the combined loading is similar to that of traffic load-induced principal stresses rather than that of environmental load-induced principal stresses; the principal stress reaches its maximum below the longitudinal steel and it is in the radial direction. Accordingly, the combined loading is likely to result in horizontal cracking in the concrete below the longitudinal steel.

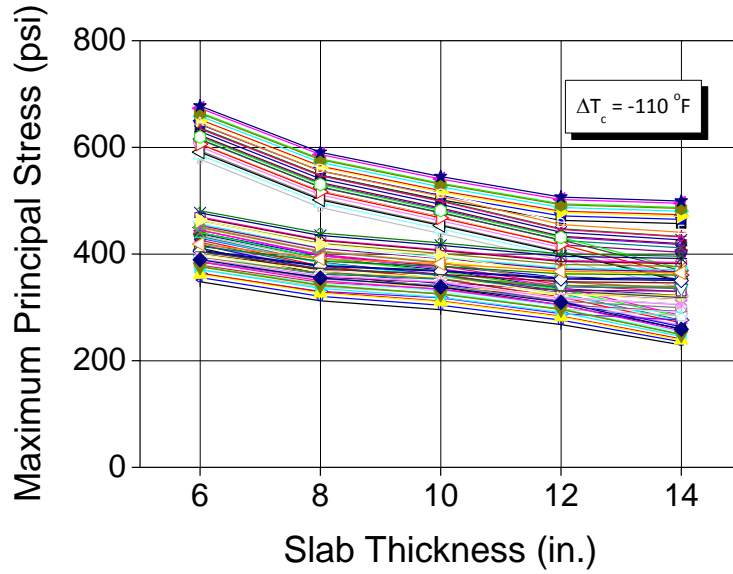
The combined loading affects the magnitude of concrete stresses. However, it should be noted that the principle of superposition cannot be used to calculate the principal stress induced by the combined loading: the principal stress caused by the combined loading is not a simple sum of that caused by traffic loading and that caused by environmental loading. For example, at an angular position of 90° , the principal stress due to the combined loading is even lower than that due to environmental loading only. This is because the principal stress caused by traffic loading and that caused by environmental loading have a different direction above the longitudinal steel (compare Figure 3.20(b) with Figure 3.23(a)). On the other hand, below the longitudinal steel, the principal stress induced by the combined loading is larger than that induced by traffic loading only or that induced by environmental loading. However, even in this location, the principal stress induced by the combined loading is not exactly the sum of the traffic load-induced principal stress and the environmental load-induced principal stress.

The maximum principal stress caused by a combined traffic and environmental loading in the concrete around the longitudinal steel was calculated in a similar manner for 7290 cases generated from changes in each influence factor. These values are summarized in Table 3.6. Since the effect of friction-slip characteristic between concrete and subgrade is insignificant, only principal stresses obtained with $K_h = 300$ psi/in. are presented in this table. Figures 3.26 through 3.32 show the general influence of each design parameter, material property, and environmental condition on the maximum principal stress. The lines in each figure are made by a combination of the variables other than those specified in the figure. For example, there are 81 lines in Figure 3.26(a) made by a combination of three levels of longitudinal steel ratio, three levels of modulus of subgrade reaction, three levels of coefficient of thermal expansion, and three levels of drying shrinkage strain. The keys for each line are not presented because there is not enough space, but the effect of the four variables can be found in Figures 3.27, 3.28, 3.30, and 3.31. From these figures, several observations can be made.

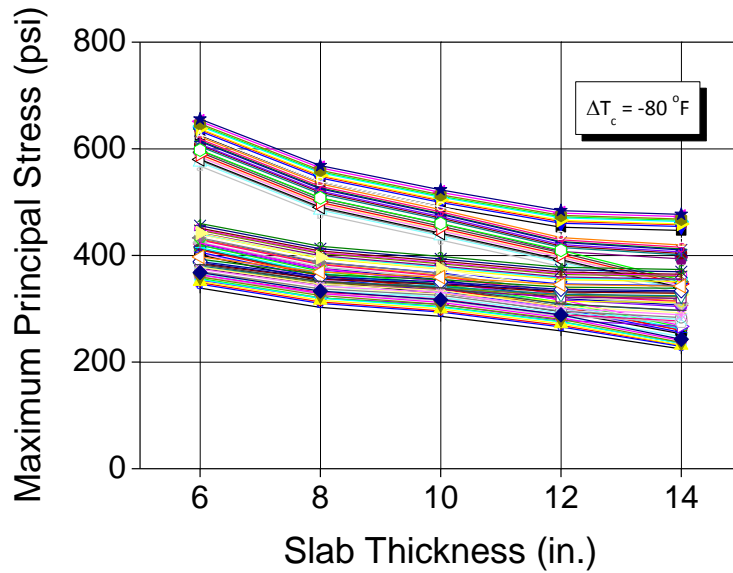
- (1) Larger concrete stress develops in thinner concrete slabs. The effect of slab thickness is more prominent as the concrete slab gets thinner.
- (2) The concrete stress is larger in concrete slabs with lower longitudinal steel ratios. The concrete stress has a nearly linear relationship with the longitudinal steel ratio.
- (3) The concrete stress increases with a decrease in the modulus of subgrade reaction. The effect of modulus of subgrade reaction is more significant as it gets smaller.
- (4) Larger concrete stress develops as the concrete slab undergoes a larger temperature drop from the setting temperature. There is a roughly bilinear relationship between concrete stresses and changes in concrete temperature. The relationship has a gradual slope if $\Delta T_c < 0$, while it has a steep slope if $\Delta T_c > 0$. This can be explained as follows: environmental loading is composed of thermal loading and drying shrinkage. The principal stress due to thermal loading and that due to drying shrinkage have the same direction when the concrete temperature drops below the setting temperature. However, the directions of the two principal stresses are different from each other when the concrete temperature rises above the setting temperature, and therefore the combined loading from thermal loading and drying shrinkage may result in a much smaller principal stress depending on the relative magnitude of thermal and drying shrinkage strains.
- (5) The concrete stress increases with an increase in the ultimate drying shrinkage strain. There is a linear gradual relationship between concrete stresses and ultimate drying shrinkage strains if $\Delta T_c < 0$. For the same reason with that stated in (4), the effect of ultimate drying shrinkage is notable if $\Delta T_c > 0$.
- (6) The concrete stress increases with an increase in the coefficient of thermal expansion of concrete. Its effect becomes more significant as the concrete slab undergoes larger temperature drop from the setting temperature. Figure 3.31(d) shows that it has little influence on concrete stresses when the concrete temperature drops by 20 °F from the setting temperature: the thermal strain is very small when $\Delta T_c = -20$ °F (see Figure 3.17). This is why the graphs (d) in Figures 3.26 ~ 3.28, 3.30, and 3.32 look as if they display fewer analytical results than the other graphs – many lines overlap. For the

same reason as stated in (4), the effect of the coefficient of thermal expansion of concrete is notable if $\Delta T_c > 0$.

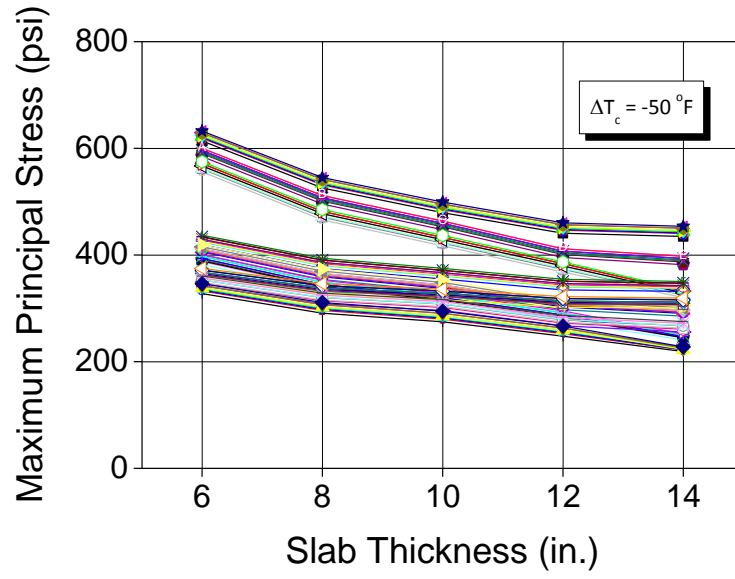
- (7) The concrete stress is almost uninfluenced by the friction-slip characteristic between concrete and subgrade.
- (8) Three influencing factors – slab thickness, the modulus of subgrade reaction, and the change in concrete temperature – have relatively large effects on concrete stresses.



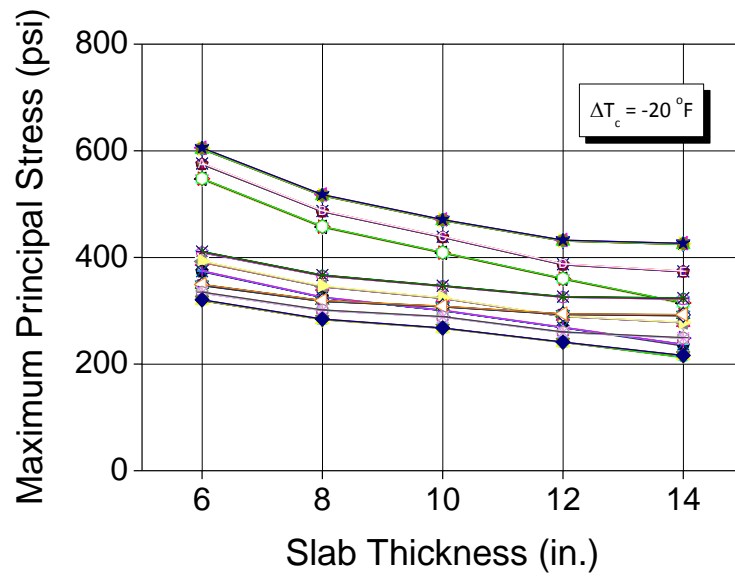
(a) $\Delta T_c = -110^\circ\text{F}$



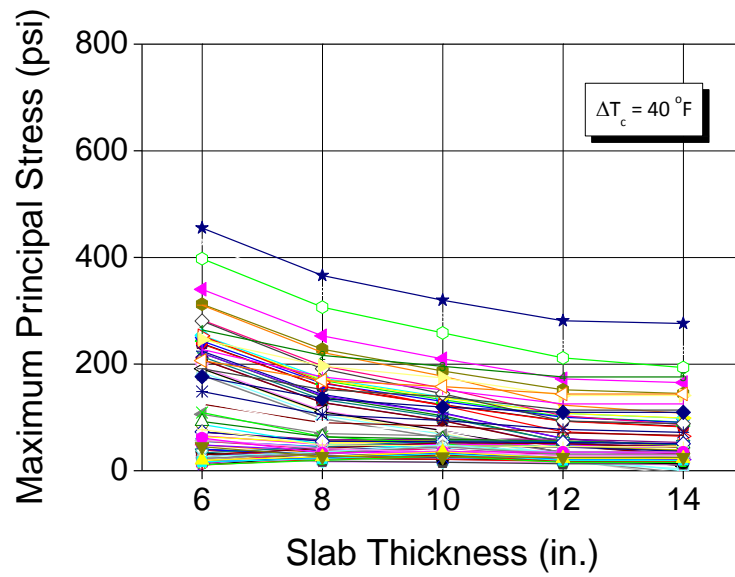
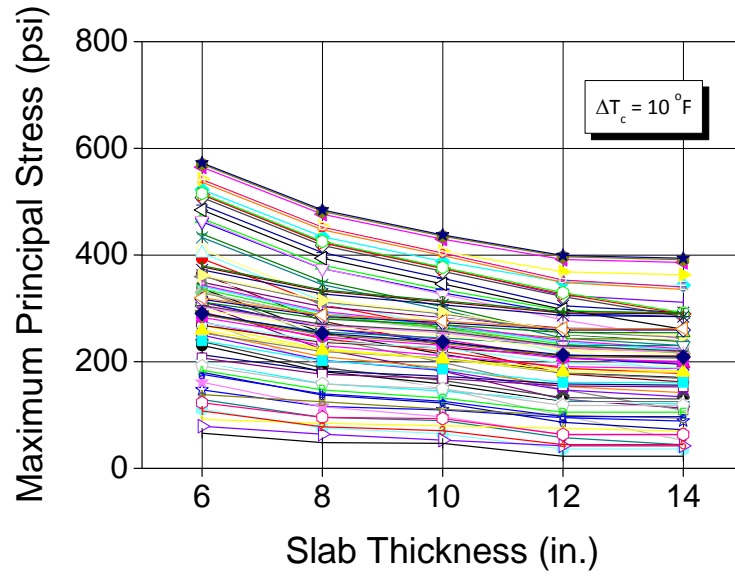
(b) $\Delta T_c = -80^\circ\text{F}$



(c) $\Delta T_c = -50^\circ\text{F}$



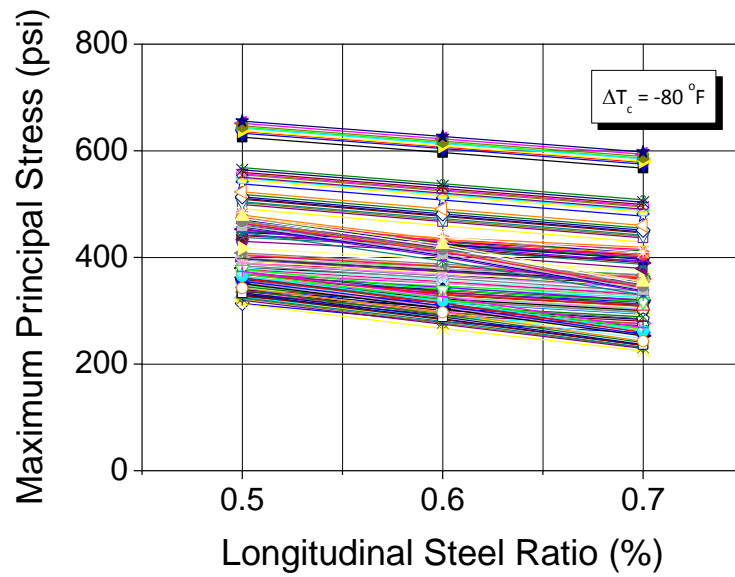
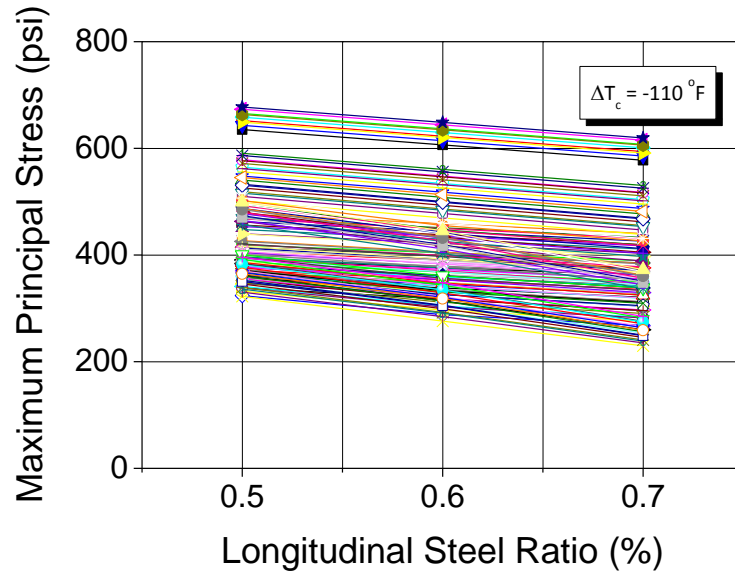
(d) $\Delta T_c = -20^\circ\text{F}$



(e) $\Delta T_c = 10^\circ\text{F}$

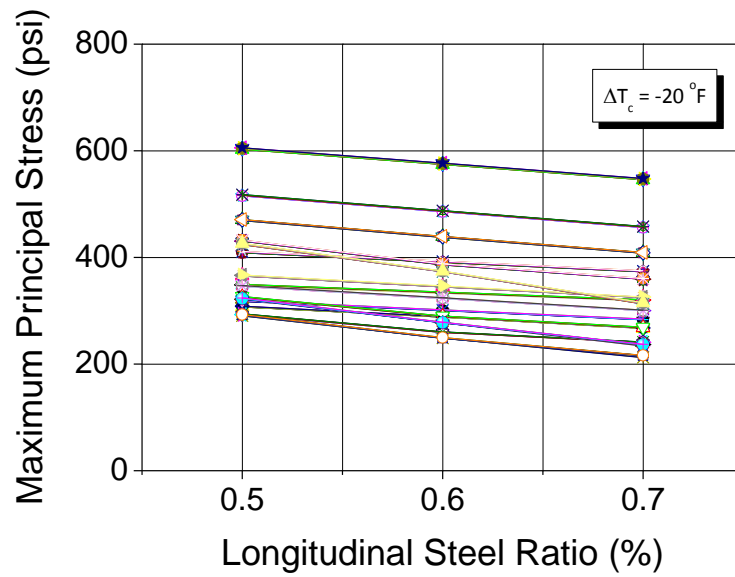
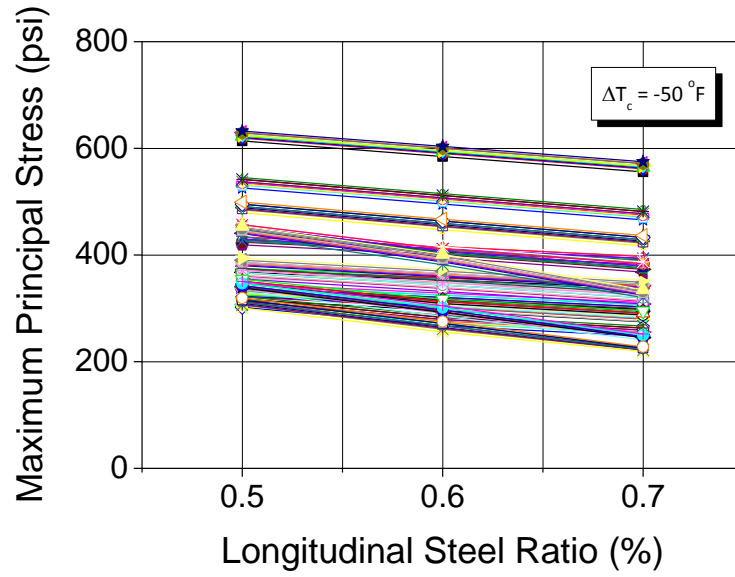
(f) $\Delta T_c = 40^\circ\text{F}$

Figure 3.26: Influence of slab thickness



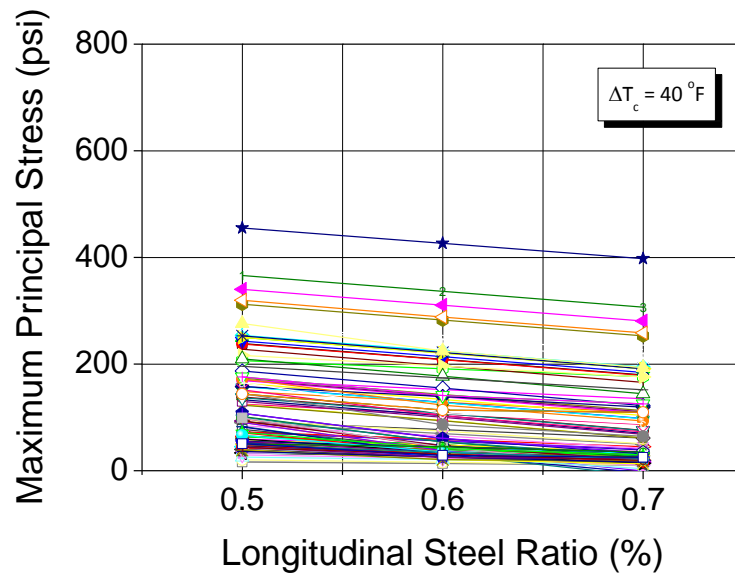
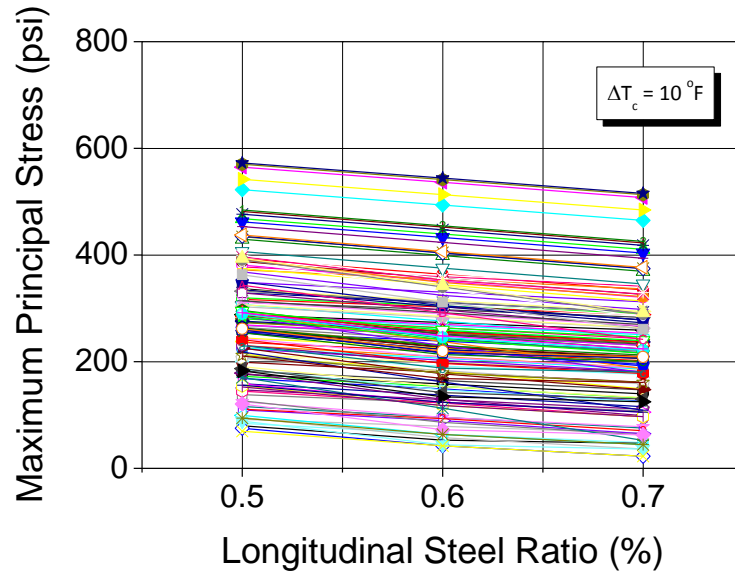
(a) $\Delta T_c = -110^\circ\text{F}$

(b) $\Delta T_c = -80^\circ\text{F}$



(c) $\Delta T_c = -50^\circ\text{F}$

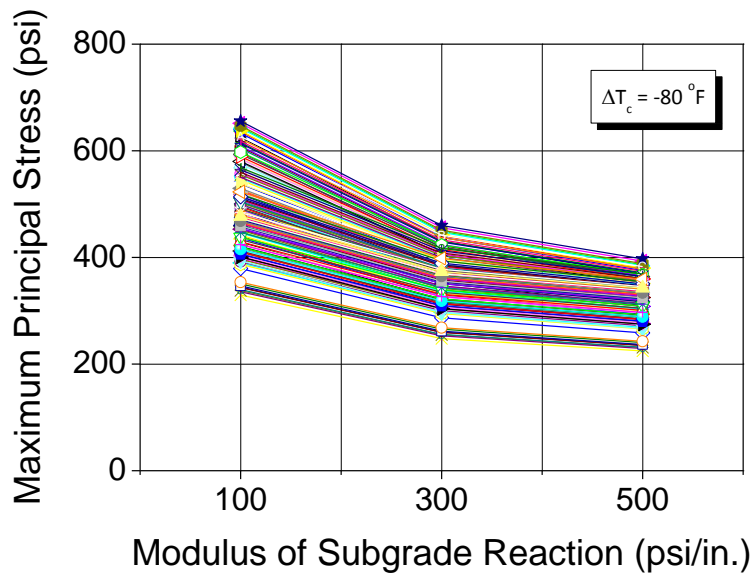
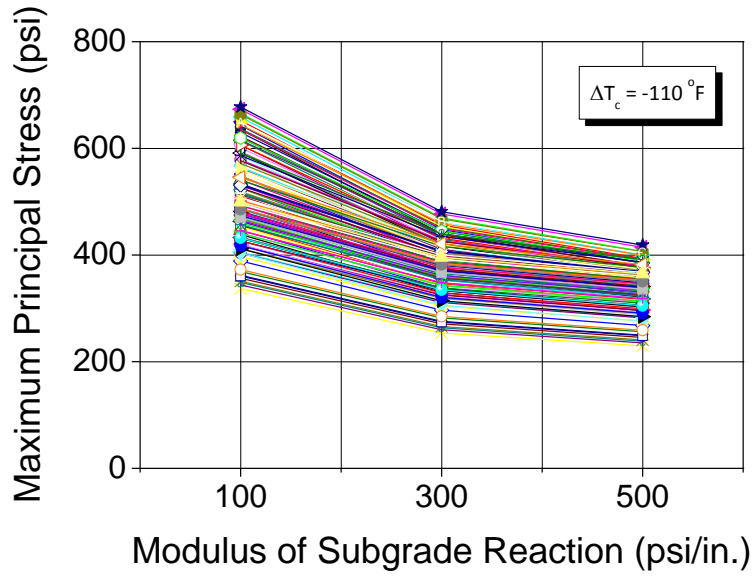
(d) $\Delta T_c = -20^\circ\text{F}$



(e) $\Delta T_c = 10^\circ\text{F}$

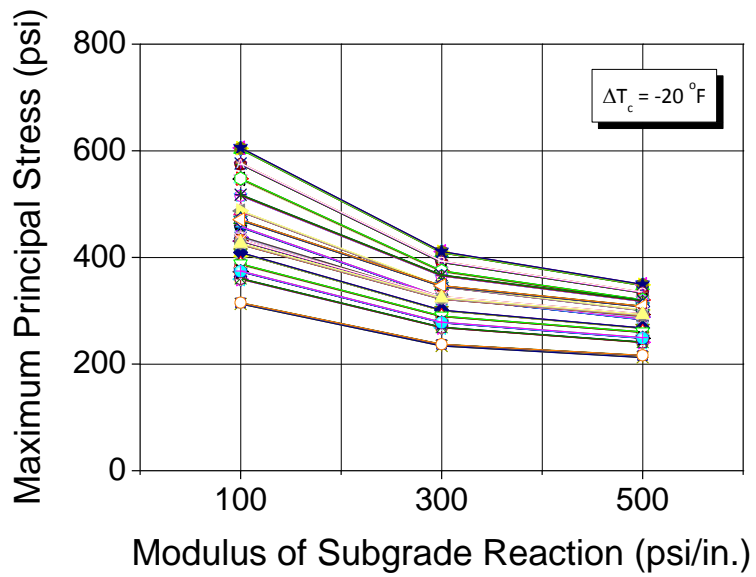
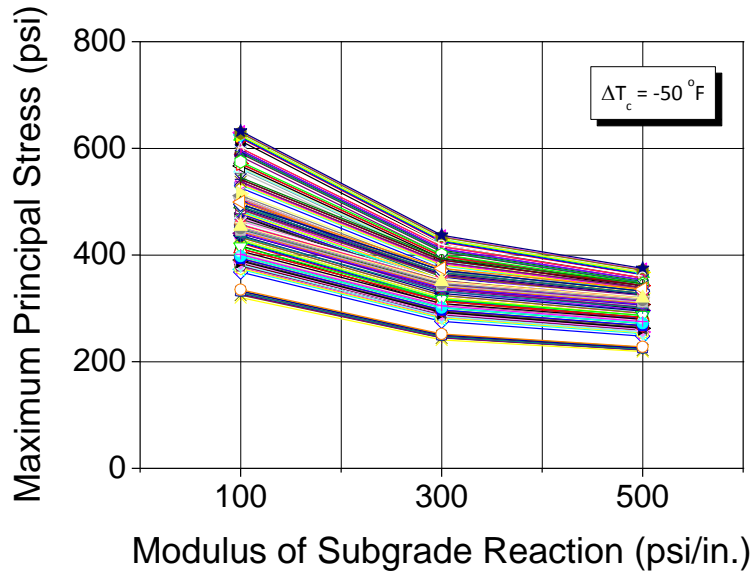
(f) $\Delta T_c = 40^\circ\text{F}$

Figure 3.27: Influence of longitudinal steel ratio



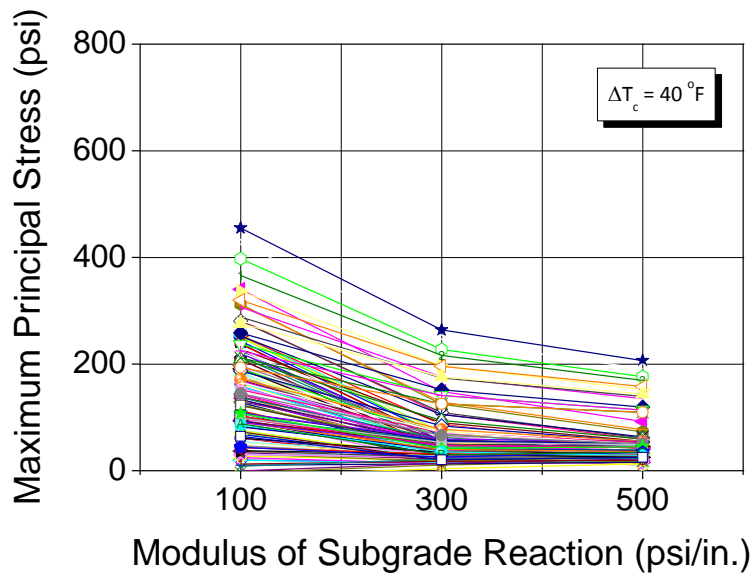
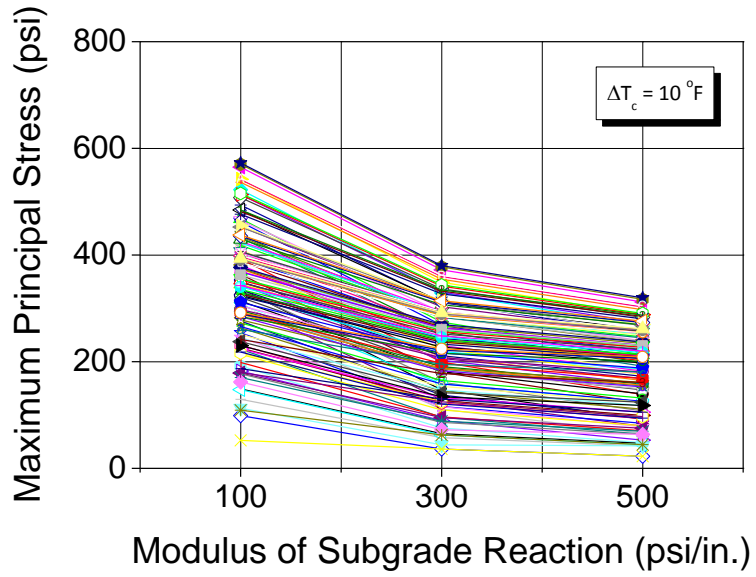
(a) $\Delta T_c = -110 \text{ }^\circ\text{F}$

(b) $\Delta T_c = -80 \text{ }^\circ\text{F}$



(c) $\Delta T_c = -50 \text{ }^\circ\text{F}$

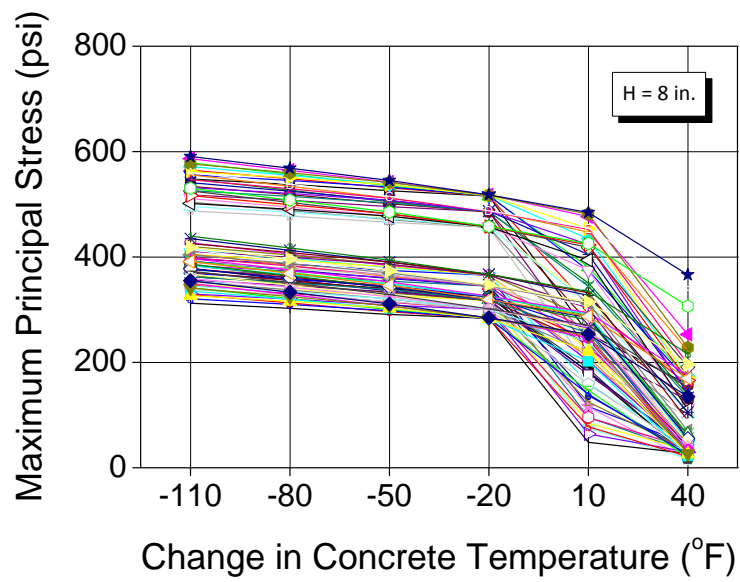
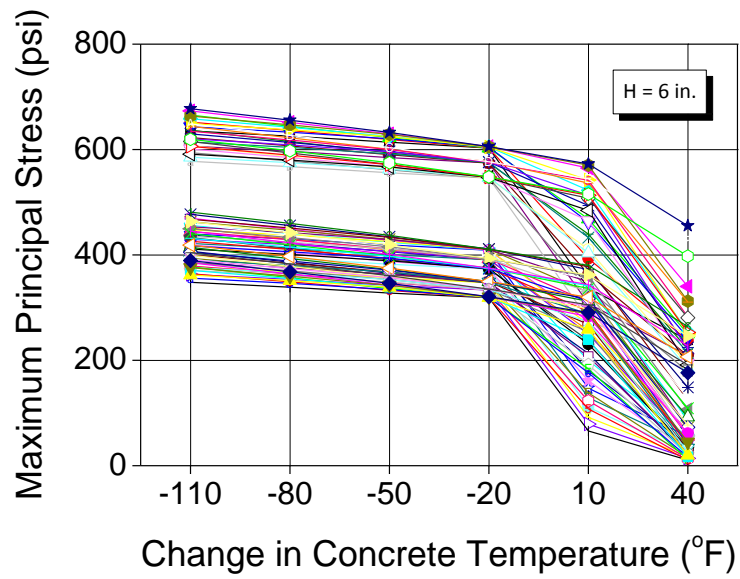
(d) $\Delta T_c = -20 \text{ }^\circ\text{F}$



(e) $\Delta T_c = 10 \text{ }^\circ\text{F}$

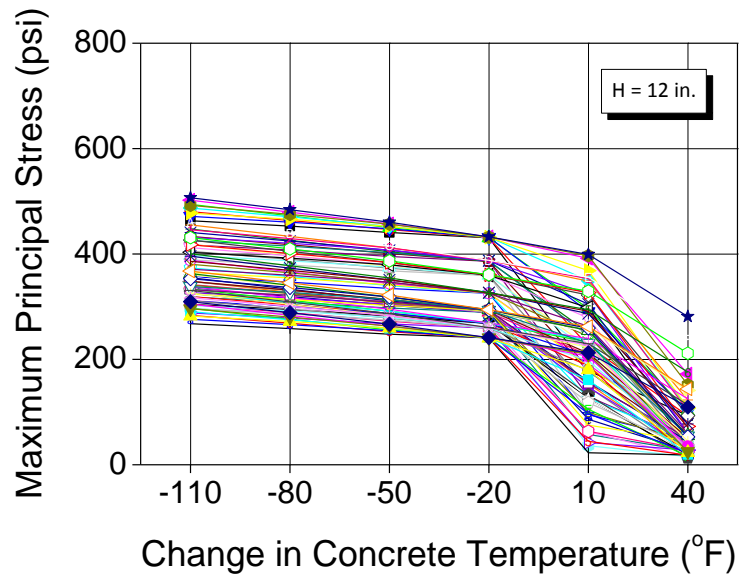
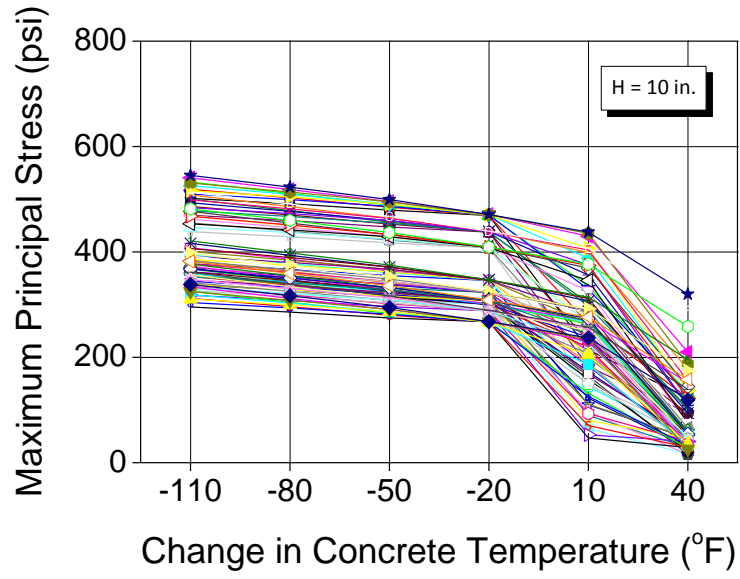
(f) $\Delta T_c = 40 \text{ }^\circ\text{F}$

Figure 3.28: Influence of the modulus of subgrade reaction



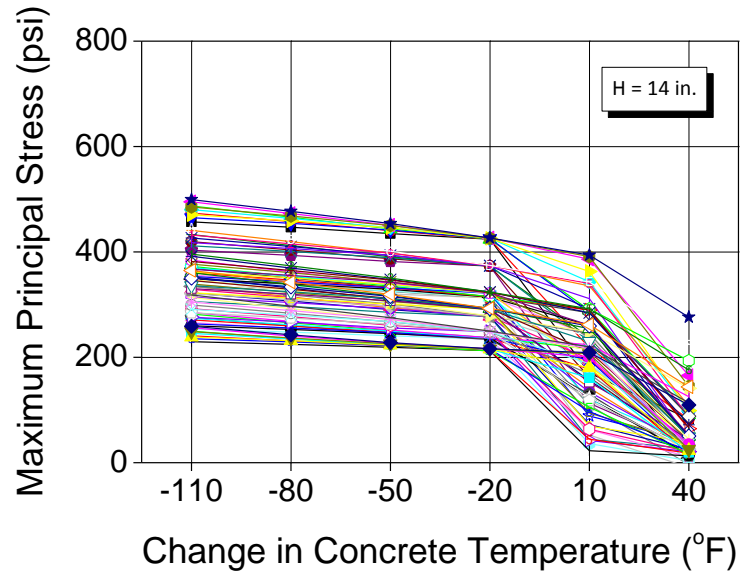
(a) $H = 6$ in.

(b) $H = 8$ in.



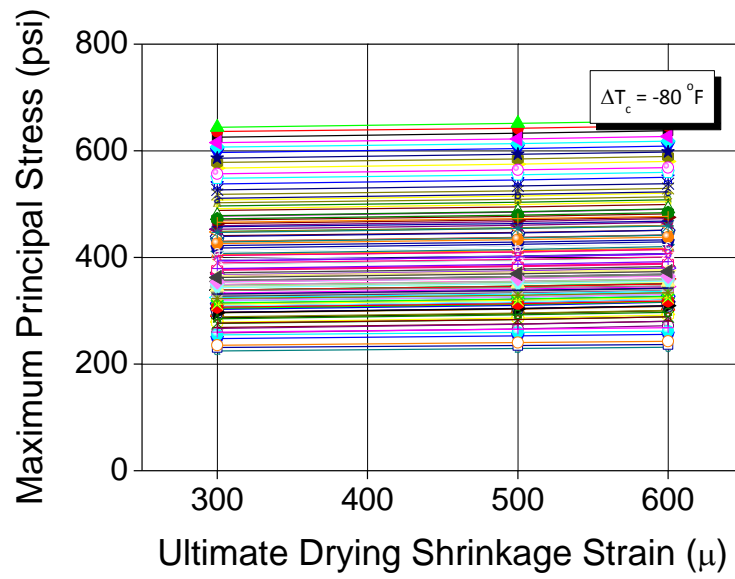
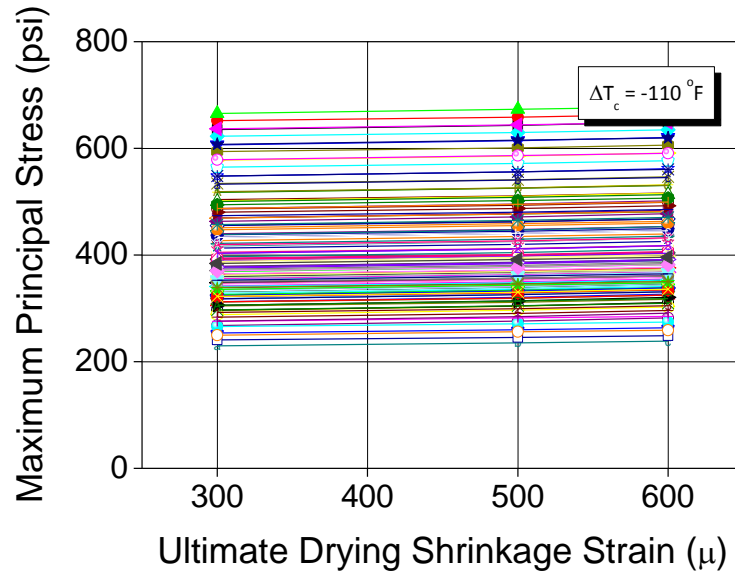
(c) $H = 10$ in.

(d) $H = 12$ in.



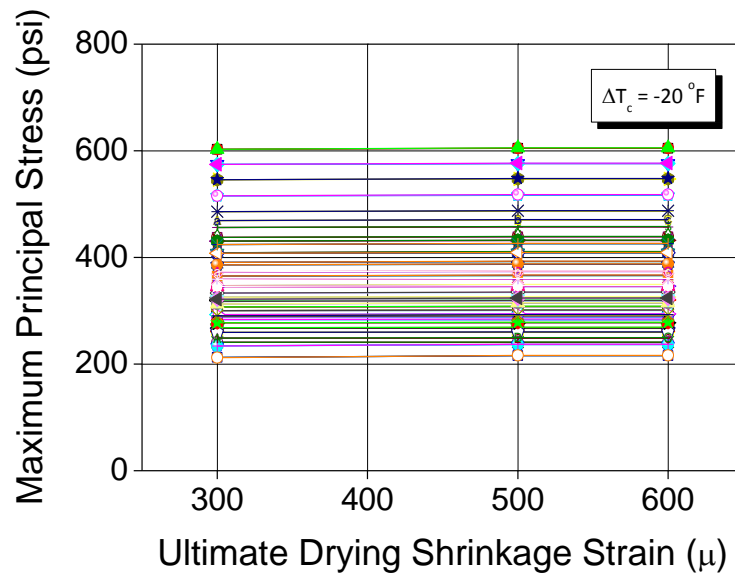
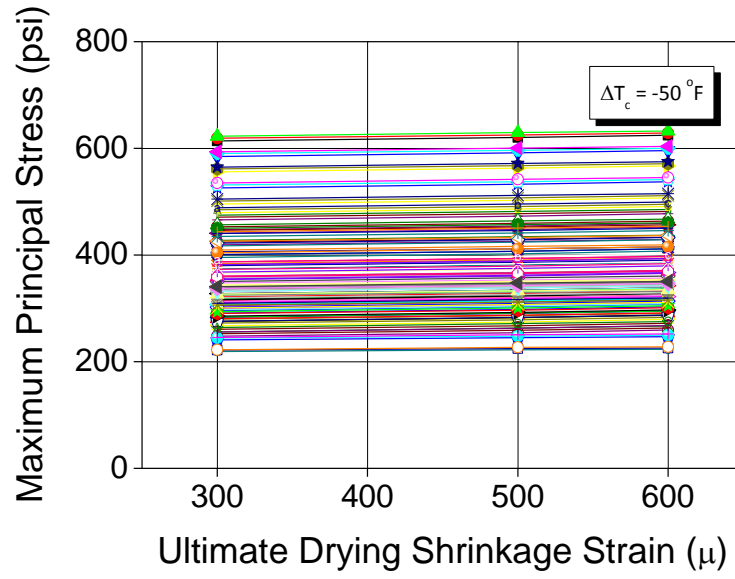
(e) $H = 14$ in.

Figure 3.29: Influence of change in concrete temperature



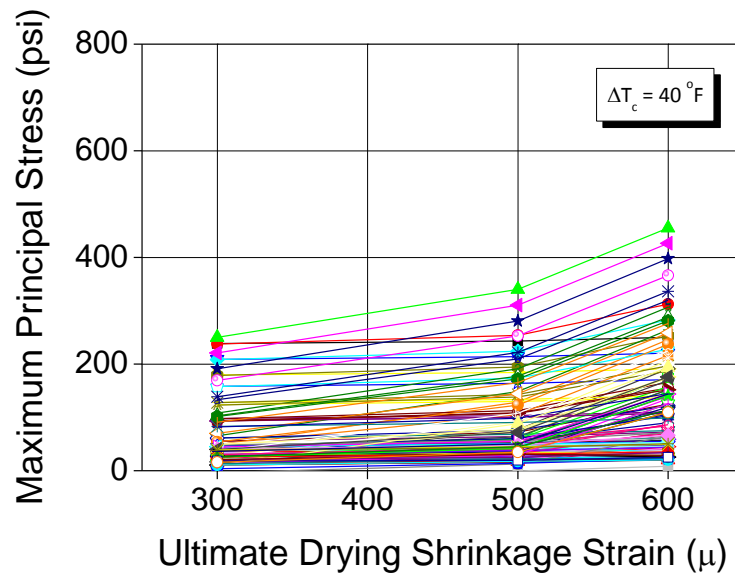
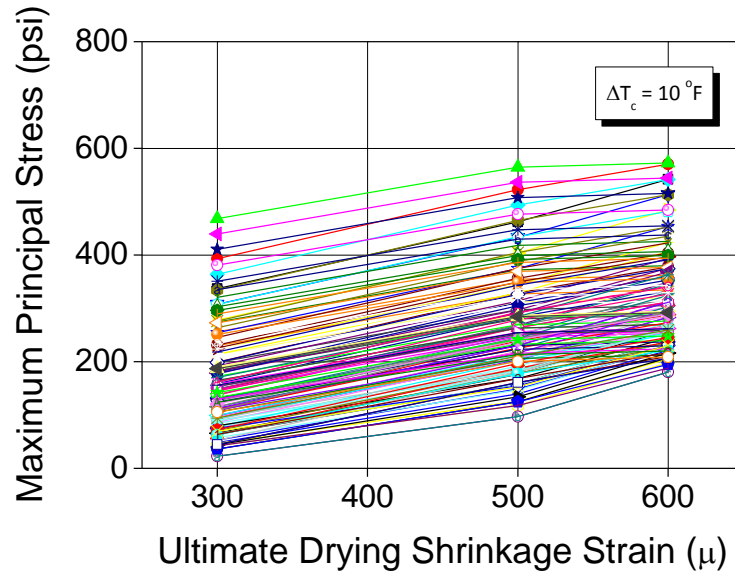
(a) $\Delta T_c = -110^\circ\text{F}$

(b) $\Delta T_c = -80^\circ\text{F}$



(c) $\Delta T_c = -50^\circ\text{F}$

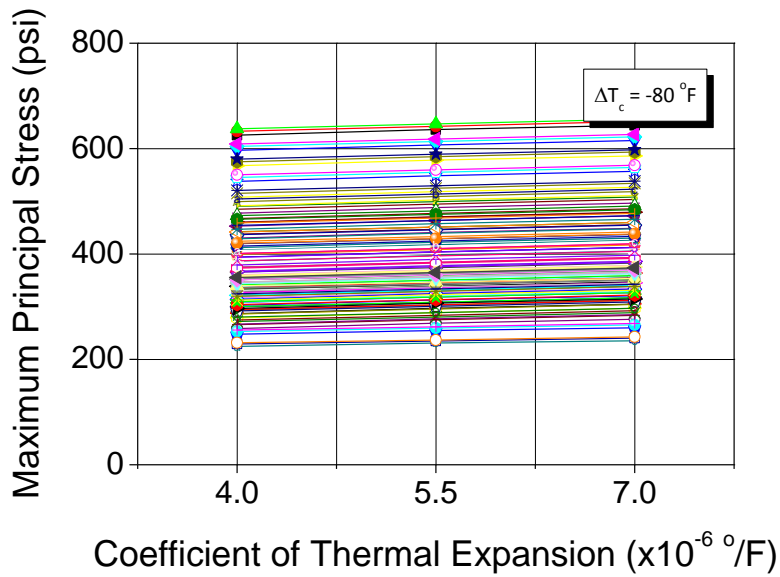
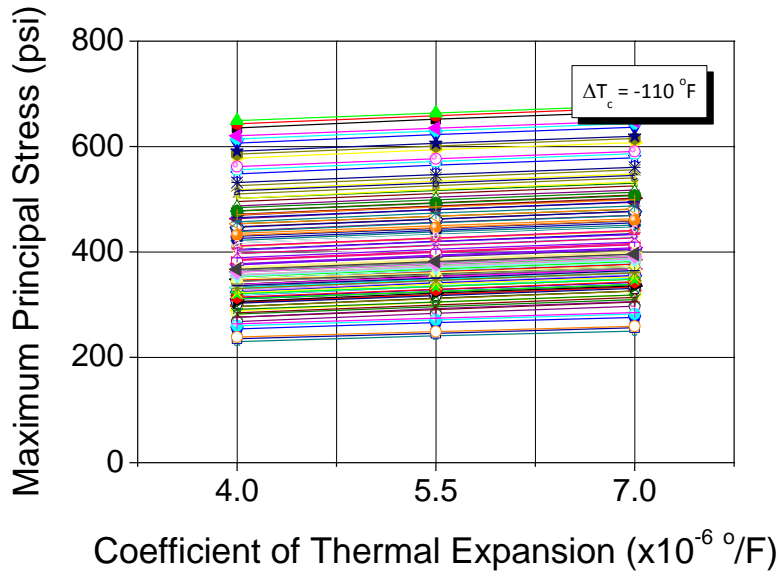
(d) $\Delta T_c = -20^\circ\text{F}$



(e) $\Delta T_c = 10^\circ\text{F}$

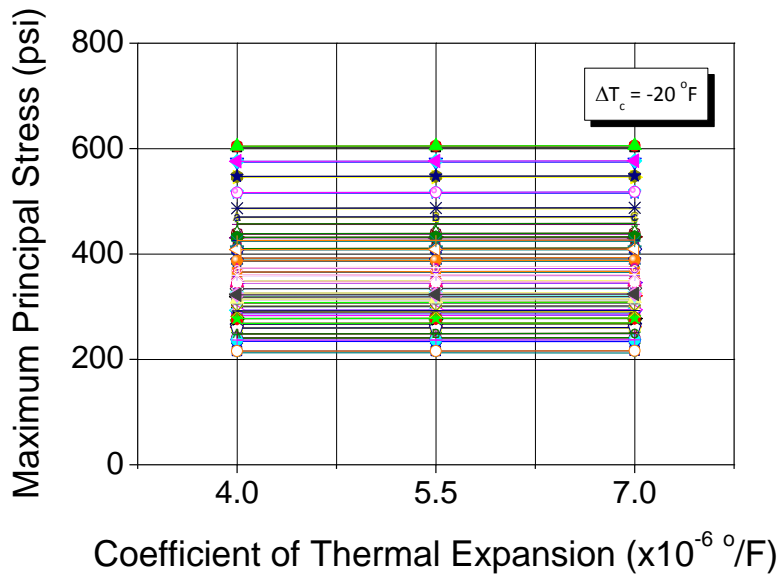
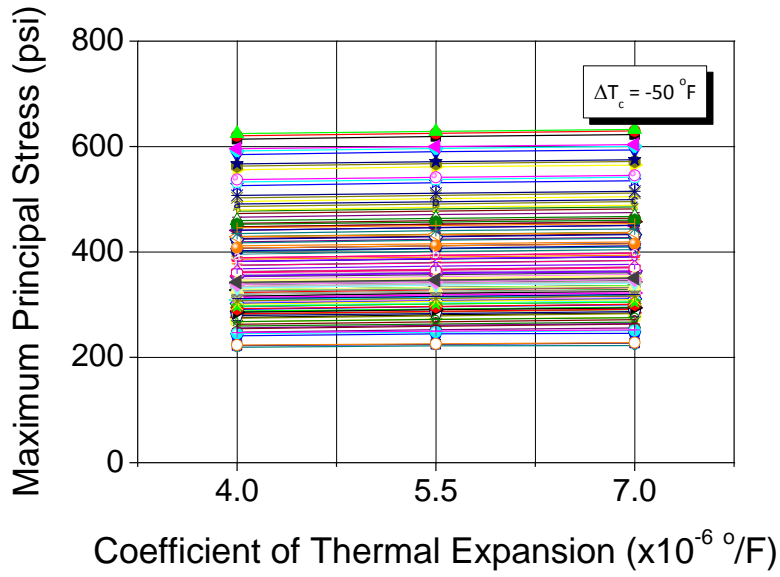
(f) $\Delta T_c = 40^\circ\text{F}$

Figure 3.30: Influence of ultimate drying shrinkage strain



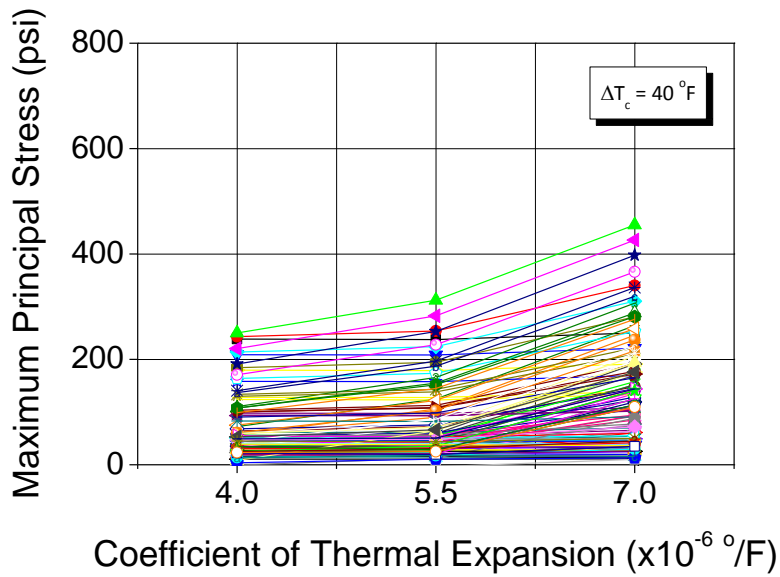
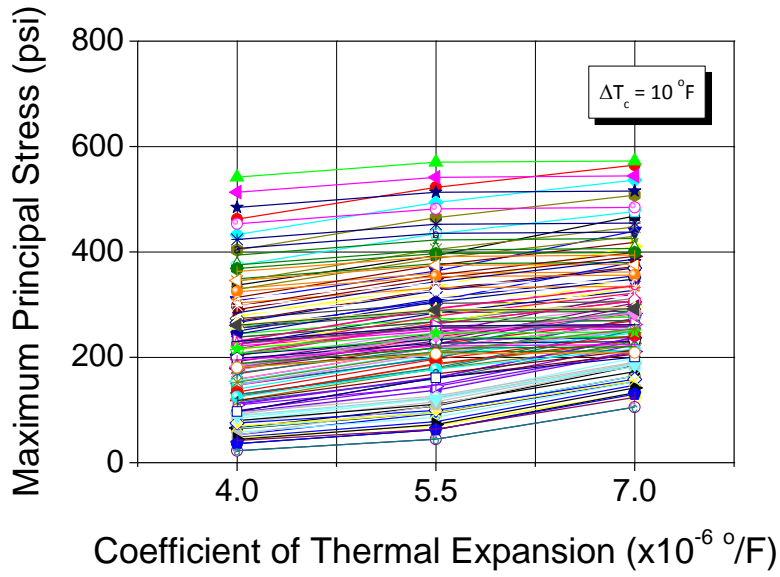
(a) $\Delta T_c = -110 \text{ }^\circ F$

(b) $\Delta T_c = -80 \text{ }^\circ F$



(c) $\Delta T_c = -50 \text{ }^\circ F$

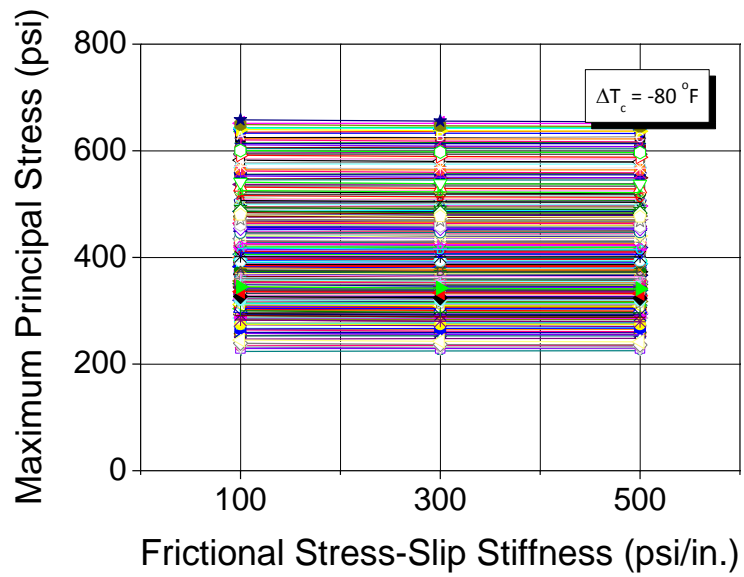
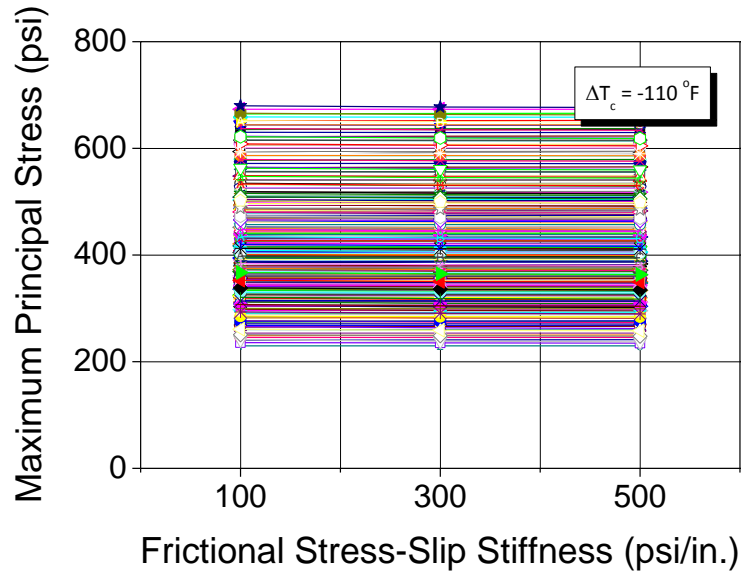
(d) $\Delta T_c = -20 \text{ }^\circ F$



(e) $\Delta T_c = 10 \text{ }^\circ F$

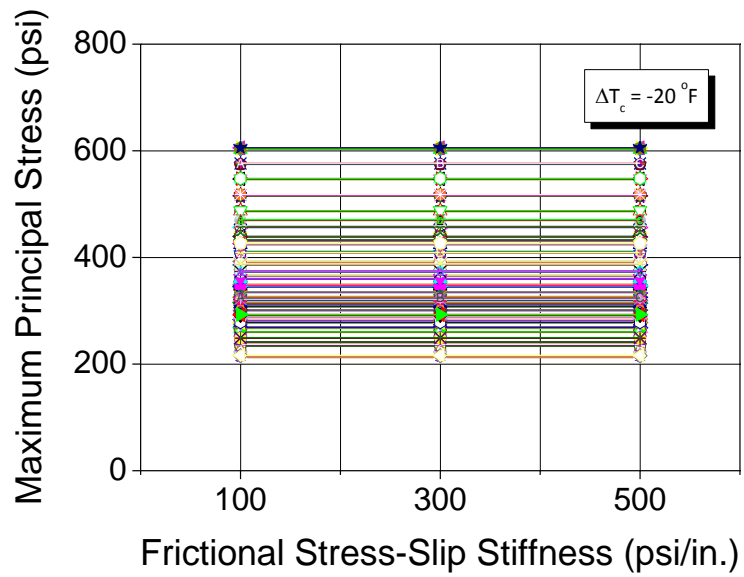
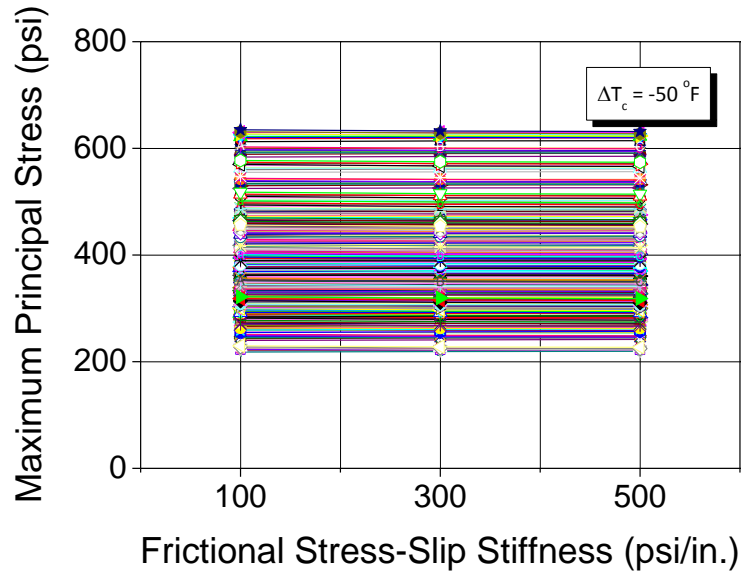
(f) $\Delta T_c = 40 \text{ }^\circ F$

Figure 3.31: Influence of the coefficient of thermal expansion of concrete



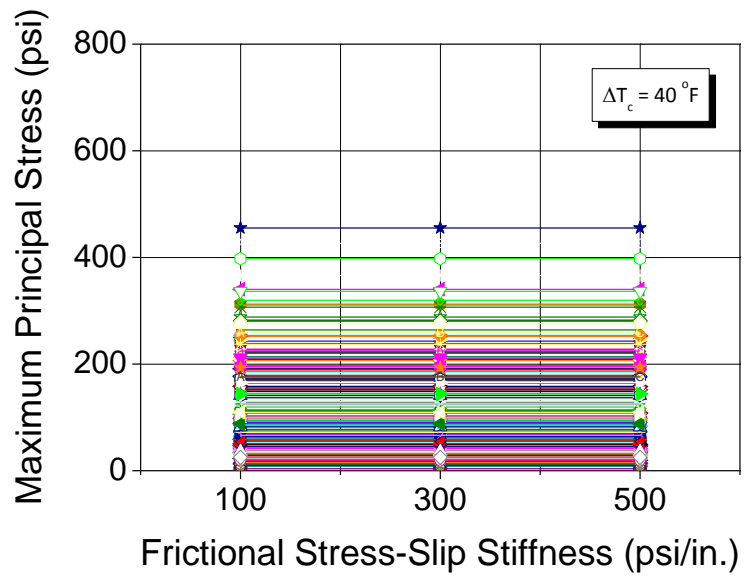
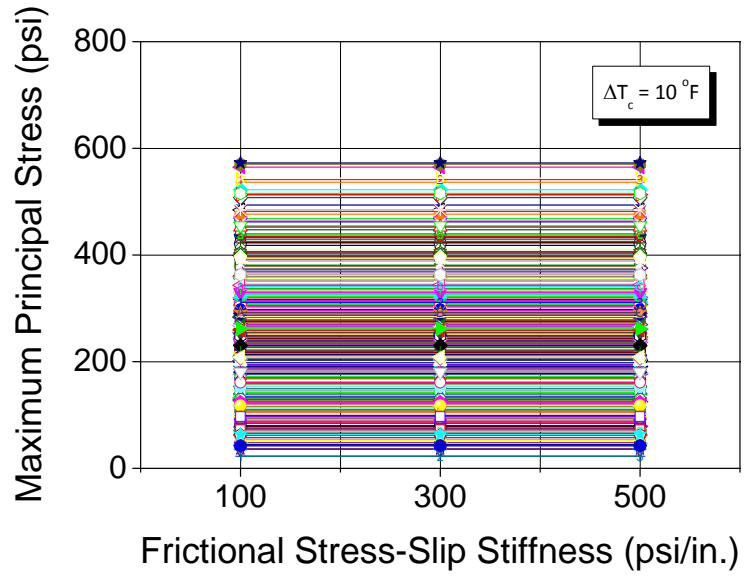
(a) $\Delta T_c = -110^\circ\text{F}$

(b) $\Delta T_c = -80^\circ\text{F}$



(c) $\Delta T_c = -50^\circ\text{F}$

(d) $\Delta T_c = -20^\circ\text{F}$



(e) $\Delta T_c = 10^\circ\text{F}$

(f) $\Delta T_c = 40^\circ\text{F}$

Figure 3.32: Influence of frictional stress-slip stiffness

Table 3.6: Maximum principal stresses due to combined loading

Slab Thickness H (in.)	Longitudinal Steel Ratio ρ_s (%)	Modulus of Subgrade Reaction K_v (psi/in.)	Change in Concrete Temperature ΔT_c (°F)	Maximum Principal Stress (psi)								
				Ultimate Drying Shrinkage Strain ϵ_{sh} (μ)								
				300			500			600		
				CTE of Concrete α_c ($\times 10^{-6}$ /°F)			CTE of Concrete α_c ($\times 10^{-6}$ /°F)			CTE of Concrete α_c ($\times 10^{-6}$ /°F)		
				4.0	5.5	7.0	4.0	5.5	7.0	4.0	5.5	7.0
6	0.5	100	-110	635.5	652.0	665.5	643.4	658.6	673.2	649.0	663.6	677.5
			-80	625.5	636.1	644.3	632.8	642.4	651.4	637.7	646.7	655.5
			-50	613.7	619.2	622.6	620.3	625.0	629.5	624.5	628.7	632.4
			-20	602.9	602.9	602.9	604.4	605.0	605.5	604.4	605.0	605.5
			10	336.9	392.9	468.4	462.0	522.4	564.7	541.8	570.3	572.8
			40	238.3	237.8	250.2	243.2	253.8	339.9	250.1	312.4	455.3
		300	-110	440.0	456.3	469.6	447.8	462.8	477.2	453.3	467.7	481.4
			-80	430.4	440.7	448.6	437.5	446.8	455.6	442.3	451.1	459.7
			-50	418.9	424.3	427.4	425.3	429.9	434.2	429.4	433.5	437.1
			-20	408.8	408.7	408.7	410.1	410.7	411.2	410.1	410.7	411.2
			10	147.3	199.0	274.3	268.1	329.1	372.3	348.8	377.6	380.1
			40	55.5	54.9	65.3	63.9	72.4	148.3	72.5	124.9	264.2
		500	-110	377.6	393.7	406.9	385.4	400.1	414.4	390.8	405.0	418.6
			-80	368.2	378.4	386.1	375.2	384.4	393.1	380.0	388.6	397.1
			-50	357.0	362.2	365.3	363.3	367.7	372.0	367.3	371.3	374.9
			-20	347.3	347.3	347.2	348.5	349.0	349.6	348.5	349.0	349.6
			10	91.8	138.1	213.2	207.0	268.4	311.9	288.2	317.2	319.7
			40	17.1	16.3	20.2	25.5	29.6	92.4	33.2	72.7	206.4
	0.6	100	-110	606.5	623.0	636.5	614.5	629.7	644.2	620.2	634.8	648.6
			-80	596.6	607.2	615.3	604.0	613.5	622.4	609.0	617.9	626.7
			-50	584.8	590.3	593.7	591.5	596.1	600.6	595.8	600.0	603.7
			-20	574.4	574.4	574.3	575.7	576.3	576.8	575.7	576.3	576.8
			10	307.6	363.7	439.6	432.9	493.7	536.3	513.1	541.7	544.2
			40	208.9	208.3	220.7	213.7	224.2	310.4	220.6	282.6	426.5

		300	-110	421.7	437.9	451.2	429.6	444.5	458.8	435.2	449.5	463.2
			-80	412.1	422.4	430.3	419.3	428.6	437.3	424.2	433.0	441.6
			-50	400.6	405.9	409.1	407.1	411.7	416.0	411.4	415.5	419.1
			-20	390.9	390.9	390.9	392.0	392.5	393.1	392.0	392.5	393.1
			10	129.2	180.2	256.1	249.4	311.0	354.4	330.6	359.5	362.1
			40	40.2	39.5	48.4	48.3	55.7	128.6	56.5	105.7	245.8
		500	-110	362.9	378.9	392.1	370.7	385.5	399.7	376.4	390.5	404.0
			-80	353.5	363.6	371.4	360.6	369.8	378.4	365.6	374.2	382.6
			-50	342.3	347.4	350.6	348.7	353.1	357.4	353.0	357.0	360.5
			-20	333.0	333.0	333.0	334.0	334.5	335.0	334.0	334.5	335.0
			10	78.8	122.8	198.5	191.8	253.8	297.5	273.5	302.6	305.1
			40	14.0	13.6	15.7	20.8	23.1	76.9	26.7	58.8	191.3
	0.7	100	-110	577.5	593.9	607.4	585.6	600.7	615.2	591.4	605.9	619.7
			-80	567.7	578.2	586.3	575.1	584.6	593.5	580.2	589.1	597.9
			-50	556.0	561.4	564.7	562.7	567.3	571.8	567.1	571.3	575.0
			-20	545.9	545.8	545.8	547.0	547.6	548.1	547.0	547.6	548.1
			10	278.2	334.4	410.8	403.9	465.0	507.8	484.4	513.1	515.6
			40	179.4	178.8	191.2	184.2	194.6	280.8	191.0	252.9	397.6
		300	-110	403.3	419.4	432.8	411.3	426.2	440.5	417.1	431.4	445.0
			-80	393.7	404.0	411.9	401.0	410.3	419.1	406.2	414.9	423.4
			-50	382.3	387.6	390.8	388.9	393.4	397.8	393.4	397.4	401.0
			-20	373.1	373.0	373.0	373.9	374.4	375.0	373.9	374.4	375.0
			10	111.0	161.3	237.8	230.7	292.8	336.5	312.4	341.4	344.0
			40	25.0	24.1	31.4	32.8	38.9	109.0	40.4	86.6	227.3
500	-110	348.1	364.1	377.3	356.1	370.8	385.1	361.9	376.0	389.5		
	-80	338.7	348.8	356.7	346.0	355.1	363.8	351.1	359.7	368.2		
	-50	327.5	332.7	335.8	334.1	338.5	342.8	338.6	342.6	346.1		
	-20	318.8	318.8	318.8	319.4	320.0	320.5	319.4	320.0	320.5		
	10	65.8	107.5	183.7	176.5	239.2	283.2	258.8	288.0	290.5		
	40	10.8	10.8	11.1	16.1	16.6	61.5	20.1	44.9	176.3		

Table 3.6: Maximum principal stresses due to combined loading (continued)

Slab Thickness H (in.)	Longitudinal Steel Ratio ρ_s (%)	Modulus of Subgrade Reaction K_v (psi/in.)	Change in Concrete Temperature ΔT_c (°F)	Maximum Principal Stress (psi)								
				Ultimate Drying Shrinkage Strain ϵ_{sh} (μ)								
				300			500			600		
				CTE of Concrete α_c ($\times 10^{-6}$ /°F)			CTE of Concrete α_c ($\times 10^{-6}$ /°F)			CTE of Concrete α_c ($\times 10^{-6}$ /°F)		
				4.0	5.5	7.0	4.0	5.5	7.0	4.0	5.5	7.0
8	0.5	100	-110	547.9	564.7	578.5	556.1	571.6	586.4	562.0	576.9	590.9
			-80	537.8	548.5	556.9	545.3	555.0	564.2	550.6	559.7	568.7
			-50	525.8	531.3	534.8	532.6	537.4	542.0	537.2	541.5	545.2
			-20	515.4	515.4	515.4	516.5	517.1	517.7	516.5	517.1	517.7
			10	254.2	307.1	380.8	374.5	434.2	476.5	453.3	481.8	484.4
			40	158.4	157.7	169.3	163.8	173.5	253.1	170.9	227.7	366.3
		300	-110	396.5	413.2	427.0	404.7	420.1	434.8	410.7	425.4	439.5
			-80	386.5	397.1	405.4	394.1	403.7	412.7	399.4	408.4	417.3
			-50	374.7	380.1	383.6	381.5	386.2	390.7	386.3	390.5	394.2
			-20	365.2	365.2	365.1	365.9	366.4	367.0	365.9	366.4	367.0
			10	115.9	158.7	230.0	224.1	284.0	327.2	303.2	332.0	334.6
			40	45.0	44.3	49.0	51.9	56.0	105.5	58.2	89.9	216.4
		500	-110	348.2	364.7	378.5	356.4	371.6	386.3	362.5	377.1	391.0
			-80	338.3	348.8	357.0	345.8	355.3	364.3	351.3	360.2	369.0
			-50	326.5	331.9	335.3	333.4	338.1	342.5	338.3	342.4	346.1
			-20	317.6	317.6	317.6	318.0	318.6	319.1	318.0	318.6	319.1
			10	84.6	124.6	182.2	176.3	236.4	280.1	255.7	284.7	287.3
			40	33.3	33.0	37.4	44.4	41.9	63.6	44.8	55.4	169.4
	0.6	100	-110	517.7	534.3	548.1	525.9	541.2	555.9	531.9	546.6	560.6
			-80	507.7	518.3	526.6	515.2	524.9	533.9	520.6	529.6	538.5
			-50	495.7	501.2	504.7	502.6	507.3	511.9	507.3	511.5	515.3
			-20	485.8	485.8	485.8	486.8	487.3	487.9	486.8	487.3	487.9

			10	223.2	276.3	350.8	344.2	404.5	447.2	423.7	452.3	454.9
			40	128.2	127.5	138.7	133.6	143.0	222.0	140.7	196.6	336.6
		300	-110	375.4	391.9	405.6	383.7	398.9	413.6	389.8	404.4	418.3
			-80	365.6	376.0	384.3	373.2	382.7	391.6	378.6	387.6	396.3
			-50	353.8	359.2	362.6	360.8	365.4	369.9	365.6	369.8	373.5
			-20	344.9	344.9	344.9	345.3	345.9	346.4	345.3	345.9	346.4
			10	95.8	137.2	209.3	202.7	263.6	307.2	282.9	311.8	314.5
			40	31.0	30.4	33.6	37.5	40.3	84.7	43.0	69.8	196.1
		500	-110	330.2	346.5	360.2	338.4	353.6	368.1	344.7	359.1	372.9
			-80	320.4	330.7	339.0	328.0	337.4	346.3	333.6	342.4	351.1
			-50	308.8	314.0	317.5	315.8	320.3	324.7	320.7	324.8	328.5
			-20	300.5	300.5	300.5	300.6	301.1	301.7	300.6	301.1	301.7
			10	63.9	95.7	164.6	158.0	219.2	263.3	238.5	267.6	270.3
			40	29.5	37.7	28.9	36.2	32.5	48.5	35.3	41.1	152.2
0.7	100	-110	487.4	503.9	517.6	495.7	510.9	525.5	501.8	516.4	530.3	
		-80	477.5	488.0	496.3	485.1	494.7	503.7	490.6	499.5	508.3	
		-50	465.7	471.1	474.6	472.6	477.3	481.8	477.4	481.6	485.4	
		-20	456.3	456.3	456.2	457.0	457.5	458.1	457.0	457.5	458.1	
		10	192.3	245.4	320.9	313.8	374.9	417.9	394.1	422.8	425.4	
		40	98.0	97.2	108.2	103.5	112.5	191.0	110.4	165.5	306.9	
	300	-110	354.3	370.7	384.3	362.6	377.7	392.3	368.9	383.3	397.1	
		-80	344.6	354.9	363.1	352.3	361.7	370.5	357.9	366.7	375.3	
		-50	333.0	338.3	341.7	340.0	344.6	349.0	345.0	349.1	352.8	
		-20	324.6	324.6	324.6	324.8	325.4	325.9	324.8	325.4	325.9	
		10	75.7	115.7	188.6	181.4	243.2	287.3	262.5	291.6	294.3	
		40	17.1	16.5	18.3	23.1	24.7	63.9	27.9	49.8	175.8	
	500	-110	312.1	328.4	342.0	320.5	335.5	350.0	326.9	341.2	354.9	
		-80	302.5	312.7	320.9	310.2	319.5	328.3	315.9	324.7	333.2	
		-50	291.0	296.2	299.6	298.1	302.6	307.0	303.2	307.3	310.9	

			-20	283.3	283.3	283.4	283.2	283.7	284.2	283.2	283.7	284.2
			10	48.3	77.8	147.0	139.7	201.9	246.5	221.3	250.5	253.2
			40	27.3	21.3	19.4	24.7	22.8	33.3	26.1	26.9	135.0

Table 3.6: Maximum principal stresses due to combined loading (continued)

Slab Thickness <i>H</i> (in.)	Longitudinal Steel Ratio ρ_s (%)	Modulus of Subgrade Reaction K_v (psi/in.)	Change in Concrete Temperature ΔT_c (°F)	Maximum Principal Stress (psi)								
				Ultimate Drying Shrinkage Strain ϵ_{sh} (μ)								
				300			500			600		
				CTE of Concrete α_c ($\times 10^{-6}$ /°F)			CTE of Concrete α_c ($\times 10^{-6}$ /°F)			CTE of Concrete α_c ($\times 10^{-6}$ /°F)		
				4.0	5.5	7.0	4.0	5.5	7.0	4.0	5.5	7.0
10	0.5	100	-110	501.8	518.7	532.7	510.0	525.6	540.6	516.1	531.0	545.3
			-80	491.5	502.3	510.8	499.1	508.9	518.2	504.5	513.7	522.8
			-50	479.4	484.9	488.5	486.3	491.1	495.7	491.0	495.3	499.2
			-20	469.1	469.1	469.1	470.1	470.7	471.2	470.1	470.7	471.2
			10	214.1	263.5	334.9	329.1	387.8	429.9	406.6	435.0	437.6
			40	123.8	123.1	133.4	129.8	138.4	209.6	137.0	187.1	319.6
		300	-110	377.2	394.0	408.1	385.5	401.1	416.0	391.7	406.6	420.8
			-80	367.0	377.7	386.2	374.7	384.4	393.6	380.2	389.3	398.3
			-50	355.0	360.4	364.0	362.0	366.7	371.3	366.9	371.1	374.9
			-20	345.5	345.5	345.5	346.1	346.6	347.2	346.1	346.6	347.2
			10	109.3	145.0	211.1	206.2	264.1	306.9	283.0	311.6	314.3
			40	46.9	46.3	49.2	53.5	56.0	94.4	58.9	84.2	196.1
		500	-110	338.2	354.9	369.0	346.5	362.0	377.0	352.7	367.6	381.7
			-80	328.0	338.7	347.2	335.7	345.4	354.6	341.4	350.4	359.4
			-50	316.1	321.5	325.1	323.1	327.9	332.4	328.2	332.4	336.1
			-20	307.2	307.1	307.1	307.5	308.0	308.5	307.5	308.0	308.5
			10	80.0	111.1	172.8	168.5	225.7	268.9	244.5	273.4	276.1
			40	46.7	46.4	46.8	52.2	52.6	59.4	56.0	54.2	157.9
	0.6	100	-110	469.7	486.4	500.3	478.0	493.4	508.3	484.1	499.0	513.1
			-80	459.5	470.2	478.6	467.2	476.9	486.1	472.7	481.8	490.8
			-50	447.5	453.0	456.6	454.5	459.3	463.8	459.3	463.6	467.4
			-20	437.8	437.8	437.7	438.5	439.1	439.6	438.5	439.1	439.6
			10	182.3	231.2	303.2	297.0	356.3	398.9	375.2	403.8	406.4
			40	94.3	93.6	103.2	100.4	108.4	177.2	107.5	155.2	288.2

		300	-110	353.8	370.5	384.4	362.2	377.6	392.4	368.5	383.2	397.3
			-80	343.8	354.4	362.8	351.5	361.1	370.2	357.2	366.2	375.1
			-50	331.9	337.3	340.9	339.0	343.7	348.2	344.1	348.3	352.0
			-20	323.2	323.2	323.2	323.4	324.0	324.5	323.4	324.0	324.5
			10	89.6	122.6	188.6	183.2	241.7	285.0	260.6	289.4	292.1
			40	28.9	28.5	29.6	34.6	35.7	74.1	38.8	65.6	173.9
		500	-110	317.9	334.5	348.5	326.3	341.7	356.5	332.7	347.4	361.4
			-80	307.9	318.4	326.8	315.7	325.3	334.3	321.5	330.4	339.3
			-50	296.2	301.5	305.1	303.3	308.0	312.4	308.5	312.7	316.4
			-20	288.0	288.0	288.0	287.9	288.5	289.0	287.9	288.5	289.0
			10	53.0	93.2	153.6	148.9	206.6	250.2	225.4	254.3	257.1
			40	40.4	40.2	39.9	45.3	45.1	46.8	48.4	34.9	139.3
	0.7	100	-110	438.7	455.2	468.9	447.0	462.3	476.9	453.2	467.8	481.7
			-80	428.8	439.3	447.6	436.5	446.0	455.0	442.0	451.0	459.7
			-50	417.0	422.4	425.9	424.0	428.7	433.1	428.9	433.1	436.8
			-20	407.9	407.9	407.8	408.4	408.9	409.5	408.4	408.9	409.5
			10	149.1	198.7	272.7	265.8	326.4	369.6	345.5	374.3	377.0
			40	61.8	61.1	70.1	68.3	75.6	144.4	75.2	122.0	258.5
		300	-110	329.5	345.9	359.6	337.9	353.0	367.6	344.2	358.7	372.5
			-80	319.8	330.1	338.3	327.5	336.9	345.8	333.2	342.0	350.7
			-50	308.2	313.4	316.9	315.3	319.8	324.2	320.4	324.5	328.1
			-20	300.2	300.2	300.2	300.2	300.7	301.2	300.2	300.7	301.2
			10	65.2	96.7	164.8	158.2	218.9	262.9	238.0	267.1	269.8
			40	16.3	15.9	15.7	21.4	21.2	50.6	24.8	42.4	151.6
500	-110	295.6	311.8	325.5	304.0	319.0	333.5	310.4	324.8	338.5		
	-80	285.9	296.2	304.4	293.7	303.0	311.8	299.5	308.2	316.8		
	-50	274.5	279.7	283.1	281.6	286.1	290.5	286.9	290.9	294.5		
	-20	267.1	267.1	267.1	266.8	267.3	267.8	266.8	267.3	267.8		
	10	46.9	70.5	132.0	125.8	186.0	230.4	205.1	234.2	237.0		
	40	28.6	28.5	27.5	33.0	31.9	36.0	35.1	26.0	119.3		

Table 3.6: Maximum principal stresses due to combined loading (continued)

Slab Thickness <i>H</i> (in.)	Longitudinal Steel Ratio ρ_s (%)	Modulus of Subgrade Reaction K_v (psi/in.)	Change in Concrete Temperature ΔT_c (°F)	Maximum Principal Stress (psi)								
				Ultimate Drying Shrinkage Strain ϵ_{sh} (μ)								
				300			500			600		
				CTE of Concrete α_c ($\times 10^{-6}$ /°F)			CTE of Concrete α_c ($\times 10^{-6}$ /°F)			CTE of Concrete α_c ($\times 10^{-6}$ /°F)		
				4.0	5.5	7.0	4.0	5.5	7.0	4.0	5.5	7.0
12	0.5	100	-110	463.2	480.1	494.1	471.4	487.0	502.0	477.4	492.4	506.6
			-80	452.9	463.7	472.2	460.5	470.3	479.6	465.9	475.1	484.1
			-50	440.8	446.4	449.9	447.7	452.5	457.1	452.4	456.7	460.5
			-20	430.6	430.6	430.6	431.6	432.1	432.7	431.6	432.1	432.7
			10	178.8	225.7	296.3	290.7	349.3	391.6	368.2	396.7	399.3
			40	93.4	92.6	101.6	100.2	107.6	172.1	107.5	151.9	281.2
		300	-110	356.9	373.8	387.8	365.1	380.7	395.7	371.3	386.2	400.4
			-80	346.7	357.5	365.9	354.3	364.1	373.3	359.8	368.9	377.9
			-50	334.7	340.2	343.7	341.7	346.4	351.0	346.5	350.8	354.5
			-20	325.2	325.2	325.2	325.8	326.4	326.9	325.8	326.4	326.9
			10	95.2	126.6	190.7	186.3	243.8	286.9	262.8	291.6	294.2
			40	48.8	48.3	49.3	55.0	56.1	77.3	59.6	70.8	175.9
		500	-110	324.1	340.9	355.0	332.3	347.9	362.9	338.5	353.4	367.6
			-80	313.9	324.6	333.1	321.6	331.3	340.5	327.1	336.2	345.1
			-50	302.0	307.4	311.0	309.0	313.7	318.2	313.9	318.1	321.9
			-20	292.9	292.9	292.9	293.3	293.9	294.4	293.3	293.9	294.4
			10	75.3	99.2	158.4	154.7	211.5	254.9	230.5	259.4	262.1
			40	45.6	45.2	44.4	51.1	50.6	55.2	54.6	53.1	143.8
	0.6	100	-110	417.2	433.6	447.4	425.4	440.6	455.3	431.5	446.1	460.0
			-80	407.3	417.7	426.0	414.9	424.4	433.4	420.3	429.3	438.0
			-50	395.5	400.9	404.3	402.4	407.1	411.6	407.3	411.4	415.1
			-20	386.3	386.3	386.3	386.9	387.4	388.0	386.9	387.4	388.0
			10	129.5	177.3	251.0	244.3	305.0	348.3	324.2	353.1	355.7
			40	47.1	46.4	53.8	54.1	60.2	123.2	61.0	102.8	237.3

		300	-110	318.5	334.8	348.5	326.8	341.9	356.4	333.0	347.4	361.2
			-80	308.8	319.1	327.3	316.4	325.8	334.6	322.0	330.8	339.4
			-50	297.2	302.5	305.9	304.2	308.8	313.1	309.2	313.3	316.9
			-20	289.1	289.1	289.1	289.2	289.7	290.2	289.2	289.7	290.2
			10	57.8	86.3	153.5	147.1	208.0	252.2	227.3	256.4	259.1
			40	26.8	26.5	25.5	31.7	31.0	41.9	34.7	35.1	141.3
		500	-110	288.2	304.4	318.0	296.5	311.5	326.0	302.8	317.1	330.8
			-80	278.5	288.7	296.9	286.2	295.5	304.3	291.9	300.6	309.1
			-50	267.1	272.3	275.7	274.1	278.6	282.9	279.2	283.2	286.8
			-20	259.5	259.5	259.5	259.3	259.8	260.4	259.3	259.8	260.4
			10	42.1	63.8	124.0	117.9	178.6	223.1	197.9	227.1	229.8
			40	28.0	27.7	25.8	32.3	30.5	45.0	34.3	28.7	113.9
	0.7	100	-110	389.0	405.2	418.6	397.2	412.1	426.5	403.3	417.6	431.2
			-80	379.4	389.6	397.7	386.9	396.2	405.0	392.3	401.1	409.6
			-50	367.9	373.1	376.5	374.8	379.3	383.6	379.5	383.6	387.2
			-20	359.2	359.2	359.2	359.7	360.2	360.7	359.7	360.2	360.7
			10	99.0	147.4	223.5	216.1	278.3	322.2	297.7	326.8	329.4
			40	20.2	19.5	24.8	27.3	31.8	93.3	33.7	72.9	211.5
		300	-110	296.3	312.3	325.6	304.5	319.2	333.5	310.7	324.8	338.2
			-80	287.0	297.0	304.9	294.5	303.6	312.2	300.0	308.5	316.9
			-50	275.8	280.9	284.1	282.7	287.1	291.3	287.6	291.5	295.1
			-20	268.3	268.3	268.3	268.2	268.7	269.3	268.2	268.7	269.3
			10	36.2	62.8	132.6	124.6	188.1	232.8	207.6	236.8	239.5
			40	15.5	15.2	13.1	19.7	17.8	29.7	21.7	20.6	125.4
500	-110	267.8	283.6	296.9	276.0	290.6	304.8	282.3	296.2	309.6		
	-80	258.6	268.5	276.3	266.1	275.1	283.6	271.7	280.1	288.4		
	-50	247.6	252.6	255.8	254.5	258.8	262.9	259.5	263.3	266.8		
	-20	240.6	240.7	240.7	240.3	240.8	241.3	240.3	240.8	241.3		
	10	22.6	44.5	105.4	96.8	161.0	205.9	180.5	209.7	212.4		
	40	18.5	18.2	15.6	22.1	19.6	34.8	23.4	25.1	109.4		

Table 3.6: Maximum principal stresses due to combined loading (continued)

Slab Thickness <i>H</i> (in.)	Longitudinal Steel Ratio ρ_s (%)	Modulus of Subgrade Reaction K_v (psi/in.)	Change in Concrete Temperature ΔT_c (°F)	Maximum Principal Stress (psi)								
				Ultimate Drying Shrinkage Strain ϵ_{sh} (μ)								
				300			500			600		
				CTE of Concrete α_c ($\times 10^{-6}$ /°F)			CTE of Concrete α_c ($\times 10^{-6}$ /°F)			CTE of Concrete α_c ($\times 10^{-6}$ /°F)		
				4.0	5.5	7.0	4.0	5.5	7.0	4.0	5.5	7.0
14	0.5	100	-110	456.9	473.6	487.5	464.8	480.3	495.2	470.5	485.4	499.5
			-80	446.7	457.5	465.8	454.1	463.8	472.9	459.1	468.2	477.1
			-50	434.8	440.3	443.7	441.4	446.2	450.7	445.7	450.0	453.7
			-20	424.1	424.1	424.1	425.5	426.0	426.6	425.5	426.0	426.6
			10	170.1	218.0	289.6	284.3	343.4	385.9	362.7	391.4	393.9
			40	82.8	82.0	91.2	90.6	98.2	165.2	98.6	144.8	276.3
		300	-110	353.5	370.2	384.0	361.4	376.8	391.7	367.0	381.8	395.9
			-80	343.5	354.1	362.3	350.7	360.3	369.4	355.7	364.7	373.6
			-50	331.7	337.1	340.5	338.2	342.9	347.4	342.5	346.7	350.4
			-20	321.5	321.5	321.4	322.6	323.2	323.7	322.6	323.2	323.7
			10	88.5	120.6	186.8	182.7	241.2	284.4	260.7	289.6	292.1
			40	40.6	39.7	39.8	47.5	48.1	71.7	52.9	66.1	175.9
		500	-110	322.3	339.0	352.8	330.2	345.6	360.4	335.8	350.6	364.7
			-80	312.4	323.0	331.2	319.6	329.2	338.2	324.6	333.5	342.4
			-50	300.7	306.1	309.4	307.2	311.8	316.3	311.5	315.6	319.3
			-20	290.7	290.7	290.7	291.8	292.3	292.9	291.8	292.3	292.9
			10	69.7	94.1	156.1	152.7	210.7	254.1	230.3	259.3	261.8
			40	38.9	38.0	36.1	45.0	43.8	50.2	49.2	50.6	143.8
	0.6	100	-110	403.2	419.4	433.0	411.4	426.4	440.9	417.6	432.0	445.7
			-80	393.5	403.8	411.9	401.1	410.4	419.3	406.5	415.3	424.0
			-50	381.9	387.2	390.6	388.8	393.4	397.8	393.7	397.8	401.4
			-20	373.2	373.2	373.2	373.6	374.1	374.7	373.6	374.1	374.7
			10	112.9	161.9	237.5	230.2	292.0	335.7	311.3	340.3	343.0
			40	30.7	30.1	36.8	37.7	43.2	107.6	44.3	86.4	224.8

		300	-110	306.0	322.0	335.5	314.2	329.1	343.4	320.5	334.7	348.2
			-80	296.5	306.6	314.6	304.1	313.3	322.0	309.7	318.3	326.8
			-50	285.2	290.3	293.7	292.2	296.6	300.9	297.2	301.2	304.8
			-20	277.7	277.7	277.7	277.5	278.1	278.6	277.5	278.1	278.6
			10	44.0	72.3	141.9	134.2	197.0	241.5	216.4	245.6	248.3
			40	26.8	25.5	25.5	31.3	31.0	41.9	25.3	35.1	141.3
		500	-110	276.3	292.2	305.6	284.6	299.3	313.5	290.9	305.0	318.4
			-80	266.9	276.9	284.9	274.6	283.6	292.2	280.3	288.8	297.1
			-50	255.8	260.8	264.1	262.8	267.1	271.4	267.9	271.8	275.3
			-20	248.8	248.8	248.9	248.4	248.9	249.5	248.4	248.9	249.5
			10	42.1	63.8	124.0	117.9	168.5	213.4	187.9	217.1	219.8
			40	21.1	21.0	25.8	24.9	30.5	45.0	34.3	28.7	113.9
	0.7	100	-110	337.0	350.7	361.8	343.9	356.5	368.8	348.6	360.8	372.5
			-80	329.4	337.9	344.1	335.6	343.2	350.4	339.5	346.7	353.8
			-50	320.4	324.7	326.8	325.8	329.3	332.8	328.9	332.2	335.1
			-20	312.7	312.6	312.6	314.0	314.5	314.9	314.0	314.5	314.9
			10	52.2	109.0	187.1	179.8	241.5	284.4	261.0	289.5	291.9
			40	-8.9	-3.9	10.1	-0.5	12.5	88.3	8.2	64.3	193.4
		300	-110	253.8	265.8	275.5	259.8	270.8	282.0	263.5	274.4	285.1
			-80	247.9	255.0	259.8	253.0	259.3	265.4	255.8	261.8	268.1
			-50	241.0	244.4	245.5	245.1	247.8	250.5	246.9	249.5	251.8
			-20	234.1	234.0	233.9	236.5	236.8	237.1	236.5	236.8	237.1
			10	36.2	62.8	130.1	124.6	177.8	216.0	195.1	221.5	224.0
			40	3.6	10.8	13.1	13.8	17.8	29.7	21.7	20.6	125.4
500	-110	229.7	240.8	249.7	235.2	245.4	256.0	238.4	248.6	258.8		
	-80	224.7	231.0	235.1	229.2	234.8	240.4	231.3	236.9	242.6		
	-50	219.1	222.0	222.4	222.4	224.6	226.9	223.4	225.6	227.6		
	-20	212.6	212.4	212.3	215.7	215.9	216.1	215.7	215.9	216.1		
	10	22.6	44.5	105.4	96.8	161.0	200.5	180.5	206.4	208.9		
	40	13.0	18.2	15.6	22.1	19.6	34.8	23.4	25.1	109.4		

3.4.4 Effect of aggregate interlock

As mentioned in Section 3.3.1, in the finite element representation of concrete pavements, the interlock action of aggregate in cracks has generally been modeled by a set of vertical linear spring elements connected between the nodes of two fractured surfaces. Since crack properties are characterized by the stiffness of these spring elements in the finite element model, spring stiffness has to be selected appropriately so that the computed response is similar to the observed response of cracks. However, proper guidelines are not available for the selection of the spring stiffness to be used in the finite element model. Accordingly, a literature review was conducted to find a rational range of spring stiffness values. Various researchers have attempted to measure load transfer at cracks through laboratory and field studies. Some of the studies are summarized in Table 3.7. Since this study modeled aggregate interlock behavior using interface elements instead of spring elements, spring stiffness values found in literature review were converted to equivalent stiffness values for interface elements, namely “crack stiffness.”

Figure 3.33 shows the range of crack stiffness values obtained from the literature review. Wide cracks have smaller crack stiffness. The crack stiffness ranges from 2×10^2 to 5×10^5 psi/in. when the crack width varies from 0.1 to 0.004 in. To evaluate the effect of aggregate interlock on concrete stresses, a 6-inch thick and a 12-inch thick concrete slab (Cases 6 and 32) were analyzed varying the crack stiffness from 1 to 10^2 , 10^4 , 10^6 , and 10^8 psi/in.

Table 3.7: Summary of laboratory and field studies on aggregate interlock

Reference	Model Size	Aggregate Size and Type	Crack Width	Finite Element Analysis	Note
Walraven (1981)	Push-off specimen with shear area of 12 in. × 5 in.	Gravel 5/8 in.	0.004 in. ~ 0.04 in.	Two-phase model	In the present study, the range of crack stiffness was estimated from shear stress-shear displacement curve presented in Walraven's study.
Korovesis (1990)	46 in.-wide and 18 ft-long slab with thicknesses of 7 in. and 9 in.	Natural gravel and crushed stone 1½ in.	0.004 in. ~ 0.1 in.	2D plate model (ILLI-SLAB)	In Korovesis's study, spring stiffness was back-calculated through correlation studies between numerical results and experimental data obtained by Colley and Humphrey (1967).
Wattar et al. (2001)	1 ft-wide and 2 ft-long beam with a depth of 1 ft	River gravel, trap rock, and limestone 1 ~ 1½ in.	0.03 in. ~ 0.08 in.	-	In Wattar et al.'s study, spring stiffness was estimated from shear stress-shear displacement curve obtained from experiments.
Khazanovich and Gotlif (2003)	FWD visits for LTPP database sections	Unknown	Unknown	2D plate model (ILLI-SLAB)	In Khazanovich and Gotlif's study, spring stiffness was back-calculated through correlation studies between numerical results and measured LTEs for each FWD pass.
Brink (2003)	24 ft-wide and 72 ft-long slab with a thickness of 9 in.	Granite and dolomite ¾ ~ 1½ in.	0.004 in. ~ 0.1 in.	2D plate model (ILLI-SLAB)	In Brink's study, field tests were also conducted in four concrete pavement sections. Spring stiffness was back-calculated through correlation studies between numerical results and measured laboratory and field data.

Jensen and Hansen (2006)	72 ft-wide and 120 ft-long slab with a thickness of 10 in.	Glacial gravel, blast furnace slag, and limestone 1 ~ 1½ in.	0.02 in. ~ 0.1 in.	3D solid model (ABAQUS)	Jensen and Hansen developed nonlinear shear stress-shear displacement relationships through correlation studies between experimental data and numerical results. In the present study, the range of crack stiffness was estimated from the nonlinear constitutive relationships.
Maitra et al. (2010)	24 ft-wide and 72 ft-long slab with a thickness of 9 in.	Granite and dolomite ¾ ~ 1½ in.	0.004 in. ~ 0.1 in.	3D solid model (ANSYS)	In Maitra et al.'s study, spring stiffness was back-calculated through correlation studies between numerical results and experimental data obtained by Brink (2003).

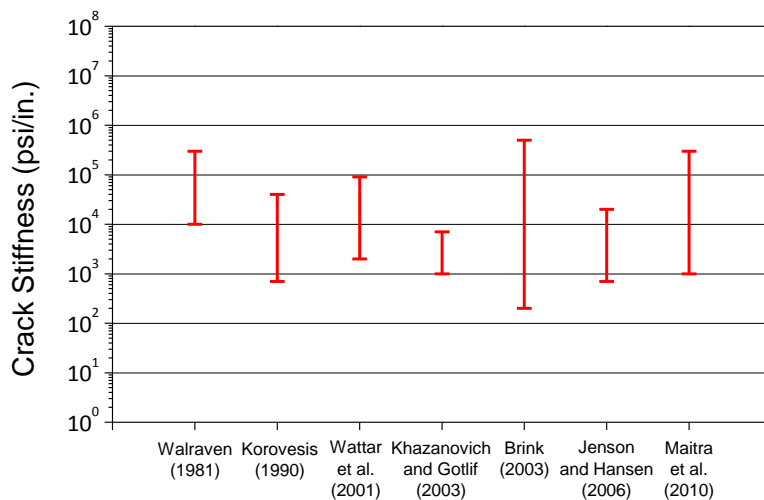
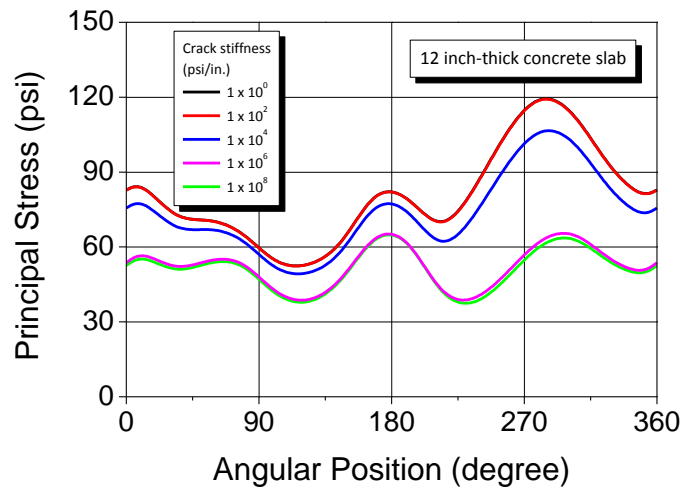
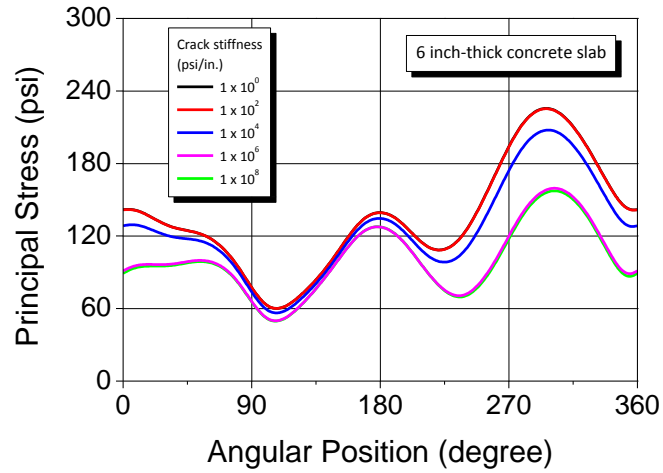


Figure 3.33: Range of crack stiffness values



(a) 6 inch-thick concrete slab

(b) 12 inch-thick concrete slab

Figure 3.34: Principal stresses in the vicinity of the longitudinal steel

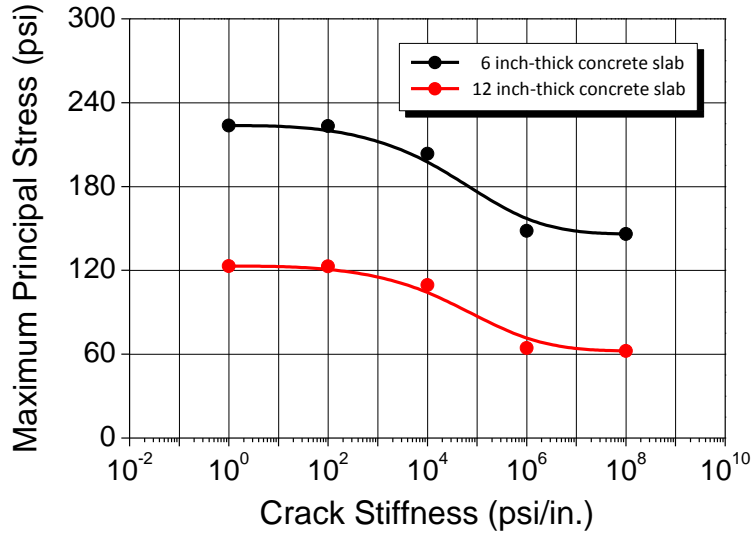


Figure 3.35: Maximum principal stresses according to crack stiffness

Figure 3.34 shows the distribution of principal stresses in the concrete around the longitudinal steel which was modeled in Figure 3.20(b). The values in this figure are the principal stress at a distance of 0.15 in. from the circumference of the longitudinal steel. The crack stiffness has little effect on the distribution tendency of principal stresses; the maximum principal stress develops below the longitudinal steel regardless of crack stiffness.

Figure 3.35 shows the effect of aggregate interlock on the maximum principal stress in the vicinity of longitudinal steel at the loaded transverse crack surface. It was found that the maximum principal stress at the top and bottom of the slab are almost uninfluenced by the crack stiffness. On the other hand, the maximum principal stress around the longitudinal steel increases with the crack width. However, the curve has a shape that looks like the graph of a logistic function; the maximum principal stress converges when the crack stiffness becomes small or large to a certain extent. This shows that aggregate interlock has a restrictive effect on concrete stresses. Especially in a range of small crack stiffness – transverse cracks which experience punchouts are usually wide due to the abrasion effect at the crack face – the decline in the concrete stress with an increase in the concrete stiffness is very slow. Accordingly, the conservative assumption of no aggregate interlock made in this study could be regarded as reasonable.

CHAPTER 4 CRCP MECHANISTIC EMPIRICAL DESIGN PROGRAM

In the previous chapter, mechanistic modeling and analysis were conducted to identify maximum principal stresses in concrete that might induce punchouts in CRCP. The results of the analysis show that, in a structurally inadequate CRCP system – CRCP with small slab thickness, low steel percentage and/or low slab support – the probability increases of longitudinal cracks along the longitudinal steel and horizontal cracking at the depth of the steel, which could result in punchouts. Field observations of punchouts support the findings of the analysis.

The numerical results of the analysis described in the previous chapter were incorporated in the mechanistic-empirical CRCP design program, called TxCRCP-ME. Figure 4.1 illustrates the overall diagram of TxCRCP-ME.

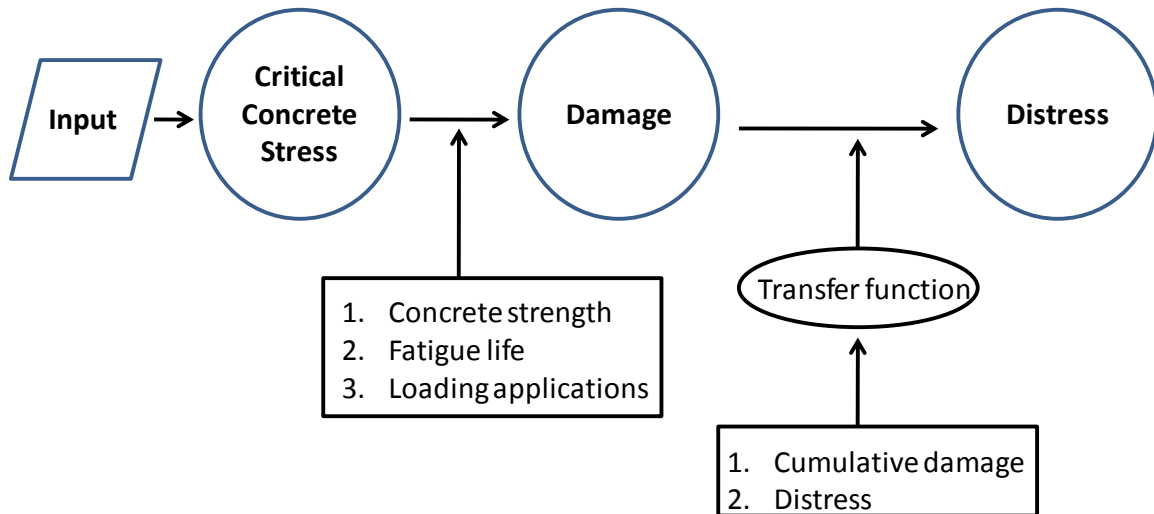


Figure 4.1 Overall algorithm of mechanistic-empirical CRCP design program

The TxCRCP-ME design program consists of five categories of modules as shown in Figure 4.1:

1. Input module
2. Stress analysis module
3. Damage estimation module
4. Punchout prediction module
5. Output presentation module

TxDOT PMC gave instructions to the research team that TxCRCP-ME should be developed in an MS Excel environment, and this algorithm was implemented in MS Excel in MS Office 2007. Detailed descriptions of each module are provided in the

0-5832-P3, “User’s Guide for CRCP ME Design Software.” This chapter discusses how the modules were combined for the development of TxCRCP-ME.

4.1 Formulation of TxCRCP-ME

4.1.1 Assembly of input values

As with any pavement design program, all the necessary input values are provided by the user in an input screen. Figure 4.2 illustrates the input screen developed. There are seven groups of inputs as follows:

- 1) Project information
- 2) Design parameters (design life and criteria on punchouts per mile)
- 3) Design traffic (design ESALs and annual growth rate)
- 4) Steel design (longitudinal steel amount and bar diameter)
- 5) Construction information (concrete placement month)
- 6) Concrete materials/layer information
 - a. Slab thickness
 - b. Coarse aggregate type
 - c. Concrete setting temperature
 - d. Coefficient of thermal expansion
 - e. Ultimate drying shrinkage
 - f. 28-day compressive or flexural strength
 - g. 28-day modulus of elasticity
- 7) Subbase layer information
 - a. Subbase type
 - b. Subbase thickness
 - c. Modulus of subbase layer
 - d. Subbase friction
 - e. Subgrade layer information (type of subgrade soil is provided per AASHTO or Unified Classification System.)

Once values for the above input variables are provided by a user, they reside in the input screen and are called upon when needed in other Excel sheets of the program. The values of the input variables are assembled and utilized in other Excel sheets for specific purposes.

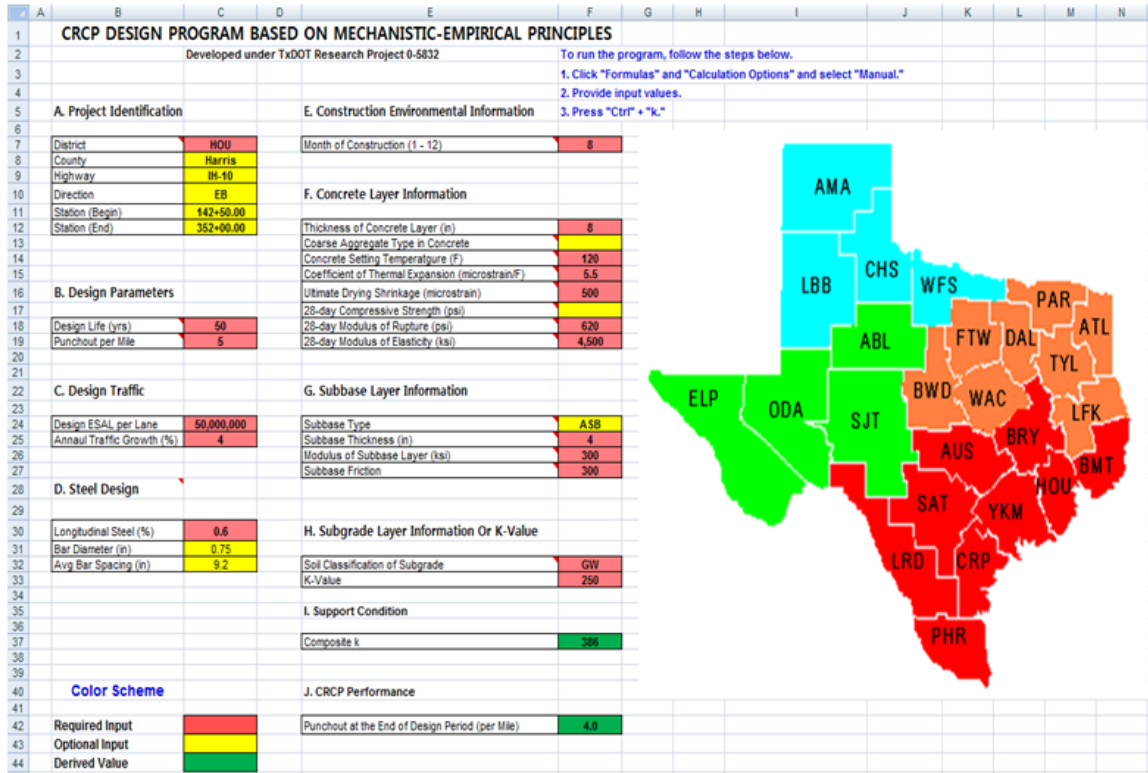


Figure 4.2 Input screen with typical input values

4.1.2 Concrete stress evaluations

4.1.2.1 Characterization of subbase support condition:

The analysis findings discussed in Chapter 3 indicate the importance of subbase support condition for concrete stresses near longitudinal steel from wheel loading applications. Closed-form solutions, such as Westergaard's, cannot evaluate concrete stresses at the mid-depth of the slab due to the interactions between longitudinal steel and surrounding concrete. Both Westergaard's and 3-D FEM analysis show that concrete stresses at the top and bottom of the concrete slab due to wheel loading applications are not highly sensitive to the support condition as characterized by modulus of subgrade reaction. On the other hand, concrete stresses at the depth of longitudinal steel are quite sensitive, and accurate evaluations of subbase support condition are important.

Subbase condition was characterized in accordance with the process below:

- 1) Concrete stresses due to wheel loading were estimated by two-dimensional FEM analysis for a wide range of soil and subbase conditions. In the modeling, soil stiffness was characterized by modulus of subgrade reaction (k) and that of subbase by modulus of elasticity.
- 2) A factorial was developed for various subgrade k and subbase modulus of elasticity and thickness. Concrete stress was estimated for each cell of the

- factorial (specific combination of subgrade k and subbase modulus).
- 3) For each cell, the “equivalent” k value was derived from FEM analysis that would provide the same concrete stresses.
 - 4) A table, called “k-Table” was developed and included in the TxCRCP-ME program.

For a factorial mentioned in the step 2) above, the following levels were selected:

- 1) Subgrade k: 7 levels (25, 50, 100, 150, 200, 250 and 300 psi/in)
- 2) Subbase thickness: 5 levels (2-in – 6-in with 1-in increment)
- 3) Subbase modulus: 34 levels (50 ksi to 100 ksi with 10 ksi increment, 100 ksi to 1,000 ksi with 50 ksi increment, 1,000 ksi to 2,000 ksi with 100 ksi increment)

A total of 1,190 combinations were analyzed and the k-Table was developed. The detailed description of the development of “equivalent” or “composite” k is provided in Appendix A.

4.1.2.2 Estimation of concrete stresses due to environmental and wheel loadings:

Concrete stresses for various design parameters, material properties, and environmental loading conditions were estimated from the three-dimensional FEM analysis per factorial experiments as described in Chapter 3. A stress table was developed for the following ranges of input variables:

- 1) slab thickness: 17 levels (6-in – 14-in with 0.5-in increment)
- 2) modulus of subgrade reaction: 41 levels (100 psi/in – 500 psi/in with 10 psi/in increment)
- 3) longitudinal steel ratio: 5 levels (0.50 % – 0.70 % with 0.05 % increment)
- 4) concrete ultimate drying shrinkage: 7 levels (300 microstrain – 600 microstrain with 50 microstrain increment)
- 5) concrete coefficient of thermal expansion: 13 levels (4.00 microstrain/°F – 7.00 microstrain/°F with 0.25 microstrain/°F increment)
- 6) subbase friction coefficient: 3 levels (100 psi/in – 500 psi/in with 200 psi/in increment)
- 7) temperature drop (setting temperature – mean monthly temperature): 6 levels (-55 °F – 95 °F with 30 °F increment)

All combinations of the above input variables yield a total of 5,708,430 cases. Each case has unique critical stress values due to environmental and wheel loadings. The TxCRCP-ME software was designed to recall the stress values from the developed “stress table” when inputs within the given ranges are provided. For the variables 1) to 6), if the input

value is between the predetermined levels, it automatically rounds off with an appropriate decimal place to avoid execution errors. For example, if the user selects 4.175 microstrain/°F for coefficient of thermal expansion of concrete, the module will recognize it as 4.25 microstrain/°F. On the other hand, the variable 7) uses linear interpolation to find the stress values between data points.

Since the stresses due to environmental loading were computed using 5000 ksi of constant elastic modulus, the stress values need to be adjusted in accordance with the elastic modulus at each age. For instance, if the modulus of elasticity at three-day is 4000 ksi, the three-day critical stress due to environmental loading should be 80% of that in the stress table. Once the critical stresses due to environmental and wheel loadings are determined, the sum of them is reflected in the fatigue equation.

4.1.3 Fatigue life of concrete slab and damage estimation

Each month, critical concrete stress is estimated and the ratio of this critical concrete stress to concrete strength is computed. This ratio is used to compute fatigue life of the slab each month. Allowable fatigue life is estimated by the equation developed by Vesic (Vesic et al., 1969), as shown in equation (4.1).

$$N_i = 225,000 \left(\frac{\sigma}{MR} \right)^4 \quad (4.1)$$

where, N_i is the fatigue number;
 MR is the modulus of rupture (psi); and
 σ is the tensile concrete stress (psi).

For concrete stress, the value in the vicinity of longitudinal steel reinforcement derived from three-dimensional analysis was used for equation (4.1). This equation was developed for modulus of rupture of concrete in plain concrete. The fatigue behavior of concrete near longitudinal steel might be a little different. There are no equations available for the fatigue behavior of concrete near reinforcement due to static and dynamic loading. However, as long as there is no large difference in the shape of the fatigue equations, errors due to not using the exact fatigue equation will be minimized by the selection of a proper transfer function.

Once the allowable fatigue life of the concrete slab is determined, damage caused by wheel load applications and environmental loading is computed by dividing the monthly traffic by the allowable fatigue number. This estimation of damage is computed in the sheet "Analysis Results." Damage computed at the end of each month is accumulated through the design period.

4.1.4 Prediction of punchouts

The accumulated damage at the end of each month is used to predict the number of punchouts each month using the transfer function. The prediction of punchouts is also computed in the sheet “Analysis Results.” Since the role of a transfer function is quite important in ME pavement design procedures, it is discussed in the next section.

4.1.5 Presentation of analysis results

In TxCRCP-ME, the results of the analysis are presented in two formats: one is in a tabular format in “Analysis Results” and the other in a graphical format in “Time vs. Punchout.” Figure 4.3 illustrates the “Analysis Results” screen. As can be seen in Figure 4.3, once concrete stresses are determined, the remainder of the computations for allowable fatigue life, damage, accumulated damage, and punchout predictions are computed in this sheet.

	A	B	C	D	G	H	I	J	K	L	M
1	Pavement Age Month	Year	Concrete Modulus of Rupture (psi)	Concrete Modulus of Elasticity (ksi)	Concrete Stress (psi)	Maximum Stress Ratio (psi/psi)	Number of Load Repetitions to Failure	Number of Load Repetitions	Pavement Damage	Cumulative Damage	Number of Punchouts per Mile
2	1	0.08	620	4.50E+03	263.67	0.425	6.88E+06	1.15E+05	1.68E-02	1.68E-02	1.58E+00
3	2	0.17	676	4.91E+03	280.89	0.415	7.56E+06	1.16E+05	1.53E-02	3.20E-02	1.59E+00
4	3	0.25	693	5.03E+03	290.27	0.419	7.32E+06	1.16E+05	1.59E-02	4.79E-02	1.59E+00
5	4	0.33	702	5.09E+03	297.84	0.424	6.94E+06	1.16E+05	1.68E-02	6.47E-02	1.60E+00
6	5	0.42	707	5.13E+03	303.39	0.429	6.64E+06	1.17E+05	1.76E-02	8.23E-02	1.60E+00
7	6	0.50	711	5.16E+03	305.57	0.430	6.59E+06	1.17E+05	1.78E-02	1.00E-01	1.61E+00
8	7	0.58	713	5.18E+03	304.34	0.427	6.79E+06	1.18E+05	1.73E-02	1.17E-01	1.62E+00
9	8	0.67	715	5.19E+03	300.86	0.421	7.19E+06	1.18E+05	1.64E-02	1.34E-01	1.62E+00
10	9	0.75	717	5.20E+03	298.11	0.416	7.53E+06	1.18E+05	1.57E-02	1.49E-01	1.62E+00
11	10	0.83	718	5.21E+03	294.39	0.410	7.97E+06	1.19E+05	1.49E-02	1.64E-01	1.63E+00
12	11	0.92	719	5.22E+03	291.47	0.405	8.34E+06	1.19E+05	1.43E-02	1.79E-01	1.63E+00
13	12	1.00	720	5.23E+03	290.53	0.404	8.49E+06	1.20E+05	1.41E-02	1.93E-01	1.64E+00
14	13	1.08	721	5.23E+03	291.02	0.404	8.46E+06	1.20E+05	1.42E-02	2.07E-01	1.64E+00
15	14	1.17	721	5.24E+03	293.23	0.407	8.24E+06	1.20E+05	1.46E-02	2.22E-01	1.65E+00
16	15	1.25	722	5.24E+03	298.34	0.413	7.71E+06	1.21E+05	1.57E-02	2.37E-01	1.65E+00
17	16	1.33	722	5.24E+03	303.74	0.420	7.20E+06	1.21E+05	1.68E-02	2.54E-01	1.66E+00
18	17	1.42	723	5.25E+03	307.95	0.426	6.83E+06	1.22E+05	1.78E-02	2.72E-01	1.66E+00
19	18	1.50	723	5.25E+03	309.20	0.428	6.73E+06	1.22E+05	1.81E-02	2.90E-01	1.67E+00
20	19	1.58	723	5.25E+03	307.28	0.425	6.91E+06	1.22E+05	1.77E-02	3.08E-01	1.67E+00
21	20	1.67	724	5.25E+03	303.26	0.419	7.30E+06	1.23E+05	1.68E-02	3.25E-01	1.68E+00
22	21	1.75	724	5.25E+03	300.12	0.415	7.62E+06	1.23E+05	1.62E-02	3.41E-01	1.68E+00
23	22	1.83	724	5.26E+03	296.08	0.409	8.06E+06	1.24E+05	1.53E-02	3.56E-01	1.69E+00
24	23	1.92	724	5.26E+03	292.92	0.404	8.42E+06	1.24E+05	1.47E-02	3.71E-01	1.69E+00
25	24	2.00	725	5.26E+03	291.80	0.403	8.56E+06	1.24E+05	1.45E-02	3.85E-01	1.70E+00
26	25	2.08	725	5.26E+03	292.15	0.403	8.53E+06	1.25E+05	1.46E-02	4.00E-01	1.70E+00
27	26	2.17	725	5.26E+03	294.25	0.406	8.29E+06	1.25E+05	1.51E-02	4.15E-01	1.71E+00
28	27	2.25	725	5.26E+03	299.28	0.413	7.76E+06	1.26E+05	1.62E-02	4.31E-01	1.71E+00
29	28	2.33	725	5.26E+03	304.61	0.420	7.23E+06	1.26E+05	1.74E-02	4.49E-01	1.72E+00
30	29	2.42	725	5.27E+03	308.76	0.426	6.86E+06	1.27E+05	1.84E-02	4.67E-01	1.72E+00
31	30	2.50	726	5.27E+03	309.94	0.427	6.76E+06	1.27E+05	1.88E-02	4.86E-01	1.73E+00
32	31	2.58	726	5.27E+03	307.95	0.424	6.94E+06	1.27E+05	1.84E-02	5.04E-01	1.74E+00
33	32	2.67	726	5.27E+03	303.87	0.419	7.33E+06	1.28E+05	1.74E-02	5.22E-01	1.74E+00
34	33	2.75	726	5.27E+03	300.67	0.414	7.65E+06	1.28E+05	1.68E-02	5.38E-01	1.75E+00
35	34	2.83	726	5.27E+03	296.59	0.408	8.08E+06	1.29E+05	1.59E-02	5.54E-01	1.75E+00
36	35	2.92	726	5.27E+03	293.38	0.404	8.44E+06	1.29E+05	1.53E-02	5.70E-01	1.76E+00
37	36	3.00	726	5.27E+03	292.23	0.402	8.58E+06	1.30E+05	1.51E-02	5.85E-01	1.76E+00
38	37	3.08	726	5.27E+03	292.54	0.403	8.55E+06	1.30E+05	1.52E-02	6.00E-01	1.77E+00
39	38	3.17	726	5.27E+03	294.62	0.406	8.31E+06	1.30E+05	1.57E-02	6.16E-01	1.77E+00
40	39	3.25	726	5.27E+03	299.64	0.412	7.77E+06	1.31E+05	1.68E-02	6.32E-01	1.78E+00
41	40	3.33	727	5.27E+03	304.96	0.420	7.25E+06	1.31E+05	1.81E-02	6.51E-01	1.78E+00
42	41	3.42	727	5.27E+03	309.10	0.425	6.87E+06	1.32E+05	1.92E-02	6.70E-01	1.79E+00

Figure 4.3 Output screen showing analysis results

Figure 4.4 illustrates the punchout predictions in a graphical form. It is observed that, even at the beginning of the project, punchouts already exist. This is due to the shape of the transfer function. Further efforts will be made to improve a transfer function with more data.

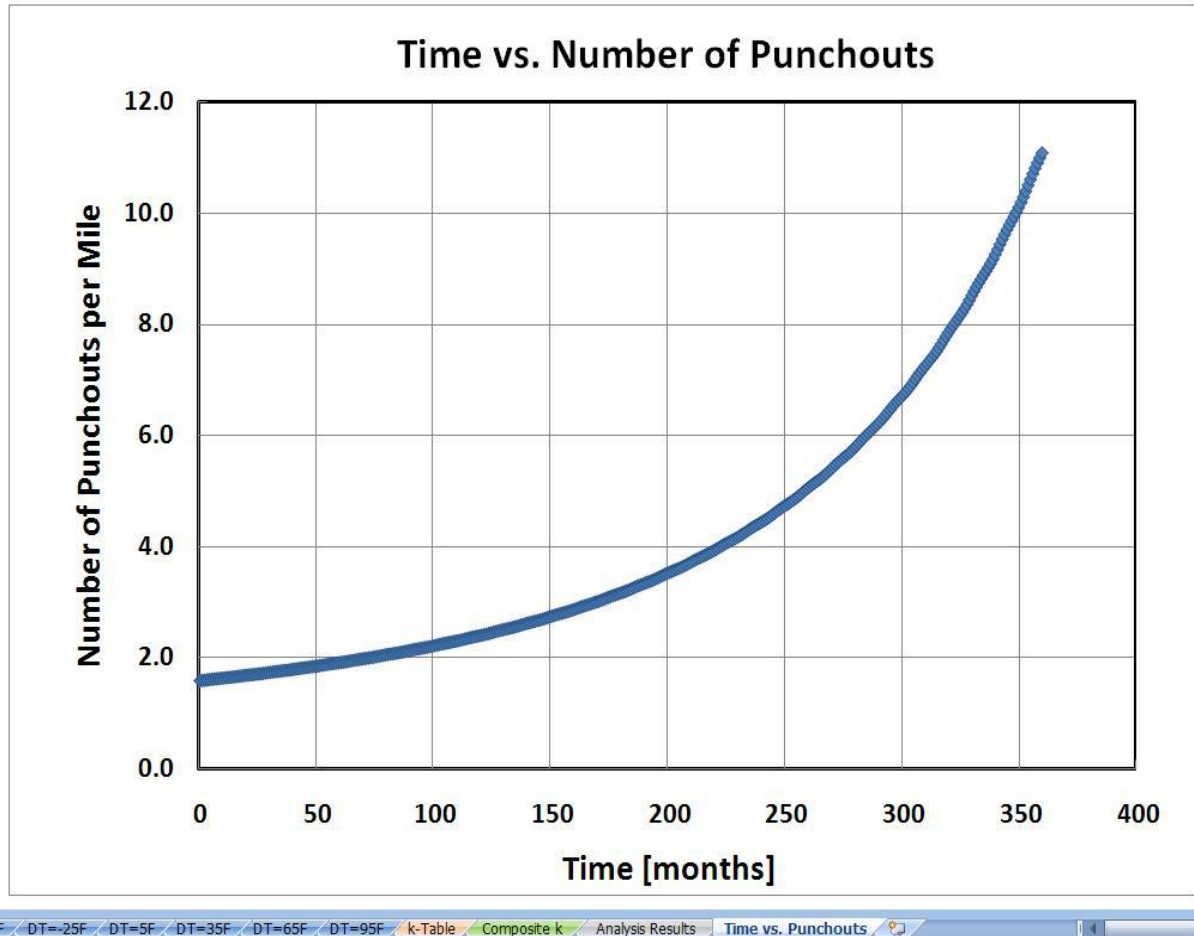


Figure 4.4 Graphical presentation of punchout prediction results

4.1.6 Summary

The task that required the most computation time and effort in TxCRCP-ME development – the estimation of concrete stresses – was conducted separately and the results were populated in a series of MS Excel sheets in terms of temperature drop. The rest of the computations, including the estimation of “equivalent” or “composite” k value, fatigue damage computations and punchout predictions, are done within Excel. This setup increased the size of the file substantially, more than 197 MB. Opening the file takes time. On the other hand, this setup makes the TxCRCP-ME program quite straight forward and easy to follow the sequence of computations. Also, this setup requires less than two minutes of run-time.

4.2 Development of a Transfer Function

A transfer function provides the conversion of cumulative damages in concrete to the frequency of punchouts. The development of a punchout is quite complicated, and it’s almost impossible to develop a purely mechanistic punchout development model. A relational function that correlates concrete damage to punchout development is required.

In mechanistic-empirical based pavement design procedures, the development of an accurate transfer function is quite critical. As discussed earlier, small deviations in estimated critical concrete stresses from accurate values do not cause serious errors in punchout predictions. On the other hand, small deviations in the coefficients in transfer functions could reduce the reasonableness of the punchout predictions and corresponding pavement designs quite substantially.

The challenge in developing a transfer function in this project was the availability of accurate traffic information. Communications were made between the research team and PMC members regarding this issue, and efforts are still underway to obtain accurate traffic information at the time of this report writing.

In this project, traffic information in PMIS was utilized. PMIS provides present annual daily traffic (ADT) and future 20-year ESALs for pavements in Texas. 2009 PMIS data was used for this purpose. The process used for the development of a transfer function is as follows:

- 1) CRCP sections with punchout information were selected.
- 2) Since there are about two years lag time between the traffic estimation and PMIS publication, it was assumed that the 20-yr ESALs were determined in 2007.
- 3) The total ESALs for 20 years from 2007 to 2027 was estimated in terms of beginning year ESALs at 2007 with an assumption of an annual traffic growth rate of 4 %.
- 4) For each selected section, the total ESALs from the completion of the project to Year 2009 was estimated, again with an assumption of an annual traffic growth rate of 4 %.
- 5) TxCRCP-ME was run with proper input values – values of most input variables are actual and not assumed, such as slab thickness, steel design, and subbase type and thickness. The most uncertain input variable was soil type. Assumptions were made on the soil type considering the geology of the surrounding areas. Damages were estimated at the end of 2009 for the selected CRCP sections.
- 6) The number of punchouts per lane mile was estimated from PMIS punchout data. It was assumed that concrete patches were to repair punchouts, and accordingly the number of patches were included as punchouts.
- 7) With cumulative damage as an independent variable and the corresponding number of punchouts per mile as a dependent variable, a transfer function was developed based on the least sum of error principle.
- 8) The transfer function thus developed was incorporated in TxCRCP-ME for the prediction of punchouts and CRCP design.

Table 4.1 Pavement and punchout information used for transfer function development

District	County	Highway	Year Built	RDBD	Slab Thickness	Subbase	Begin	End	Length (Miles)	Traffic (Mil ESAL)	Cum Damage	# PO	#AP	#CP	PO Rate
Atlanta	Bowie	US59	2001	R1	12	4-in AC	0220+01.6	0222+01.5	1.9	12.6	0.90	2	0	0	1.1
Dallas	Dallas	SL12	1963	L1	6	6-in LTS	0628+01.0	0630+00.5	1.5	7.05	7.90	8	0	8	10.7
El Paso	Hudspeth	IH10	1995	L1	13	4-in AC	0096+00.5	0107+00.5	11	36.8	2.00	5	0	12	1.5
Ft Worth	Tarrant	IH 20	1985	R1	8	4-in AC + LTS	0423+00.5	0429+00.5	6	12.5	4.64	11	0	10	3.5
Houston	Harris	US290	1985	R1	10	1-in AC + 6-in CSB	0732+00	0736+00	4	41.3	6.37	19	0	31	12.5
Lubbock	Lubbock	IH27	1982	R1	9	4-in AC	0018+00.0	0021+00.2	3.2	11.2	2.75	11	0	7	5.6
WFS	Wichita	US287	1970	R1	8	4-in AC	0326+00.0	0328+00.6	2.6	34	12.62	6	0	27	12.7

Table 4.1 illustrates the data used for the transfer function development. A graph was developed with cumulative damage as an independent variable and the number of punchouts per mile as an independent variable. Figure 4.5 presents the transfer function developed.

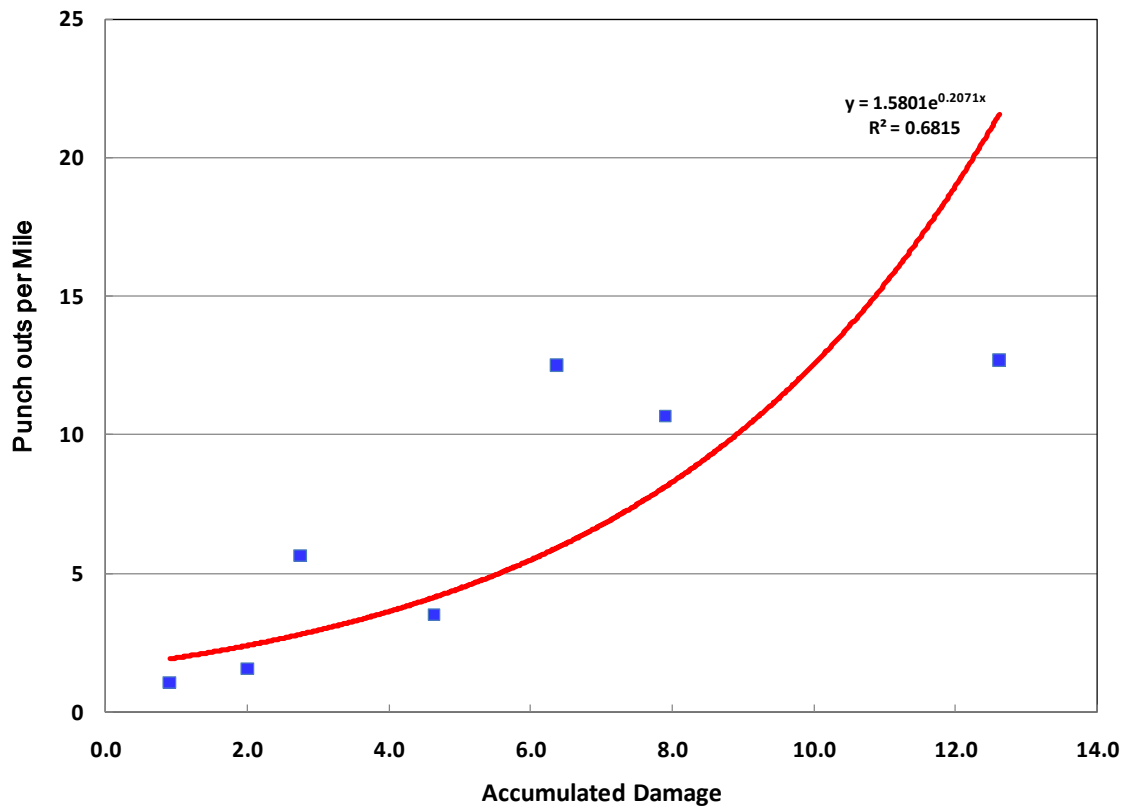


Figure 4.5 Accumulated damage and punchout per mile with transfer function

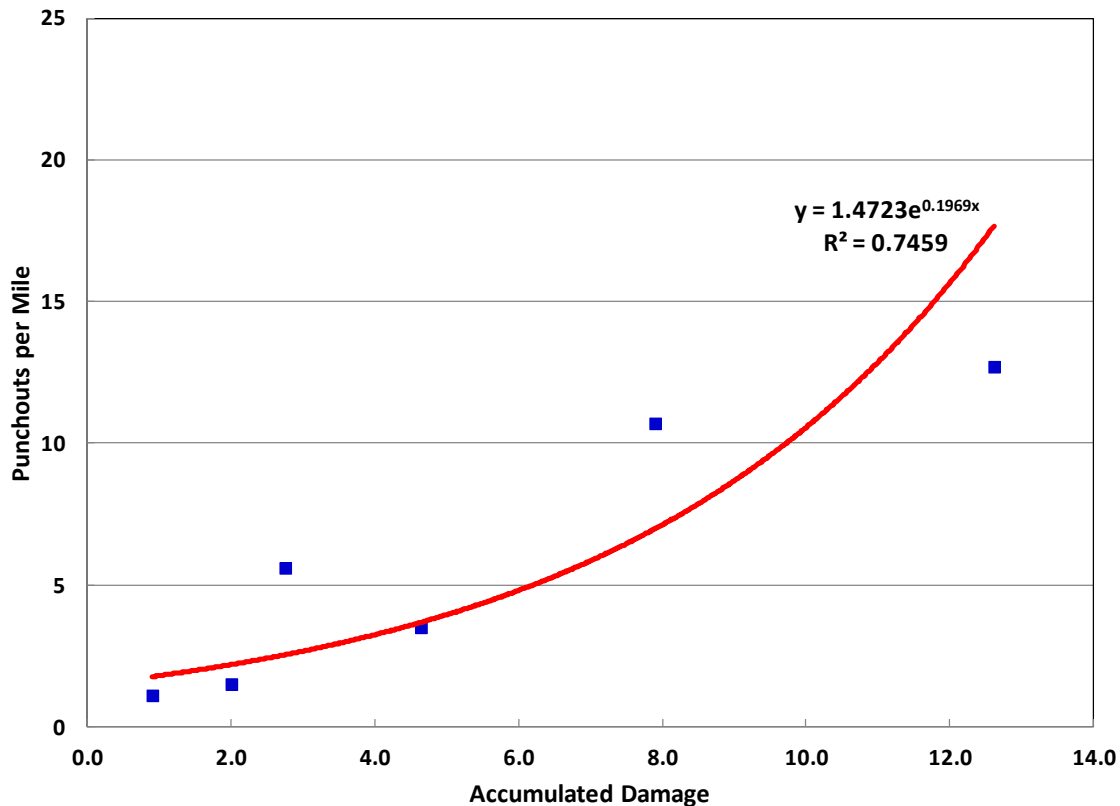


Figure 4.6 Revised transfer function without data from US290 section in Houston

The accuracy of the data on US290 in Houston is highly questionable. The research team investigated the accuracy of the punchout data in this section, and discovered that there were no punchouts. Also, it appeared that all 31 concrete patches were the repair of severe spalling on that highway. A new transfer function was developed after the US290 section was removed from the data. Figure 4.6 shows a revised transfer function.

Comparison between Figures 4.5 and 4.6 shows a rather remarkable difference with just one data point removed. This is partly due to the limited number of data points used in this example. As more data points are included in the transfer function development, the effect will become much less. Nonetheless, this exemplifies the importance of collecting accurate punchout data.

Figure 4.7 shows the comparison of punchout predictions from the two different transfer functions obtained above. When the accumulated damage is small, there is little difference between them. However, as accumulated damages increase, the difference becomes larger. Whether there is little difference in the number of punchouts when the accumulated damage is small does not have any significance, because we do not design pavement for that level of accumulated damage. From a practical standpoint, what's more

important is the difference in punchouts per mile at about 10. If the accumulated damage is small enough that the number of punchouts per mile is much less than 10, the pavement design engineer will reduce slab thickness or take other cost-cutting measures until the approximate punchout rate of 10 per mile is achieved. In this case, there is about a two punchouts per mile difference. This difference could result in a change of slab thickness in the design. This illustrates the need for an accurate transfer function to make any ME pavement design procedure reasonable.

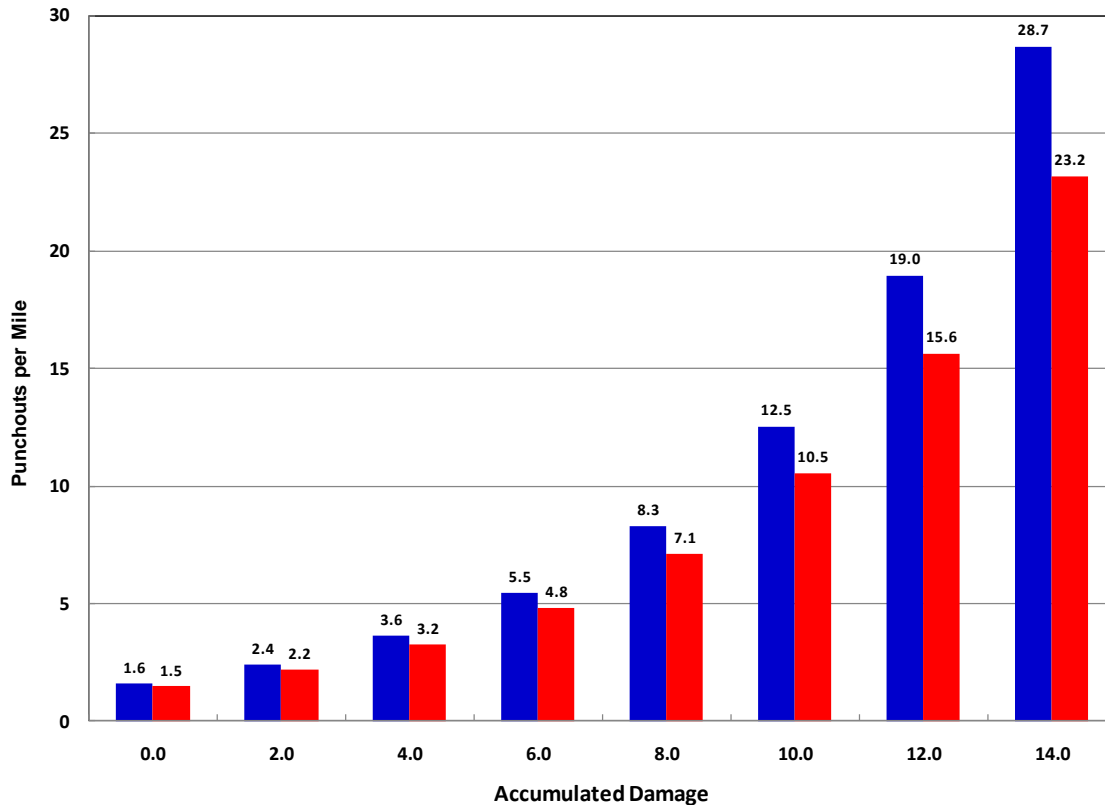


Figure 4.7 Comparison of punchouts per mile with two different transfer functions

Continued effort has been made under TxDOT’s rigid pavement database project (0-6274) to improve the accuracy of a transfer function. Table 4.2 summarizes the punchout data in Dallas, Fort Worth, Wichita Falls, and Childress districts. In 2009 PMIS, a total of 219 punchouts were recorded. The research team made an effort to evaluate every punchout in those four districts to identify the types of punchout and potentially the causes of different punchouts. “PCH” indicates punchouts under the wheel path. “E-PCH” denotes punchouts observed at the pavement edge, some with pumping evidence and some without. “Repair or Not Found” indicates that the research team could not find punchouts, but repairs were observed. Therefore, it is believed that the punchouts were already repaired. “Not Investigated” means that some punchouts were not evaluated, because it was not feasible to evaluate some punchouts, especially if they were in the

second or third lanes from the outside lane or there was no outside shoulder. However, those distresses in the inside lanes might not have been caused by damages from truck traffic and structural deficiency, since the majority of the truck traffic is on the outside lane. “Incorrect” means that the research team was not able to find punchouts or repairs. Descriptions for other acronyms are provided under Table 4.2. Among the punchouts evaluated, those that appeared to have been caused by structural deficiency of the CRCP were about 33 percent (PCH+E-PCH+E-PCH-PTB). The remaining 67 percent of the punchouts evaluated were caused by non-structure related issues, such as construction or material quality control issues. Based on this finding, efforts will be made to develop a more accurate transfer function. Accessing accurate traffic information presents a difficulty in developing an accurate transfer function, and TxDOT Construction Division, Pavements and Materials Section is taking the lead in acquiring accurate traffic data.

Table 4.2 Detailed Classification of Punchouts

District	Punchout									
	PCH	E-PCH	E-PCH-PTB	PCH-CJ	PCH-RJ	BS-PCW	Repair or Not Found	Not Investigated	Incorrect	TOTAL
Dallas	10	8	2	7	8	6	9	19	15	84
Fort Worth	0	1	0	6	10	11	26	12	2	68
Wichita Falls	4	0	4	10	0	5	34	2	3	62
Childress	2	0	0	1	0	0	1	1	0	5
Sub Total	16	9	6	24	18	22	70	34	20	219
Ratio	16.8%	9.5%	6.3%	25.3%	18.9%	23.2%				

PCH: punchout, E-PCH: edge punchout, E-PCH-PTB: edge punchout with poor tie bar, PCH-CJ: punchout at construction joint, PCH-RJ: punchout at repair joint, BS-PCW: big spalling with poor concrete work

4.3 Sensitivity Analysis

When new design procedures are developed, the reasonableness of the solutions need to be evaluated by comparing the results with well-accepted field performance trends. One of the best ways to evaluate the reasonableness of the solutions is the sensitivity analysis for major input variables. For the sensitivity analysis, input values were fixed for all the input variables, and a value for a single input variable was changed from low to medium and high.

Table 4.3 Default input values selected for sensitivity analysis

Input Variable	Value	Input Variable	Value
District	Houston	Setting temperature (°F)	95
Design life (years)	30	CTE (10 ⁻⁶ in/in/F)	5
Design ESAL	40,000,000	Ultimate drying shrinkage (10 ⁻⁶ in/in)	500
Annual traffic growth (%)	4	28-day concrete flexural strength (psi)	620
Longitudinal steel (%)	0.6	28-day concrete modulus of elasticity (ksi)	5,000
Bar diameter (in)	0.75	Subbase friction	300
Month of Const.	May	Subbase thickness (in)	6
Slab thickness (in)	10	Composite k (psi/in)	400

In this analysis, soil type was not selected; instead, its effect was evaluated by varying composite k values. Table 4.3 shows the default values used for this analysis. With the default values, the number of punchouts per mile was 9.1. The effect of six input variables was evaluated: (1) design equivalent single axle loads, (2) longitudinal steel amount, (3) slab thickness, (4) concrete setting temperature, (5) concrete coefficient of thermal expansion and (6) concrete strength and modulus of elasticity.

It should be noted that the output (number of punchouts per mile) is highly dependent on the transfer function, and as a new and improved transfer function is obtained and incorporated into the program, the sensitivity of each variable might change.

4.3.1 Effect of Design ESALs

The effect of design ESALs was investigated from 20 million to 60 million ESALs. Figure 4.8 shows the effect of design ESALs on the number of punchouts per mile (output).

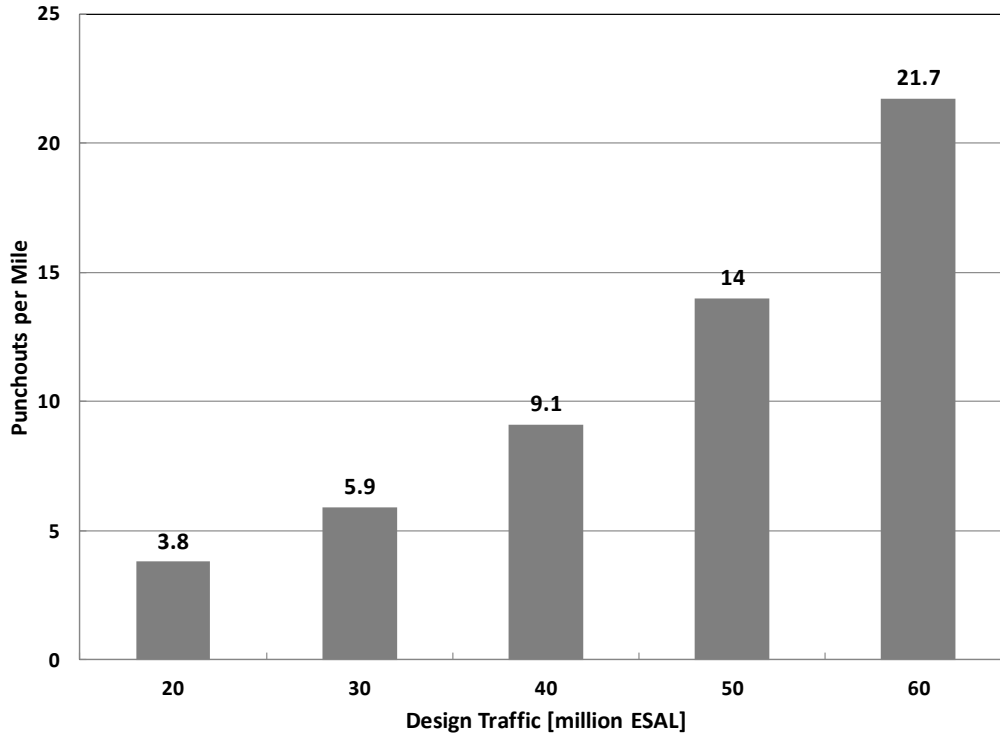


Figure 4.8 Effect of design traffic on punchouts per mile

Figure 4.8 shows that a 10-in thick slab is adequate for up to 40 million ESALs. The effect of ESALs becomes more pronounced as the ESALs increase.

4.3.2 Effect of longitudinal steel amount

It is known that the amount of longitudinal steel affects CRCP behavior and performance. Figure 4.9 illustrates a rather large effect of longitudinal steel amount on structural performance. This is due to the ability of longitudinal steel to reduce slab deflections and the resulting concrete strains from wheel loading applications.

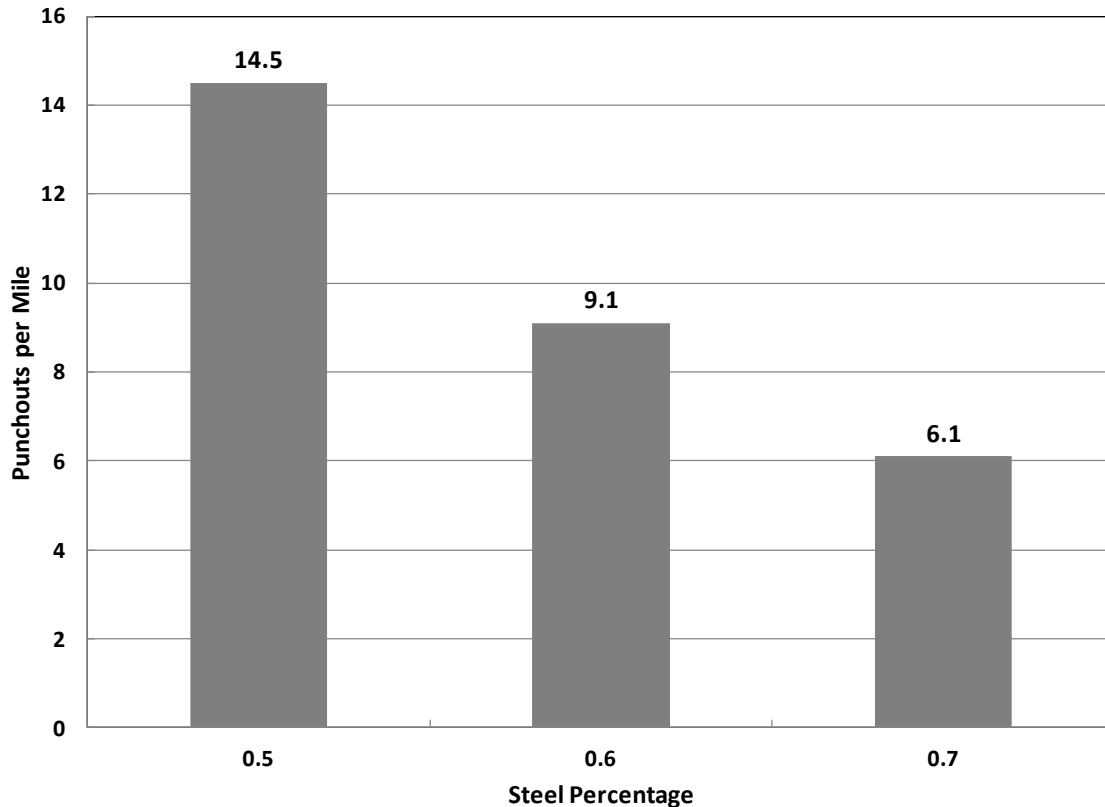


Figure 4.9 Effect of longitudinal steel amount on punchouts per mile

4.3.3 Effect of slab thickness

Wheel load stress in concrete slabs varies with slab thickness, and a significant portion of the past research on PCC pavement was on slab thickness and pavement performance. Figure 4.10 shows the number of punchouts decreases with increased slab thickness. However, the rate of decrease is not as much as expected, especially compared to the trends from the 93 Guide (AASHTO, 1993). It should be noted that this trend must vary depending on the transfer function.

4.3.4 Effect of concrete setting temperature

Figure 4.11 illustrates the effect of concrete setting temperature on the number of punchouts per mile. As setting temperature increases, the number of punchouts increases. This is expected because concrete stresses depend on the setting temperature; the higher the setting temperature, the larger the concrete stress. Larger concrete stresses will result in more punchouts. However, the effect of setting temperature is not that simple, since there are a number of variables that interact with each other. For example, with a higher setting temperature, a temperature drop at a specific time (called delta T) will be larger and greater concrete thermal stress will result. On the other hand, there will be more cracks, which will alleviate some of the high concrete stresses. One consideration is whether setting temperature should be a design variable. Past research shows that setting

temperatures vary 10 F or more within a day. With the difficulty predicting at which season the pavement will be placed, this daily variation in concrete setting temperature adds more uncertainty in the pavement design process. Using a fixed value statewide may be a realistic option.

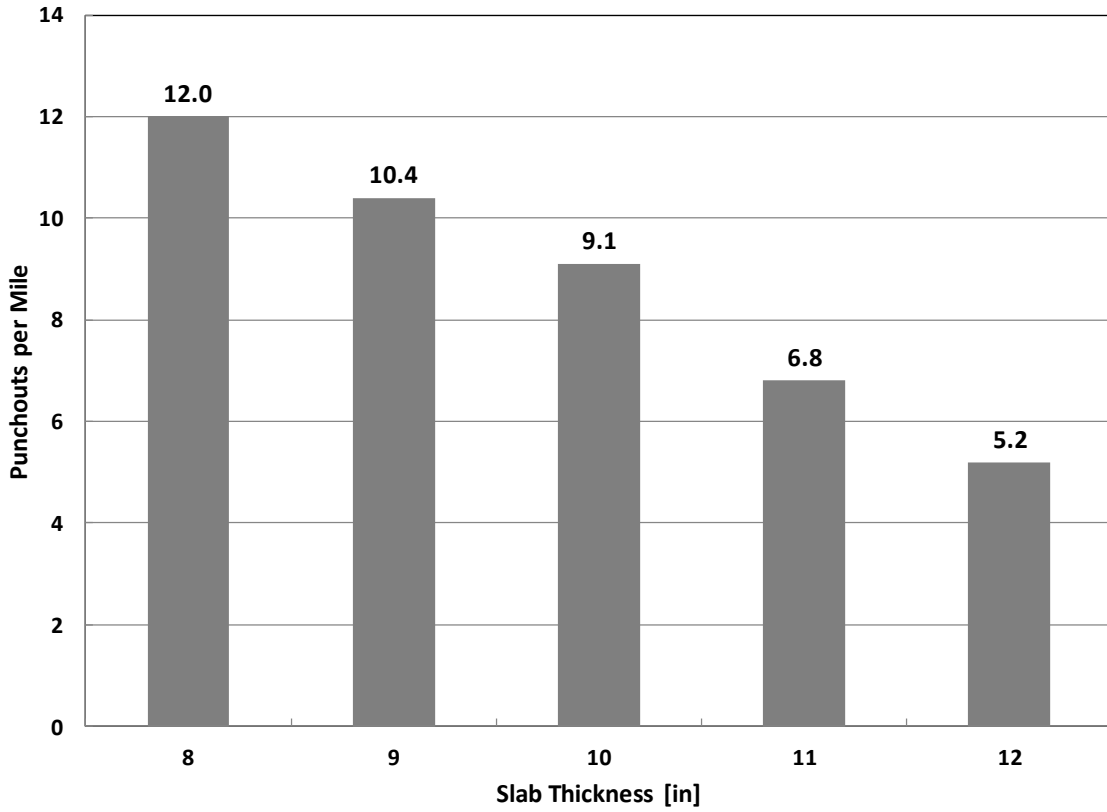


Figure 4.10 Effect of slab thickness on punchouts per mile

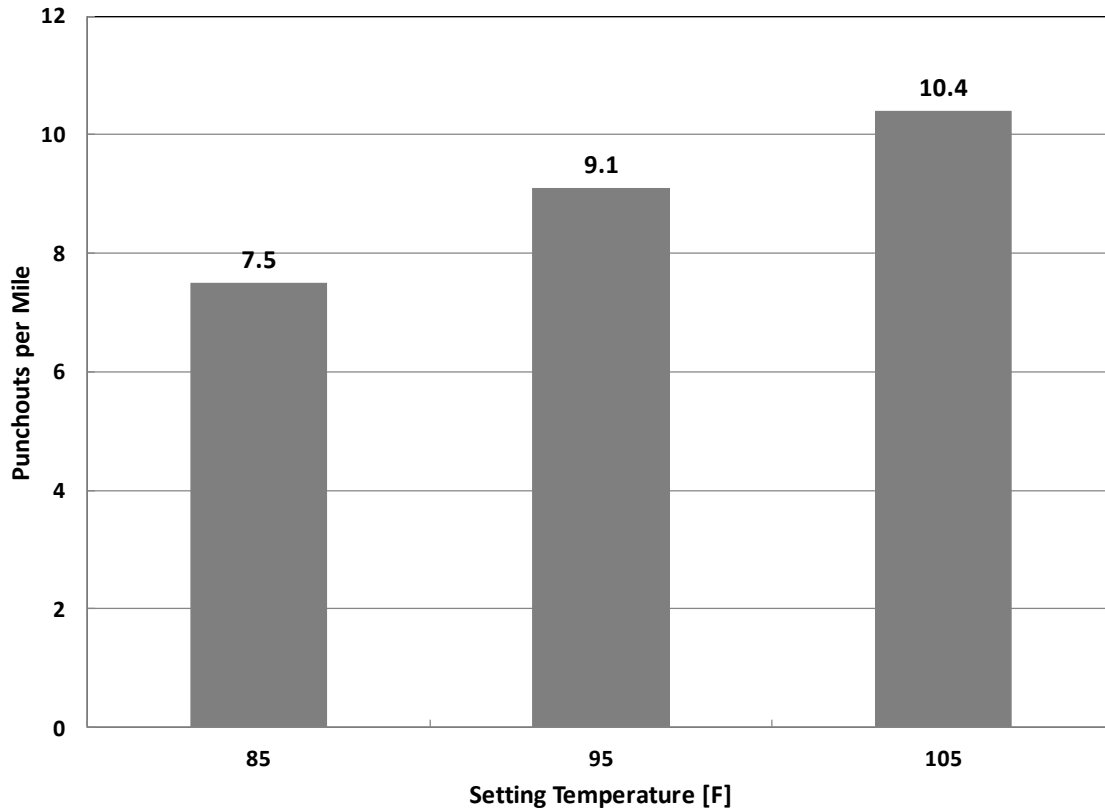


Figure 4.11 Effect of concrete setting temperature on punchouts per mile

4.3.5 Effect of concrete coefficient of thermal expansion (CTE)

It is known that CTE affects the performance of CRCP. Over the years, TxDOT has had performance issues when concrete with a high CTE was used. Figure 4.12 shows the effect of CTE on punchouts. It shows little effect of concrete CTE on punchout development, which appears to be contradictory to TxDOT's experience.

The primary distress types in CRCP with high CTE concrete have been spalling and other volume change-related failures, not necessarily structural capacity-related failures. Increasing the slab thickness might not alleviate the distress in a pavement with high CTE concrete. This leads to the question: should CTE be an input variable for slab thickness determination? There are interactions between concrete volume changes and longitudinal steel, and the CTE issue might need to be addressed in terms of longitudinal steel design.

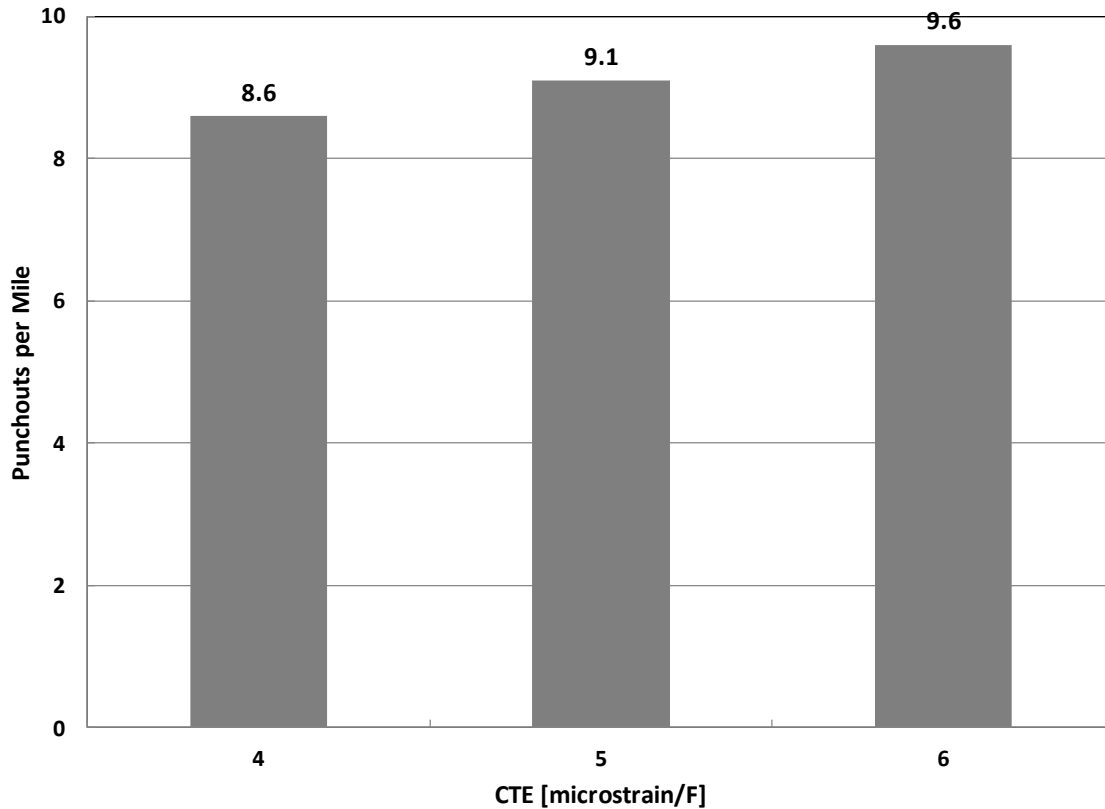


Figure 4.12 Effect of concrete coefficient of thermal expansion on punchouts per mile

4.3.6 Effect of concrete strength and modulus of elasticity

Figure 4.12 shows the effect of concrete strength. As expected, it illustrates that stronger concrete provides better performance. Concrete modulus of elasticity and strength are closely related, and in this analysis, modulus values corresponding to concrete strength were used. Modulus of elasticity was derived from the following ACI equation (ACI, 2002):

$$E_c = 33 \times uw^{1.5} \times \text{sqrt}(f'_c)$$

$$f'_c = (f_r/7.5)^2$$

where, E_c = modulus of elasticity, psi
 uw = unit weight of concrete, lb/cu. ft
 f'_c = compressive strength, psi
 f_r = flexural strength, psi

From the above equations, 4,769 ksi, 5,011 ksi, and 5,254 ksi of concrete modulus of elasticity were used for 590 psi, 620 psi, and 650 psi of concrete flexural strength, respectively.

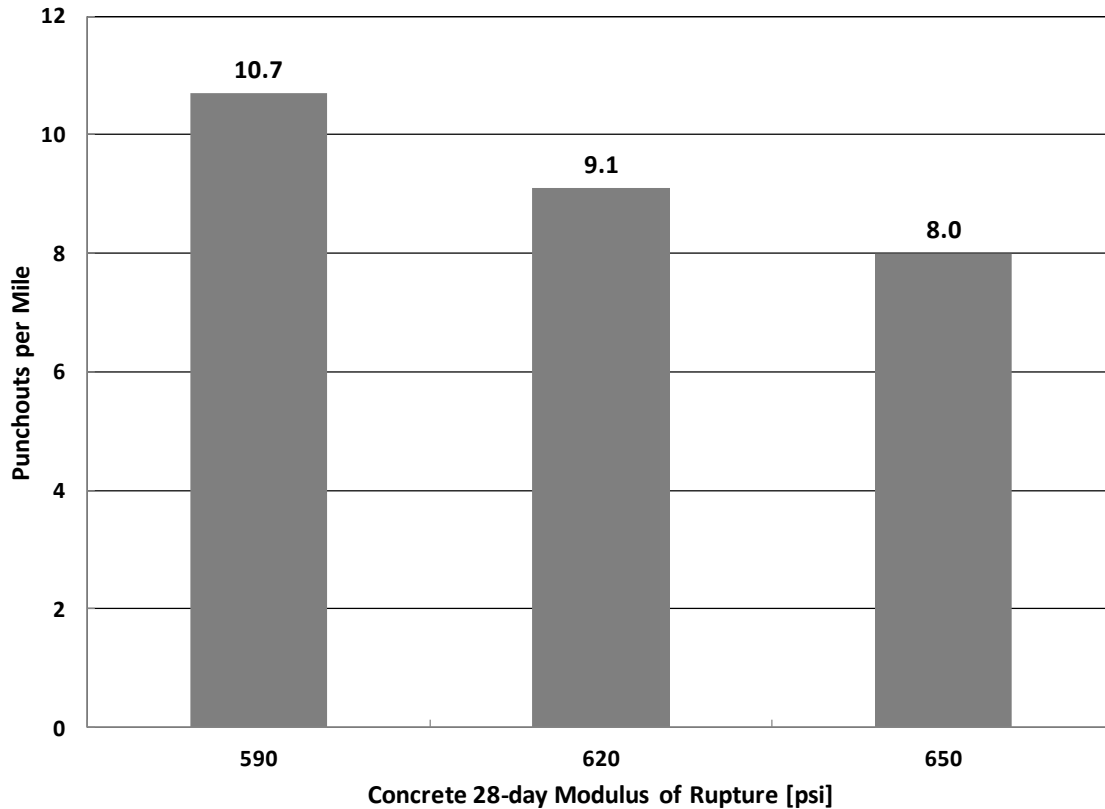


Figure 4.13 Effect of concrete strength on punchout per mile

Figure 4.12 shows that there was about one punchout per mile difference for a 5 % difference in concrete flexural strength. The beneficial effect of high strength is counterbalanced with the increase in modulus of elasticity.

4.3.7 Summary

Sensitivity analysis shows that the results from TxCRCP-ME appear to be reasonable, even though the punchout predictions depend on, to a large extent, a transfer function. The use of different transfer functions will change the number of predicted punchouts; however, it won't change the trend of the relationship between input values and predicted punchouts. From that perspective, the sensitivity analysis conducted in this study indicates that trends in the results from TxCRCP-ME are reasonable, and with a more accurate transfer function, TxCRCP-ME could provide reasonable designs.

CHAPTER 5 SPALLING PERFORMANCE

Spalling distress mainly affects the functional aspects of concrete pavement performance and has been manifest in a variety of forms caused by a variety of factors – most of which are tied to construction practice or climatic conditions at the time of construction. As shown in Figure 5.1-(a), spalling is the breakdown or dislodging of concrete segments along or within six to 12 inches of a joint or crack in a concrete slab (Zollinger et al., 1994) that can affect the functionality of a concrete pavement. A significant contributor to spalling is the existence of horizontal delaminations that are oriented parallel to the alignment of a transverse crack or joint and at a shallow depth below the surface of the pavement (Figure 5.1-(b)). The formation of delamination has been researched for several years and has been found to be affected by a variety of factors, but one of the more prevalent of these factors is the quality of the curing process and the evaporation of pore water from the concrete. Evaporation typically causes a moisture gradient to form, as shown in Figure 5.2, soon after the placement of the paving concrete. The rate of evaporation is much faster at the top part (one to two inches) of the pavement than at the interior portions below the surface; this difference leads to a non-uniform distribution of relative humidity and creates a moisture gradient in the pavement. The development of an evaporation-induced moisture gradient is largely a function of the ambient weather and curing conditions during and after placement of the concrete. If the moisture gradient due to evaporation is sufficiently severe it can create differentially distributed horizontal shear stresses high enough to shear the concrete along the aggregate paste interface and lead to the development of shallow delaminations (i.e. horizontal shear planes near the surface). The presence of delaminations in the vicinity of transverse cracking (in CRC pavement) can eventually lead to the development of spall damage due to repeated traffic loading or any number of mechanisms causing in-plane bending stress in the delaminated segments.



(a) Spalling damage



(b) Delamination

Figure 5.1 Spalling and Delamination (Soares et al., 1997)

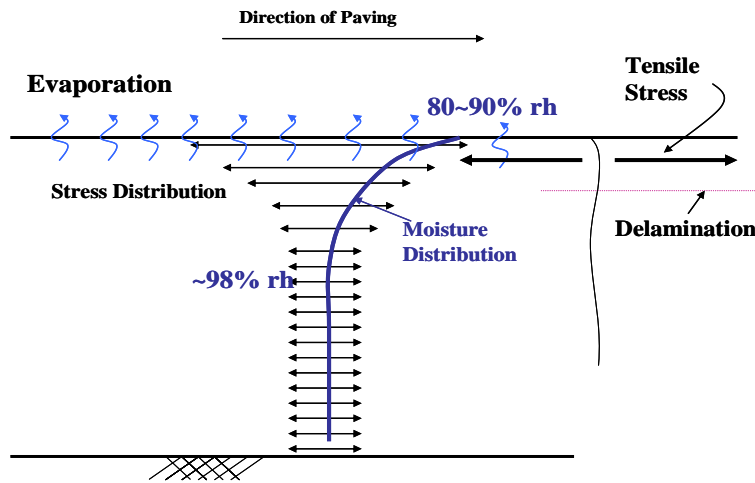


Figure 5.2 Formation of Horizontal Delamination

Early age delamination occurs when shear stresses caused by the moisture variation surpass the concrete shear strength. Gravel concrete is particularly sensitive to this type of failure since its early strength may be affected by the presence of a layer of hydrated lime on the aggregate-mortar interface. A design framework for delamination and subsequent spalling development was introduced by Soares and Zollinger (1997), where stresses due to moisture variation were considered relative to the formation of a delaminated shear plane based on fracture mechanics, closed-form shear stress functions, and median-thick plate theory similar to that shown by Westergaard (1927) and Tang et al. (1993).

Conditions necessary for formation of delamination include low shear strength (that typically occurs at the interior face between the aggregate and mortar) and sufficient evaporation of pore water from the hydrating concrete resulting in differential drying shrinkage near the pavement surface (Wang et al., 2000). In the past, concrete mixtures made with siliceous river gravel coarse aggregates were particularly susceptible to early age delamination and eventual spalling due to the susceptibility of the aggregate-mortar interface to low strength development. Recent research, however has led to a better understanding of the role of aggregate types in terms of the aggregate-mortar bond characteristics and measures to improve resistance to delamination and subsequent spall distress (Liu et al., 2009).

5.1 Field Performance

It is useful to describe spalling distress in terms of three different categories: chipping, shallow spalling and spalling. These categories of distress are based on both length and depth.

5.2 Nature of Spalling

Based on depth, a distress is categorized as a) chipping (shown in Figure 5.3,) which consists of dislodged concrete mortar at the surface along the transverse crack that is 0.25 inch or less in depth; b) shallow spalling (shown in Figure 5.4,) which is along the transverse crack and includes dislodged aggregate particles or c) spalling, which is defined as deeper than 0.5 inches. Although rather unsightly, neither chipping nor shallow spalling affects performance significantly enough to warrant repair or routine maintenance.

If the affected length of crack is less than 15%, it is considered as low severity. If the length of crack ranges from 15 to 85%, it is classified as medium severity. A crack which is affected more than 85% is classified as high severity.

Spalling at depths greater than 0.5 inch requires maintenance after a certain amount of damage occurs on the pavement surface. The field survey data suggests that TxDOT conducts spall repair at approximately 3 to 5% spalling. In the case of the above categories of spall related distress, delamination is assumed to be the primary initiating factor causing the concrete along a transverse crack or joint to be highly susceptible to dislodging under applied shear stresses by rolling truck tires and differential movement at the joint or crack.



Figure 5.3 Low and Medium Severity Chipping, on US 290, Cypress



Figure 5.4 Low and Medium Severity Shallow Spalling, on US 290, Hempstead

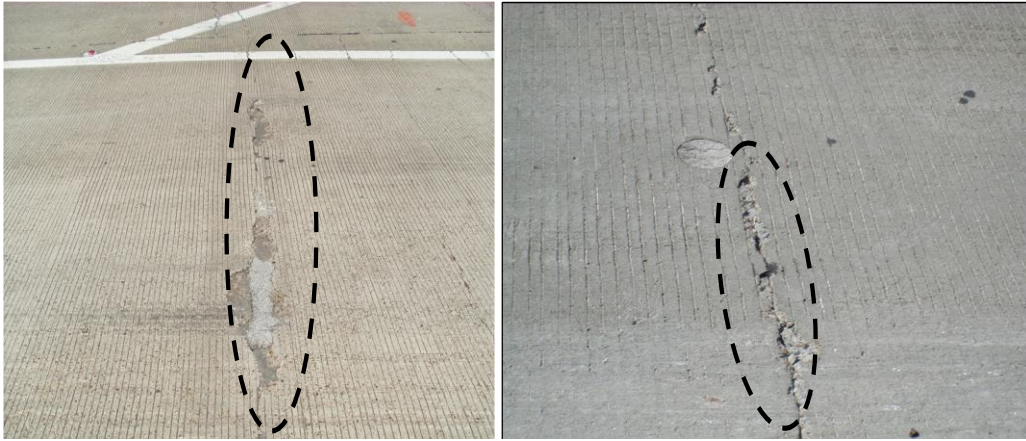


Figure 5.5 Medium Severity Spalling, SH 225 and Low Severity Spalling, SH 288

If the length of crack is affected by 50% spalling and the depth is greater than 0.5 inch, a medium severity level of spalling exists. If depth of spalling distress is less than 0.5 inch, the level of spalling can be categorized as shallow with medium severity. Table 5.1 summarizes the definitions of spalling classification used in this study. It is noted that spalling distress as characterized in the Pavement Management Information System (PMIS) database is not used in this discussion. The definition of spalling distress as depicted by PMIS is an area along a transverse crack or joint that is greater than 3.0 inches long and 12.0 inches wide across the lane. A more descriptive scheme for spalling was needed because other forms of spalling distress not documented in the PMIS database were noticeable by experienced pavement engineers and are needed to better represent spalling behavior in design. Most PMIS-defined spalling distress will fit the low severity category in the scheme outlined in Table 5.1.

Table 5.1 Project Categories of Spalling Distress

Distress Type	Depth	Severity Level (L, M, and H)	Definition
Shallow Spalling	≤ a depth of 0.5 inch	low severity	0% ≤ spalled length of crack < 15%
		medium severity	15% ≤ spalled length of crack ≤ 85%
		high severity	85% < spalled length of crack ≤ 100%
Spalling	> a depth of 0.5 inch	low severity	0 % ≤ spalled length of crack < 15%
		medium severity	15% ≤ spalled length of crack ≤ 85%
		high severity	85% < spalled length of crack ≤ 100%
Chipping	No consideration	low severity	0% < chipping length of crack < 15%
		medium severity	15% ≤ chipping length of crack ≤ 85%
		high severity	85% < chipping length of crack ≤ 100%

5.3 Field Performance Sites

Seven sites in Houston district were visually surveyed to document chipping, shallow spalling, and spalling performance data based on visual observation:

- US- 290 Cypress
- US-290 Hempstead
- SH – 99
- SH – 225
- SH - 288
- FM – 1960

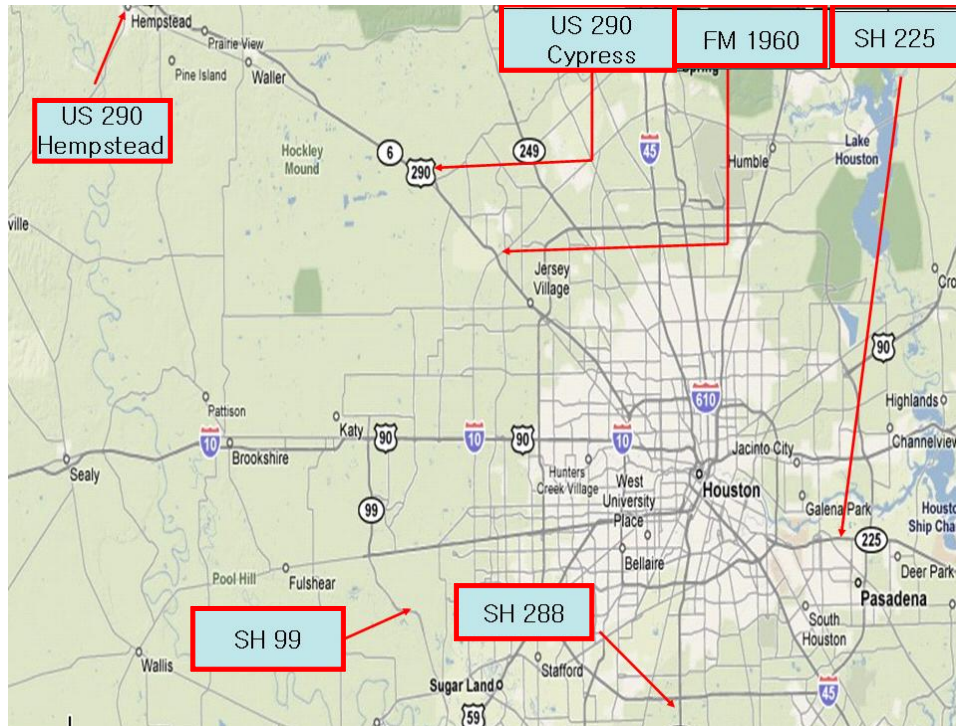


Figure 5.6 Map of the Investigated Sections in Houston

The following discusses chipping, shallow spalling and spalling performance in terms of the method of curing, mix proportion, evaporation potential, and aggregate characteristics with respect to specific sites such as SH-225, and SH-288, etc. Data relevant to the distress surveys is summarized for all sites in Appendix B. Coring was conducted on selected sites to facilitate petrographic information and to delineate aggregate characteristics of the existing concrete with respect to spalling.

5.3.1 US 290-Hempstead

A large test section was constructed near Hempstead, Texas on US 290 in the summer of 1995. Key information of this test section is summarized in Table 5.2, and weather information relevant to climatic conditions during construction is summarized in Table 5.3. The layout of the different test sections are shown in Figure 5.7. The eastbound outside lane and shoulders in this project comprised the test sections which were batched with siliceous river gravel concrete. Among the 11 different test sections (shown in Figure 5.), four sections were closely researched in order to obtain spalling data sensitive to the method of curing, time of paving, transverse-saw cutting, etc.

The features of US 290–Hempstead test sections include different construction methods applied during paving, different mix combinations, and different placement timing which were useful to broaden the applicable range of the model calibration effort described later. Since the source of coarse aggregate type can be considered as a critical factor, gravel and other related characteristics are provided to the extent possible. Moreover,

aggregate characteristics are identified with respect to the observed performance such that physical, geometric, and chemical properties were considered relative to determination of aggregate rating data. An aggregate rating scheme used in this project is described in Appendix C. Traffic data was computed based on information from the PMIS database for specific sites. Potential evaporation rate (PE) was determined for each site with respect to prevailing conditions such as temperature, wind speed, and humidity during paving operations as a means of accounting for environmental effects on delamination potential.

Table 5.2 Sample Section Inventory at US 290-Hempstead

Features	Construction Date	Slab thickness	Gravel Source & Agg rating	Traffic (ADT)	PE
Time of paving, method of crack control, aggregate blend, and method of curing	31 May through 17-18 June 1995	12 (inches)	Hanson Altair, TX, 6.1	17,530	0.04 0.02

Table 5.3 Weather Information during Paving Operations

Weather information	21E-22E (Day paving)	28E-31E (Day paving)
Avg. Temp.	84.25 (°F)	75 (°F)
Avg. RH	70 (%)	79 (%)
Avg. SR (solar radiation)	0.009 (kW/m ²)	0.29 (kW/m ²)
Avg. WS	2.3(mph)	3.2 (mph)
PE	0.04	0.02

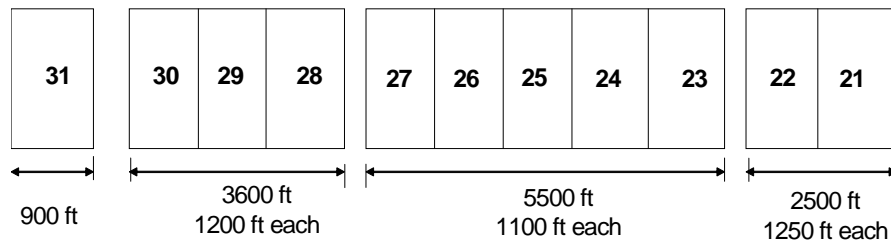


Figure 5.7 Layout of Numbered Test Sections in US 290-Hempstead. (McCullough et al 2000)

Table 5.4 shows the synopsis of the construction methods used in the Hempstead test section placements. For example, Sections 21 and 22 were placed under the same day-time weather conditions using a blended coarse aggregate concrete mixture. Section 22 was sawcut transversely, while Section 21 was allowed to crack randomly. Section 25, 26, and 27 were constructed under nighttime conditions. Section 26 and 27 were respectively placed with skewed transverse steel and transverse saw cutting. The other sections are listed in Table 5.4.

Detailed information of mix proportions are listed in Table 5.5. As it was noted previously, three types of aggregate were used to proportion the mixtures: limestone, river gravel, and a blended aggregate combination as stated below in the table.

Comprehensive surveys performed on US 290 (Hempstead) are summarized in Table 5. Spalling distress on Sections 28 to 31 was analyzed with respect to the effect on performance that various methods of construction had. Overall, shallow spalling was the most evident type of spalling ranging from 7.5 to 34 %. Some low and medium severity spalled cracks were also observed and detailed in Table 5.

Table 5.4 Construction Methods Used in US 290 –Hempstead (McCullough et al 2000)

Sections	Construction Methods/Features	
	Similarities	Differences
21, 22	Day paving Blended aggregate	Transverse cuts (22)
23, 24, 25, 26, 27	Night paving Day paving	Skewed steel, Transverse cuts
28, 29	CRCP 89 steel standard Two coats curing	Skewed steel, Transverse cuts
30, 31	Day paving CRCP 89 steel stan Poly curing	Transverse cuts

Table 5.5 Concrete Mix Proportions, US 290-Hempstead Sections 21 and 22 (McCullough et al 2000)

Component	Limestone	River Gravel	Blended
Coarse Agg.	1760 (lbs)	1825 (lbs)	574 (lbs)–Limestone 580 (lbs)– SRG
Intermediate Agg. (lbs)	/	/	673 (lbs) -SRG
Fine Agg. (lbs)	1345 (lbs)	1250	1289
Cement	6 sk/ Texas Lehigh		
Fly ash	139/30% Ahman (WA Parish)		
Air factor	5%		
Water factor	4.5 gals per sk		

Table 5.6 Results of Spalling Surveyed in US 290 – Hempstead

Section	Surveyed Distance (ft)	Chipping (%)	Shallow spalling(%)	Spalling (%)	Severity
21	1,250	35	7.5	0.0	Low and Medium
22	1,250	35	19.0	0.0	Low
25	1,100	70	11.8	0.0	Medium
26	1,100	50~60	20.1	0.0	Low
27	1,100		9.4	0.0	Medium
28	1,200		11.8	0.59	Medium
29	1,200		23.4	1.95	Low
30	1,200		34.0	1.91	Low
31	900		23.8	1.00	Medium

The percentage of shallow spalling and spalling were calculated based on the field observations. The number of cracks per 100 ft of pavement manifesting shallow spalling or spalling were divided by the total number of cracks to establish the percentage of shallow spalling and spalling (per 100 ft). As it was noted previously, the level of

severity was determined according to the criteria listed in Table 5.1. Overall, the level of severity was found to be low to medium with respect to shallow spalling and spalling. A few of the spalled cracks were found in test sections 28 to 31. More detailed analysis with respect to the construction methods and curing compounds is discussed in the following section.

Figure 5.8 shows the average crack spacing of all sections surveyed in this segment of US 290. Sections 22, 26, 29, and 30 were transversely sawcut at six-foot intervals. Clearly, sawcutting had an effect on the resulting crack pattern even when the tendency for random crack initiates at closer intervals.

Sections such as 25, 26, and 27 can be compared with respect to construction methods such as use of transverse saw cutting, skewed steel, and without either of these. All three sections were constructed under night time paving conditions. Section 25 was a control section while Sections 26 and 27 were used with transverse cuts and skewed steel, respectively. Shallow spalling in Section 25 and 27 was respectively 12 % and 9 % which was classified mainly as medium severity. The 20 % shallow spalling in Section 26 was classified as low severity.

Section 26 manifests less than 20% low severity shallow spalling. However, a medium level of shallow spalling occurred in Sections 25 and 27. Though the percentage of shallow spalling is less than that in Section 26, spalling severity is higher. Transverse cuts generally have been found to improve upon spalling severity over time. The use of skewed steel apparently has a minimal effect on spalling as noted in Figure 5.9.

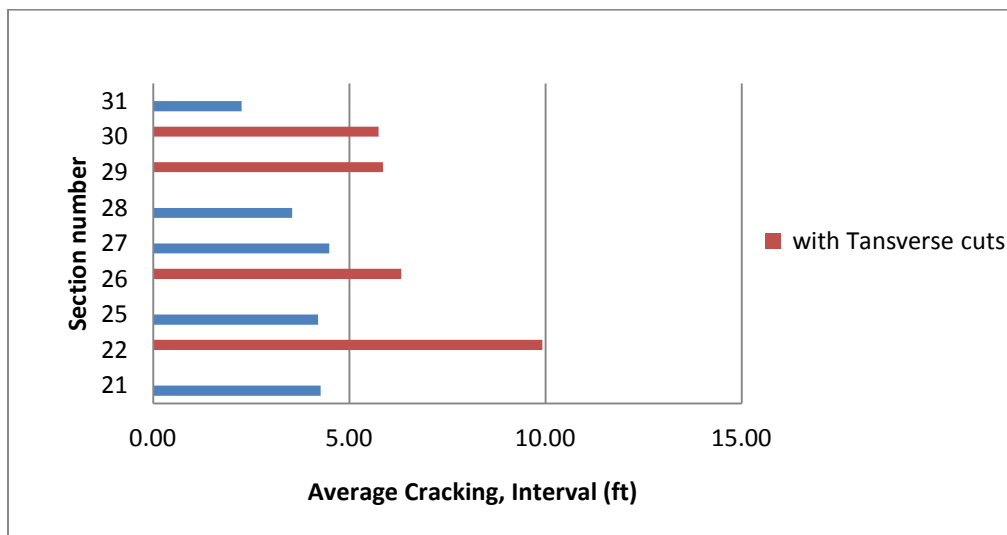


Figure 5.8 Average Crack Spacing over Each Section.

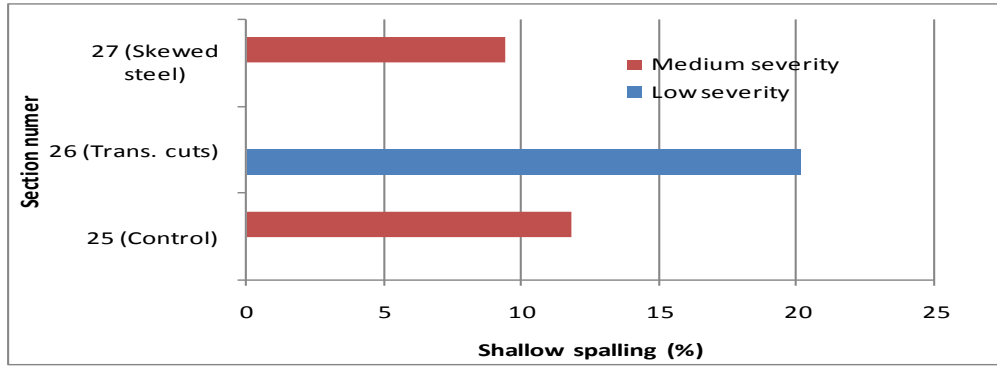


Figure 5.9 Methods of Construction (skewed steel, transverse cuts, and control)

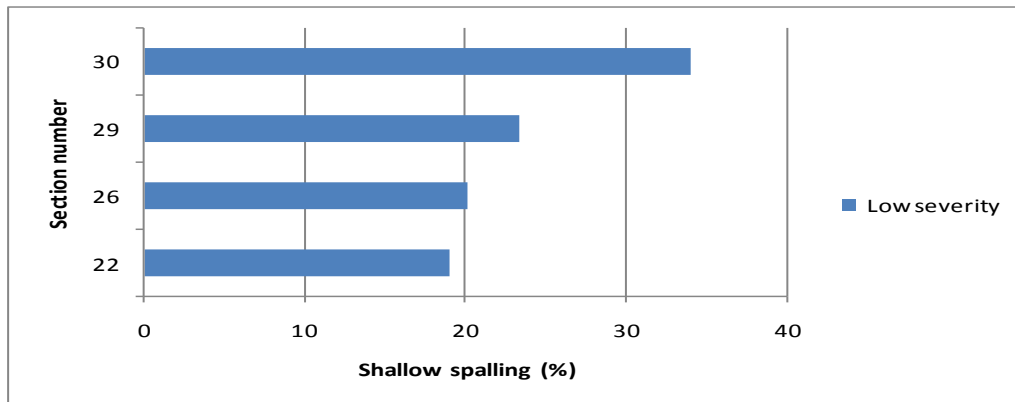


Figure 5.10 Shallow Spalling of Section Used with Transverse cuts

All of the sections placed with transverse sawcuts are compared in Figure 5.10. These sections manifest low severity shallow spalling ranging from 19 to 34%. In comparison with sections without transverse sawcuts, low severity spalling is approximately 24%. The method of curing used in Section 30 was polyethylene sheeting as noted in Table 5.4. The performance results listed in Table 5.6 indicate, perhaps unexpectedly, a poor quality of curing protection was provided with respect to shallow spalling.

Method of curing is a significant quality control factor affecting concrete pavement spalling performance. Figure 5.11 compares the results of the performance with respect to method of curing and the percentage of shallow spalling in Sections 29 and 30. Two sections were paved under the same climatic conditions. Two coats of curing compound caused less shallow spalling than that resulting from the use of polyethylene curing. However, polyethylene sheeting showed less spalling than two coats of curing compound, as shown in Figure 5.12. Done correctly, polyethylene curing is considered to be effective in preventing spalling.

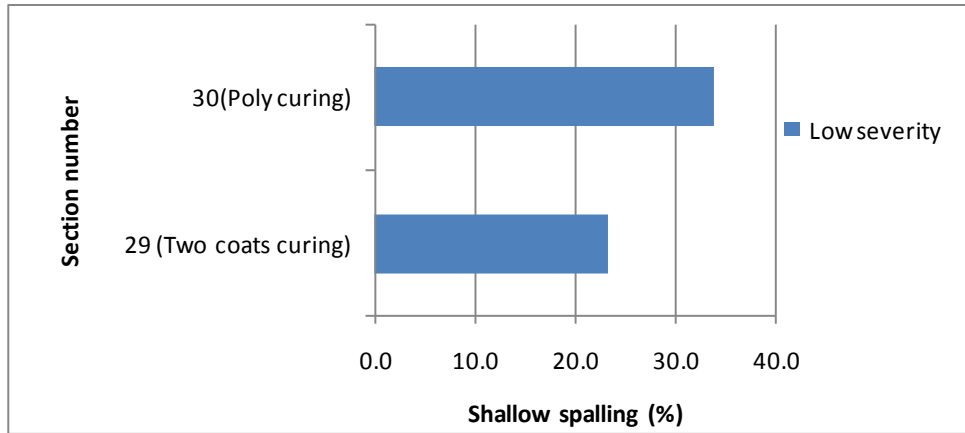


Figure 5.11 Curing Methods with respect to Shallow Spalling Distress

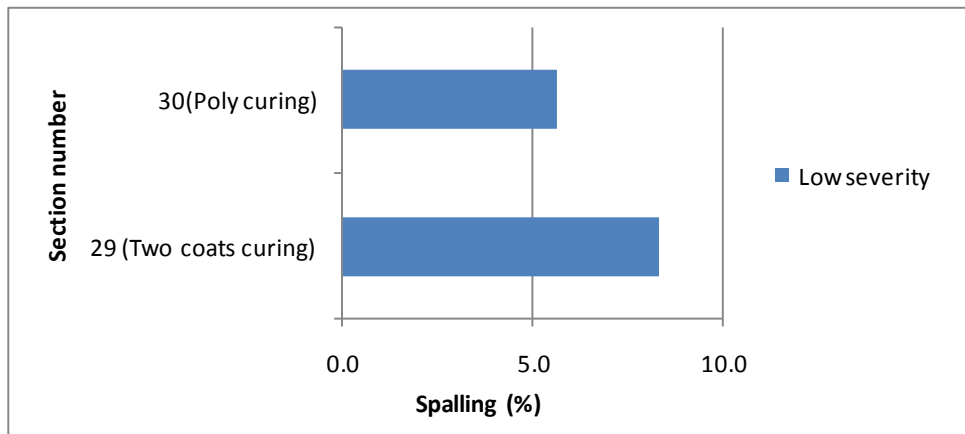


Figure 5.12 Curing Methods with Respect to Spalling

Section 31 shown in Figure 5.13 was constructed during the day and cured using polyethylene sheeting. Shallow and low severity spalling was found in this section but chipping was the most common distress noted.

Section 21, shown in Figure 5.14. was also paved in the daytime but consisted of a blended aggregate. This section showed only low severity chipping of approximately 35%.

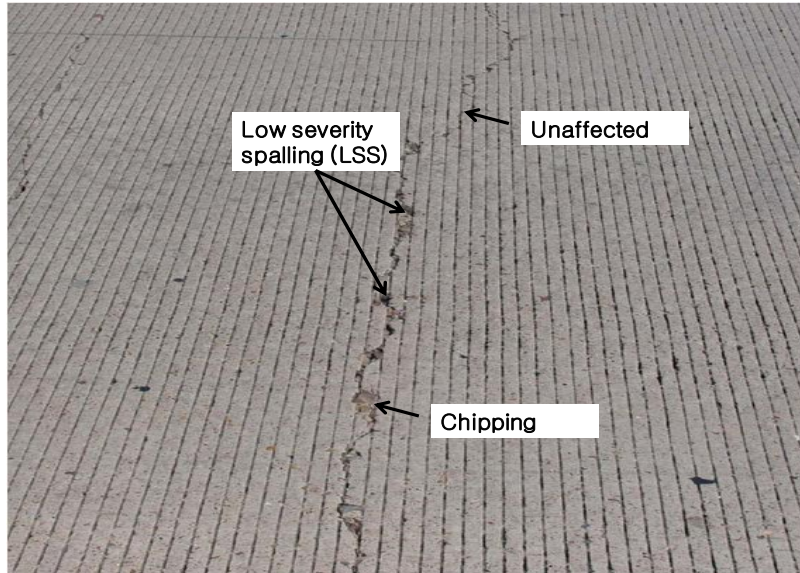


Figure 5.13 US-290 Hempstead Section 31 (day paving, poly curing).

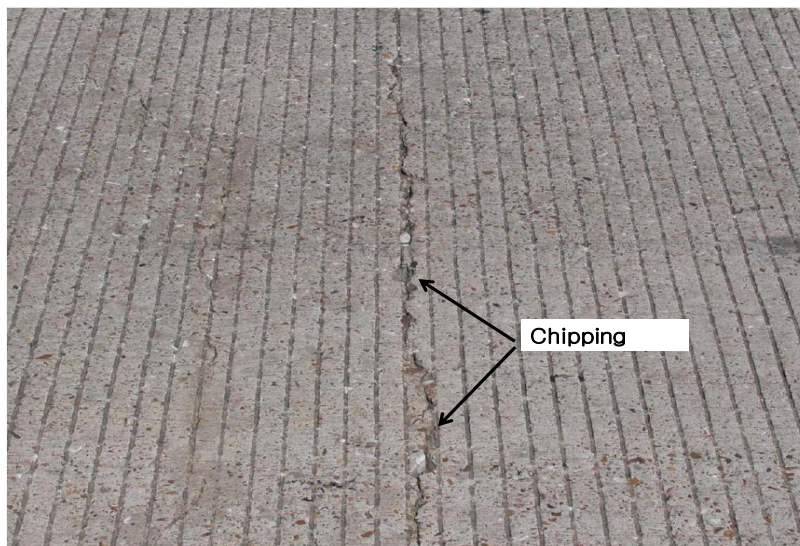


Figure 5.14 US-290 Hempstead Section 21 (day paving and blended aggregate).

5.3.2 US 290 – Cypress

A test section involving the use of varying amounts of gravel aggregate and different curing methods was constructed on US 290 near Cypress, Texas in August of 1992. This section included several factors affecting spalling including some related to curing. The thickness of pavement was 13 inches with a single mat of reinforcement. Additional construction information regarding the US 290-Cypress test site is summarized in Table 5.7 and weather information is in Table 5.8

Figure 5.15 shows the configuration of some the test sections. A control mixture was placed at the end of the test section as shown. Four different coarse aggregate mixture

combinations were used. Specifically, detailed methods of curing were employed as shown in Figure 5.. Most of the test sections, except for control mix areas, were cured with a double coat of curing compound (D curing), polyethylene sheet curing (P curing), and a single coat of waxed-base membrane curing compound (S curing).

Table 5.7 Sample Section Inventory at US 290-Cypress.

Features	Construction Date	Slab thickness	Gravel Source & Aggregate rating	Traffic (ADT)	PE
Method of crack control	Aug 18-24, 1992	13 (inches)	Hanson Aggregates 6.1	36,875	0.04

Table 5.8 Weather Information during Construction Period.

Weather information	US 290-Cypress
Avg. Temp.	77.5 (°F)
Avg. RH	77.5 (%)
Avg. SR	/
Avg. WS	6.21 (mph)

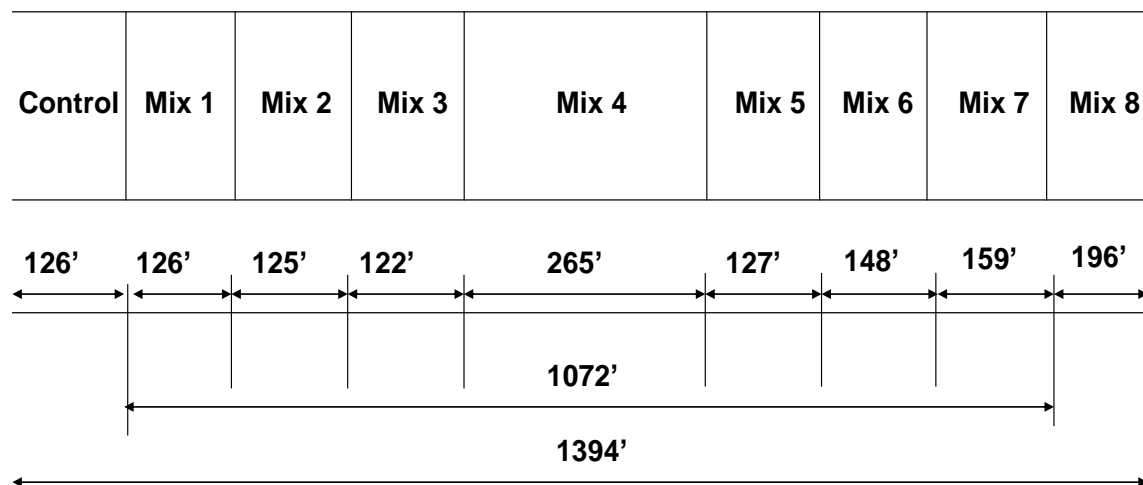


Figure 5.15 Layout of Test Sections in US 290-Cypress (McCullough et al 2000)

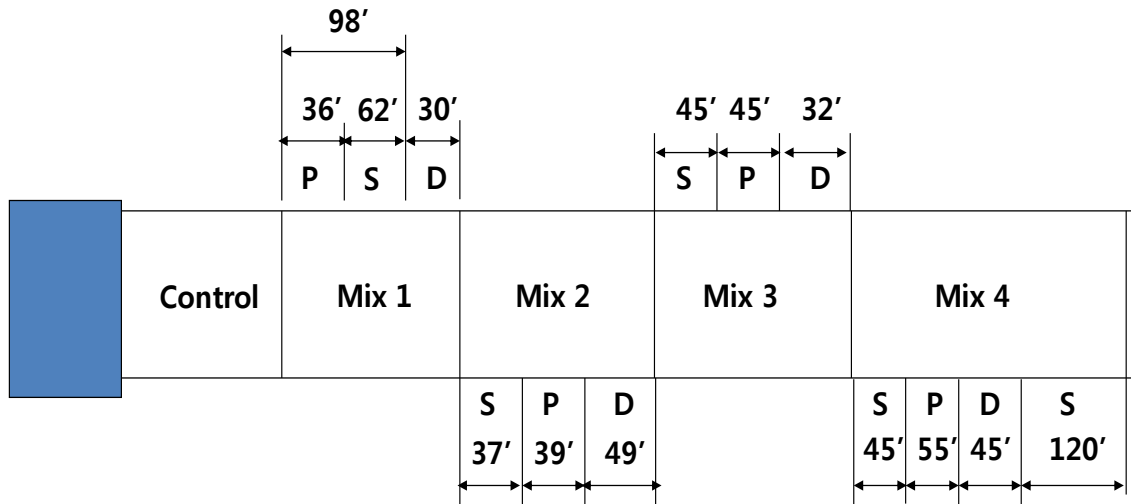


Figure 5.16 Layout of Test Section Methods of Curing US 290-Cypress (McCullough et al 2000)

Mixture combinations are detailed in Table 5.9. Factors such as water-cement ratio, cement content, and cementitious material were held constant over the different mix proportions except for the coarse aggregate content and type. For instance, Mix 1 and Mix 4 were respectively batched with 100% limestone and gravel. Both Mix 2 and Mix 3 were blended with a certain percentage of each aggregate type (limestone and/or gravel). Therefore, the results from this test section can indicate the effect of coarse aggregate type on spalling distress.

Table 5.9 Four Mix Design Combination used in US 290-Cypress Test Section (McCullough et al 2000)

Composition (lb/ft ³)	Mix 1	Mix 2	Mix 3	Mix 4
Amount and Type of aggregate	100 % LS	67% LS, 37%RG	67% RG 37 % LS	100% RG
Coarse aggregate	87.9	58.9 /30.6	62.2 /29	92.8
Water	11.1	11.1	11.1	11.1
Cement	20.9	20.9	20.9	20.9
Entrained Air	4.5 %	6.4 %	5.5 %	4.6 %
Max. CA size(in)	1.5	1.5	1.5	1.5
w/c	0.53	0.53	0.53	0.53

Mixture proportions were varied with limestone content to determine the effect shown in Figure 5.17Figure 5. with respect to the percentage of spalling. Mixtures using higher contents of limestone showed the best performance. In other words, the more limestone used, the less spalling occurred. Hence, the choice of aggregate type and content affects the spalling severity level of the pavement surface.

Generally, the surface conditions of the Cypress test sections were fairly good. Nonetheless, the method of curing made a difference on chipping performance as shown in Figure 5.18Figure 5.. Three different kinds of curing methods were used with Mix 4 where the aggregate type was 100% gravel. P curing showed the best performance, but the D curing showed less than 10% chipping. The standard curing in Mix 4 showed a higher percentage of chipping compared to other curing methods.

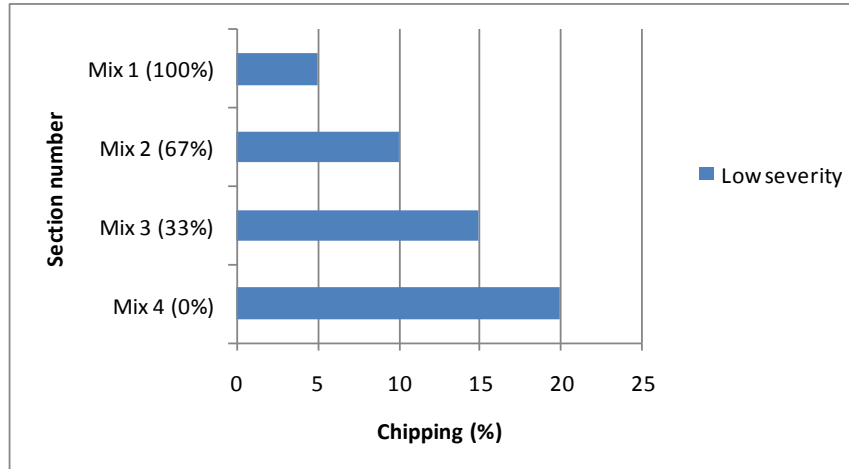


Figure 5.17 Aggregate Contents (% Limestone content)

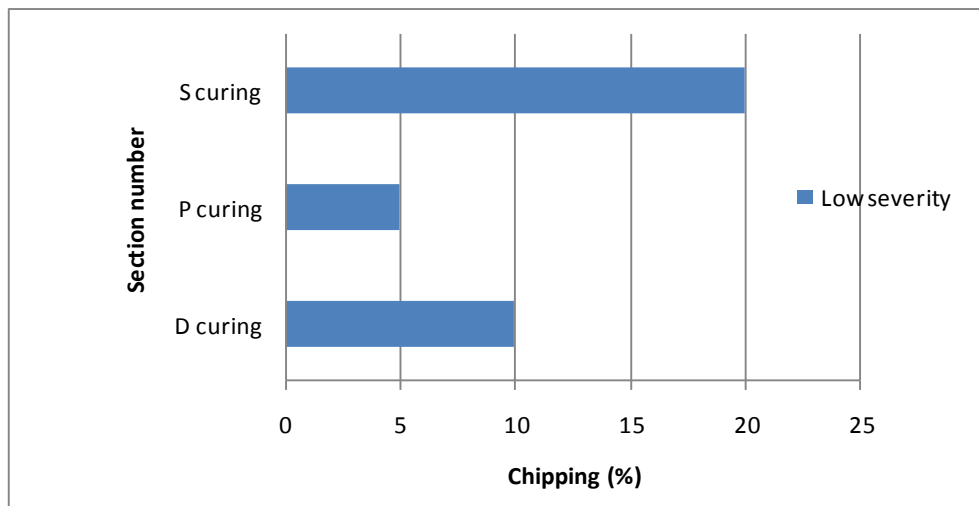


Figure 5.18 Method of Curing in US 290-Cypress (Mix 4)

Weather conditions during the construction of the four different mix combinations were generally hot and windy. Low severity chipping was predominant in these sections; furthermore, spalling was not evident over most of the US-290 Cypress test sections. Figure 5.19 and Figure 5.20 show relatively tight transverse cracking with chipping less than 10% of the length of the transverse crack, so it was considered as low severity.

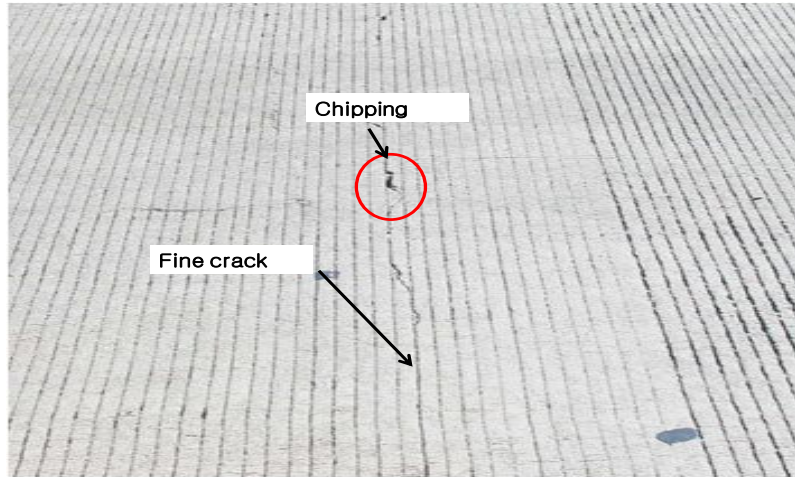


Figure 5.19 US- 290, Cypress, Water base, Mix 1 (100% Limestone).

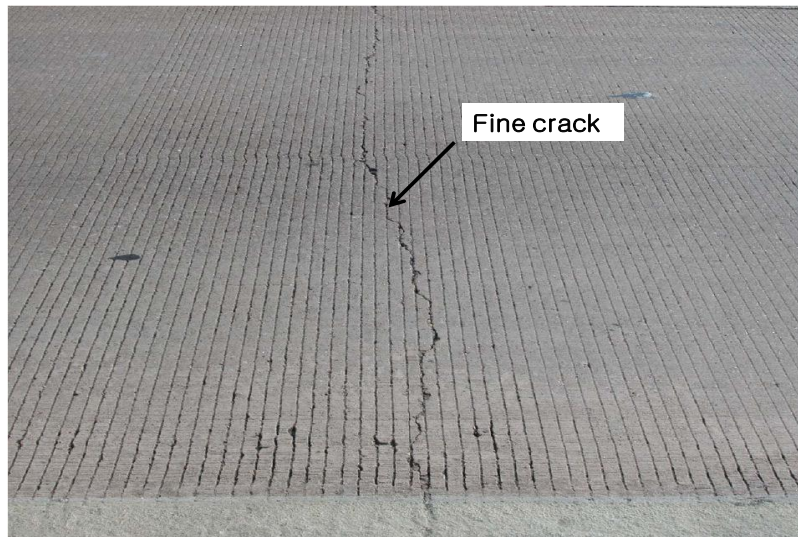


Figure 5.20 US- 290, Cypress, Mix 1 (100% Limestone).

The Cypress section was relatively undamaged by chipping and spalling. Figure 5.21 shows a section of Mixture 4 (gravel) with a medium level of chipping (20 % to 25 %). However, chipping was generally less than 10%. A few spalled areas were detected in this test section.

Although no PMIS data was available for this segment of pavement, Figure 5.22 shows the incidence of spalling at selected intervals illustrating the random nature of its occurrence. The amount of spalling varies even under the same level of traffic. The average spalling over this section of pavement and standard deviation were respectively 1.11 and 0.99.

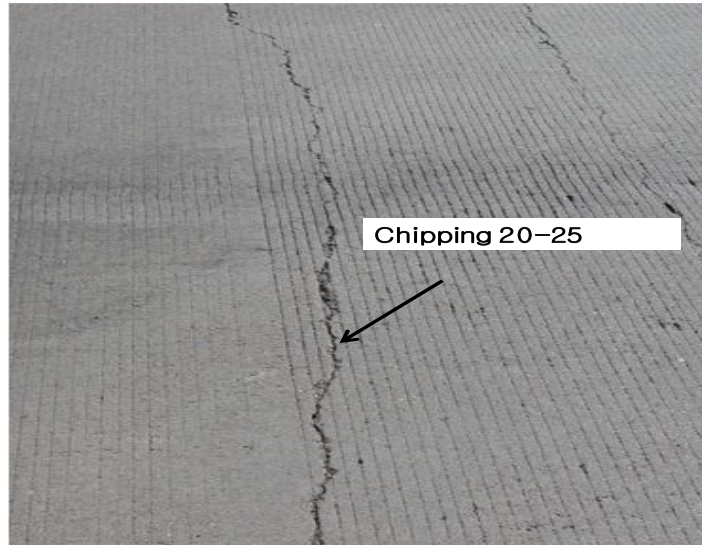


Figure 5.21 US- 290 Cypress, Mix 4 (100% gravel)

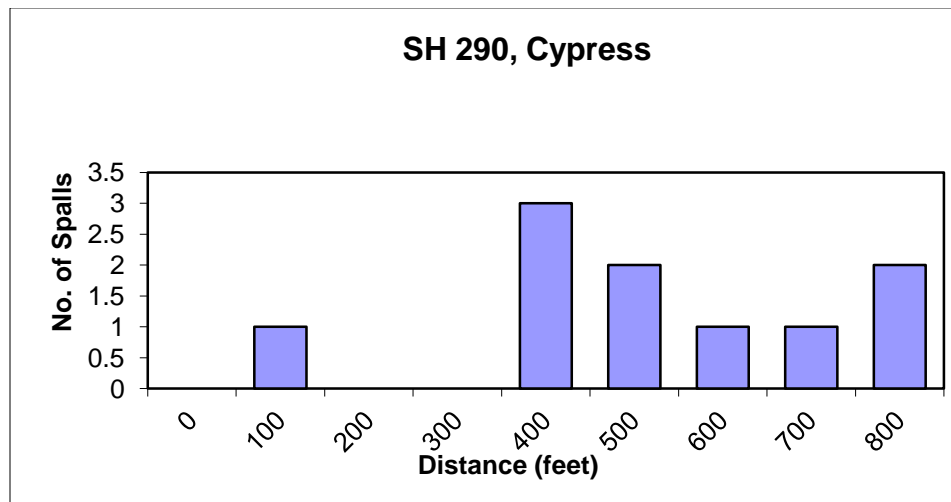


Figure 5.22 Distance vs. Incidence of Spalling

5.3.3 SH 99

A sample section of SH 99 was constructed in April of 1991. The results of the distress survey on a section of SH 99 are shown in Figure 5.23. Medium and high severity spalling were evident over the SH 99 sample section. Chipping was 60%, while the percentages of shallow spalling and spalling are respectively 10% and 7%. The amount of spalling distress is shown in Figure 5.23, and Figure 5.24. Figure 5. shows an example of it. The surface condition at this percentage of spalling may soon require maintenance over portions of the sample section.

Table 5.10 Sample Section Inventory at SH99

Features	Construction Date	Slab thickness	Gravel Source & Aggregate rating	Traffic (ADT)	PE
	April, 1991			10,504 (average)	0.08

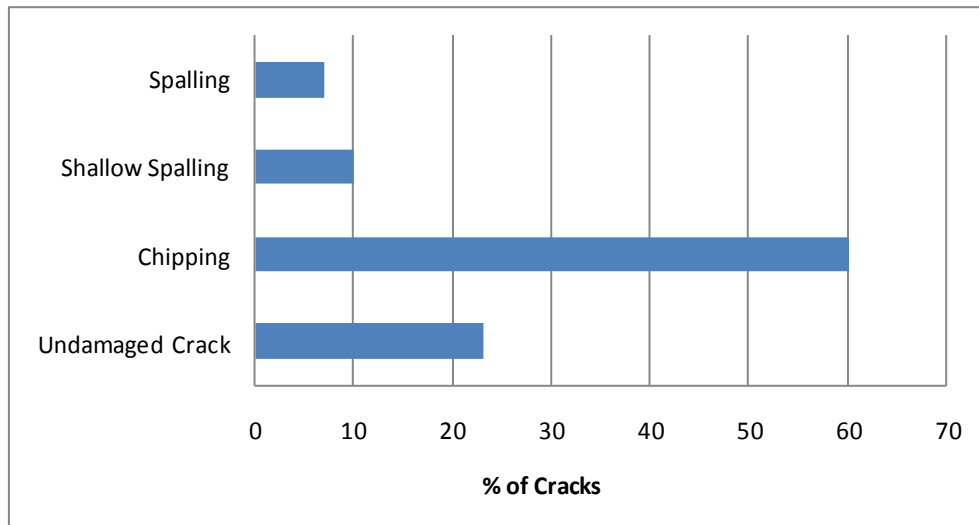


Figure 5.23 Percentage of Spalling Distress on SH 99



(a) Medium Spalling

(b) High Severity Spalling

Figure 5.24 SH99 Spalling Distress

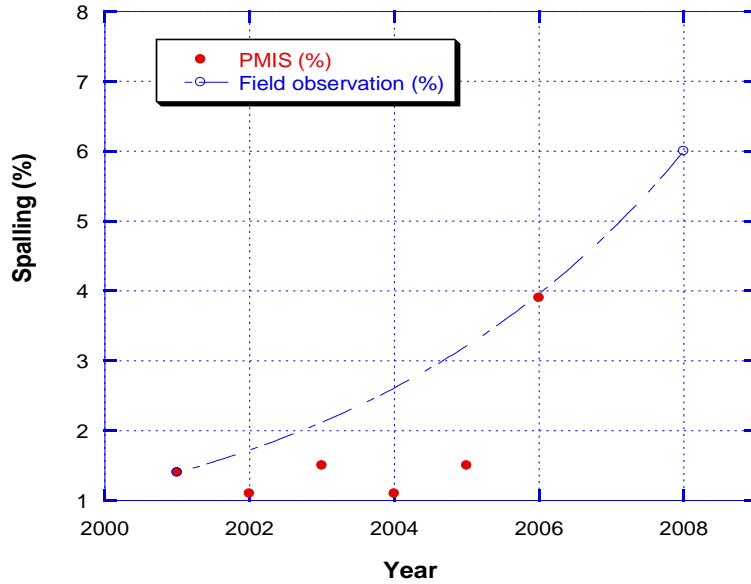


Figure 5.25 SH 99 PMIS Data vs. Field Observation with respect to Spalling (%)

PMIS and field data variation is due to the incidence of patching. In this project, spalling was rated without regard to whether it was patched. The PMIS data appears to agree with field observed data where this collected data may be useful for calibration purposes.

5.3.4 SH 225

Test sections (Figure 5.26) on SH 225 were constructed in November of 1991 using a combination of curing and transverse sawcutting to control the development of the crack patterns. Other detailed information is listed in Table 5.11 and Table 5.12. Since the section thickness was 13 inches, it contained two layers of steel. All the sections were surveyed to investigate the effect of curing methods and transverse saw-cutting on spalling performance. Three types of curing methods were used including standard curing, cotton mat curing, and polyethene sheet curing. Moreover, skewed transverse steel was included in the test section construction. Procrete, a commercial silica-polymerization compound, was used on one section to determine if it could effectively increase bonding between the aggregate and the concrete matrix so that resistance to spalling distress and cracking would be increased through chemical reaction.

Table 5.11 Sample Section Inventory at SH 225

Features	Construction Date	Slab thickness	Gravel Source & Agg rating	Traffic (ADT)	PE
Method of curing Method of crack control	Nov 11, 1991	13 in	Fordyce Victoria, Tx 4.5	40,020	0.02

Table 5.12 Weather Information during Construction Period

Weather information	SH-225
Avg. Temp.	56.8 (°F)
Avg. RH	66.04 (%)
Avg. SR	/
Avg. WS	3.13 (mph)

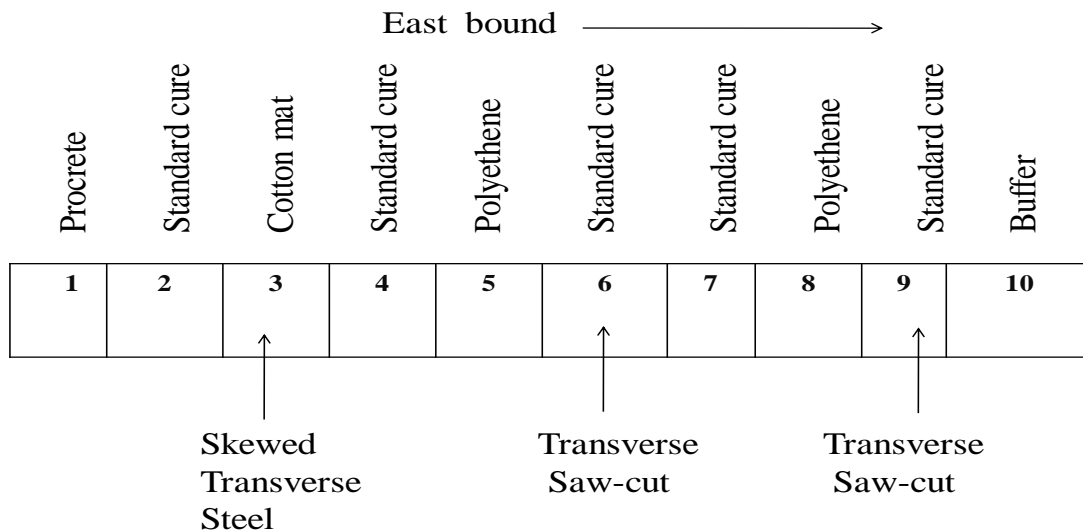


Figure 5.26 Layout of Test Sections of SH 225. (After Senadheera and Zollinger, 1995)

As noted, various curing methods were used on the SH 225 test sections. Chipping results from the pavement survey for each section are shown in Figure 5.27. Transverse saw-cutting was done in Section 6. Chipping performance may not be directly related to transverse sawcutting but it appears to be reduced to some extent. The use of cotton mat shows to have the best beneficial effect on chipping performance. Similar to other test sections, polyethylene sheet curing was effective against delamination but apparently did not show better performance than the other methods of curing in these sections.

Shallow spalling performance with respect to methods of curing is shown in Figure 5.28. Shallow spalling was not evident in the section cured with cotton mats. However, furthermore, shallow spalling in Section 3 (cured with cotton mats) was much

less than the average for these sections. Again, cotton mat curing appears to be effective in reducing spalling in comparison to other curing methods. Sections cured with polyethylene sheeting, on the whole, demonstrated average performance. The performance of sections cured with standard curing ranged from 2.0% to 7.5% and normally showed higher than average shallow spalling damage.

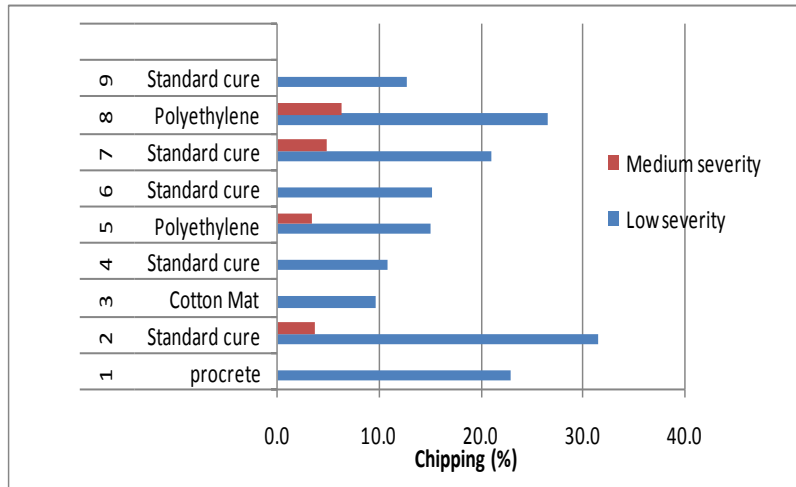


Figure 5.27 Percentage of Chipping on SH 225 with Respect to Curing Methods

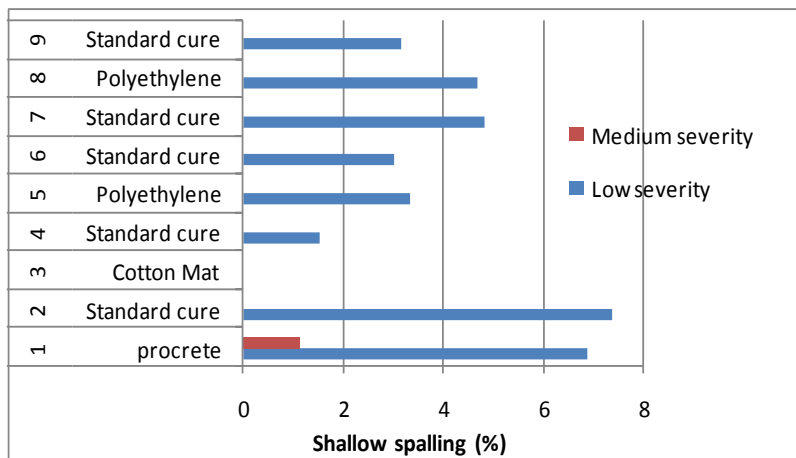


Figure 5.28 Method of Curing to Shallow Spalling

The average shallow spalling when transverse sawcutting was used is 3.1%, while sections without sawcutting had an average of 4.7%. Although sections without crack control (such as Section 4) showed good performance, overall performance was not particularly good. Standard deviation of sections without crack control and sections with crack control were 2.3 and 0.1, respectively (based on SH 225 surveyed data) indicating

the effectiveness of transverse saw cutting, which perhaps would improve with curing of the fresh face of the sawcut after placement, with an additional coat of curing compound.

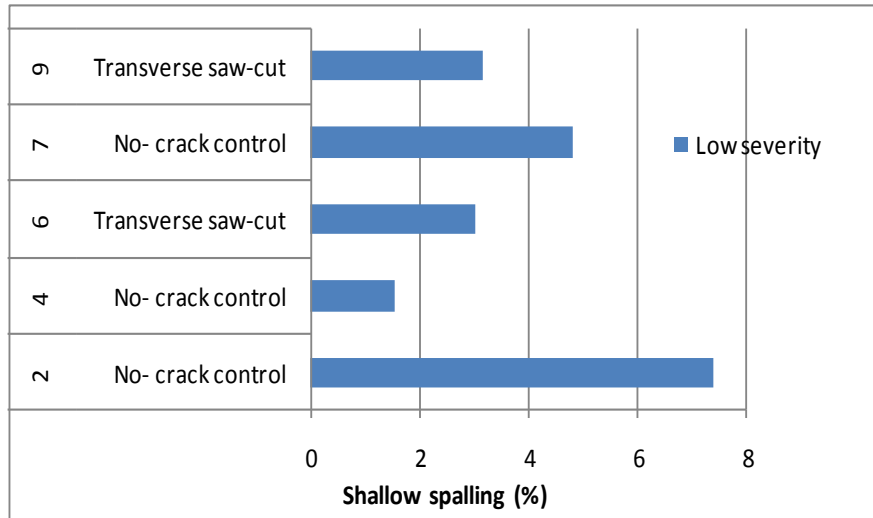


Figure 5.29 Effect of Method of Crack Control on Shallow Spalling

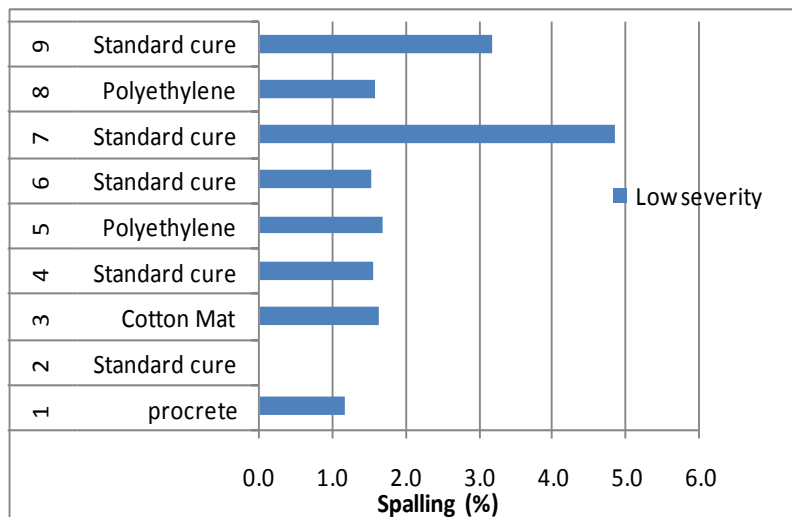


Figure 5.30 Effect of Method of Curing on Spalling

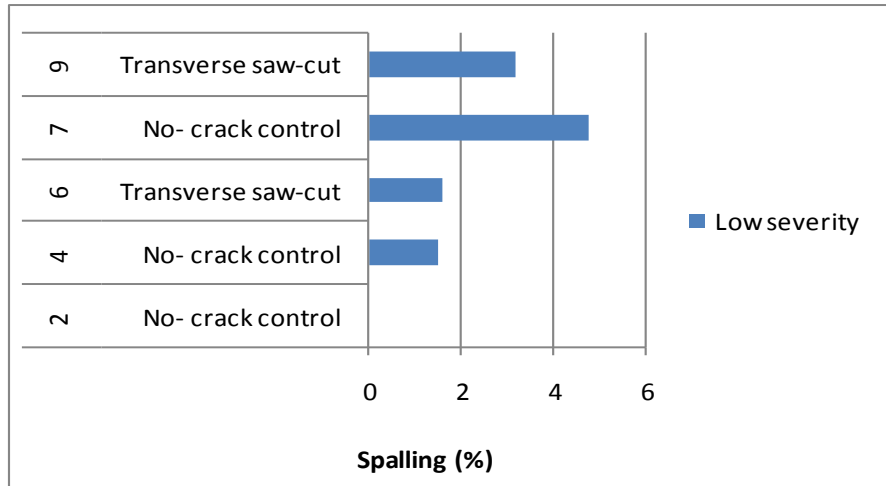


Figure 5.31 Effect of the Method of Crack Control in SH 225 Test Sections

The result of various methods of curing with respect to spalling is shown in Figure 5.31. In general, the percentage of spalling is less than 2.0 % excluding sections 7 and 9, which means that a very small amount of spalling occurred on these sections. Spalling was not found in Section 2, which had standard curing. Based on the results of the distress survey, the performance of Section 2 cannot be fully explained. However, the variation in performance among the sections placed with standard curing is typical of spalling behavior. The performance of polyethylene and cotton mat curing were 1.5 % spalling, while sections cured with standard curing were approximately 2.2%. Polyethylene and cotton mat curing seemed to reduce spalling in these sections to some degree.

Figure 5.33 shows a comparison of the effect of transverse sawcutting on spall distress. Although all the distress levels are relatively low, sawcutting appears to have a beneficial effect in limiting the extent of spalling. It can only be speculated that curing the exposed sawcuts with an additional coat of curing compound may improve the effectiveness of transverse cutting.

A number of patches, such as shown in Figure 5.32, have been placed in the SH 225 sample section presumably for spalling repair. Overall, cotton mat curing appeared to be the most effective in limiting any type of spall-related distress. The amount of spalling was somewhat differentiated between each method of curing except for the standard method of curing. The average spalling was 1.5% but was greater than 3.0 % in the sections cured with the standard method.



Figure 5.32 Medium Severity Spalling, SH 225

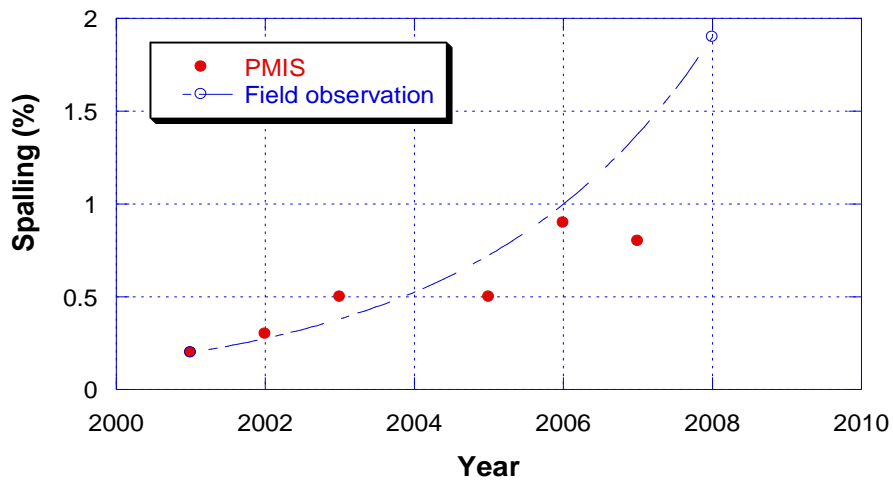


Figure 5.33 SH 225 PMIS Data vs Field Observation with respect to Spalling (%)

Figure 5.33Figure 5. shows the percentage of spalling based on the PMIS database, as well as the field observed distress levels, plotted on a year-by-year basis. The figure shows that low severity spalling is evident throughout the past years. The field observation data trends well with the PMIS data, which would pertain to the standard method of curing. As an upper limit, 3% again appears to be the level of distress before spall repair measures are implemented.

5.3.5 SH 288

The SH 288 test sections were paved 12 inches thick in November of 2005. This test section consisted of a variety of factors including the effect of curing, batching sequence, and type of secondary cementitious material (SCM) used in the concrete mixture. Other

pertinent information is shown in Table 5.13. The weather information during construction period is shown in Table 5.14. Different portions of this section were paved under different weather conditions, causing PE values to vary somewhat. The conditions were generally cold and windy – much different than the paving conditions during the placement of the SH 225 test sections, also placed in the month of November. A total of ten test sections were constructed with various curing methods such as high reflective curing compound (HRC), normal curing compound (NC), and wet mat (WC). In addition, the charging sequence was modified during mixing of the concrete for selected test sections. The type of cementitious materials (i.e. fly ash) was varied to evaluate the effect on spalling performance. Two types of SCM were used: ultra fine fly ash (UFFA) and Class F fly ash (see Table 5.15).

Table 5.13 Sample Section Inventory at SH 288

Features	Construction Date	Slab thickness	Gravel Source & Agg rating	Traffic (ADT)	PE
Method of curing, Method of batching Type of SCM	Nov 16 through 18 (paving), 2005	12 (inches)	Fordyce Victoria, TX 4.5	15,315	See T

Table 5.14 Weather Information during Construction Period

Climic Factors Test section	#7,2 (11/16/05)	#4,8,1,5 (11/17/05)	#10,6,9,3 (11/18/05)
Avg. Temp.	55.4 (°F)	48.2 (°F)	53.6 (°F)
Avg. RH	35 (%)	45 (%)	35 (%)
Avg. SR	0	0	0
Avg. WS	6.1 (mph)	1.9 (mph)	2.2 (mph)
PE	0.05	0.02	0.03

Table 5.15 Specific Information Used in SH 288 (Liu et al 2009)

Tests	Fly ash(%) (UFFA+Class F)	Curing	Charging Sequence
1	(10+15)	HRC	Normal
2	(10+15)	HRC	Modified
3	(10+15)	NC	Normal
4	(10+15)	NC	Modified
5	25 (Class F)	HRC	Normal
6	25	Wet Mat	Modified
7	25	NC	Normal
8	25	NC	Modified
9	(10+15)	Wet Mat	Normal
10	25	Wet Mat	Normal

Typically, UFFA is manufactured with a mean particle diameter ranging from 1 to 5 μm , whereas a Class F fly ash is produced in sizes ranges from 15 to 20 μm . Pozzolanic reaction is accelerated in the smaller particle size due to the greater surface area; a mixture containing UFFA should provide higher strength at an early age in comparison to the mixture containing straight Class F fly ash.

As seen in Figure 5.34, low severity chipping is fairly consistent across all the SH 288 test sections except for Section 2, where a higher percentage of medium chipping occurred. Nonetheless, Sections 3 and 4, 7 and 8, and 6 and 10 are useful to compare and evaluate the effect of charging sequence (the order the coarse aggregates were added to the mixing process.) Section 3 showed 5% higher low severity chipping than Section 4. Section 8 using a modified charging sequence showed a lower high severity chipping than Section 7 using a normal charging sequence. In the case of Sections 6 and 10, Section 6 using a modified charging sequence was 5% less than Section 10 with respect to medium severity spalling. Moreover, Section 6 showed 20% less low severity chipping. Sections utilizing the modified charging sequence showed better performance with respect to chipping distress than a normal charging sequence.

Comparing Section 1 with Section 5 in terms of the use of UFFA, Section 1 is 5% higher than Section 5 with respect to medium severity chipping; Section 1 is also 15% less than Section 5 with respect to low severity chipping. Sections 9 and 10 were placed under the

same conditions except for the use of UFFA. Section 9 showed lower chipping than Section 10 using only Class F fly ash. With respect to type of curing, Sections 5 and 6 provide a good comparison of performance between HRC and WC curing. The percentage of medium severity chipping is similar in each section while low severity spalling in Section 5 is 14% higher.

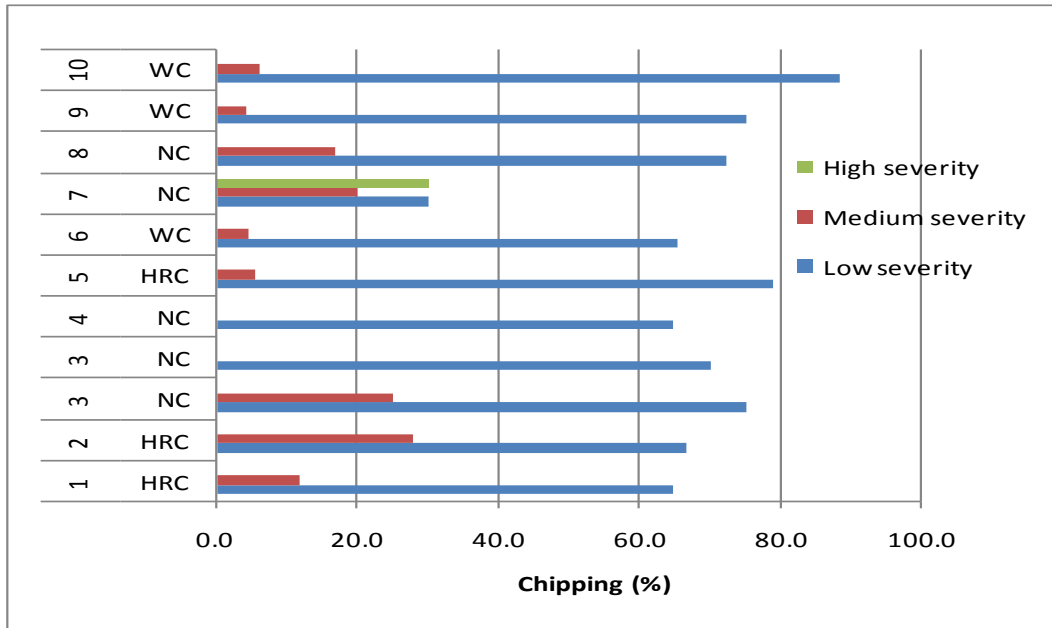


Figure 5.34 Chipping in SH 288 with Respect to Curing Methods

The effect of curing on performance is shown in Figure 5.35. Three groups using three types of curing compounds (NC, HRC, and WC) are compared across the relevant test sections. The first group comparing HRC and NC curing shows that standard curing was more effective but this conclusion may be confounded by other factors.

The second group comparing HRC and NC shows that the section cured using HRC has less shallow spalling than the section using NC. Shallow spalling was 4% less in the section cured using HRC than the section using NC.

The third group using WC or NC shows that the section cured using WC has 5.9% less shallow spalling than the section using NC. As a result, sections cured using HRC and WC showed better spalling distress performance, resulting in approximately 5% less shallow spalling except for the first group.

Sections 1 and 2 used different charging sequences but show similar levels of low severity spalling. Low severity spalling occurred in Sections 3 and 4 where these sections differed in charging sequence such that the section using modified charging sequence showed less spalling than Section 4 which used a normal charging sequence.

In almost every instance, the use of modified mixing resulted in less distress. Section 8, for instance, showed less low severity spalling than Section 7, which was placed using a normal charging sequence. Sections 6 and 10 were batched differently; Section 6 (using modified charging sequence) had 0% spalling, while Section 10 using normal charging sequence had 6% spalling (with wet mat curing). Even though there are some confounding features, it appears that modified charging can reduce the percentage of spalling over the normal charging sequence.

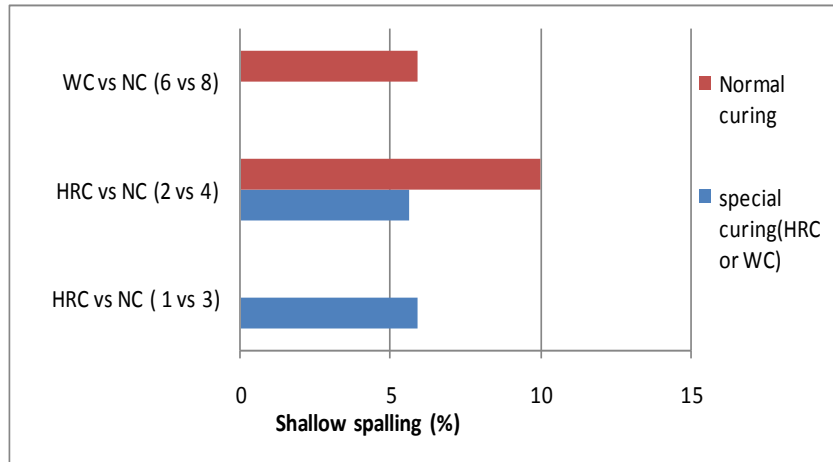


Figure 5.35 Method of Curing (HRC vs WC vs NC)

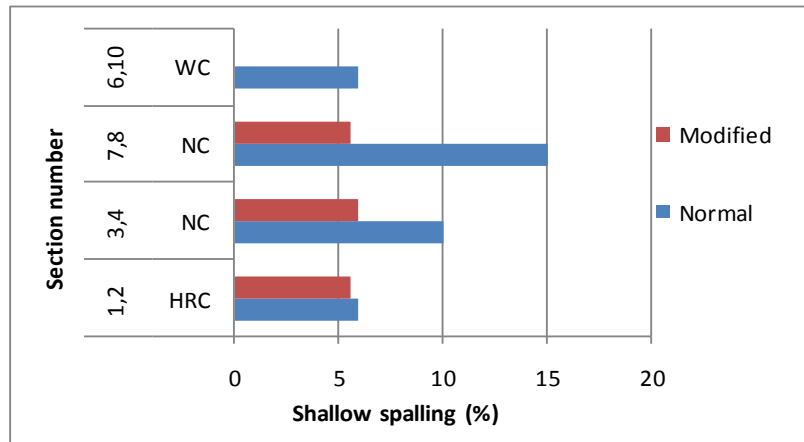


Figure 5.36 Method of Batching (Normal vs. Modified charging sequence)

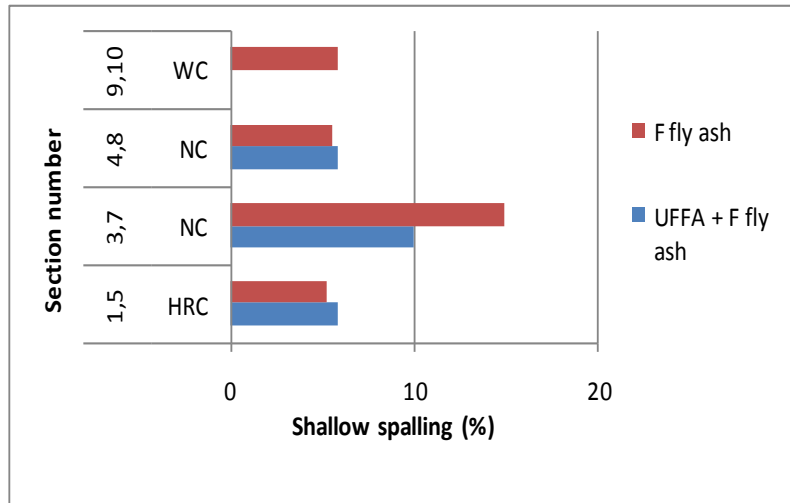


Figure 5.37 Type of SCM (F fly ash vs UFFA + F fly ash)

Sections using SCM were compared to each other with respect to the use of UFFA. The performance of two combinations of SCM is shown in Figure 5.37. One combination consisted of Class F fly ash while another consisted of a combination of UFFA and Class F fly ash. Sections 4 and 8 showed similar results with normal curing. Section 3 batched with mixed fly ash showed 5% less spalling than Section 7 batched with Class F fly ash. Section 9 batched with mixed fly ash showed less spalling than Section 10, which was batched with Class F fly ash. Among the four groups, the two former groups showed a difference between two different combination of fly ash, while the latter two groups showed that mixtures with UFFA and Class F fly ash facilitated a reduction of spalling.

With respect to the time of crack initiation, early cracking is thought to play a role in the propensity of a transverse crack to develop spalling damage. One benefit of sawcutting is that it reduces this effect by improving the uniformity of the formation of cracking. In the SH 288 test sections, crack initiation took place over a few days ranging from Day 3 to Day 7. Survey data indicated that 100% of the cracks that initiated within three days after paving developed either low severity chipping or medium severity chipping (see Figure 5.38). Moreover, cracks initiated from four to six days developed shallow spalling (see Figure 5.39). The earlier a crack initiates, the less the propensity it has to delaminate and spall. However, spalling seemed to also be associated with cracks forming at a later age and perhaps after creep strain has diminished sufficiently and drying shrinkage has had time to build up.

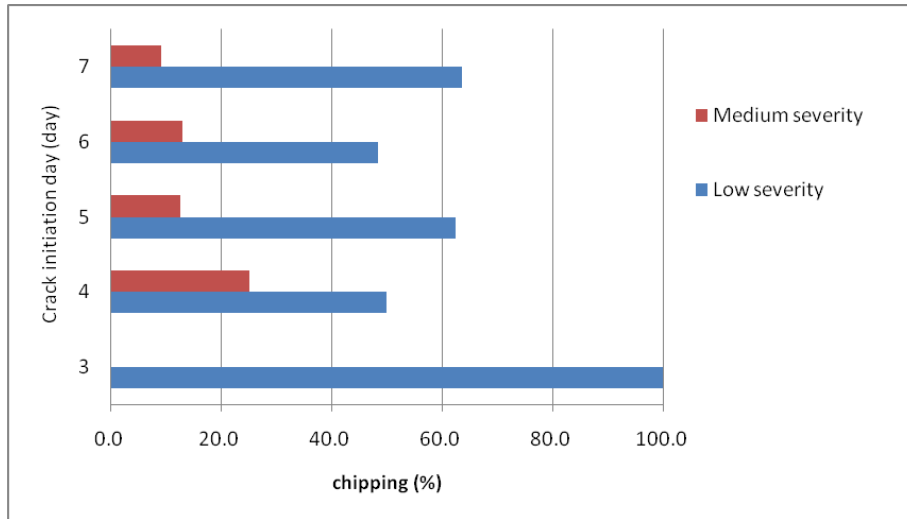


Figure 5.38 Crack Initiation Day vs % of Chipping in SH 288

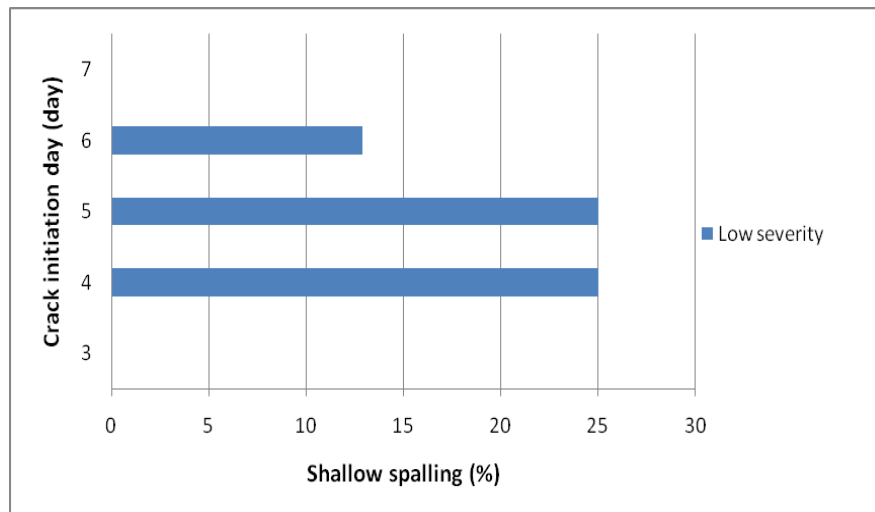


Figure 5.39 Crack Initiation Day vs % of Spalling in SH 288

5.3.6 FM 1960

FM 1960 was constructed in 1991 but little detailed information was available regarding associated dates and times of placements, as indicated in Table 5.16. A number of patches were evident due to severe spalling distress as shown in Figure 5.40. The percentage of chipping is approximately 50%. The percentage of shallow spalling and spalling are 30% and 20% respectively based on visual observation. The average of the number of spalls and standard deviation were 90.0 and 72.5 % respectively. Figure 5.42 indicates the variability of spalling distress along the sampled section.

Table 5.16 Sample Section Inventory at FM 1960

Features	Construction Date	Slab thickness	Gravel Source & Agg rating	Traffic (ADT)	PE
	1991	/	/	44,000	/



Figure 5.40 High Severity Spalling, FM 1960

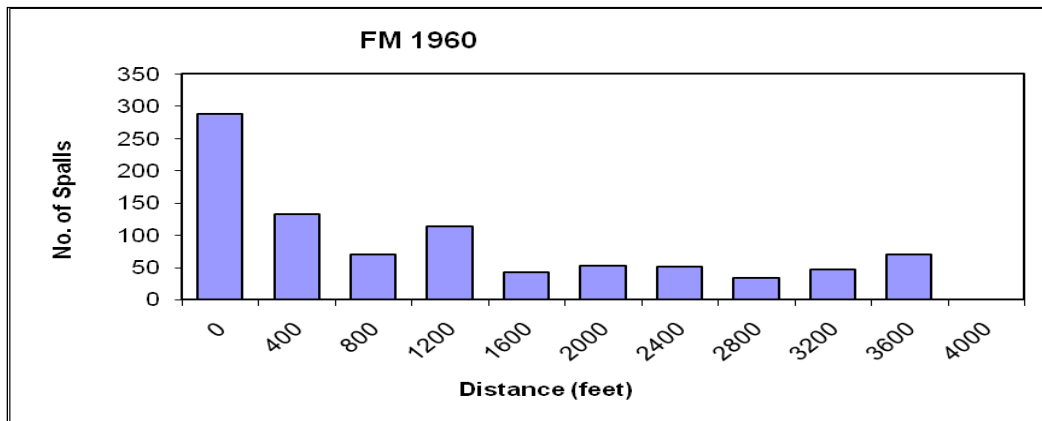


Figure 5.41 Spalling (%) vs Distance

5.4 Summary Observation from Field Survey

Table 5.17 summarizes the field performance of the entire list of sites included in this survey. Key factors or special construction methods such as curing compounds, batching sequence as well as PE and effectiveness are included in the table. Aggregate rating data are provided to consider their interaction between environmental condition and material properties on spalling performance.

The features of US 290-Hempstead are stated in Table 5.2. Methods of crack control and curing were analyzed as to their effect on the severity of spalled cracking. The PE value

ranges from 0.03 to 0.04, which is low considering the season that placement was carried out but the quality of curing and the evaporation rate were most likely less of a factor in these test sections.

Aggregate type and curing methods were evaluated from the US 290-Cypress field data. Aggregate types limestone, gravel, and blended aggregate were compared for their affect on chipping or spalling. The percentage of chipping decreased with an increase in the use of limestone aggregate. Curing compound in combination with polyethylene sheeting was determined to be the most effective curing method among the methods used.

Similarly, methods of curing and crack control were investigated at SH 255. Two effective curing methods such as cotton mat and polyethylene sheeting were employed in reducing the severity of spalled cracking. Aggregate rating was comparably lower than the other sites investigated.

Various construction methods such as different curing compounds, fly ash contents and type, and charging sequence were evaluated in terms of their affect on spalling. Wet mat curing compound and high reflective curing compound were effective in decreasing the severity of spalled cracking. Moreover, charging sequence and fly ash type were effective in reducing spalled cracking as well.

It is evident that a critical combination of curing quality and prevailing weather conditions create a threshold above which spall damage of all categories can be significantly reduced. A means to assess this critical combination is described later in this report.

Table 5.17 Summaries of Findings in All Surveyed Sites

Number	Site	Factor	Effectiveness
1	US 290- Hempstead	Transverse cuts	Reduced severity
		Skewed steel	3 % reduction of shallow spalling
		Polyethylene sheet curing	Most effective curing with respect to spalling
		PE	0.04, 0.03
		Aggregate rating	6.1
2	US 290- Cypress	Limestone	Less chipping than gravel (15% reduction of chipping)
		Polyethylene sheet curing	Most effective curing
		PE	0.02
		Aggregate rating	6.1
3	SH 99	N/A	N/A
4	SH 225	Cotton Mat curing	the most effective curing
		Polyethylene sheet curing	Normally effective but does not show good performance.
		Saw cutting	A beneficial effect
		PE	0.02
		Aggregate rating	4.5
5	SH 288	Wet mat curing	10 % reduction of shallow spalling (the most effective)
		High reflective curing compound	Similar to normal curing but it needs more data to validate the performance
		Ultra fine fly ash	2% of shallow spalling less than F fly ash

Number	Site	Factor	Effectiveness
		Modified charge sequence	50% reduction of shallow spalling compared with normal charge sequence
		PE	0.05, 0.02, 0.03
		Aggregate rating	4.5
6	FM 1960	N/A	N/A

CHAPTER 6 MODELING SPALLING PERFORMANCE

During hydration, concrete tends to change in strength and in volume with a gain or a loss in moisture or temperature. Immediately after placement, the concrete may undergo a certain amount of shrinkage as a result of water loss by evaporation from the surface of the pavement. This shrinkage tends to inducing tensile strain at the surface of concrete, and also contributes to the overall contraction of the slab that contributes to the generation of the characteristic cracking pattern of the CRC pavement. However, sharp shrinkage gradients may create sufficient shear stress to delaminate the concrete immediately below the pavement surface.

Concrete exposed to the natural environment typically undergoes a certain amount of drying shrinkage which is comprised of both reversible and non-reversible components. Drying shrinkage in concrete is affected by ambient relative humidity, aggregate content, volume to exposed surface ratio, and water to cement ratio of the concrete mixture. In the opinion of the authors, approximately 15 to 20 % of the ultimate shrinkage takes place within the first two to three weeks for concrete exposed to ambient conditions. However, these percentages may be low for surface concrete manifesting delamination.

6.1 Delamination Modeling

Shear stress (or delamination stress) can be determined based on slab curling and warping behavior under the effect of drying shrinkage and temperature change. Slab warping (mainly driven by differential drying shrinkage) can occur in two stages as denoted by Tang et al (1993) and delineated by separation of the slab corner from the subbase (i.e. liftoff) versus where the slab remains in contact with the subbase (i.e. zero liftoff). A set of functions developed in this respect was formulated assuming the following model form (Tang et al, 1993):

$$w = \frac{(A_1 \cos x + A_2 \sin x)(B_1 \cos y \cosh y + B_2 \sin y \sinh y)}{e^x} \quad (6.1)$$

where, w : Edge gap (inch)

$$y = \frac{Y}{l}$$

$$x = \frac{X}{l}$$

Y = distance from slab corner perpendicular to the corner diagonal

X = distance from slab corner along corner diagonal

A_i, B_i = function coefficients

l = Radius of relative stiffness (inch)

Medium-thick plate theory provides the basis for several boundary conditions that were considered in the development of the coefficient equations summarized in Table 6.1. Two sets of solutions of the coefficient equations were developed depending on whether the bottom of the slab was in contact with the subgrade or base support. A non-contact condition is referred to in this report as lift-off, and a contact condition is referred to as zero lift-off condition. The coordinate system adopted for the corner curling and warping model are shown in Figure 6.1. Several parameters listed above and their definitions are explained in Table 6.1. Since some of the coefficients are not independent of one another, evaluation of them is best accomplished using an appropriate numerical method to interactively calculate the coefficients. Curling and warping curvature within the x - y plane was modeled by deriving the curling and warping deformation model with respect to x and y (Eq. 6.1)

The coefficients substituted into the curling and warping curvature model can be used to determine the twisting moment (M_{xy}) and the shear or delamination stress (τ_{xy}) derived from plate theory as:

$$M_{xy} = -D(1-\nu)w_{,xy} \quad (6.2)$$

$$\tau_{xy} = \frac{E_c z}{1+\nu} w_{,xy} \quad (6.3)$$

$$w_{,xy} = \frac{[\cos x(A_2 - A_1) - \sin x(A_2 + A_1)][(B_2 - B_1) \sin y \cosh y + (B_2 + B_1) \cos y \sinh y]}{e^x \ell^2} \quad (6.2)$$

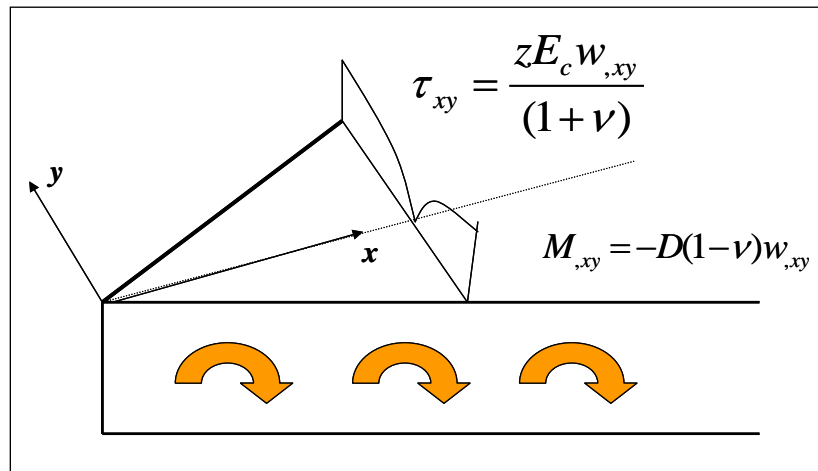


Figure 6.1 Coordination of Corner Curling and Warping Deformation Model (Wang and Zollinger 2000)

Table 6.1 Corner Curling and Warping Curvature Coefficients

$w_{,xy} = \frac{[\cos x(A_2 - A_1) - \sin x(A_2 + A_1)][(B_2 - B_1) \sin y \cosh y + (B_2 + B_1) \cos y \sinh y]}{e^x \ell^2}$	
Zero Liftoff Case	Liftoff Case ($0 > x \leq s$)
$A_1 = T_R A_2$	$A_1 = T_R A_2$
$A_2 = \frac{w_0}{B_1 - \nu B_2 T_R}$	$A_2 = \frac{e^s \left(w_0 - \frac{w_c s^3}{3\ell^2} \right)}{\nu B_2 \sin s + B_1 \cos s - T_R (B_1 \sin s + \nu B_2 \cos s)}$
$B_1 = 1$	$B_1 = 1$
$B_2 = B_1 \frac{T_R + 1}{T_R - 1}$	$B_2 = \frac{\frac{w_c x^2 e^x}{2A_2} - B_1 [C_2 + T_R C_1]}{C_1 - T_R C_2}$
<p>Note:</p> <p>(1) $T_R = \frac{1 + \tan \frac{w}{2\ell}}{1 - \tan \frac{w}{2\ell}}$</p> <p>(2) $w_0 = A_0(1 + \nu)\ell^2$; $A_0 = \frac{\varepsilon}{h}$; $\varepsilon = \alpha \Delta T_{eq} + \varepsilon_\infty \Delta(1 - H^3)_{eq}$; $w_c = -\frac{\rho h}{k}$</p> <p>(3) $C_1 = \cos s - \sin s$</p> <p>(4) $C_2 = \cos s + \sin s$</p> <p>(5) $s = \frac{S}{\ell}$; S = length of liftoff along the corner diagonal</p> $= -\ln \left[\frac{w_c}{B_1 A_2 (T_R \cos s + \sin s)} \right] \ell$	

where, $D =$ flexural rigidity of the slab $= \frac{Eh^3}{12(1-\nu^2)}$

$E_c =$ concrete modulus of elasticity

$z =$ distance from the middle surface of the slab

$\nu =$ Poisson's ratio

6.2 Sensitivity of Moisture on Delamination Stress

The sensitivity of delamination stress to moisture profiles was examined by fixing other parameters to typical levels. However, temperature-related parameters (temperature difference and coefficient of thermal expansion) were excluded in the analysis to examine the net moisture effect on the delamination stress development. The types of parameters are listed in Table 6. 2 while the values of the parameters used in the sensitivity study are summarized in Table 6.3. The delamination stress is affected by moisture profiles in the concrete as shown in Figure 6.2-(a). The delamination stress increases with increase of the equivalent linear humidity difference coefficient ($\Delta(1-H^3)_{eq}$) (Vepakomma et al. 2002). Because a larger humidity difference coefficient is calculated by larger changes in concrete moisture profiles, the potential for delamination will be greater. The maximum equivalent linear humidity difference coefficient for a 10-inch slab was assumed to be 0.4 based on typical test results obtained by Jeong and Zollinger (2002).

A larger maximum value may result under more severe curing conditions. Sensitivity of temperature difference on the delamination stress was also examined as shown in Figure 6.2 (b) and compared to its sensitivity to moisture difference. Generally, the maximum temperature gradient has been assumed to be about 3 °F/inch during the daytime and about 1 °F/inch at night. Thus, the largest equivalent linear temperature difference for a 10-inch thick pavement was assumed to be 30 °F.

Table 6.2 Key Parameters of Corner Curling and Warping Coefficient Equations

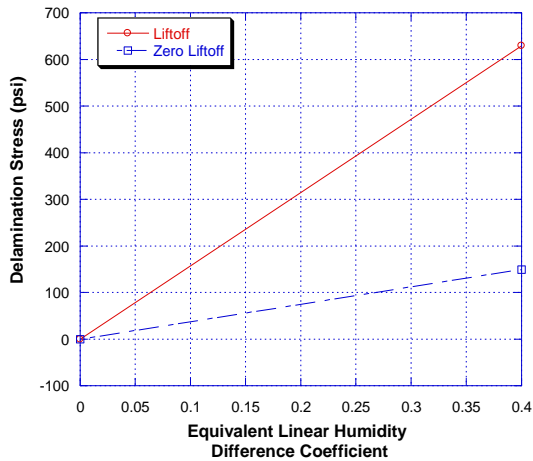
Parameters	Symbols
Ultimate Concrete Shrinkage (micro strain)	ϵ_{∞}
Concrete Humidity (%)	H
Coefficient of Thermal Expansion (micro strains/ °F)	α_T
Concrete Temperature (°F)	T
Slab Thickness (inch)	h
Slab Width (ft)	W
Concrete Poisson Ratio	ν
Radius of Relative Stiffness (inch)	ℓ
Dimensionless Length of Liftoff	s
Edge Gap (inch)	w_0

Table 6.3 Typical Values of Parameters of Delamination Model

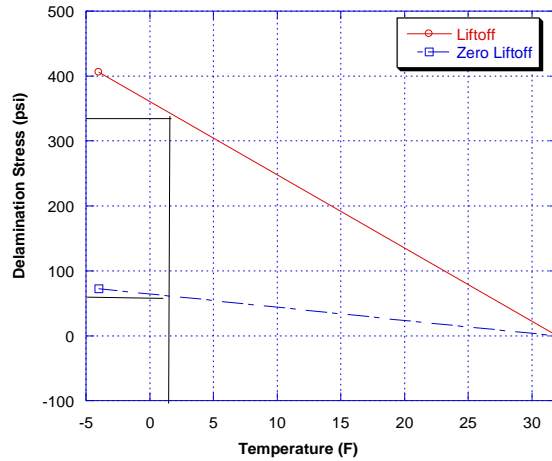
Parameters	Values
Ultimate Concrete Shrinkage (ϵ_{cs})	800 micro strains
Equivalent Linear Humidity Difference Coefficient ($\epsilon(1-H^3)_{eq}$)	0.2
Coefficient of Thermal Expansion (α_T)	5.6 micro strins/°F
Equivalent Linear Temperature Difference (ΔT_{eq})	- 14.4 °F
Slab Thickness (h)	10 inch
Slab Width (W)	12 ft
Concrete Elastic Modulus (E_c)	3000 ksi
Concrete Poisson Ratio (ν)	0.15
Modulus of Subgrade Reaction (k)	100 psi/in
Delamination Depth ($h/2-z$)	1 inch

As compared in Figure 6.2, the moisture effect on the delamination stress development is much larger than the temperature effect. Ultimate drying shrinkage of concrete and coefficient of thermal expansion (CTE) have a significant effect on the delamination stress as shown in Figure 6.2-(c) and (d), although the effects were smaller than those due do moisture effects. The minimum and maximum ultimate shrinkage strain and CTE values were assumed to be 400 and 1200 micro strains, and 6 and 14 micro strains, respectively. Slab widths, subgrade reaction modulus, depth of delamination, and slab thickness also affect the magnitude of delamination stress.

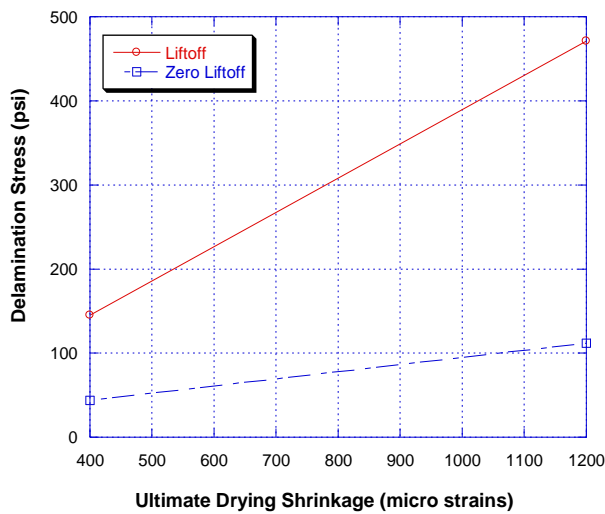
The probability of delamination can be determined as a function of the factors that affect strength and delamination stress. Delamination is governed by shear stress, evaporation potential, and the amount of curing and warping. Both the strength and the stress are a function of the quality of curing. As the quality improves, the stress goes down and the strength up. In the deeper process, if delamination occurs, spalling is assessed.



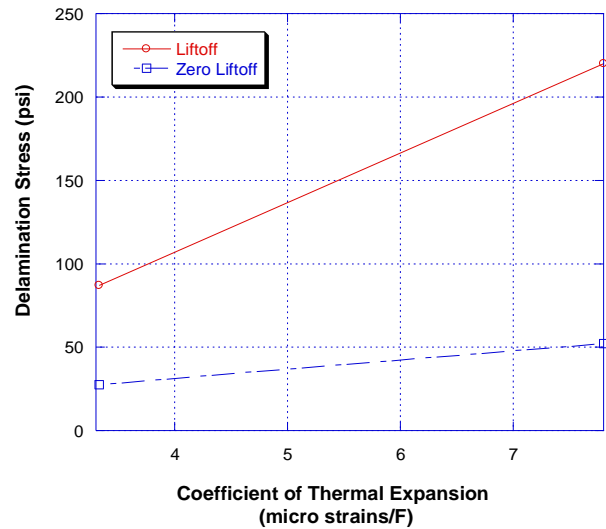
(a) Humidity Difference



(b) Temperature Difference



(c) Ultimate Shrinkage



(d) Thermal Expansion

Figure 6.2 Sensitivity Study for Delamination Stress

Strength factors are those related to the degree of hydration and the amount of moisture available for hydration which can be an issue for near surface concrete. When the relative humidity of concrete drops to 80% or below, hydration nearly ceases. The characteristics of the coarse aggregate and its propensity to attract moisture to its surface is sometimes a factor in delamination and in the capability of the aggregate to bond to the cement paste. Physical properties of aggregate such as absorption, angularity, texture, and percent flat particles are useful geometric properties in which to rate the aggregate relative to its capability to form a strong bond to the paste; this is depicted by the aggregate rating scheme described in Appendix C. The percentage of quartzite is, however, the most significant aggregate factor in terms of chemical properties affecting bonding.

6.3 Concrete Strength Related to Delamination

Clearly, the most prevalent strength associated with delamination is shear strength and its assessment should be a function of the degree of hydration experienced by the surface concrete. The degree of hydration is directly affected by the quality of the curing as elaborated in the research under Project 0-5106 “Evaluation of Curing Membranes Effectiveness to Reduce Evaporation.” Figure 6.3 illustrates the relationship between the rate of application of a curing compound to the potential for evaporation, the degree of hydration of the surface concrete, and the quality of the curing compound. For a given quality of curing compound (as dictated by the evaluation index (EI)) and the rate of application, the degree of hydration can be assessed depending on the prevailing evaporative conditions as depicted in Figure 6.3. Potential evaporation (PE) is a function of the ambient weather conditions, which depend upon ambient temperature, wind speed, relative humidity, as well as the temperature of the fresh concrete when it is placed.

The relationship between strength and the degree of hydration is often facilitated by the use of the maturity method, which is commonly assumed to be only a function of the concrete temperature conditions but can also account for the effect of moisture on strength and the resultant effect on delamination potential with a slight modification. Freiesleben Hansen and Pedersen developed a maturity function for equivalent age shown in Eq. (6.5) that can be modified to account for moisture conditions (Carino, 1991).

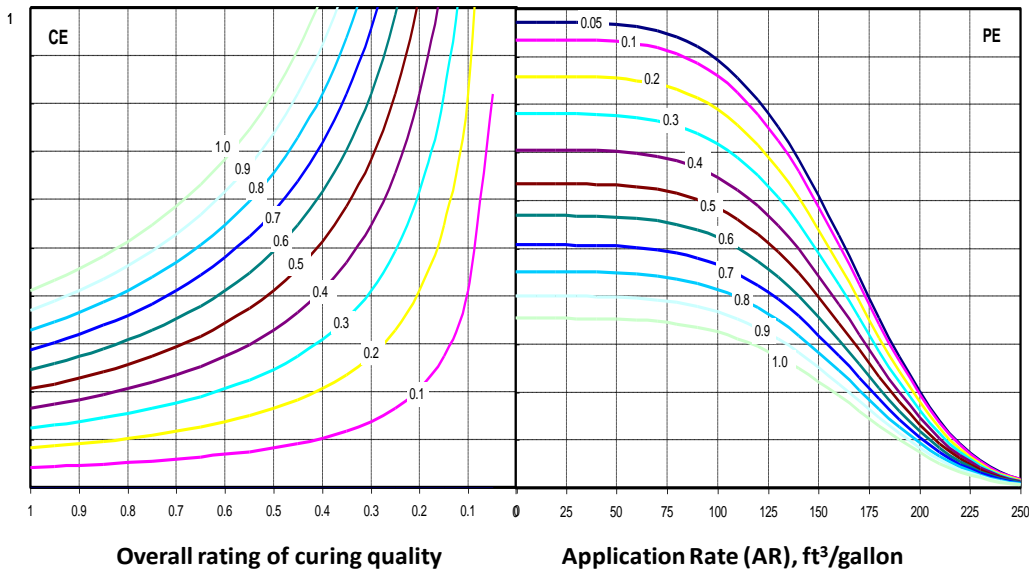


Figure 6.3 Curing Quality Relationship.(Ye et al 2008)

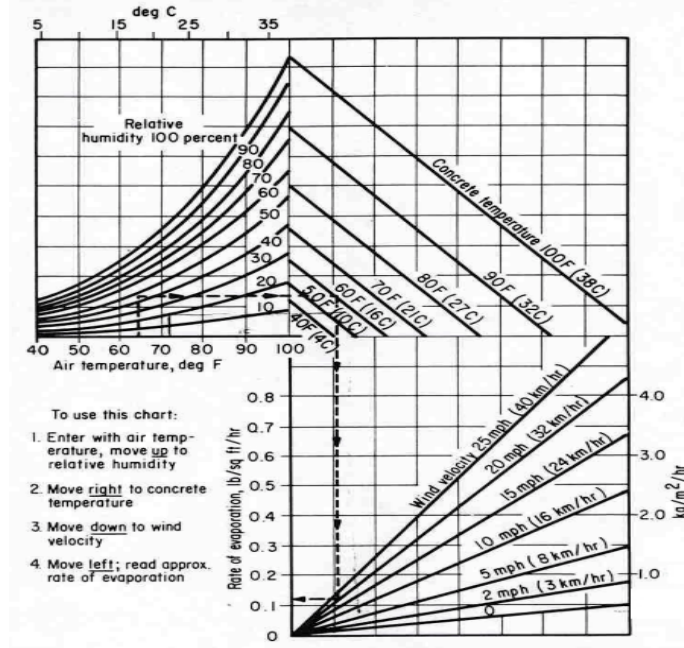


Figure 6.4 Evaporation Rate Nomograph for ACI (ACI Committee 308)

$$t_e = \sum_0^t \exp \left[\frac{E}{R} \left(\frac{1}{273 + T_r} - \frac{1}{273 + T_c} \right) \right] \cdot \Delta t \quad (6.4)$$

where, t_e = maturity in terms of equivalent age (h)

E = activation energy (J/mol)

R = universal gas constant (8.3144 J/mol /K)

T_r = reference temperature

T_c = the average concrete temperature

Modifying the above expression for moisture effects reformulates the expression by using the β parameter as:

$$M'_H = \beta'_H \cdot \sum_0^t (T - T_0) \cdot \Delta t = \frac{\sum_0^t (T - T_0) \cdot \Delta t}{1 + (5 - 5H)} \quad (6.5)$$

A relationship between strength and maturity has been suggested (Carino, 1991) which can be readily associated with the degree of hydration (α) in terms of shear stress (τ):

$$\frac{\tau}{\tau_u} = \alpha_{hyd} = e^{-\left(\frac{\beta}{t_e}\right)^\alpha} \quad (6.6)$$

where, τ = shear strength at age t_e (psi)

- τ_u = ultimate shear strength (psi)
- a = shape constant
- β = time constant
- t_e = equivalent age (time)

The shear strength can be found in terms of α_{hyd} (or CE) as :

$$\tau = \alpha_{hyd} \tau_u \tag{6.7}$$

where α is a function of the potential evaporation (PE). τ_u can be approximately determined from the relationship between shear stress and unconfined strength (f_c'') as :

$$\tau_u = \frac{f_c''}{2} \tag{6.8}$$

where, f_c'' = ultimate unconfined strength (psi)

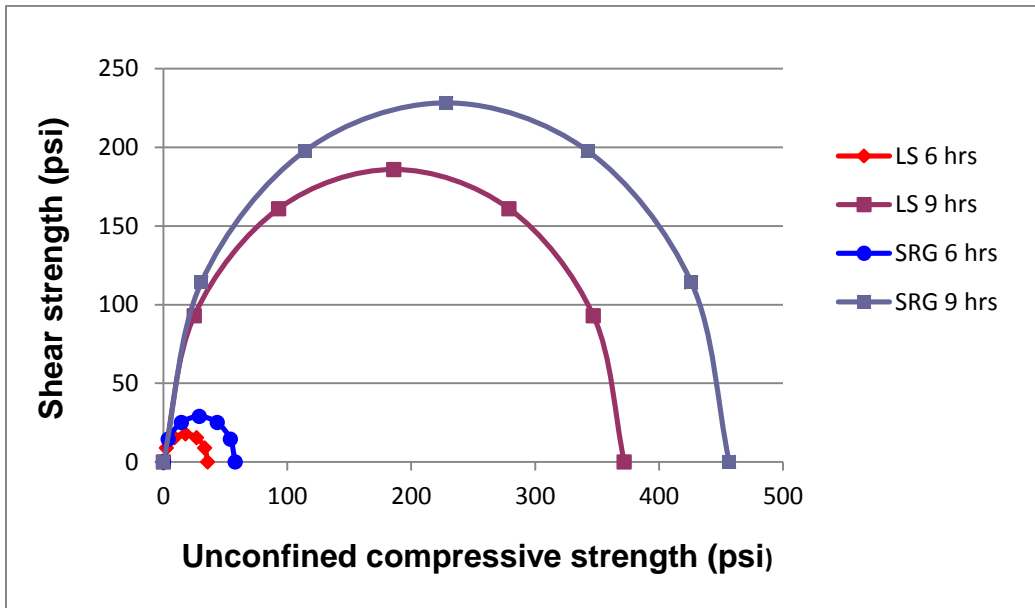


Figure 6.5 Laboratory Shear Strength at 6 and 9 hours

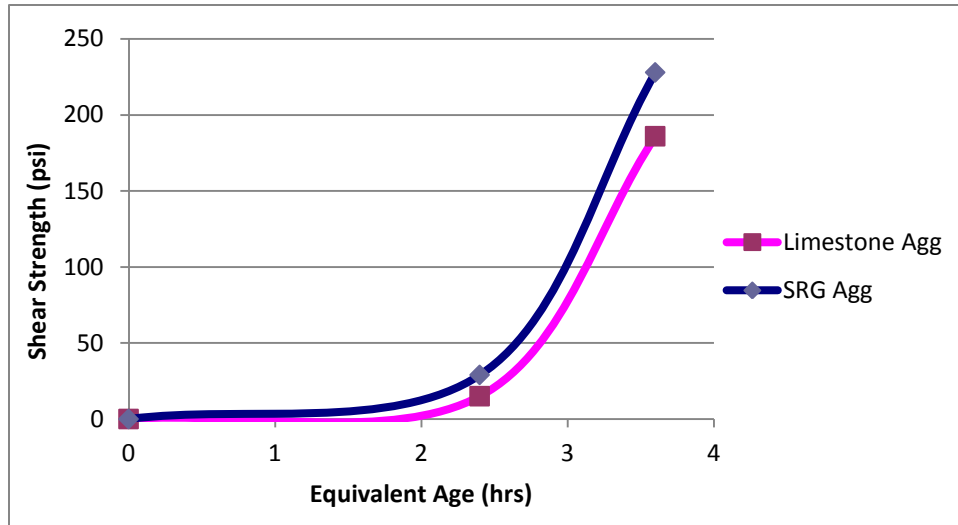


Figure 6.6 Shear Strength vs Equivalent Age (hours)

Early age strength of the interfacial bond governs the potential for delamination. Since shear strength depends upon the characteristics of the coarse rock, shear strength of two coarse aggregate types is plotted as a function of equivalent age in Figure 6.5. and 6.6. Compressive strength at an early age (under high deformation) was based on cylindrical samples that were batched with either limestone or siliceous river gravel. τ_u of limestone and siliceous river gravel concrete at nine hours of age were found to be 225 and 190 (psi) from Figure 6.5 and Figure 6.6, respectively.

In Figure 6.6, τ_u of both strengths with respect to aggregate type are shown in terms of equivalent age. Using the maturity approach, the sensitivity of shear strength to environmental effects can be assessed for design purposes. Furthermore, if the delamination-related shear stress and its inherent variability can be defined, it is possible to describe the potential for delamination in terms of probability.

6.4 Delamination Prediction

The projection of spalling can be made in terms of the potential or probability for spalling to occur along a transverse crack. Spalling is not expected to occur without the presence of delamination, so the probability of delamination should be determined to assess the possible number of spalled cracks that may occur based on the relation between concrete shear stress and strength under a specific set of site conditions. Specifically, the degree that the concrete shear stress surpasses the concrete shear strength govern the degree that delamination can initiate. The probability that concrete shear stress exceeds in shear strength was expressed as:

$$\text{Prob}(\tau_{xy} - \tau_0 > 0) \tag{6.9}$$

where, τ_{xy} = shear stress (delamination stress)

$$\begin{aligned} \tau_0 &= \text{shear strength (} \tau_0 \sim \frac{f_t}{2} \sim \frac{1}{4} \cdot MoR \sim \frac{1}{20} f_c \text{ ;} \\ f_t &= \text{tensile strength, } MoR : \text{ modulus of rupture,} \\ f_c &= \text{compressive strength} \end{aligned}$$

τ_0 is often determined from other strength properties of concrete. In this project, the shear strength was derived from compressive strength one day after placement (Liu et al 2009). In addition, τ_{xy} is determined from Eq. (6.3) where τ_{xy} is induced based on slab curing and warping behavior under prevailing climatic conditions and shrinkage. τ_{xy} is found from the gain or loss in moisture or temperature under the climatic conditions of each test section.

The mean of the population of stress can be found from Eq. (6.3) and Table 6.1 The standard deviation of stress ($\sigma_{\tau_{xy}}$) which describes the dispersion of τ_{xy} can be determined with respect to three variables (X_i) such as the modulus of elasticity E_c , the parameter A_0 (listed in Table 6.4) and the radius of relative stiffness (ℓ) as factors that govern the variability of the shear stress. The use of $\sigma_{\tau_{xy}}$ allows for the definition of the possible range of the shear stress; combining with the variance of the shear strength, it is possible to determine the area under the curve shown in Figure 6.7, which is the normal distribution of the differences of means that contains the value of zero. Specifically, the probability is based on the difference of means of two populations of shear strength and stress which have a standard deviation made up from the variances of the two populations. The equation of this curve gives:

$$f(x: \bar{X}, \sigma) = \frac{1}{\sqrt{2\pi}\sigma} \exp \left[-\frac{(x - \bar{X})^2}{2\sigma^2} \right], \quad -\infty < \bar{X} < \infty, \quad \sigma > 0 \quad (6.10)$$

where, \bar{X} = mean value
 σ = standard deviation

Since the frequency distribution of the differences of means (shown in Figure 6.7) contains the value of zero, the area under the frequency curve beyond zero represents the probability of delamination.

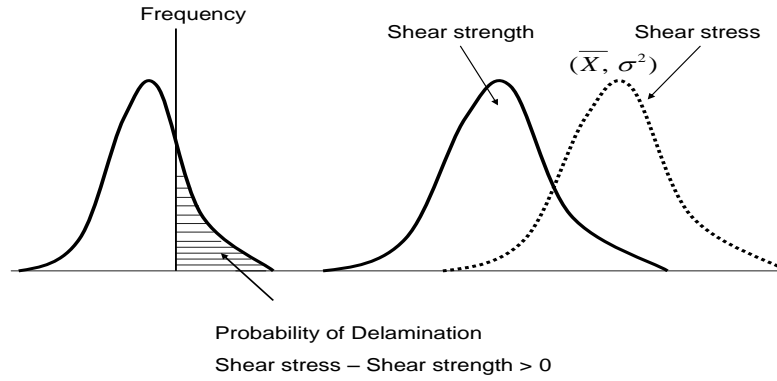


Figure 6.7 Determination of Probability of Delamination

$\sigma_{\tau_{xy}}$ can be expressed with use of the X_i variables as

$$\left(\sigma_{\tau_{xy}}\right)^2 = \left(\frac{\partial \tau_{xy}}{\partial X_i}\right)^2 \text{Var}(X_i) \quad (6.11)$$

where, $X_i = E_c, \ell$, and A_0

$\text{Cov}\{X_i\}$ can be used to determine the variance in Eq. 6.11; the COVs are approximated as $\text{Cov}\{E_c\} = 0.15$, $\text{Cov}\{A_0\} = 0.25$, and $\text{Cov}\{\ell\} = 0.20$. Shear stress, standard deviation, and the percentage of probability were computed for each site. To determine the shear stress, equivalent total strain differences were determined as noted in Table 6. Table 6.10 Equivalent total strain difference between pavement surface and bottom can be determined from four parameters such as coefficient of thermal expansion (α_{CTE}), equivalent linear temperature difference (ΔT_{eq}), ultimate shrinkage (ε_{∞}), and the equivalent linear humidity difference coefficient ($\Delta(1 - RH^3)_{eq}$).

Temperature and moisture gradients were determined using transport theory. With respect to temperature and heat transport:

$$\frac{\partial}{\partial x} \left(k \frac{\partial T}{\partial x} \right) + Q_h(t, T) = \rho c_p \frac{\partial T}{\partial t} \quad (6.12)$$

where, T = temperature in concrete pavement ($^{\circ}\text{C}$),

t = time (hrs),

x = depth and longitudinal coordinates in concrete pavement (m),

k = thermal conductivities of concrete ($\text{W}/\text{m}/^{\circ}\text{C}$),

ρ = concrete density (kg/m^3),

c_p = specific heat ($\text{J}/\text{kg}/^{\circ}\text{C}$), and

$Q_H =$ generated heat from heat of hydration of cement and external sources(W/m^3).

Diffusivity is important in modeling moisture flow in hardening concrete. At a constant water content (w), diffusivity changes little with time in hardened concrete though it changes greatly during the first 24 hours after placement of concrete. Diffusivity has been found to be a function of humidity, age of concrete, and porosity of cement paste. The rate of moisture flow through concrete can be expressed by the velocity of flow (J) representing the mass of evaporable water passing through a unit area perpendicular to the direction of flow per unit time. The governing equation of moisture diffusion is derived from Darcy's law by introducing moisture isotherm concept, hygrothermic coefficient (K), and humidity at self-desiccation of a sealed sample (h_s) as:

$$\frac{\partial h}{\partial t} = D \frac{\partial^2 h}{\partial x^2} + \frac{\partial h_s}{\partial t} + K \frac{\partial T}{\partial t} \quad (6.13)$$

where, D is diffusivity (L^2/t), dh_s is change in relative humidity due to hydration at a constant water content and time, and K is the hygrothermic coefficient representing the change in relative humidity due to a one degree change in temperature.

These models were utilized to determine not only the equivalent linear humidity difference coefficient but also the equivalent linear temperature difference. In addition, the coefficient of thermal expansion with respect to aggregate source and ultimate shrinkage was incorporated in the detailed calculations elaborated in Appendix D. Accordingly, the number of cracks that delaminate can be estimated using the calculated probability of delamination. Using the above approach, the probabilities of delamination were determined and listed for the four sites shown in Table 6.4.

Table 6.4 Probability of Delamination and the Number of Cracks that Could Delaminate in Each Site

	US 290- Hempstead	US 290- Cypress	SH 255	SH 288
Season	Summer	Summer	Winter	Winter
Shear strength, τ_0 (psi)	139	134	142	152
Standard deviation of shear stress, τ_0 (psi)	34.7	33.5	35.5	38
Shear stress, τ_{xy} (psi)	64.24	78.52	27.67	114.2
Standard deviation of shear stress, $\sigma_{\tau_{xy}}$ (psi)	19.1	21.2	9.45	33.9
% of Prob($\tau_{xy} - \tau_0 > 0$)	3	8	0.1	23
Total number of cracks	2253	N/A	583	187
The number of cracks that yield delamination	68	N/A	1	43

The shear strength of each site was determined as a function of the prevailing climatic conditions in terms of the equivalent age (t_e) of the concrete. Equivalent age is a maturity parameter representing the effective age of concrete that correlates well to the degree of hydration (α_{hyd}) and the strength of concrete (in terms of the ultimate strength of concrete). The ultimate shear strength of concrete at all sites was estimated in terms of the curing conditions prevalent at the SH 288 site, since this was the only available set of concrete shear strength data (Liu et al 2009). The shear strength ratio as determined using Equation (6.6) and a laboratory based shear strength curve was defined in Figure 6.8, from which the time constant and shape parameters could be defined. The ultimate shear strength, although based on a single set of site conditions, nonetheless facilitated the determination of 24 hour shear strengths for each site listed in Table 6.4. The resulting probabilities of delamination are also shown.

6.5 Spall Stress Performance Modeling

A spalling stress model by Tang et al. (1993) and Jeong, Zollinger (2002) serves as a means to determine tensile stress caused by passing wheel loads leading to spall development. The Tang model for spall stress (σ_{spall}) is illustrated in Figure 6.8 which has since been modified from the original expression to account for tensile stress effects of vertical shear on the crack face due to load transfer. As can be observed in Figure 6.8, several key parameters are included in the model and are redefined as:

$$\sigma_{spall} = \left[(\tau_p - \tau_f) \frac{l^*}{t} + \frac{\tau_f}{\tan \theta} \right] + \frac{6M}{t^2} \quad (6.14)$$

where, τ_p = shear stress from tire loading

τ_f = friction resistance at bottom of spall

l^* = length of spall

θ = angle of spall fracture

M = spall bending moment due to shear from load transfer effects

s = slab thickness

The bracketed term of Eq. (6.14) are used to calculate the stress that a passing wheel load causes on the surface concrete leading to chipping and shallow spalling. In the case of spalling, the second term principally applies.

Discussion of the details related to the development of Eq. (6.14) is presented elsewhere (Zollinger et al. 1994) but an average value for the parameter l^* is suggested to simplify the stress analysis even though variations from this may be observed in field studies. The first term in equation Eq. (6.10) represents the shear stress induced by the presence of a passing tire. The tire causes shear on the surface of the pavement that is directed inward longitudinally along the tire contact region (Tielking, 1991). In the case of chipping, the shear component consequently can be determined as a function of the transfer of shear strain through the joint sealant material (which is only applicable in jointed pavements, as previously noted).

The key contributor to spall stress is the moment component that is a function of the degree of load transfer and the width of the joint or crack as it opens and closes (and the shear stiffness of a joint sealant if it is present, as in the case of a jointed pavement). A bending moment is induced from the combined effect of the load transfer-induced shear and the leverage arm ' l^* '. In the case of spalling, the net effect is that bending moments can be generated leading to tensile failure.

The movement associated with this shear effect also has some effect on the shear resistance along the bottom face of the spall boundary (which defines the bottom of the delamination.) Since this analysis does not account for the effect of the longitudinal steel on delamination development, delamination depths greater than 1.5 to 2 in (40 to 50 mm) are not expected to develop into spall distress, even though deeper spalls would certainly be less tolerable.

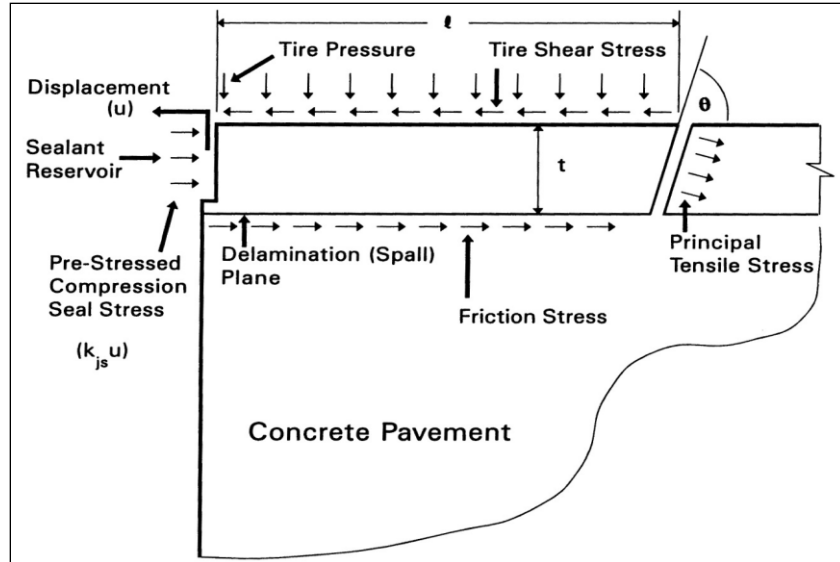


Figure 6.8 Concrete Pavement Spall Mechanism and Model. (Tang et al 1993)

6.6 Spalling Stress

Assuming delamination has occurred, the bending stress (σ_{spall}) acting on the spalled section takes place each time a vehicle passes over the adjacent joint or crack, causing a differential deflection in the delaminated segment and incrementally damaging the concrete. Specifically, the differential deflection is accounted for in the bending moment (M) term. Once a vehicle wheel load passes over the crack, the crack moves differentially according to the level of load transfer efficiency (LTE) prevalent in the joint or crack. When the slab is loaded at the crack, a bending moment (M) is induced by the cantilever effect on the delaminated slab segment. In addition, shear components acting on the cracked section are combined with M to induce σ_{spall} :

$$\sigma_{spall} = \frac{6M}{t^2} \quad (6.15)$$

This bending stress, the main factor causing spall formation, can be easily calculated as a function of the load transfer of the transverse crack as imposed by $\Delta\delta$, which is the deflection between the loaded slab and unloaded slab:

$$M = \frac{E_c t^3 \Delta\delta}{4(l^{*2})} \quad (6.16)$$

where, l^* = length of delamination (assumed to be 3 inches),

- $\Delta\delta$ = delamination opening at the face of the crack due to movement across the joint or crack reflected in the load transfer efficiency,
 t = depth of spalling (in), and
 E_c = concrete modulus (psi)

Since the bending moment is primarily affected by the aggregate interlock along the transverse crack, the spalling stress (σ_{spall}) depends both on the induced bending moment and indirectly on slab thickness through its effect on the LTE of the transverse crack.

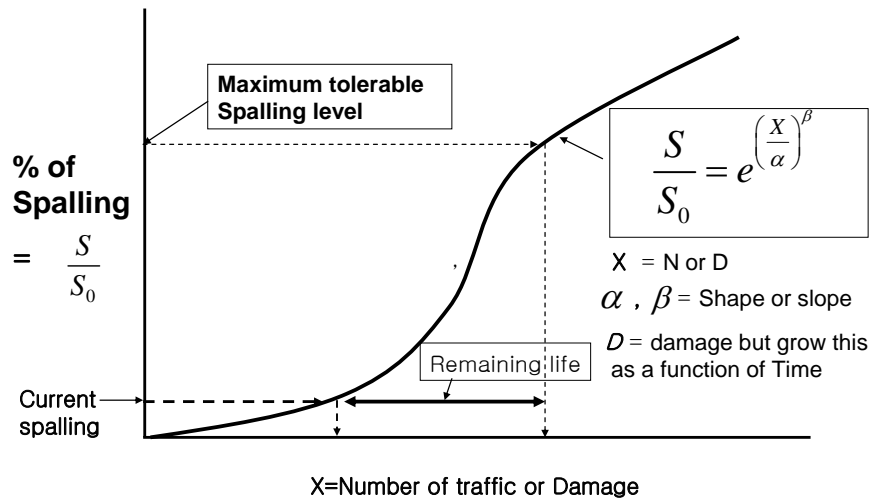


Figure 6.9 Calibration Concept for Spalling Performance

6.7 Approach to Spalling Calibration

A spall distress model, shown subsequently, is suggested for calibration and for spalling prediction due to accumulated fatigue damage calibrated to field performance data. The spall performance model with its attendant calibration parameters is illustrated in Figure 6.9 which represents the exponential growth of spalling distress (S) with either traffic (N) or damage. Relative to damage accumulation, the Weibull distribution α and β parameters control the shape and the rate of spall development predicted by the spall model, while the S_0 term represents the maximum amount of spalled cracks. A unique feature of the shape parameters is its relationship to the variability of performance where its determination being based on field data not only establishes a calibrated mean value but also calibrates the performance reliability (from the same set of data). The α and β parameters are therefore derived from performance data.

6.8 Assessment of Traffic Data

Traffic determination for calibration purposes was defined in terms of an 18 kip single axle load with respect to spall distress. The PMIS database was used since it contained

site specific service period data and average daily traffic (ADT), data necessary to determine the accumulated traffic loads with respect to equivalent single axle loading ($ESAL_i$) as

$$ESAL_i = \% \text{ of truck} \cdot \frac{ADT}{2} \cdot LDF \cdot \sum_{j=1}^3 \sum_{i=1}^3 [(\% ADT_{i+1} - \% ADT_i) A_i \cdot ELF_i] \cdot EAF_j \quad (6.17)$$

where, i = Load group
j = Axle configuration (SA, TA, and Tridem)
 A_j = Load group (%)
 ELF_j = Equivalent load spalling factor = $10^{17.61(r_{18k} - r_j)}$
LDF = Lane distribution factor

Specific load group data (10-22k) for single axle (SA) and for (22-38k) tandem axle (TA) was not available in the PMIS database. Lane distribution factor (LDF) as 0.9 and 60% of single axles and 40% of tandem axles were assumed for purposes of calibration.

ELF is determined as

$$ELF_j = 10^{17.61(r_{SA} - r_{TA})} \quad (6.18)$$

where, $r = \frac{\sigma_{spall}}{MoR}$
 σ_{spall} = Defined in Appendix E

ELC of a single axle is considered as 1, and that of a tandem axle is calculated using Equation 6.18. The final design of ESALs is expressed as:

$$ESAL_s = \sum ESAL_i \cdot EWF \quad (6.19)$$

where, EWF = Equivalent damage ratio to account for the effect of traffic wander within the wheel path

An equivalent damage ratio (EWF) is “the ratio of the traffic applied at a critical location that will produce the same accumulated damage as the total traffic distributed over all locations within the wheel path” (Huang, 2000). It is a means of accounting for wander of vehicular traffic within the driving lane. An EWF is used to convert traffic that is laterally distributed across the wheel path into critical applications at the location which produces the maximum tensile stress in the slab. A detailed discussion of EWF as it pertains to spalling distress is provided in Appendix E.

The value of EWF must be considered in rigid pavement design analysis because the location of the applied load greatly influences the magnitude of the resulting distress. For spalling analysis, the critical design position was found to be at the edge of the slab as verified with finite element analysis using ISLAB2000 finite element analysis program for rigid pavements. The factors assumed for the analysis were:

- 1) Joint Spacing, 100in.
- 2) Loading with 18 kip single axle load

Since EWF for spalling is a deflection-related factor, it was assumed that variation in joint spacing would not affect EWF significantly. Free edge pavement condition was also considered to be the worst condition, although the analysis was done with a variety of pavement LTE conditions. For determination of the critical position along the transverse crack and calculation of spall damage for a CRC pavement configuration, the traffic was assumed to be normally distributed within the wheel path.

EWF determination involved the calculation of deflections at various positions along the transverse crack for various loading positions, load transfer efficiencies, and radius of relative stiffness (ℓ) at several locations within the wheel path. Further details are presented in Appendix C. EWF was found to be insignificantly affected by variation in longitudinal and transverse load transfer efficiencies. Since the variation in load transfer efficiencies has equal effect on damage in the wheel path, its impact on EWF is expected to be minimal. However, EWF was determined to vary significantly with the radius of relative stiffness (ℓ). With an increase in the radius of relative stiffness the EWF was found to increase and as a consequence should be considered in design.

6.9 Calibrating Loads to Failure

Calibration of the loads to failure for spalling can be carried out by defining the coefficients of Weibull distribution factors in the following expression:

$$S = S_0 e^{-\left(\frac{N}{\lambda}\right)^\gamma} \quad (6.20)$$

where, S = number of spalls per 100 ft of pavement
 S_0 = ultimate number of spalls per 100 ft of pavement
 N = traffic volume
 λ = scale factor of Weibull function dependent upon initial field conditions
 γ = shape factor of Weibull function dependent upon initial field conditions

Taking the natural log of each side of Eq. 6.20 respectively:

$$\ln\left(\frac{S}{S_0}\right) = -\left(\frac{N}{\lambda}\right)^\gamma \quad (6.21)$$

$$\ln\left[-\ln\left(\frac{S}{S_0}\right)\right] = \gamma \ln N - \gamma \ln \lambda \quad (6.22)$$

Considering Eq. (6.22) in a linear format: $y = mx_i + b$ gives:

$$\begin{aligned}
 y &= \ln \left[-\ln \left(\frac{S}{S_0} \right) \right] \\
 x &= \ln N \\
 m &= \gamma \\
 b &= -\gamma \ln \lambda
 \end{aligned}
 \tag{6.23}$$

A minimum of two data points are required for each site to determine the coefficients with respect to percentage of spalled cracks and traffic volume. Scale factor (γ) can be expressed as:

$$\gamma = \frac{\ln[-\ln(y_2)] - \ln[-\ln(y_1)]}{\ln(x_2) - \ln(x_1)}
 \tag{6.24}$$

where, y_1 = % of spalled cracking at initial condition
 y_2 = % of spalled cracking at surveyed condition
 x_1 = % of spalled cracking at initial condition
 x_2 = % of damage at surveyed condition

Also, the scale factor (λ) can be determined as follows:

$$\lambda = e^{-b/\gamma}
 \tag{6.25}$$

Determining these parameters calibrates the loads to failure (N_{fc}); rearranging equation (6.4) accordingly yields:

$$N_{fc} = \frac{1}{\lambda} \left(-\ln \frac{S}{S_0} \right)^{\frac{1}{\gamma}}
 \tag{6.26}$$

The number of traffic loads to failure for design (N_{fd}) can be adjusted to include (N_{fc}) as:

$$N_{fd} = 10^{17.61 - 17.61 r_{Calib}}
 \tag{6.27}$$

where, r_{Calib} = stress ratio determined from field conditions
and, S / S_0 was considered as 3 % in the calibration since this appears from the
field data to be the threshold percentage that initiated spall repair activities. And

$$10^{17.61-17.61r_{Calib}} = \frac{1}{\lambda} \left(-\ln \frac{S}{S_0} \right)^{\frac{1}{\gamma}} \quad (6.28)$$

r_{Calib} can be determined from Eq. (6.26). r_{Calib} can be expressed as:

$$r_{Calib} = r_{Lab} + \Delta r \quad (6.29)$$

where, r_{Lab} = Lab stress ratio $\left(\frac{\sigma_{spall}}{f_t} \right)$; f_t = concrete modulus of rupture)

Since r_{Lab} can also be based on the design strength, Δr can be determined from Eq. (6.27) and used to adjust the design r ratio to more accurately reflect the stress levels in the field. Consequently, N_{fd} and number of accumulated traffic loads (n_i) can be used to determine the damage factor at a specific site as given in Equation (6.30).

$$D = \sum \frac{n_i}{N_{fd}} \quad (6.30)$$

Table 6.5 Database Used to Determine Load to Failure Parameters (λ, γ)-SH 255

Number	Year	% Spalling	$y = \ln(-\ln(\%spalling))$	Traffic(N)	$x = \ln(N)$ x
1	2001	0.1	1.9	1.3E+07	16.40
2	2002	0.3	1.8	1.5E+07	16.50
3	2003	0.1	1.9	1.6E+07	16.60
4	2004	0.1	1.9	1.8E+07	16.68
5	2005	0.4	1.7	1.9E+07	16.97
6	2008	1.92	1.4	2.3E+07	16.84

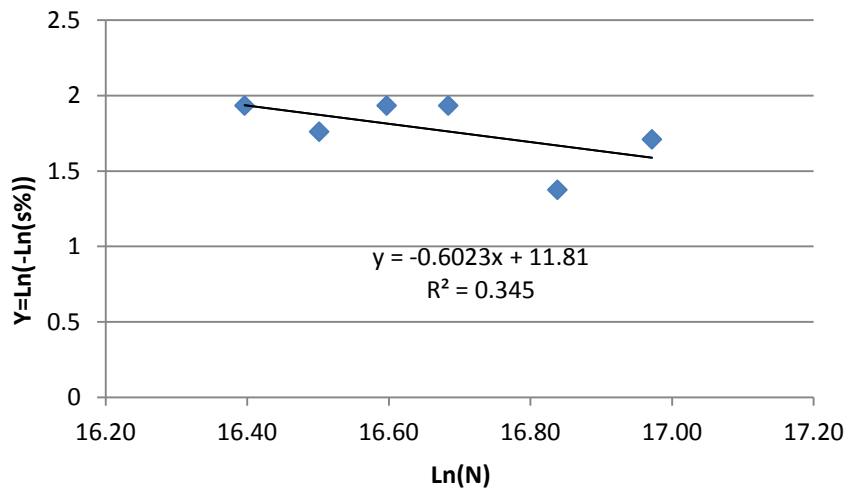


Figure 6.10 λ and γ Determined from Trends of Spalling and Traffic

Shown in Figure 6.10 is the determination of the λ and γ parameters in the x and y linear forms as shown in Table 6.5. The slope of the trend line and constant the equation are respectively γ and b . In addition, λ is obtained from Eq. 6.23. Thus, cracking parameters were found as using data shown in Figure 6.10.

6.10 Spalling – Damage Model Calibration

Calibration of the spalling–damage relationship follows a procedure similar to the way the calibration of the load to failure was carried out. Similar scale and shape Weibull

coefficients are determined but are instead based on accumulated damage relative to the following expression previously introduced:

$$\%S = S_0 e^{-\left(\frac{D}{\alpha}\right)^\beta} \quad (6.31)$$

where, %S = number of spalls per 100 ft of pavement
 S_0 = ultimate number of spalls per 100 ft of pavement
 D = accumulated damage
 α = damage scale factor of Weibull function, and
 β = damage shape factor of Weibull function

Taking the natural log of each side of Eq. (6.31) respectively:

$$\ln\left(\frac{S}{S_0}\right) = -\left[\frac{D}{\alpha}\right]^\beta \quad (6.32)$$

Again, taking the natural log of each side of Eq. (6.32) :

$$\ln\left[-\ln\left(\frac{S}{S_0}\right)\right] = \beta \ln D - \beta \ln \alpha \quad (6.33)$$

Considering Eq. (6.31) is in the linear format: $y = mx_i + b$ gives :

$$\begin{aligned} y &= \ln\left[-\ln\left(\frac{S}{S_0}\right)\right] \\ x &= \ln D \\ m &= \beta \\ b &= -\beta \ln \alpha \end{aligned} \quad (6.34)$$

Again, a minimum of two data points are required for each site to determine the site coefficients with respect to percent of spalled cracking (S/S_0) and damage. Scale factor (β) can be expressed using data from the field.

$$\beta = \frac{\ln[-\ln(y_2)] - \ln[-\ln(y_1)]}{\ln(x_2) - \ln(x_1)} \quad (6.35)$$

where, y_1 = % of spalled cracking at initial condition
 y_2 = % of spalled cracking at surveyed condition
 x_1 = % of spalled cracking at initial condition
 x_2 = % of damage at surveyed condition

Also, scale Weibull coefficients gives:

$$\alpha = e^{\left(\frac{\beta x_2 - y_2}{\beta}\right)} \quad (6.36)$$

The calibrated model based on the damage factor can be expressed as:

$$\%S = S_0 e^{\left(\frac{D}{\alpha}\right)^\beta} \quad (6.37)$$

Since cracking parameters were determined from above, N_{fd} was obtained from Eq. (6.27). Damage was calculated using Eq. (6.30), which led to the determination of the damage parameters using linear regression. Then, the natural log of damage was used to determine the x parameter shown in Table 6.6

Table 6.6 Database Used to Determine Damage Parameters (α, β)-SH 255

Number	Year	% Spalling	y	D	$x = Ln(D)$
1	2001	0.1	1.93	0.3234	-1.129
2	2002	0.3	1.76	0.3593	-1.024
3	2003	0.1	1.93	0.3953	-0.928
4	2004	0.1	1.93	0.4312	-0.841
5	2005	0.4	1.71	0.5749	-0.553
6	2008	1.92	1.37	0.5031	-0.687

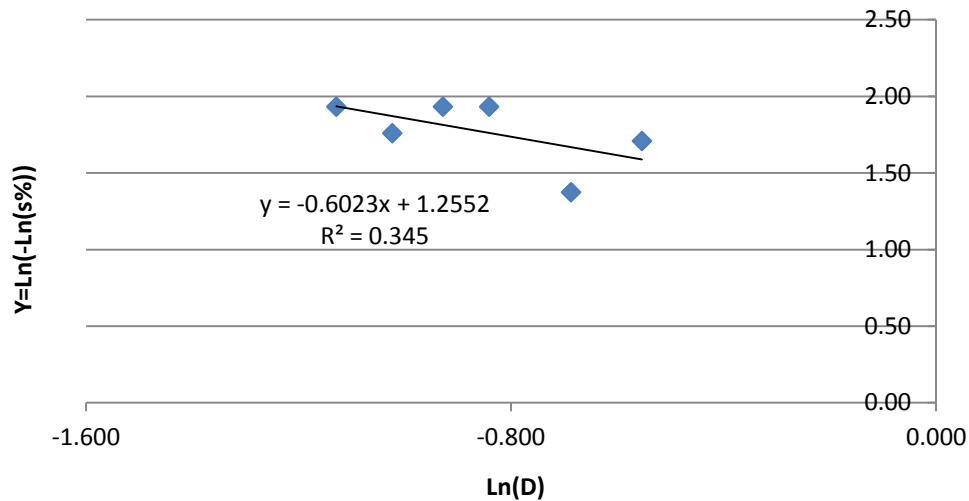


Figure 6.11 α and β Determined from Trends Displayed

The α and β parameters are directly determined from the values of x and y shown in Figure 6.11. The trend slope and the equation constant are respectively β and b . In addition, α is obtained from Eq. (6.34). Damage parameters were characterized by using data shown in Table 6.6. Thus, coefficients from both spalling-traffic and spalling-damage models were linearly determined.

6.11 Application of Field Performance Calibration to Design

The α and β parameters represent a variety of site-related characteristics that may affect spalling behavior. However, with respect to spalling distress, α and β don't apply unless delamination has occurred. In this regard, the effect of environmental factors in the calibration of spalling is imbedded in the probability of delamination. In terms of shallow spalling and chipping, the α and β terms have a more direct application as far as accounting for environmental factors in the calibration process. Accordingly, environmental factors including charging sequence and aggregate type affect the α and β parameters, making it necessary to adjust these parameters for environmental effects for shallow spalling and chipping since the probability of delamination analysis does not apply to these distress types. In this regard, test sections such as SH 288 explicitly included some of these factors to facilitate a factorial analysis of the performance results. The tolerable percentage of chipping and shallow spalling was taken as 40 % in the loads to failure analysis. In addition, Δr values which are used in the design process are shown in Table 6.7.

The design calibration process with respect to chipping, shallow spalling, and spalling distress yielded the design parameters α , β , and Δr listed in Table 6.7. Each test section was characterized by specific damage parameters. In the case of chipping distress, the SH 255 and SH 288 test sections were used to determine the prediction of model calibration

parameters. In the case of shallow spalling, the US 290-Hempstead, SH 255 and SH 288 test sections were used to determine the calibration parameters; the US -290 and SH 255 sections were used to determine the spalling calibration parameters previously described. The loads to failure (N_f) parameter was obtained by Eq. (6.26) using the Δr parameter for damage calculations.

Table 6.7 Determination of Loads to failure Parameters Among All Test Sections

Distress Type	Site	Section Number	Severity	$\lambda(\times 10^{-8})$	γ	α	β	Δr
Chipping	SH 255	#5	15	3.01	-2.24	0.087	-2.23	0.07
	SH 288	Average of all section	44.8	68.1	-3.84	0.79	-0.38	0.06
	US 290-Hempstead	# 30	34	5.78	-0.33	0.76	-0.33	0.02
Shallow Spalling	SH 255	# 5	3.33	1.48	-1.23	0.17	-1.22	0.05
	SH 288	Average of all section	5.4	1.08	-0.29	0.74	-0.30	0.06
	US 290-Hempstead	# 30	1.9	0.02	-0.25	156	-0.25	0.02
Spalling	SH 255	# 5	17	3.05	-0.6	2.84	-0.9	0.01

6.12 Adjustment of Design Parameters for Chipping and Shallow Spalling

Two factorial designs are configured in terms of charging sequence, fly ash type, curing conditions, aggregate type, and curing method to extend the value of α for chipping and shallow spalling to a broader range. Specifically, use of factorial designs in this manner organizes the field data to establish major trends of the relevant factors. Major trends can be considered related to the critical factors affecting α such as batching, charging sequence, curing, PE, and aggregate rating in this project. From Table 6.8 and Table 6.9 the levels of UFFA and Class F fly ash respectively were digitized by a positive and negative sign. Main effects were digitized using the following expression:

$$\text{denoted value} = \frac{\text{given value} - \text{average of high and low value}}{0.5(\text{high value} - \text{low value})} \quad (6.38)$$

An expression for α can be determined from the given field data listed in Table 6.8 as a function of the main effects (E_i). Specifically, E_i is represented as the effect on α , which is determined through the analysis of the factorial designs. The curing conditions (HRC) for the cell listed under Test #2 were actually cured with a wet mat, but the performance for this cell was estimated based on the trends established by extrapolating the trends in other cells similar to it.

The quantities associated with each main effect were analyzed using Eq. (6.36) resulting in the values shown in Table 6.9. Modified and normal charging sequences were assumed as 1 (modified batching) and 0 (normal batching). Similarly, curing quality was represented using a curing evaluation index (EI). HRC and NC were considered as 1 and -1. As a result, three denoted values were listed in Table 6.9. In addition, a second factorial design is shown in Table 6.10 based on curing quality, aggregate rating, and PE value (Ye et al 2008). Main effects (E_i) were calculated using analysis as associated with the structure of a 2^3 factorial design depicted in Table 6.9 and Table 6.10.

Table 6.8 Factorial Design and Shape Factor of Shallow Spalling Percentage at SH 288

Test	E_1 (UFFA)	E_2 (charging)	E_3 (curing)	Section Number	% Shallow Spalling	α
1	+	+	+	2	5.6	0.746
2	-	+	+	Extrapolate	0.1	0.694
3	+	-	+	1	5.9	0.747
4	-	-	+	5	5.6	0.746
5	+	+	-	4	5.9	0.747
6	-	+	-	8	5.6	0.746
7	+	-	-	3	10	0.756
8	-	-	-	7	15	0.765

Table 6.9 First Factorial Design of Main Effects and Levels with Respect to Shallow Spalling

	Level	$E_1 (1.125 \times 10^{-2})$	$E_2 (-2.025 \times 10^{-2})$	$E_3 (-2.025 \times 10^{-2})$
Parameters		UFFA	Mod	HRC
		Class F	Normal	NC
Coded Value	High	1	1	1
	Low	-1	-1	-1

Table 6.10 Second Factorial Design of Main Effects and Levels

	Level	$E_1 (2.5 \times 10^{-4})$	$E_2 (-1.25 \times 10^{-3})$	$E_3 (-2.5 \times 10^{-4})$
Parameters		HRC	Aggregate rate (6.1)	PE(0.04)
		NC	(4.5)	(0.02)
Coded Value	High	1	1	1
	Low	-1	-1	-1

Table 6.11 List of α Equations with Respect to Chipping and Shallow Spalling Distress

Distress Type	Number	α_{SH288}	Standard Error	C_v
Chipping	1 st factorial design	$(0.25x_1 - 12.5x_2 - 0.25x_3) \times 10^{-3} + a$ ($a = 0.79$)	0.00	1.2 %
Shallow Spalling	1 st factorial design	$(1.125x_1 - 2.025x_2 - 2.025x_3) \times 10^{-2} + a$ ($a = 0.74$)	± 0.01	0.4 %
	2 nd factorial design	$(2.5x_1 - 2.5x_2 + 2.5x_3) \times 10^{-3} + a$ ($a = 0.75$)	0.00	0.4 %

The α parameter can be described in terms of three factors included in Tables 6.8 through 6.11 as:

$$\alpha = E_1(x_1) + E_2(x_2) + E_3(x_3) + a \quad (6.39)$$

where , E_1, E_2 and E_3 = main effect coefficients

x_i = main effect
 a = average of all α

For the factors included in the considered sites with respect to chipping and shallow spalling, α can be expressed using the first and second factorial design configurations. In addition, the main effects standard errors can be assessed. Coefficients of Variation (C_v) of the first and second factorial designs were calculated, and C_v is used to represent the measure of dispersion in terms of the mean value and standard deviation.

Accordingly, α can be expressed in terms of E_i and x_i such that the SH 288 conditions can be established as a base with respect to chipping and shallow spalling distress (shown in Table 6.11.) The parameter x_i varies in the each case by distress type and factorial design.

6.13 Application of Factorial Design Analysis to Calibration

The second factorial design was created based on information from the US 290-Hempstead and SH 288 sites because aggregate rating data was included. The α parameter can be adjusted by a $\Delta\alpha$ parameter which is estimated and, for validation purposes (subsequently discussed), compared with the measured values of $\Delta\alpha$ to determine the likelihood of the estimated value to adequately adjust the value of α . In addition, to account for the aggregate rating included in the second factorial design, it is important to better estimate $\Delta\alpha$ since shallow spalling and chipping distress are susceptible to the type of aggregate due to bond characteristics.

The α parameter for other site conditions can be estimated in terms of the effects represented in Table 6.11. The difference ($\Delta\alpha$) between $\alpha_{SH\ 288}$ and α of the site of interest indicate that the adjustment in α needed to account for the differences in site conditions (in terms of the main effects included in Table 6.11). For example, the α for a site at SH 225 was found by modifying the α for SH 288 with respect to UFFA, charging sequence and curing methods. $\Delta\alpha$ is expressed as :

$$\Delta\alpha = \alpha_{SH\ 288} - \alpha_{site} \quad (6.40)$$

where, $\alpha_{SH\ 288}$ = determined α at SH 288

α_{site} = determined α at a site of interest

Since $\Delta\alpha$ and E_i are determined from the above coded values (x_i) were determined accounting for the difference between the sites of interest and SH 225 (Table 6.12 and 6.13). Thus, x_i can be expressed based on SH 225 conditions such that α of another site can be estimated.

6.14 Validation of α and β Parameters for Prediction of Spalling

Estimated and measured $\Delta\alpha$'s are compared to the accuracy of the established α equations. Regarding chipping and shallow spalling distress, x_1 , x_2 , and x_3 are represented accordingly by the different sites. Since US 290–Hempstead and SH 225 were placed without the UFFA and a modified charging sequence, x_1 and x_2 were determined as -1. In addition, both sites were cured with polyethylene sheeting, which was considered as a special curing compound similarly as HRC so that x_3 is numbered as 1.

As can be observed, the difference between the measured and calculated $\Delta\alpha$ is small; nonetheless, hypothesis testing can be employed to verify whether the estimated $\Delta\alpha$ is acceptable in comparison with the measured $\Delta\alpha$. As the measured $\Delta\alpha$ and the estimated $\Delta\alpha$ are very close, the likelihood of rejecting the null hypothesis is high. In short, at a level of significance of 0.05, the estimated $\Delta\alpha$ can be replaced by the measured value. It is noted that any adjustment in α dictates a change in β .

Table 6.12 Comparison Estimated $\Delta\alpha$ with Measured $\Delta\alpha$
Used with 1st Factorial Design

Distress Type	Site	x_1	x_2	x_3	Measured $\Delta\alpha$	Estimated $\Delta\alpha$
Chipping	SH 225	-1	-1	1	0.73	0.72
Shallow spalling	SH 225	-1	-1	1	0.57	0.56
	US 290-Hempstead	-1	-1	1	-0.02	-0.03

Table 6.13 Comparison Estimated $\Delta\alpha$ with Measured $\Delta\alpha$
Used with 2nd Factorial Design

Distress Type	Site	x_1	x_2	x_3	Measured $\Delta\alpha$	Estimated $\Delta\alpha$
Shallow spalling	SH 225	-1	-1	1	2.088	2.090

6.15 Spalling Validation

US 290-Hempstead showed 1.9% spalling at 13 years of service, while SH 255 showed 1.7 % shallow spalling at 17 years of service. It seemed that the former was the normal case and the latter was the more severe case. Thus, no matter the level of spalling severity with respect to service period or traffic, model calibration should apply.

In Figures 6.12 and 6.13, the SH 225 calibration included five data points where α was determined according to the established trends. The US 290-Hempstead performance fits the established trend well in terms of service period and damage.

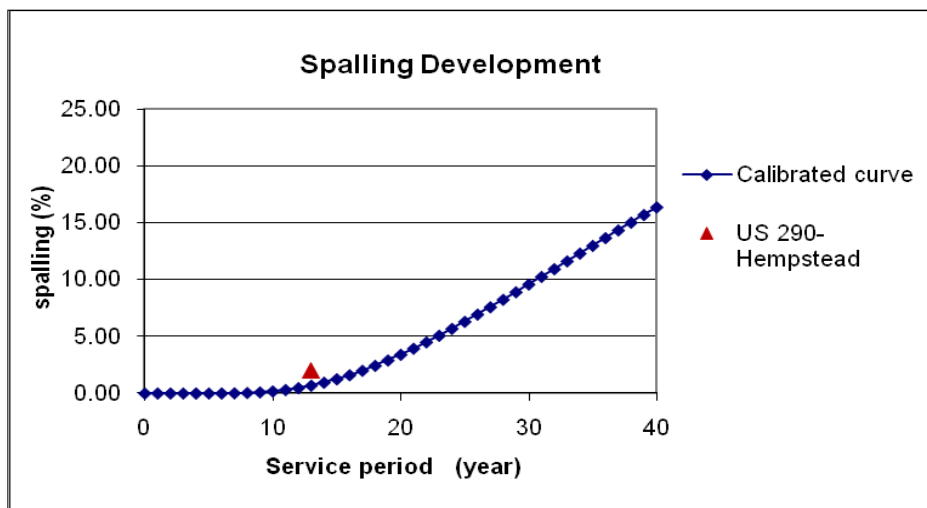


Figure 6.12 Calibrated Curve in SH 225 vs US 290-Hempstead with Respect to Service Year

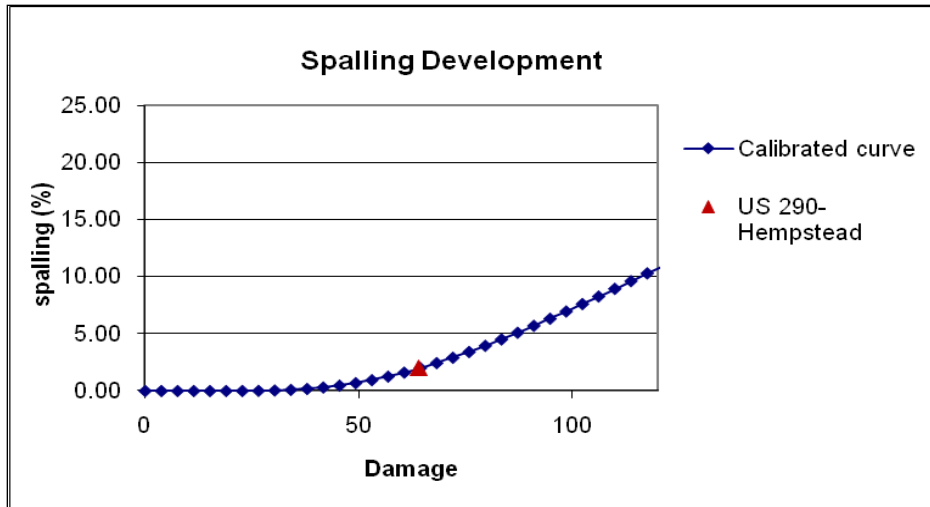


Figure 6.13 Calibrated Curve in SH 225 vs US 290-Hempstead with R Respect to Damage

6.16 Conclusions

The ultimate goal of this project was to develop a model to predict the level of spalling distress as a function of several factors such as construction method, traffic level, and climatic conditions. Field surveys to obtain the level of spalling and to determine model calibration of spalling distress types were performed. Construction methods used to establish test sections were analyzed for their effect on the level of spalling. Traffic was characterized in terms of total traffic and EDR to mechanistically compute the traffic loading with the use of the PMIS database. In addition, climatic factors were considered for their effect on the level of spalling damage.

The model calibration co-efficients Δr , α , and β were determined from field performance data based on reasonable fits to existing spalling data, to establish performance trends. As a minimum, two data point are needed to develop the trends in which to predict spalling behavior at a certain site. However, several data points can be encompassed within the technique outlined in this paper to characterize the trends inherent in the spalling distress for a specific site. The plots illustrated how spalling would develop with respect to service life and damage. Spalling is based on the probability of delamination, whereas shallow spalling and chipping are based on a modified effect of climate, materials, and methods of construction on spalling distress.

The modification of α with respect to shallow spalling and chipping for specific site conditions was developed using a factorial design that organized the field data in order to establish the relevant factor relationship. The accounting factors such as charging sequence, curing method, aggregate rating, and PE value were utilized to establish the trends of α in the prediction of chipping and shallow spalling distress. The spalling behavior of a site of interest was also validated from the trends of other site data. The spalling prediction model developed in this study was incorporated into an Excel program. The descriptions of the program are included in Product 0-5832-P1 "User's

Guide for TxCRCP-ME Design Software Volume I” and the design manual in Product 0-5832-P2, “User's Guide for CRCP ME Design Software-Volume II”.

CHAPTER 7 CONCLUSIONS AND RECOMMENDATIONS

7.1 Conclusions

CRCP design has two components: slab thickness design and steel reinforcement design. Currently, TxDOT uses the AASHTO 93 Design Guide for the slab thickness design of CRCP. TxDOT does not have design procedures for reinforcement. Instead, reinforcement design was developed for various slab thicknesses based on past performance and is provided in the design standards.

The AASHTO 93 Design Guide was developed based on the AASHTO Road Test, in which CRCP was not included. From a purely technical standpoint, because the mechanisms of distresses in JCP are quite different from those in CRCP, the AASHTO 93 Design Guide is not appropriate for the design of CRCP.

In 2004, NCHRP 1-37 reports and mechanistic-empirical pavement design guide software (MEPDG) were released. MEPDG is an advanced and sophisticated program which incorporated state-of-the-practice information available at that time. TxDOT initiated a research study to evaluate the MEPDG for potential implementation at TxDOT. The study recommended, for various reasons, not to implement the MEPDG as a replacement for the design methods used at that time. TxDOT initiated a research study to develop mechanistic-empirical (ME) based design procedures for CRCP.

In the development of ME CRCP design procedures, limitations were imposed on CRCP structures as follows:

- 1) CRCP with tied concrete shoulders
- 2) Non-erodible, stabilized subbase

The reasons for these limitations were two-fold. First, TxDOT over the years improved CRCP design and construction practices based on the field performance. The use of tied concrete shoulders and non-erodible, stabilized subbase enhanced CRCP performance substantially. TxDOT feels that all future CRCP will be built with tied concrete shoulders and stabilized subbase. Second, by limiting the mechanical models to be developed in the research study to CRCP systems with these two design features, the progress can be accelerated.

To identify the structural distress (punchout) mechanisms in CRCP, extensive field evaluations were made. It was discovered that there are various types of distresses that are currently classified as punchouts. Some are due to structural deficiency of the CRCP system and increasing slab thickness will address the issue. On the other hand, there were a number of distresses that were not directly related to deficient slab thickness. These distresses were related to design details, quality control issues in material and construction, and/or concrete material property issues such as coefficient of thermal expansion. Efforts were made to identify the mechanism of distresses that were caused by the deficiency of the CRCP structural capacity. It was evident that the interactions

between longitudinal steel and concrete due to environmental loading (temperature and moisture variations) and wheel loading played a major role in the development of punchouts. Those interactions cannot be modeled with two-dimensional analysis; they can only be modeled with three-dimensional analysis. A factorial experiment was developed that included major input variables and three-dimensional finite element models were developed. Mechanistic analysis was conducted with the aid of the commercial finite element analysis program DIANA in accordance with the factorial experiment. The analysis results are summarized as follows:

- 1) There was good agreement between Westergaard's closed-form solutions and analysis results from DIANA for wheel load concrete stress at the top or bottom of the slab at three loading conditions – interior, edge and corner. The wheel load stresses in concrete at the top or bottom of the slab were not substantially affected by modulus of subgrade reaction (k).
- 2) Maximum wheel load concrete stress occurred at the mid-depth of the concrete slab due to interactions between longitudinal steel and surrounding concrete, which could cause horizontal cracking. This stress was more sensitive to modulus of subgrade reaction than the stresses at the top or bottom of the slab.
- 3) Larger concrete stress develops at the depth of steel as the concrete slab undergoes a larger temperature drop from the setting temperature. There is a roughly bilinear relationship between concrete stresses and changes in concrete temperature.
- 4) Three influencing factors – slab thickness, the modulus of subgrade reaction, and the change in concrete temperature – have relatively large effects on the wheel load concrete stress.
- 5) Crack stiffness as affected by aggregate interlock at transverse cracks has little effect on the wheel load concrete stress at the top and bottom of the slab. On the other hand, wheel load concrete stress around the longitudinal steel increases with the crack width. However, the effect has a shape that looks like the graph of a logistic function: the maximum principal stress converges when the crack stiffness becomes small or large to a certain extent. This shows that aggregate interlock has a restrictive effect on concrete stresses.

The analysis results were incorporated in the mechanistic-empirical CRCP design program, called TxCRCP-ME. TxDOT requested that the program be developed in MS Excel. The program has five modules; (1) input module, (2) stress analysis module, (3) damage estimation module, (4) punchout prediction module, and (5) output presentation module. Among these, the stress analysis module requires the most computation time and effort. To make the program more efficient, the concrete stress analysis results were populated in a series of Excel sheets in terms of temperature drop. The rest of the computations, including the estimation of “equivalent” or “composite” k value, fatigue damage computations and punchout predictions, are done within Excel. This setup increased the size of the file substantially, to more than 197 MB. This large file size has a disadvantage in that it takes time to load the program. On the other hand, this setup makes the TxCRCP-ME program quite straight forward and easy to follow the sequence of computations. Also, this setup requires less than two minutes of run-time.

The reasonableness of any mechanistic-empirical based pavement design program depends to a large extent on the accuracy of a transfer function. If the transfer function is not accurate, pavement designs developed may not be reasonable. Developing an accurate transfer function is not an easy task. Development of an accurate transfer function requires (1) reasonably accurate traffic information, (2) availability of design and construction data and (3) accurate distress information. Values for some of the variables are available, such as slab and subbase thicknesses. However, there are variables whose values are not readily available, such as in-situ concrete strength. Those values were estimated based on specification requirements at that time, and in-situ concrete strength can vary from specification requirements. It is recognized that much effort will be needed for the development of a transfer function. Among these, obtaining an accurate count of traffic load applications since the opening of the pavement is a challenge. For the development of a transfer function for TxCRCP ME, information in TxDOT PMIS was utilized with some assumptions.

Sensitivity analysis shows that the results from TxCRCP-ME appear to be reasonable. As discussed above, the use of different transfer functions will change the number of predicted punchouts; however, it won't change the trend of the relationship between input values and predicted punchouts. From that perspective, the sensitivity analysis conducted in this study indicates that trends in the results from TxCRCP-ME are reasonable, and with a more accurate transfer function, TxCRCP-ME could provide more optimized designs.

Another major task in this project was to address spalling in CRCP. Spalling models were developed and efforts were made to calibrate with field-observed data. Extensive field evaluations were conducted.

The ultimate goal of the spalling task was to develop a model to predict the level of spalling distress as a function of several factors such as construction method, traffic level, and climatic conditions. Field surveys were performed to obtain the level of spalling, and were used to determine model calibration of spalling distress types. Construction methods used in established test sections were analyzed for their effect on the level of spalling. Traffic was characterized in terms of total traffic and EDR to mechanistically compute the traffic loading with the use of the PMIS database. In addition, the climatic factors were considered for their effect on the level of spalling damage.

The model calibration coefficients Δr , α , and β as described in Chapter 6 were determined from field performance data based on reasonable fits to existing spalling data to establish performance trends. As a minimum, two data points are needed to develop the trends in which to predict spalling behavior at a certain site. However, several data points can be encompassed within the technique discussed in this report to characterize the trends inherent of the spalling distress trends for a specific site. The plots illustrated how spalling would develop with respect to service life and damage. Spalling is based on the probability of delamination, where shallow spalling and chipping are based on a modified effect of climate, materials, and methods of construction on spalling distress.

The modification of α with respect to shallow spalling and chipping for specific site conditions was developed using a factorial design that organized the field data to establish the relevant factor relationship. The accounting factors such as charging

sequence, curing method, aggregate rating, and PE value were utilized to establish the trends of α in the prediction for chipping and shallow spalling distress. The spalling behavior of a certain site was also validated from the trends of other site data.

7.2 Recommendations

The analysis conducted in this study and field observations reveal that subbase support is quite important for CRCP performance. Further efforts need to be made to evaluate the support conditions under CRCP.

The inference space for longitudinal steel amount in the transfer function development was quite limited. Caution needs to be exercised when the steel percentage is used that is outside the range used in Texas.

In the program TxCRCP-ME, the effect of non-uniformity of subbase support, or the effect of erosion, was not directly addressed. From a theoretical standpoint, the effect is included in a transfer function. However, further direct evaluation of the effect of non-uniformity and erosion of the subbase on CRCP performance would be beneficial and is recommended.

Since the reasonableness of TxCRCP-ME depends on the accuracy of a transfer function, further efforts are recommended to refine the transfer function by collecting more accurate information on traffic, construction information, and distress data. Once an accurate transfer function is developed, further sensitivity analysis will be needed to evaluate the reasonableness of the TxCRP-ME.

REFERENCES

- American Association of State Highway and Transportation Officials, (1981), "*1972 AASHTO Interim Guide for Design of Pavement Structures*", Washington, D.C.
- American Association of State Highway and Transportation Officials, (1993), "*AASHTO Guide for Design of Pavement Structures*", American Association of State Highway and Transportation Officials, Washington, D.C.
- ARA, Inc., ERES Division, (2004), "*Guide for Mechanistic-Empirical Design of New and Rehabilitated Pavement Structures*", Final Report, Champaign, Illinois
- ACI Committee 308, (2001), "*Guide to Curing Concrete (ACI 308R-01)*", American Concrete Institute, Farmington Hills, MI, 431 pp.
- ACI Committee 318, (2002), "*Building Code Requirements for Structural Concrete (ACI 318-02) and Commentary (318R-02)*", American Concrete Institute, Farmington Hills, Mich., 443 pp.
- Bazant, Z. P., (1972), "*Prediction of Concrete Creep Effects Using Age-Adjusted Effective Modulus Method*", Journal of the American Concrete Institute, Vol. 69, No. 4, pp. 212-217.
- Bazant, Z.P., and S.T. Wu., (1974), "*Creep and Shrinkage Law for Concrete at Variable Humidity*", J. Eng. Mech., ASCE, 100(6), pp. 1183-1209.
- Brink, A. C., (2003), "*Modeling Aggregate Interlock Load Transfer at Concrete Pavement Joints*", Ph.D. Dissertation, University of Pretoria, South Africa
- Carino, N. J., (1991), "*The maturity method,*" *CRC handbook on nondestructive testing of concrete*", V. M. Malhotra and N. J. Carino eds., Chap. 5, CRC, Boca Raton, Fla., 101-146.
- Choi S., M.C. Won and Nasr Seifollah, (2010), "*Horizontal Cracking in Concrete Pavements*", Center for Multidisciplinary Research in Transportation (TechMRT)-Texas Tech University, Center for Transportation Research (CTR)-The University of Texas at Austin, University of North Texas (UNT)
- Choi, S., and M. C. Won, (2009), "*Design of Tie Bars in Portland Cement Concrete Pavement Considering Nonlinear Temperature Variations*", In Transportation Research Record: Journal of the Transportation Research Board, No. 2095, Transportation Research Board of the National Academies, Washington, D.C., pp. 24-33.
- Colley, B. E. and H. A. Humphrey, (1967), "*Aggregate Interlock at Joints in Concrete Pavements*", Highway Research Record, No. 189, pp. 1-18.

- Comité Euro-International du Béton, (1993), “*CEB-FIP Model Code 1990: Design Code*”, Thomas Telford, London
- Continuously Reinforced Concrete Pavements, (2003), “*One Layer Steel Bar Placement*”, TxDOT, September 2003. ftp://ftp.dot.state.tx.us/pub/txdot-info/cmd/cserve/standard/roadway/crcp_103.pdf. Accessed July 312010
- Continuously Reinforced Concrete Pavements, (2003), “*Two Layer Steel Bar Placement*”, TxDOT, September 2003. ftp://ftp.dot.state.tx.us/pub/txdot-info/cmd/cserve/standard/roadway/crcp_203.pdf. Accessed July 312010
- Dere, Y., A. Asgari, E. D. Sotelino, and G. C. Archer. (2006), “*Failure Prediction of Skewed Jointed Plain Concrete Pavements Using 3D FE Analysis*”, Engineering Failure Analysis, Vol. 13, No. 6, pp. 898-913.
- DIANA 8.1.2 User’s Manual, (2003), TNO Building Construction, the Netherlands.
- E.J. Yoder and M.W. Witzak, (1975), “*Principles of Pavement Design*”, 2nd Edition, John Wiley & Sons, Inc.
- Freiesleben Hansen, P. and Pedersen, J., (1985), “*Curing of Concrete Structures*”, CEB Information Bulletin 166, May, 42p.
- Freeman, T., Uzan, J., Zollinger, D. and Park, E., (2006), “*Sensitivity Analysis of and Strategic Plan Development for the Implementation of the M-E Design Guide in TxDOT Operations*”, Report No. FHWA/TX-05/0-4714-1, Texas Transportation Institute, Texas A&M University, College Station, Texas
- Ghali, A., R. Favre, and M. Eldbadry, (2002), “*Concrete Structures: Stresses and Deformation*”, Spon Press, New York
- Huang, Y., H., (2004), “*Pavement Analysis and Design*”, 2nd ed., Prentice Hall, Upper Saddle, River, NJ
- Jefferson, A. D., (2002), “*Constitutive Modelling of Aggregate Interlock in Concrete*”, International Journal for Numerical and Analytical Methods in Geomechanics, Vol. 26, No. 5, pp. 515-535.
- Jensen, E. A., and W. Hansen ,(2006), “*Nonlinear Aggregate Interlock Model for Concrete Pavements*”, International Journal of Pavement Engineering, Vol. 7, No. 4, pp. 261-273.
- Jeong, J. H. and Zollinger, D. G., (2002). “*Environmental Effects on the Behavior of Jointed Plain Concrete Pavements*”, Journal of Transportation Engineering, ASCE, submitted.
- John S. Miller and William Y. Bellinger, (2003), “*Distress Identification Manual for the Long Term Pavement – Fourth Revised Edition*”, FHWA-RD-03-031 Report.

- Khazanovich, L., and A. Gotlif, (2003), “*Evaluation of Joint and Crack Load Transfer*”, Final Report FHWA-RD-02-088, ERES Division, ARA, Inc.
- Kim, S.-M., M. C. Won, and B. F. McCullough, (1997), “*Development of a Finite Element Program for Continuously Reinforced Concrete Pavements*”, Research Report 1758-S, Center for Transportation Research, University of Texas at Austin
- Kim, S.-M., M. C. Won, and B. F. McCullough, (2000), “*Three-Dimensional Nonlinear Finite Element Analysis of Continuously Reinforced Concrete Pavements*”, Research Report 1831-1, Center for Transportation Research, University of Texas at Austin
- Korovesis, G. T., (1990), “*Analysis of Slab-on-Grade Pavement Systems Subjected to Wheel and Temperature Loadings*” Ph.D. Dissertation, University of Illinois at Urbana-Champaign
- Liu, J. (2006), “*Early Age Delamination in Concrete Pavements Made with Gravel Aggregates*”, Ph.D. Dissertation, Texas A&M University, College Station, Texas
- Liu, J., Mukhopadhyay, A. K., Celaya, M., Nazarian, S., and Zollinger, D. G., (2009), “*Best Practices for the Use of Silicious River Gravel in Concrete Paving*”, Report FWHA 0-4826-1, Texas Transportation Institute, Texas A&M University System, College Station, Texas
- Maitra, S. R., K. S. Reddy, and L. S. Ramachandra, (2010), “*Load Transfer Characteristics of Aggregate Interlocking in Concrete Pavement*”, Journal of Transportation Engineering – ASCE, Vol. 136, No. 3, pp. 190-195.
- McCullough, B. F., Zollinger, D. G., Dossey, T, (2000), “*Evaluation of the Performance of Texas Pavements Made With Different Coarse Aggregates*”, Report TX-01/7-3925-1, Center for Transportation Research, The University of Texas at Austin 3208 Red River, Suite 200
- Senadheera, S., Zollinger, D. G., (1995), “*Influence of Coarse Aggregate In Portland Cement Concrete on Spalling of Concrete Pavements*”, Report FWHA 97-1244-11, Texas Transportation Institute, Texas A&M University System, College Station, Texas
- Shoukry, S. N., M. Fahmy, J. Prucz, and G. William, (2007), “*Validation of 3DFE Analysis of Rigid Pavement Dynamic Response to Moving Traffic and Nonlinear Temperature Gradient Effects*”, International Journal of Geomechanics, Vol. 7, No. 1, pp. 16-24.
- Soares, J. B., Zollinger, D.G., (1997), “*Concrete Characterization Through Fracture Mechanics and Selected Pavement Applications*”, Ph.D. Dissertation, Texas A&M University, College Station, Texas
- Tang, T., Zollinger, D.G., and Senadheera, S.P., (1993), “*Analysis of Concave Curling in Concrete Slabs*”, Vol. 119 No. 4, ASCE Journal of Transportation Engineering, July/August, pp. 618-633.

Tang, T., Senadheera, S. P., Zollinger, D. G., (1999), “*Determination of fracture energy and process zone length using variable-notch one-size specimens*”, ACI Materials Journal, 96 (1), 3-10

Texas Department of Transportation, (2009), “*Pavement Management Information System - Rater’s Manual*”

Tielking, J. T. (1991), “*Pavement Shear Forces Produced by Truck Tires*”, Memorandum User’s Guide for “*ISLAB2000—Finite Element Analysis Program for Rigid and Composite Pavements*”, ERES Consultants, A Division of Applied Research Associates, Inc. 505 W. University Avenue Champaign, IL 61820

Vepakomma, S., Jeong, J. H., and Zollinger, D. G., (2002), “*Characterization of Cracking Restraint at Saw-Cut Joints Using the German Cracking Frame*”, Transportation Research Record 1813, National Research Council, pp. 28-35.

Vesic, A. S., and S. K. Saxena, (1969), “*Analysis of Structural Behavior of Road Test Rigid Pavements*”, Highway Research Record 291, HRB, National Research Council, Washington, D.C., pp. 156-158.

Walraven, J. C., (1981), “*Fundamental Analysis of Aggregate Interlock*”, Journal of the Structural Division - ASCE, Vol. 107, No. 11, pp. 2245-2270.

Wang, L., Zollinger, D.G., (2000), “*Mechanistic Design Framework for Spalling Distress*”, Transportation Research Record 1730, National Research Council, pp. 18-24.

Wattar, S. W., N. M. Hawkins, and E. J. Barenberg, (2001), “*Aggregate Interlock Behavior of Large Crack Width Concrete Joints in PCC Airport Pavements*”, Technical Report, Department of Civil and Environmental Engineering, University of Illinois at Urbana-Champaign

Westergaard, H.M., (1926), “*Stresses in Concrete Pavements Computed by Theoretical Analysis*”, Public Roads, Vol. 7, pp.25-35.

Westergaard, H.M., (1927), “*Analysis of Stresses in Concrete Pavements Due to Variations of Temperature*”, Highway Research Board Proceedings, 6, pp. 201-215.

Won, M.C. (2009), “*Evaluation of MEPDG with TxDOT Rigid Pavement Database*”, Research Report 5445-3. Center for Transportation Research, University of Texas at Austin

Won, M.C. (2010), “*Develop Mechanistic/Empirical Design for CRCP*”, Center for Transportation Research, University of Texas at Austin

Won, M.C. and Zhang, Z. (2009), “*Project Level Performance Database for Rigid Pavements in Texas, Phase II*”, Center for Transportation Research, University of Texas

at Austin

Ye, D., Mukhopadhyay, A., Zollinger, D.G., (2008), "*Laboratory And Field Evaluation of Concrete Paving Curing Effectiveness*", Report FWHA 0-5106-3, Texas Transportation Institute, Texas A&M University System, College Station, Texas

Zollinger, D. G., Senadheera, S. P., and Tianxi, T., (1994) "*Spalling of Continuously Reinforced Concrete Pavements*", Vol. 120 No.3, ASCE Journal of Transportation Engineering, pp.394-411.

Zollinger, D. G. and Barenberg, E.J., (1989), "*Proposed Mechanistic Based Design Procedure for Jointed Concrete Pavements*", Research Report FHWA/IL/UI 225, Illinois Cooperative Highway Research Program, University of Illinois at Urbana-Champaign, Urbana, Illinois

APPENDIX A

DEVELOPMENT OF COMPOSITE K

For an accurate analysis of the behavior and performance of portland cement concrete (PCC) pavement systems, proper characterizations of support conditions provided by the layers below the PCC slabs is important. Modulus of subgrade reaction (k -value), by itself or in combination with other properties, has been historically used to characterize support conditions provided by the layers which are comprised of base and subgrade below the PCC slab. Also, the k -value has been an essential element in characterizing the support layers. However, determining an appropriate k -value that accurately represents the support layer conditions has been a challenge.

Considering an appropriate support model for the rigid pavement structures is one of the most important factors in evaluating and estimating behavior and performance of the rigid pavement systems. However, because real behavior of the foundation layer that consists of fine-grained soil and aggregates is very complex, simplified support models have been developed and are used. As for the modeling of the support layers, two different models, an elastic-isotropic solid model [Burmister et al., 1943; Hogg, 1938; Pickett and Ray, 1951] and the Winkler model [Westergaard, 1925; Westergaard, 1927a; Losberg, 1961], have been used. The Winkler model has been more widely used in modern rigid pavement design algorithms such as the '93 AASHTO Guide or MEPDG because of its simplicity. Currently, two different approaches based on the Winkler foundation model are in use for rigid pavement design. These two pavement design algorithms have been and will be the most widely used. It is therefore important to identify the effects of these two methods in characterizing the support conditions on the analysis of the behavior and performance of rigid pavement structures. This will help in the selection process of the best pavement design.

A.1 Support Models for Determination of Design Input Value

MEPDG uses the concept of effective k to characterize the support condition, especially subgrade condition. To determine an effective k , the support condition of all the layers beneath a stabilized base is characterized by the k -value and that of a stabilized base is analyzed by the elastic-isotropic solid model [NCHRP, 2004]. Figure A.2 shows the illustration of an elastic layer and k -value composite support model. Material properties of the stabilized base layer including elastic modulus and Poisson's ratio could be more easily measured than those of unbound soil properties. Subgrade k -value could be also estimated from previously developed methods such as FWD, DCP, or static plate load test.

Using this support model for the analysis of concrete pavement behavior is more complicated than the use of a simple composite k -value that includes all layers beneath the PCC slab (Figure A.); however, recently developed computer-based analysis programs make it possible to solve the complicated problems more conveniently.

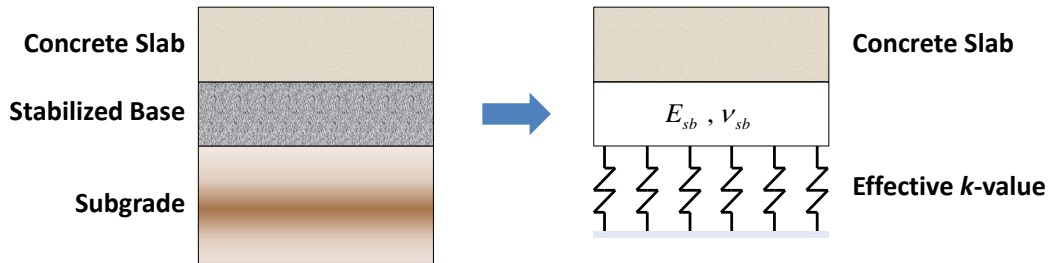


Figure A.2 Elastic layer and k -value composite support model

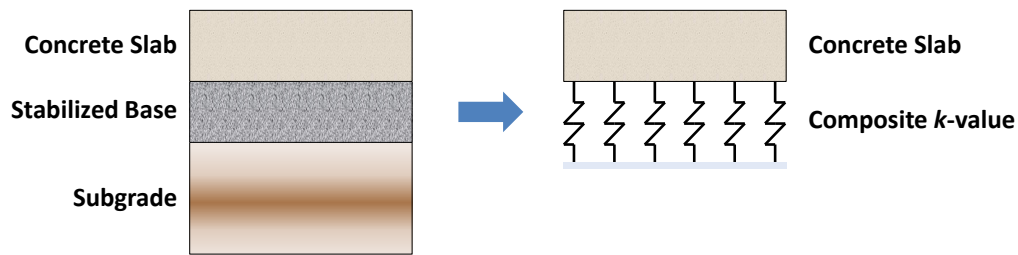


Figure A.1 Composite k -value support model

A.2 Procedure for Composite k -value Computation

To determine an appropriate support input value, the composite k -value on top of a base layer in this study, numerical analyses were conducted using the ABAQUS 6.7, general purpose Finite Element (FE) analysis computer program. Using the FE program, non-repetitive static plate load tests were simulated. The elastic layer and effective k -value composite support model was selected for the FE model. In this model, a stabilized base layer is characterized by elastic solid elements and the subgrade is modeled by a set of springs which have coefficient k (termed 'effective k -value' in MEPDG). Figure A. illustrates the FE model and deflection contour after simulating the plate load test. To compute the composite k -value on the top surface of the base layer, beneath the concrete slab, it is required to obtain support layer properties: elastic modulus of the stabilized base material, Poisson's ratio of the base material, thickness of the stabilized base layer, and modulus of subgrade reaction, the effective k -value. Figure A. illustrates the computation procedure of composite k -value as a design input representing the support system of concrete pavement structures. Static pressure loading is applied on the

top surface of the stabilized base layer with a 30-in diameter load, and the average vertical deflection corresponding to the applied pressure load between the center and edge of the loaded area is measured. The composite k -value is computed by dividing the magnitude of the applied pressure load by the average vertical deflection. Finally, the computed composite k -value will be directly used to determine and evaluate behavior and performance of the concrete pavement system.

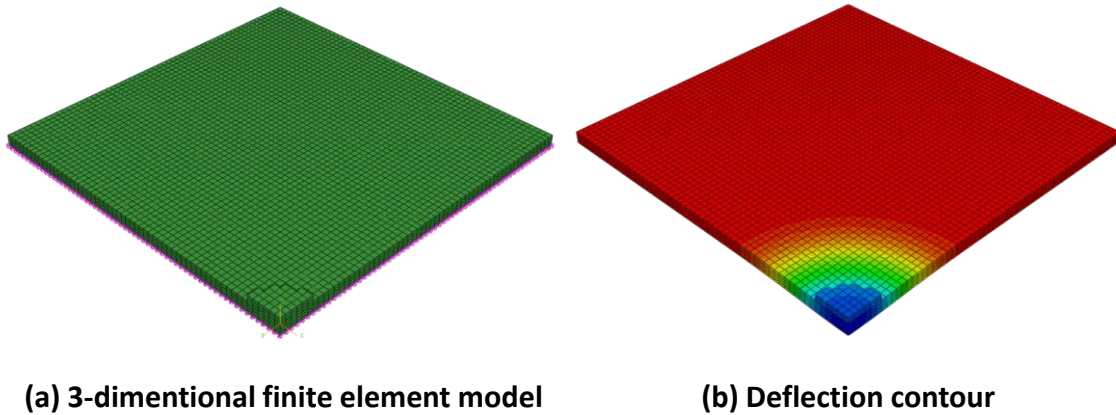


Figure A.2 Three-dimensional elastic layer and k -value composite support FE model

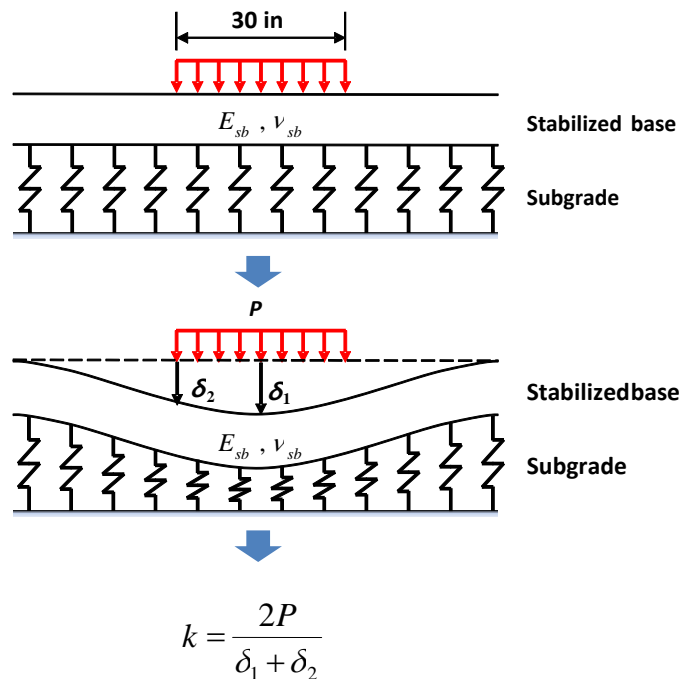


Figure A.3 Procedure of composite k -value computation

A.3 Computation of Composite k -value

To compute the composite k -value of the support system as a design input for rigid pavement design, non-repetitive static plate load tests were simulated and composite k -values were computed using the ABAQUS FE analysis program for diverse combinations of support layer properties. As variables which could contribute to determination of composite k -value, thickness of the stabilized base layer, elastic modulus of the stabilized base material, and subgrade k -value (effective k) were considered. However, Poisson's ratio of the base material was not considered. The input variables and their ranges are shown in Table A.1. These values represent typical ranges of currently used materials in fields. The composite k -values were computed from the average deflection at the center and edge of a 30-in diameter loading area with 100 psi pressure loading applied on the top surface.

Table A.2 presents the computed composite k -values due to the various support properties. As shown in the table, the composite k -value increases as the values of variables increases. However, the increasing rates are different depending on the variables including thickness of stabilized base, elastic modulus of the base material, and subgrade k -value.

Table A.1 Input variables and values for computing composite k -values

Variables	Values
Thickness of stabilized base [in]	2, 3, 4, 5, 6
Elastic modulus of stabilized base [ksi]	50, 100, 300, 500, 1000, 2000
Subgrade k -value [psi/in]	50, 100, 150, 200, 250, 300

Table A.2 Computed composite *k*-value due to various support properties

Thickness of base layer [in]	Elastic modulus of base material [ksi]	Subgrade <i>k</i> -value [psi/in]					
		50	100	150	200	250	300
2	50	69	128	189	251	314	378
	100	76	134	194	255	316	377
	300	92	156	217	278	339	399
	500	103	172	236	299	361	422
	1000	124	201	272	340	406	470
	2000	154	244	324	400	472	542
3	50	81	142	201	261	320	380
	100	93	158	221	282	342	402
	300	124	202	274	341	407	472
	500	145	233	311	384	455	523
	1000	184	289	380	464	544	620
	2000	239	367	476	576	669	758
4	50	95	161	223	284	343	402
	100	114	188	256	320	384	445
	300	161	255	338	415	489	560
	500	193	300	394	480	562	640
	1000	251	384	497	600	695	787
	2000	332	500	640	766	883	993
5	50	114	186	252	316	377	437
	100	141	226	301	372	440	507

	300	207	321	419	509	593	674
	500	250	382	494	596	691	781
	1000	330	498	637	762	878	986
	2000	441	660	837	994	1138	1273
6	50	133	214	286	353	418	480
	100	169	265	349	426	500	570
	300	255	389	502	604	695	790
	500	311	470	602	720	830	933
	1000	416	621	789	938	1074	1202
	2000	557	830	1049	1241	1415	1577

Table A.3 Regression coefficients for composite k -value

Independent variables	Un-standardized coefficient	Standardized Coefficient
Constant	-395.669	-
Thickness of base	92.335	0.475
Elastic modulus of base material	0.223	0.550
Subgrade k -value	1.829	0.568

A.4 Estimation of Composite k -value

To estimate the composite k -value (k_{∞} , psi/in) that could be determined from the values which are considered in the Table A.3, regression analysis was performed using the SPSS computer program. The composite k -value is set as a dependent variable, and independent variables are base thickness (T_b , in), base material elastic modulus (E_b , ksi), and subgrade k -value (k_{sg} , psi/in). In this analysis, it has been assumed that the dependent and independent variables show a linear relationship. Table A.3 presents obtained regression coefficients used to estimate the composite k -value. Non-standardized coefficients have

been adopted to develop a regression equation which could be expressed by equation A.1. This has an R^2 -value of 85.1%.

Relative effects of the independent variables on the composite k -value could not be compared using non-standardized coefficients because the variables are measured in different units such as inches, ksi, and psi/in. Accordingly, standardized coefficients (β) are used, which are defined as equation A.2:

The subgrade k -value has the greatest effect on the composite k -value, then the elastic modulus of the base material, and the last is the thickness of the base layer. However, the differences among those are relatively very small. Therefore, it could be assumed that the effect of support layer properties defining the composite k -value are almost identical.

$$k_{\infty} = -395.7 + 92.3T_b + 0.223E_b + 1.829k_{sg} \quad (\text{A.1})$$

$$\beta = \text{Unstandardized coefficient} \times \frac{S.D. \text{ of } \textit{Dependent variable}}{S.D. \text{ of } \textit{Independent variable}} \quad (\text{A.2})$$

APPENDIX B

SUMMARY OF SITES AND RESULTS FOR SPALLING DISTRESS SURVEY

Table B.1 Brief Summary of Results Surveyed

Roadway	Section	Features	Const. Date	Traffic (ADT)	Slab Thickness	Coarse aggregate type	PE	Chipping (%)	Avg. shallow spalling (%)	Avg. spalling (%)
US 290	Hempstead	Time paving Method of crack control Aggregate blends Method of curing	June 1995	17,530	12	Hanson	0.04 0.02	25	17.9	0.6
US 290	Cypress	Aggregate blend Method of curing	Aug, 1992	36,875	13	Hanson	0.04	/	22	2
SH 99			April, 1991	10,504			0.08	/	10	7
SH 225		Method of curing Method of crack control	Nov,1991	40,020	13	Fordyce	0.02	16.5	3.5	1.7
SH 288	NB (Pearland)	Method of curing Method of batching Method of SCM	2005	15,315	12	Fordyce	0.02, 0.03, 0.05	44.8	5.4	0
FM 1960	NB RM (666-671)		1991					/		

APPENDIX C

PAVEMENT CORING and AGGREGATE TYPE RATING

To identify aggregate characteristics relative to the observed performance, cores were obtained from selected project sites. Cores were obtained from both good and poor performing areas. Thin sections were obtained from each core to facilitate identification of aggregate characteristics and the investigation of spalling distress. Core samples included the base material.

The cores were used to rate the coarse aggregate with respect to spalling potential (see table C.1). Since aggregate rating includes physical, geometric, and chemical properties, detailed information can be classified into three categories. Physical properties include size and absorption capacity (AC). Fineness modulus (FM) is typically used to determine size effect for physical properties of aggregate rating. Texture, angularity, shape of aggregate are used to determine geometric properties of aggregates used in specific areas. Chemical properties contain aggregate mineralogy which can be sorted as chert, quartzite, granitic, etc. Weights of these properties are different such that a specific aggregate rating can be determined based on this weighting system.



Figure C.1 Coring Site and Coring Equipment Setup in SH 1960

Table C.1 Overall Evaluation for Aggregates (Liu et al 2009)

	Weight*	Attribute	Weight*	Rating	
				Hanson	Fordyce
Physical properties	4	Size effect	5	5	3
		AC	5	4	4
Geometric properties	3	Angularity	3.5	8	3
		Texture	3.5	6	8
		Percent of flat Particle	3	5	8
Chemical properties	3	N/A	8	8	4
Overall rating				6.1	4.5

* For detailed discussion on how these variables used for rating computation, refer to the report by Liu, et al.(2009)

A Hanson gravel aggregate source was used in the US 290-Cypress and Hempstead (Altair, TX). Fordyce gravel aggregate was used in SH 225, and SH 288. Table C.2 summarizes the aggregate ratings for the Hanson and Fordyce materials.

The cores also yielded petrographic information for parameters such as the ITZ, w/c ratio, and the degree of hydration while the aggregate rating pertains to properties of the aggregate with respect to spalling potential.

The performance of spalling distress is compared based on aggregate rating. Although each site may be constructed under various methods, the aggregate rating is shown in Table C.3.

Briefly, US 290-Hempstead and Cypress using Hanson aggregate seemed less spalled than either SH 255 or SH 288, which used Fordyce aggregate.

Table C.2 Percent of Spalled Cracking Based on Standard Curing

Aggregate	Site	Construction year	Avg. % of shallow spalling	Avg. % of Spalling	Aggregate Rating
Hanson	Hempstead	1995	17.9	0.6	6.1
	Cypress	1992	0	0	6.1
Fordyce	SH 255	1991	3.5	1.7	4.5
	SH 288	2005	5.4	0	4.5

Table C.3 Summary of Aggregate Rating

	SH 225	FM 1960	FM 523	SH 99
Mineralogy	66% Chert, 11% Quartzite, 22% Granitic	Chert – 69% Granite – 31%	83% Chert 17% quartzite	72% Quartzite / granitic 27% Chert
Texture / Angularity	Both texture and angularity are slightly higher – the particles are not very smooth	Slightly more than SH 99	In general low, but some chert particles are not really very smooth	In general, particles are smooth
Flat and elongated particles	Relatively less	Considerable amount of chert particles	Present but less than 1960, mostly equant	less
Air void distribution	High, more entrapped voids			normal
Depth of carbonation at the top	Relatively less but high at places – curing normal	High – poor curing or severe weather	Relatively less (lesser than 1960) – possibly good curing	Relatively less – possibly good curing
Fly ash	Present	Present	Present (possibly high)	Present

Presence of cracks	Some observed (vertical), in general the concrete looks good; very fine cracks at top parallel to the surface in the carbonated zone	fine cracks at aggregate-paste interfaces	Observed at top	Less numbers of shrinkage cracks, some parallel to surface cracks were also observed, concrete looks good in general
	SH 225	1960	523	SH 99
Degree of hydration	Lower than normal – lots of unhydrated cement particles if they are nor due to more cement factor	Normal	Possibly lower than normal as lots of unhydrated cement particles, it could due to more cement factor	Normal to good
ITZ		Fine cracks at aggregate-paste interfaces and thin porous zones around aggregates	Looks better with no such fine cracks at the aggregate-paste interfaces and thin porous zones	Presence of v. fine cracks around quartzite / granite particles is more than that at Chert, Presence of thin porous zone around all aggregates particles is common
Remarks	Should perform OK / normal	May perform badly because of high w/cm, poor curing, more flat and elongated particles, although the aggregate. rating is normal	Poor aggregate rating based on mineralogy	Higher w/cm ratio was the only issue

APPENDIX D

THE DETERMINATION OF EQUIVALENT TOTAL STRAIN DIFFERENCE

For the purpose of determination temperature and moisture gradients related to delamination potential, climatic conditions of each site were examined to determine internal moisture and temperature profiles based on climatic condition of each site. Temperature and moisture profile obtained were used to determine shear stress associated with delamination potential. In Table D.1, weather conditions relevant to selected sites were found to determine moisture and temperature profiles. The days of year refer to the construction time of year. Latitude and cloud cover fraction were assumed to be 30 and 0.5, respectively. Maximum and minimum ambient relative humidity values were calculated using average variations representative of the site. Maximum and minimum ambient temperatures are obtained similarly to relative humidity.

Moisture and temperature profiles of each site are plotted with respect to depth. A boundary condition at the bottom of the slab was assumed to be zero flux, and that at the top surface was governed by many factors described in Table D.1. The curing compound was applied at the top boundary of the slab for the moisture transport, and a certain diffusivity of the curing compound was assumed.

Relative humidity below the surface of pavement was different for each site. Relative humidity of SH 225 and SH 288 were respectively 90 % and 83 % at the depth of 1 inch below the surface. Both SH 225 and SH 288 were constructed in November, but the temperatures of each were very different, as were the wind conditions.

Relative humidity of US 290-Hempstead, Cypress is as 97.0 %, and 96.5 % at one inch below the surface. Climatic conditions are similar to Hempstead and Cypress except for wind velocity. In addition, the relationship between temperature, relative humidity, and depth were plotted in Figures D.2 and D.3.

Table D.1 Climatic Condition Utilized of Each Site

Weather condition	US 290- Hempstead	US 290- Cypress	SH -255	SH 288
Day of year (of 365)	240	260	340	335
Latitude (degrees)	30	30	30	30
Cloud cover fraction (0-1)	0.5	0.5	0.5	0.5
Wind velocity (mph)	3.2	6.2	3.1	1.4
Maximum ambient RH (%)	89	87.5	76.04	48.3
Minimum ambient RH (%)	69	66.5	56.04	28.3
Maximum ambient temperature (C)	29.4	30.8	19.3	16.8
Minimum ambient temperature (C)	18.3	19.6	8.2	5.8
Time of casting (0-24)	8	8	8	8

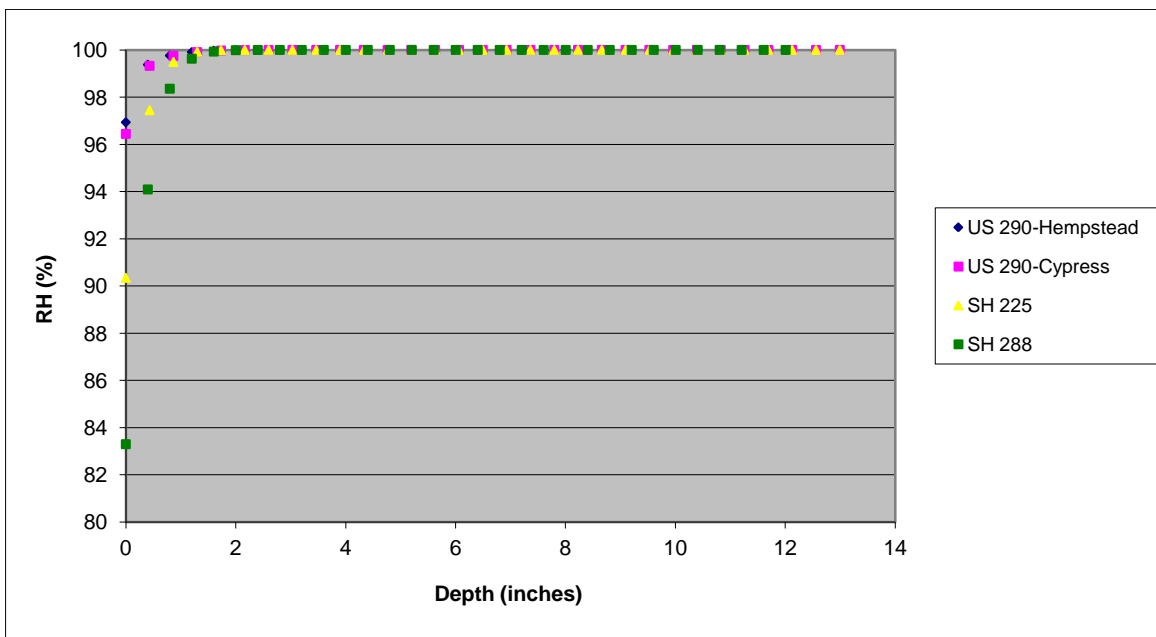


Figure D.1 Depth vs RH.

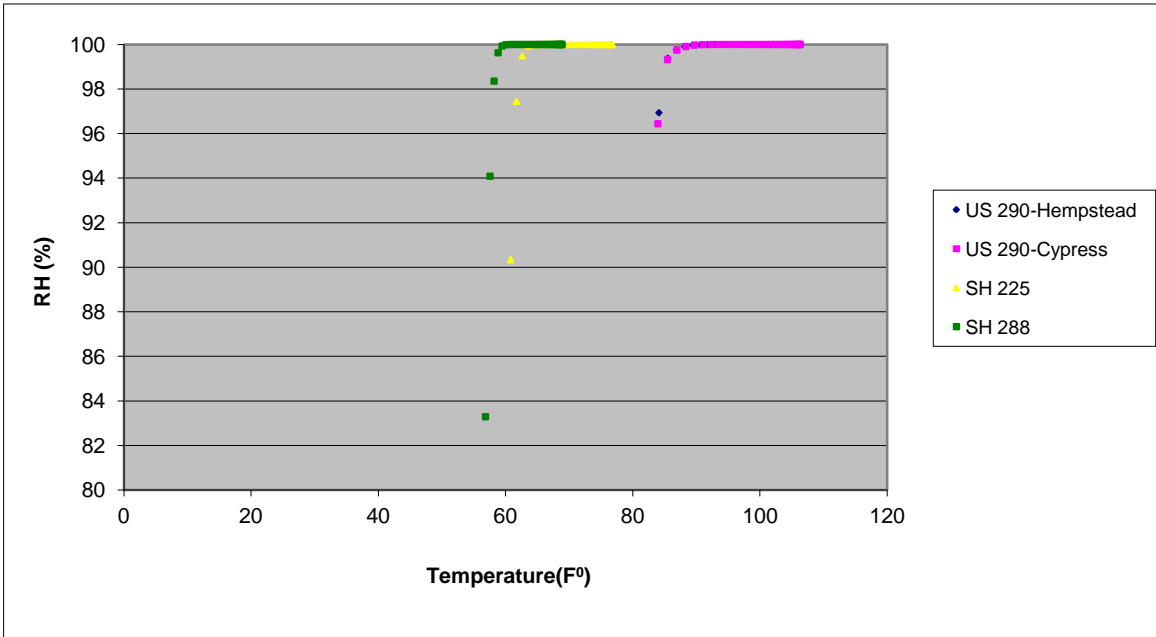


Figure D.2 Temperature vs RH

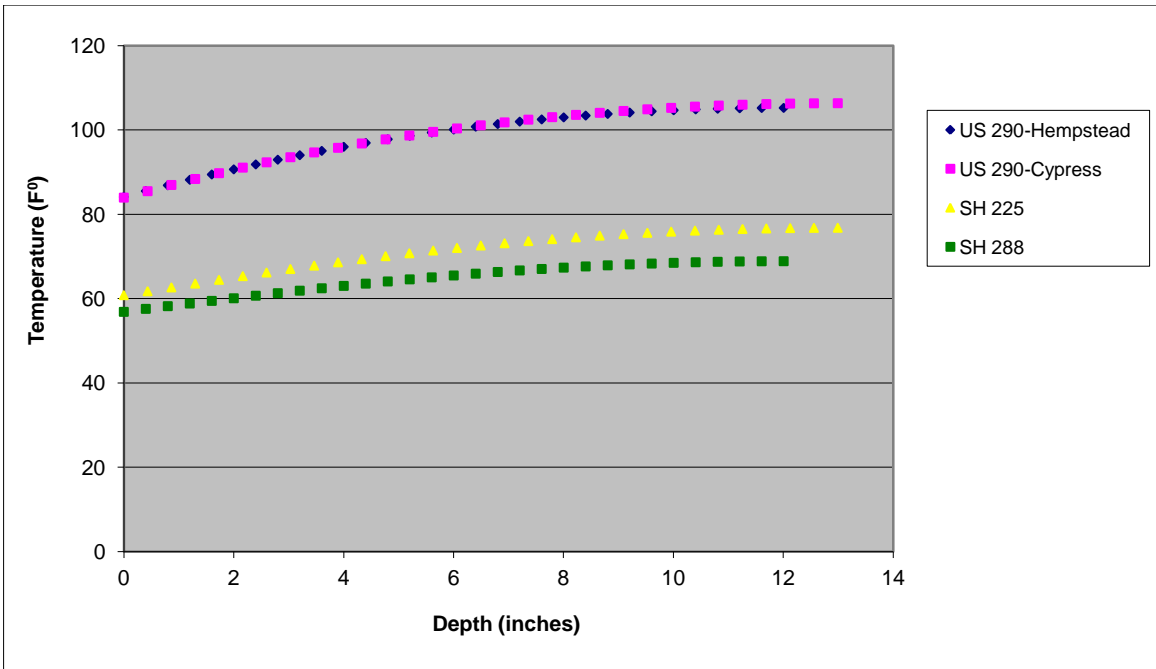


Figure D.3 Temperature vs Depth

Drying shrinkage was determined from the obtained moisture gradients, which causes shear stress components in the surface of a concrete slab. Thus, equivalent total strain difference between pavement surface and bottom is expressed as:

$$\Delta\varepsilon = \alpha_{\text{CTE}}\Delta T_{\text{eq}} + \varepsilon_{\infty}\Delta(1-\text{RH}^3)_{\text{eq}} \quad (\text{D.1})$$

where, α_{CTE} = coefficient of thermal expansion
 ΔT_{eq} = equivalent linear temperature difference
 ε_{∞} = ultimate shrinkage
 $\Delta(1-\text{RH}^3)_{\text{eq}}$ = equivalent linear humidity difference coefficient

α_{CTE} was examined in terms of aggregate type and the mineral components of the coarse aggregate. Specifically, an α of 6.96×10^{-6} was used for the US 290-Hempstead and Cypress Hanson source. α of SH 225 and 288 was 6.2×10^{-6} for the Fordyce source. ΔT_{eq} and $\Delta(1-\text{RH}^3)_{\text{eq}}$ are used to account for non-linear trends of heat and RH gradients since the temperature and moisture are not linearly distributed with respect to the depth of slab. In this project, $\Delta(1-\text{RH}^3)_{\text{eq}}$ was determined from the Concrete Modeling Software as stated previously, instead of equation D.2.

$$\Delta T_{\text{eq}} = Bh - \frac{3D}{20}h^3, \Delta\varepsilon_{\text{eq}} = Bh - \frac{3D}{20}h^3 \quad (\text{D.2})$$

where, B and D = coefficients (-0.003, and -0.001 respectively)

h = thickness of slab (inch)

ε_{∞} induces wrapping stress in concrete slab due to a pavement restraint (Bazant and Wu, 1974). ε_{∞} can be calculated using the following equation

$$\varepsilon_{\infty} = 1330 - 970y \quad (\text{D.3})$$

and y and z can be expressed respectively as :

$$y = (390z^{-4} + 1)^{-1} \quad (\text{D.4})$$

and

$$z = .0381\sqrt{f'_{c28}} \left[1.25\sqrt{\frac{a}{cm}} + 0.5\left(\frac{g}{s}\right)^2 \right] \left(\frac{1+s/c}{w/cm} \right)^{1/3} - 12. \quad (D.5)$$

where, a/cm = aggregate-cementitious material ratio
 g/s = gravel-sand ratio
 s/c = sand-cement ratio
 w/cm = water-cementitious material ratio
 f'_{c28} = compressive strength at 28 days in ksi

Table D.2 Assumed Factor Used to Compute Ultimate Shrinkage

Parameters	Value
a/cm	4.2
g/s	3.6
s/c	1.8
w/cm	0.45
f'_{c28}	4.5

The equivalent linear temperature and humidity difference coefficients were calculated for each site as shown in Table D.3. The equivalent strain gradient is calculated using equation D.1. Climatic conditions dedicated the strain causing shear stress in each site.

Table D.3 Equivalent Linear Humidity Difference Coefficient in Each Site

	US 290-Hempstead	US 290-Cypress	SH 225	SH 288
Thickness (in)	12	13	12	12
ΔT_{eq}	0.2232	0.29055	0.2232	0.2232
α	6.90E-06	6.90E-06	6.50E-06	6.50E-06
ε_{∞}	1.00E-03	1.00E-03	1.00E-03	1.00E-03
$\Delta(1-RH^3)_{eq}$	0.09	0.11	0.25	0.43
$\Delta\varepsilon$	6.30E-04	7.00E-04	5.25E-04	1.12E-03

Equivalent strain gradients obtained from each site are used to determine A_0 as shown in Table 6.1. A_0 is utilized to calculate A_1 and A_2 which directly affect the shear stress of each site (see Table 6.1).

APPENDIX E

EQUIVALENCIES FOR SPALL DAMAGE CALCULATION

In order to facilitate efficient computation of accumulated damage, equivalencies for traffic loading can be employed. Such equivalencies can be used to convert traffic that is often distributed by both load and axle type as well as laterally across the wheel path to a standard loading. An equivalent wander factor (EWF) is used to convert traffic that is laterally distributed across the wheel path into the minimum number of applications at a designated critical location (the slab corner) which typically produces the maximum level of spall damage in the slab. This concept has been used in the past in the development of the PCA method (1984), early versions of IDOT's JPCP procedure (Zollinger and Barenberg, 1989), and the FAA Airfield pavement design guide (1995). Accounting for traffic wander is essential in rigid pavement design because the location of the applied load greatly influences the magnitude of the resulting damage.

E.1 Calculation Procedure

The equivalency for damage due to load groups (ELF) or axle types (EAF) is determined as:

$$\text{ELF or EAF} = \frac{N_j}{\sum n_i} \quad (\text{E.1})$$

Where, N_j = traffic applied at the slab corner (position j) causing the same amount of damage as the total traffic in the wheel path.

$$\sum n_i = \text{total traffic in the wheel path}$$

The axle types included are single axle (SA), tandem axle (TA), and tridem axle (Tri). Total damage at the corner is equivalent to the damage at the wheel path (position j):

$$D_j = \sum \frac{n_i}{N_{f_d}} \quad (\text{E.2})$$

Where, n_i = component of the wheel path traffic associated with load position i causing shear stress at critical position j

D_j = total damage due to all the load positions i in wheel path at critical position j

The allowable loads to failure are defined as:

$$N_{f_i} = 10^{k_1 + k_2 r_i} \quad (\text{E.3})$$

Where: $r_i = \frac{\sigma_{spall}}{MoR}$; I – load group or axle type

$$\sigma_{spall} = \text{spall stress (F/L}^2) = \frac{6M}{t^2}$$

MoR = modulus of rupture (F/L²)

$$M = \text{spall bending moment (FL)} = \frac{E_c t^3 \Delta\delta}{4(l^{*2})}$$

t = depth of spall (L)

l^* = length of spall (L)

E_c = concrete modulus of elasticity (F/L²)

$\Delta\delta$ = delta deflection across the transverse crack at the slab corner (position j) due to load at loaded position i

$$= \delta_L - \delta_U = \delta_L (1 - LTE) = \frac{2 \cdot DE}{k\delta_L} \left\{ \frac{1}{1 + LTE} \right\} (\text{L})$$

δ_L = loaded deflection (L)

δ_U = unloaded deflection (L)

LTE = load transfer efficiency

DE = differential energy (subsequently defined)

Bending moment or the DE at the slab corner was determined from loaded deflections at selected positions (across the wheel path) along the transverse crack or joint using the ISLAB2000 finite element modeling software. The resulting spall stresses are used in the accumulated damage at the slab corner; ELF or EAF values are calculated using the deflection equations noted below.

E.2 Transverse Single Axle Dimensionless Deflection Profile

ISLAB2000 finite element program was used to develop transverse dimensionless deflection profiles based on an 18 kip single axle (SA) load for the corner position. Three different slab thicknesses were considered i.e. 6 in., 10 in., and 16 in with three different load transfer efficiencies (LTE) such as zero LTE, 45% LTE, and 95% LTE. The SA wheel load was placed at the slab-corner for a given slab thickness and load transfer configuration and the deflection at the corner was obtained. The load was placed at 6 in. increments across the slab width up to 60 in. from the corner and deflections at the corner for each loaded position were obtained. The dimensionless deflection was expressed in terms of radius of relative stiffness (l) and load position in the transverse direction from the corner. The relationship of the dimensionless deflection for the SA with radius of relative stiffness and load position is shown in equation E.4. Note that when the individual deflections were expressed in terms of, $\frac{\delta k l^2}{P}$, the profiles were similar for different LTEs for a given slab thickness and load position.

$$\delta^* = \frac{\delta k l^2}{P} = a + b \sqrt{x} + c \sqrt{y} \ln(y) \quad (E.4)$$

Where: a = 0.004920832

b = 0.16834363

c = -0.025856456

x = radius of relative stiffness (l), in.

y = load position in the transverse direction of the slab, in.

k = modulus of subgrade reaction (psi per in.)

P = total load (in.)

E.3 Equivalent Wander Factor (EWF)

The deformation energy (DE) at the slab-corner due to SA load applications across the slab was computed using Equation. E.5. The variation of DE at the slab-corner due to load applications at different positions across the slab width is presented in Figure E.1.

$$DE = \frac{k}{2} \delta_L^2 \left\{ 1 - \left(\frac{LTE}{100} \right)^2 \right\} \quad (E.5)$$

Traffic was assumed to be normally distributed across the slab width. A typical distribution of traffic across the slab width is presented in Figure E.2. The center of the normal distribution was placed/ superimposed at distance D from the corner of the slab. This distance D is the mean of the assumed traffic distribution. An illustration of distance D is given in Figure E.5. Three different lateral distances (D) were considered such as 12 in., 24 in., and 36 in. as the mean of the normal distribution having a standard deviation of 10 in. The DEs at the slab corner for load applications across the slab width were computed for different combinations of slab thicknesses (6 in., 10 in., and 16 in.) and LTEs (no load transfer, 45% LTE, and 95% LTE). For a given slab thickness and LTE combination, the variation of DE at the slab-corner for different load positions were produced similar to Figure E.1. The normal distributions with different D values were superimposed on those DE-graphs. The cumulative deformation energy at the slab-corner due to normally distributed traffic applications across the slab width was then computed. The summation of the DEs at the slab-corner considering normally distributed traffic across the slab width is the equivalent wander factor (EWF).

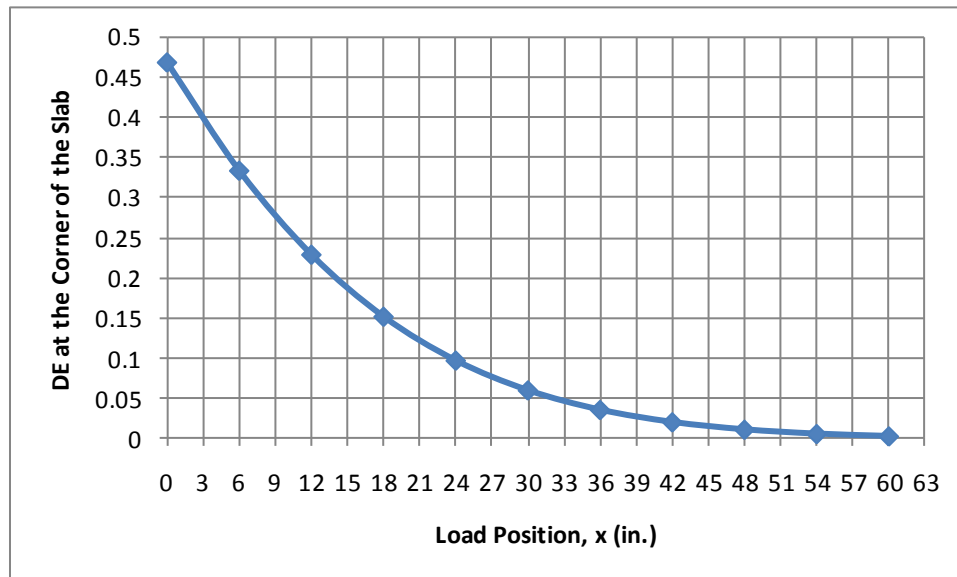


Figure E.1 Deformation Energy at the Slab Corner due to Different Load Positions.

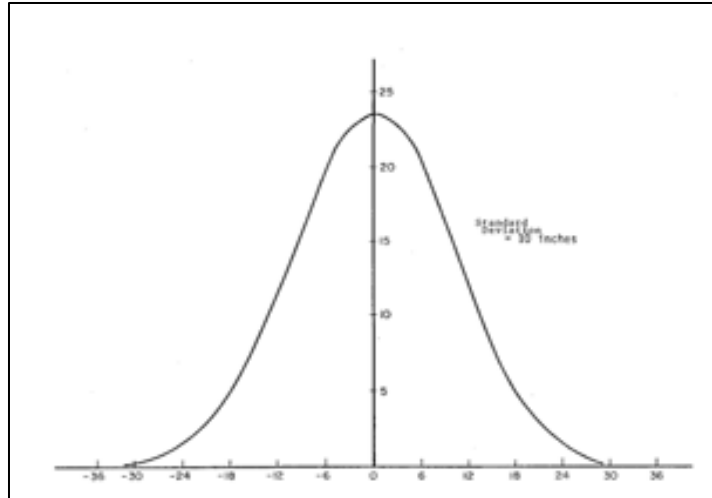


Figure E.2 Typical Distribution of Wheel Load across the Slab.

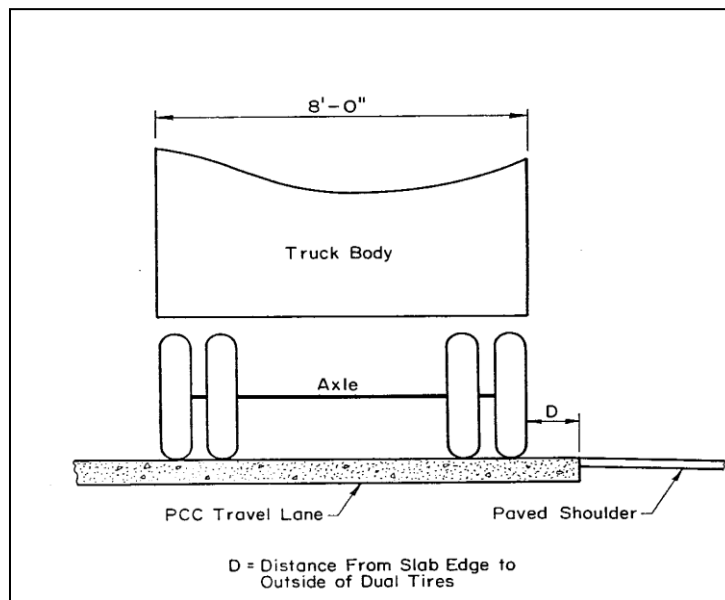


Figure E.3 Illustration of Mean Distance from Slab Edge to Outside of Dual Tires (D).

For a given D value, EWF was expressed in terms of radius of relative stiffness and LTE (i.e. zero LTE, 45% or 95%) as per equation E.3 where a, b, and c are different coefficients. Similar expressions of EWF were formulated for different values of D (12, 24, or 36 in.). Using the EWF expressions, equations for coefficients a, b, and c were formulated in terms of the D-value as shown. For a given D value, the coefficients a, b,

and c can be obtained. Then for a given radius of relative stiffness and LTE, the EWF can be obtained according to Equation E.6.

$$\ln(EWF) = a + b\sqrt{x} + cy^{1.5} \quad (E.6)$$

Where: $a = -0.0017 D^2 - 0.0948 D + 5.2251$
 $b = 0.0002 D^2 - 0.0113 D - 1.221$
 $c = -2 \times 10^{-7} D^2 - 2 \times 10^{-5} D - 0.003$
 x = radius of relative stiffness
 y = LTE (%)

E.4 Equivalent Load Factor and Equivalent Axle Factor (EAF)

Equivalent load factor (ELF) and equivalent axle factor (EAF) are obtained by taking the ratio of the DE of an axle type to the DE of an 18 kip load according to Equation E.7. The DE is obtained according to equation E.5.

$$ELF \text{ or } EAF = \frac{DE_i}{DE_{18 \text{ kip}}} \quad (E.7)$$

where: I = axle type (tandem axle or tridem axle)
 DE_i = deformation energy for an axle type

$DE_{18 \text{ kip}}$ = deformation energy for 18 kip load

For ELF, equation D.1 can be used to obtain dimensionless deflection for a given load group. DE for that load group can be computed using Equation D.2. Then ELF can be obtained for that load group according to Equation E.7.

To develop EAF for a tandem axle (36 kip) and a tridem axle (54 kip), three different slab thicknesses such as 6, 10, and 16 in. were considered along with the three different load transfer efficiencies (no load transfer, 45% load transfer, and 95% load transfer). For the tandem axle, the load was positioned at the corner to obtain the deflection at the corner. Deflections were obtained by placing the load in two different ways: (i) the leading axle was placed at the corner of the approach slab, and (ii) the rear axle was placed at the corner of the approach slab with the leading axle residing on the leading slab. The average of these deflections was used to obtain the dimensionless deflection for the tandem axle as a function of radius of relative stiffness and load transfer efficiency. Similarly to the tridem axle, the lead axle, the middle axle, and the rear axle were placed

at the corner of the slab to obtain the deflections. The average of the deflections was utilized to obtain the dimensionless deflection function for the tridem axle in terms of radius of relative stiffness and load transfer efficiency. The dimensionless deflection equations for single axle, tandem axle, and tridem axle are shown in Equations E.8, E.9, and E.10, respectively.

$$\ln z = a + b \sqrt{x} + c y \quad (\text{E.8})$$

where: $a = -0.55669065$
 $b = 0.094778826$
 $c = -0.0070261469$
 $x =$ radius of relative stiffness (l), in.
 $y =$ load transfer efficiency
 $z =$ dimensionless deflection at corner

$$\ln z = a + b \sqrt{x} \ln(x) + c \sqrt{y} \ln(y) \quad (\text{E.9})$$

where: $a = -2.1498456$
 $b = 0.044667408$
 $c = -0.011383783$
 $x =$ radius of relative stiffness (l), in.
 $y =$ load transfer efficiency
 $z =$ dimensionless deflection at corner

$$\ln z = a + b \frac{x}{\ln(x)} + c \sqrt{y} \ln(y) \quad (\text{E.10})$$

where: $a = -2.7649205$
 $b = 0.12025817$
 $c = -0.0097651654$
 $x =$ radius of relative stiffness (l), in.
 $y =$ load transfer efficiency
 $z =$ dimensionless deflection at corner

After obtaining the dimensionless deflection for a given axle, deflection of the loaded slab can be obtained and then the DE can be computed using equation E.5. EAF can then be obtained using equation E.7. To compute EAF, the DE for an 18 kip SA load will have to be used in the denominator of Equation E.7.

E.5 Spalling Traffic Model

Once all the factors such as EWF, ELF, and EAF are obtained, the design traffic (N_{Design}) can be obtained according to Equation E.11.

$$N_{Design} = N_k = EWF_k \sum_j \{EAF_j \sum_i (EAL_i n_i)\} \quad (E.11)$$

where: i = load group (e.g. 12 - 14 kip, 14 – 16 kip, etc.)

j = axle type (single axle, tandem axle, and tridem axle)

k = wander

n_i = number of load application per load group i

EAL_i = equivalent load factor for load group i

EAF_j = equivalent axle factor for axle type j

EWF_k = equivalent wander factor for wander



TEXAS TECH UNIVERSITY
Multidisciplinary Research in Transportation

Texas Tech University | Lubbock, Texas 79409
P 806.742.3503 | F 806.742.4168